Functional Characterisation Of Arrhythmia And Cardiomyopathy-Linked Mutations At R1051 In The Cardiac Ryanodine Receptor: Effects At Different Organisational Levels Of Calcium Release

Tessa Harris

A thesis submitted for the degree of
Doctor of Philosophy

Cardiff University

July 2025

Summary

The human cardiac ryanodine receptor (hRyR2) is a calcium (Ca^{2+}) ion channel found on the sarcoplasmic reticulum of cardiomyocytes. It plays a key role in excitation-contraction coupling, and dysfunction of hRyR2 due to mutation is associated with arrhythmias and cardiomyopathies. Clustering of hRyR2 via inter-channel interactions is proposed to regulate its function, preventing uncontrolled Ca^{2+} release. This study aimed to characterise three arrhythmia and cardiomyopathy-associated mutations – R1051P, R1051C, and R1051H – that are found in a domain thought to be involved in the inter-channel interaction, to determine whether they cause dysfunctional Ca^{2+} release from hRyR2 and if this is due to changes to the clustering interaction.

The research comprised three main parts to assess hRyR2 function at the whole cell, population (i.e. cluster), and single channel level. Spontaneous whole cell Ca^{2+} release from human embryonic kidney cells expressing R1051-mutant hRyR2 was significantly different for each mutant compared to the Wild Type (WT) and showed slowed Ca^{2+} release kinetics and increased abnormalities that are indicative of dysfunction. All mutants also showed significantly reduced endoplasmic reticulum Ca^{2+} store loads, likely caused by Ca^{2+} leak; this is strongly associated with channel gain of function and arrhythmia. Droplet interface bilayers and total internal reflection fluorescence microscopy were used to assess Ca^{2+} release from populations of hRyR2. This revealed increased activity and increased cooperativity of Ca^{2+} release from R1051P populations, and R1051C / R1051H appeared to form larger clusters than the WT. Single channel analysis of R1051P gating compared to the WT revealed no differences at sub-activating and saturating Ca^{2+} concentrations.

This indicates that dysfunction of R1051-mutants most likely arises at the population level possibly due to altered inter-channel clustering, which contributes to abnormal Ca^{2+} handling in whole cells. This highlights a potentially novel mechanism that may contribute to the development of arrhythmia and cardiomyopathy.

Acknowledgements

Firstly, to my supervisor, Dr Lowri Thomas; thank you for your unwavering patience, kindness, and support throughout my PhD. You have always been there when I have needed anything and never fail to provide the right advice, whether that be experiment or life related. I couldn't have asked for a better supervisor. Thank you.

I'd like to thank Dr Ollie Castell, my second supervisor, for always being eager to explore new questions, even if the answers weren't always clear. I also have to thank Dr David Jamieson and Hannah Baird for their help in droplet interface bilayer experiments and answering my (sometimes basic) questions, and Dr Bevan Cumbes for providing the initial DIBs research that forms the basis of much of my project; you have all been invaluable. Thanks also to Dr Kathryn Taylor and Dr Sam Jones for your feedback each year.

Thanks to Aisha for being a wonderful friend and lab partner, even if we have different ideas about how to organise pipette tips.

To my parents and brother, thank you for encouraging me to keep going even when things are tough, and instilling a love of science in me from a young age. I also have to acknowledge the infallible wisdom of my cats, Beans and Purrito, for being there when I came home every day and reminding me that life goes on.

Finally, to my partner Rhys, thank you for being there through the good days and the bad, for putting up with my stressing, and for always supporting me no matter what.

Publications

Published abstracts arising from this thesis

Harris, T., Thomas, NL. 2024. Investigation of RyR2 Arg1051 arrhythmia and cardiomyopathy-linked mutations: functional effects at the single channel, population and whole cell level. *Physiology in Focus 2024*. Northumbria University, Newcastle. PCA011.

Other peer reviewed publications

Koulouris, C.R., Gardiner, S.E., Harris, T.K., Elvers, K.T., Roe, S.M., Gillespie, J.A., Ward, S.E., Grubisha, O., Nicholls, R.A., Atack, J.R., Bax, B.D. 2022. Tyrosine 121 moves revealing a ligandable pocket that couples catalysis to ATP-binding in serine racemase. *Commun Biol* 5(346). doi: 10.1038/s42003-022-03264-5

Auhim HS, Grigorenko BL, Harris TK, Aksakal OE, Polyakov IV, Berry C, Gomes GDP, Alabugin IV, Rizkallah PJ, Nemukhin AV, Jones DD. 2021. Stalling chromophore synthesis of the fluorescent protein Venus reveals the molecular basis of the final oxidation step. *Chem Sci* 12(22), pp: 7735-7745. doi: 10.1039/d0sc06693a

Contents

Summary ____ **II**

Acknowledgements ____ **III**

List of publications ____ **IV**

Contents ____ **V**

List of figures and tables ____ **XIII**

Abbreviations ____ **XVIII**

Chapter 1 Introduction ____ **1**

1.1 Calcium signalling in the heart ____ **2**

1.1.1 Heart structure and cardiomyocyte contraction ... 2

1.1.2 The cardiac action potential ... 4

1.1.3 Excitation-contraction coupling ... 5

1.1.4 Beta-adrenergic pathway ... 7

1.2 RyR2 as an ion channel ____ **8**

1.2.1 Ryanodine receptor isoforms ... 8

1.2.2 RyR2 structure ... 9

1.2.3 Structural basis for RyR2 gating and permeation properties ... 11

1.2.4 Ultrastructural arrangement and coupled gating of RyR2 clusters ... 12

1.3 Regulation of RyR2 by ions and small molecules ____ **16**

1.3.1 Activation of RyR2 by cytosolic Ca^{2+} ... 16

1.3.2 Luminal Ca^{2+} as an activator of RyR2 ... 17

1.3.3 Termination of CICR ... 18

1.3.4 Activation and inhibition by ATP and Mg^{2+} ... 19

1.4 Post-translational modifications of RyR2 ____ **20**

1.4.1 Phosphorylation of RyR2 by PKA and CaMKII ... 20

1.4.2 Oxidative modification of RyR2: reactive oxygen species, *S*-nitrosylation and *S*-glutathionylation ... 22

1.5 Regulation by accessory proteins ____ **23**

1.5.1 Regulation by FKBP12 and FKBP12.6 ... 23

1.5.2 Regulation by Calmodulin and EF-hand proteins 26
1.5.3 Regulation by Calsequestrin-2, Junctin and Triadin 27
1.5.4 Regulation by Junctophilin-2 28
1.6 Dysregulation of RyR2 and its role in arrhythmias and cardiomyopathies ___29
1.6.1 RyR2-associated diseases 29
1.6.2 Catecholaminergic polymorphic ventricular tachycardia 29
1.6.2.1 Mechanisms of dysfunction in CPVT 33
1.6.2.2 Treatment of CPVT 36
1.6.3 Arrhythmogenic right ventricular dysplasia 38
1.6.4 Loss-of-function RyR2 diseases 38
1.6.5 RyR2 in heart failure 39
1.6.6 Dilated cardiomyopathy 40
1.6.7 Hypertrophic cardiomyopathy 41
1.7 Project Rationale _____43
1.7.1 Mutation at arginine 1051 in the P1 domain 43
1.7.2 Structure of the P1 domain 44
1.7.3 R1051P 46
1.7.4 R1051C 47
1.7.5 R1051H 48
1.7.6 R1051L and R1051G 48
1.8 Project hypotheses and aims _____49

Chapter 2 Materials and methods _____51
2.1 Materials List _____52
2.1.1 General laboratory reagents, chemicals and equipment 52
2.1.2 Site directed mutagenesis 52
2.1.3 Cloning 52
2.1.4 Transformation and propagation 53
2.1.5 Miniprep – small-scale plasmid isolation 53
2.1.6 Maxiprep – large-scale plasmid isolation 53
2.1.7 Restriction digest 54

2.1.8 Agarose gel electrophoresis....54
2.1.9 Mammalian Cell Culture....54
2.1.10 Effectene® transfection....55
2.1.11 $CaPO_4$ transfection....55
2.1.12 Preparation of cell homogenate....55
2.1.13 Preparation of mixed membranes....55
2.1.14 Protein Quantification....55
2.1.15 Solubilisation and purification....56
2.2 Methods 57
2.2.1 Site Directed Mutagenesis of SpeI/SanDI Cassette....57
2.2.2 Cloning of R1051P eGFP-hRyR2....60
2.2.3 Transformation and propagation of WT and mutant RyR2....60
2.2.4 Miniprep of plasmid DNA....61
2.2.5 Maxiprep of plasmid DNA....62
2.2.6 Restriction digest....63
2.2.7 Agarose gel electrophoresis....64
2.2.8 Mammalian cell culture and routine maintenance....64
2.2.9 Effectene transfection of HEK293 cells with WT or mutant eGFP-hRyR2 plasmid DNA....65
2.2.10 $CaPO_4$ transfection of HEK293 cells with WT or mutant eGFP-hRyR2 plasmid DNA....65
2.2.11 Preparation of cell homogenate from transfected HEK293 cells for Western blotting....66
2.2.12 Preparation of mixed membrane microsomal fractions from transfected HEK293 cells for solubilisation and purification....66
2.2.13 Protein assay for quantification of protein concentration....67
2.2.14 Solubilisation and purification via sucrose density centrifugation of hRyR2 from microsomal material....67

Chapter 3 Generation of R1501-mutant hRyR2 constructs and their expression in HEK293 cells ____ 69

3.1 Introduction ____ 70

3.1.1 Engineering recombinant hRyR2 mutations and transfection into a suitable cell system ____ 70

3.1.2 HEK293 cells as a system for recombinant hRyR2 expression ____ 71

3.1.3 Chapter Aims ____ 71

3.2 Materials & Methods ____ 73

3.2.1 Materials ____ 73

3.2.1.1 Immunofluorescence Antibodies, Reagents and Buffers ____ 73

3.2.1.2 SDS-PAGE ____ 73

3.2.1.3 Western Blotting Antibodies, Reagents and Buffers ____ 73

3.2.2 Immunofluorescence analysis ____ 74

3.2.3 Sodium Dodecyl Sulphate Polyacrylamide Gel Electrophoresis (SDS-PAGE) ____ 75

3.2.4 Western Blotting for Protein Expression ____ 75

3.2.5 Assessing phosphorylation at S2808 via Western Blotting ____ 76

3.3 Results ____ 78

3.3.1 Generation of R1051-mutant hRyR2 constructs was successful ____ 78

3.3.2 The transfection efficiency of R1051-mutant hRyR2 was comparable to the WT ____ 82

3.3.3 Immunofluorescence analysis indicated R1051P and R1051C-hRyR2 were not correctly trafficked within the cell. ____ 83

3.3.4 R1051-mutants did not significantly differ in their expression level compared to WT-hRyR2 but do indicate reduced expression ____ 87

3.3.5 Phosphorylation at S2808 is not significantly different in R1051-mutant hRyR2. ____ 87

3.4 Discussion ____ 90

3.4.1 All R1051-mutant hRyR2 constructs were successfully engineered and expressed in HEK293 cells ____ 90

3.4.2 Immunofluorescence and expression analysis suggests varying levels of degradation of the different R1051-mutants ____ 90

3.4.3 Phosphorylation at S2808 is unaffected by mutations at R1051 93
3.4.4 Conclusions 95

Chapter 4 Assessing the effect of R1051-mutation in hRyR2 on whole cell Ca^{2+} release via live cell Ca^{2+} imaging in HEK293 cells _____96

4.1 Introduction _____97
4.1.1 Functional characterisation of hRyR2 mutations 97
4.1.2 Ca^{2+} imaging for assessing whole cell calcium release 97
4.1.3 Measuring spontaneous Ca^{2+} release in a recombinant cell system.....99
4.1.4 Chapter Aims.....100
4.2 Materials & Methods _____101
4.2.1 Materials 101
4.2.2 Live cell Ca^{2+} imaging in HEK293 cells.....101
4.2.3 Data processing and analysis 102
4.2.4 Caffeine experiments.....103
4.3 Results _____104
4.3.1 R1051 mutation desynchronises spontaneous hRyR2-mediated Ca^{2+} release from HEK293 cells. 104
4.3.2 Aberrant Ca^{2+} release is increased in R1051-mutant hRyR2. 109
4.3.3 Caffeine response of R1051-mutant hRyR2 is impaired and SR Ca^{2+} load is reduced. 113
4.4 Discussion _____116
4.4.1 R1051 mutations result in slower Ca^{2+} release kinetics that may indicate Ca^{2+} leak 116
4.4.2 Ca^{2+} transient abnormalities may indicate the mechanism of dysfunction in R1051-mutant hRyR2.....120
4.4.3 Altered Ca^{2+} release can contribute to the generation of cardiomyopathy..124
4.4.4 Conclusions 126

Chapter 5 Investigating Ca^{2+} release from populations of R1051-mutant hRyR2 using droplet interface bilayers ____ 127

5.1 Introduction ____ 128

5.1.1 Analysing population function in droplet interface bilayers with total internal reflection fluorescence microscopy ____ 128

5.1.2 Chapter Aims ____ 129

5.2 Materials and Methods ____ 131

5.2.1 Materials ____ 131

5.2.2 Droplet interface bilayers and total internal reflection fluorescence microscopy ____ 131

5.2.3 Processing of droplet interface bilayer and total internal reflection microscopy data ____ 134

5.2.4 Classifying Ca^{2+} flux behaviours from hRyR2 populations and quantifying cluster size from Gaussian Fitting Suite data ____ 136

5.3 Results ____ 138

5.3.1 R1051P-hRyR2 populations display a different Ca^{2+} release profile in droplet interface bilayers than WT-hRyR2 ____ 138

5.3.2 Distribution of common behaviours is relatively comparable between different hRyR2 variants ____ 141

5.3.3 R1051C-hRyR2 and R1051H-hRyR2 appear to form larger clusters than WT-hRyR2 ____ 142

5.3.4 The distribution of Ca^{2+} flux behaviours changes as the estimated number of channels increases ____ 144

5.3.5 Novel behaviours observed in R1051P-hRyR2 have a higher activtiy regardless of cluster size ____ 148

5.4 Discussion ____ 150

5.4.1 R1051C-hRyR2 and R1051H-hRyR2 mutants may have the capacity to form larger clusters than WT-hRyR2 ____ 150

5.4.2 Limitations in calculating cluster size ____ 151

5.4.3 Novel Ca^{2+} release behaviours in R1051P-hRyR2 populations indicate dysfunction that could cause Ca^{2+} leak ____ 154

5.4.4 Possible mechanisms of R1051-mutant hRyR2 dysfunction 157
5.4.5 Conclusions 159

Chapter 6 Analysis of single channel gating of R1051P-hRyR2 and WT-hRyR2 _____ 160

6.1 Introduction _____ 161
6.1.1 Analysing single channel function in artificial lipid bilayers 161
6.1.2 Idealisation of RyR2 single channel currents 162
6.1.3 Potential impact of R1051-mutation on single channel function 165
6.1.4 Chapter Aims 165
6.2 Materials and Methods _____ 167
6.2.1 Materials 167
6.2.2 Single channel recording in artificial lipid bilayers 167
6.2.3 hRyR2 channel shutdown and activation 170
6.2.4 Maximal activation of hRyR2 channels present in the bilayer 170
6.2.5 Analysis of channel gating.....171
6.2.6 Modelling of channel gating 172
6.3 Results _____ 174
6.3.1 Open probability and dwell times of R1051P-hRyR2 under saturating Ca^{2+} conditions are not significantly different from WT-hRyR2.....174
6.3.2 Modelling indicates no significant difference in the gating of R1051P-hRyR2 channels compared to WT-hRyR2 176
6.3.3 WT and R1051P-hRyR2 both demonstrate modal gating.....179
6.4 Discussion _____ 181
6.4.1 P_O and modelling reveal no conclusive evidence for a difference in function at the single channel level of R1051P and WT-hRyR2. 181
6.4.2 Channels in high activating Ca^{2+} conditions do not always achieve a high P_O 183
6.4.3 Conclusions 185

Chapter 7 General discussion _____186

7.1 General discussion and future work_____187

7.1.1 Are R1051P, R1051C and R1051H-hRyR2 dysfunctional and at which organisational level is that dysfunction evident? 187

7.1.2 What is the mechanism of dysfunction in R1051P-hRyR2? 189

7.1.3 How does the dysfunction of R1051-mutants fit with the mechanisms proposed for CPVT? 192

7.1.4 Do R1051C and R1051H-hRyR2 cause dysfunction by a different mechanism to R1051P? 194

7.1.5 How would HCM and DCM arise from the altered Ca^{2+} release of R1051-mutants? 196

7.1.6 What treatment options are likely to be most effective for mutations at R1051? 199

7.1.7 Future work 201

7.1.8 Concluding remarks 202

List of figures and tables

Chapter 1

Figures

Figure 1.1. Structure of cardiac muscle 3
Figure 1.2. Phases of the cardiac action potential....5
Figure 1.3. Schematic of EC-coupling within a cardiomyocyte....6
Figure 1.4. Schematic of β-adrenergic stimulation in cardiomyocytes 7
Figure 1.5. Structure of RyR2 in the closed state and schematic of domains 10
Figure 1.6. Structure of the RyR2 pore in the open and closed state 12
Figure 1.7. Clustering of RyR2 and the proposed interacting regions 14
Figure 1.8. Proposed locations of binding sites for Ca^{2+} and divalent cations on RyR2 17
Figure 1.9. Location of the phosphorylation hotspot in the P2 domain and the main phosphorylation sites....21
Figure 1.10. Schematic of binding sites for main regulatory accessory proteins of RyR2 26
Figure 1.11. Diagram of normal systolic function vs aberrant diastolic function contributing to DADs 31
Figure 1.12. Location of disease-associated mutations and hotspot domains in RyR2 32
Figure 1.13 Proposed mechanism of SOICR dysfunction in CPVT-RyR2 mutants 35
Figure 1.14. Changes to SOICR threshold in CRDS RyR2 mutations 39
Figure 1.15. Changes to SOICR threshold in E3DS RyR2 mutations 42
Figure 1.16. Location and structure of the P1 domain in RyR2 and RyR1. 45

Tables

Table 1.1. In silico predictions of pathogenicity for all identified R1051-hRyR2 missense mutations....47

Chapter 2

Figures

Figure 2.1 Schematic demonstrating the cassette-based site-directed mutagenesis strategy and ligation into the full-length pcDNA3-eGFP-hRyR2 construct with R1051-mutation 58

Tables

Table 2.1 Oligonucleotide primers for site-directed mutagenesis for R1051-mutant hRyR2 .59
Table 2.2. Thermal cycling conditions for site-directed mutagenesis....59

Chapter 3

Figures

Figure 3.1 Restriction digest of WT, R1051P, R1051C and R1051H-hRyR2 following maxiprep indicate the expected fingerprint pattern of full-length hRyR2. 79

Figure 3.2. Chromatograms show successful introduction of R1051-mutations into the pcDNA3-eGFP-hRyR2 plasmid 80

Figure 3.3. Restriction digest of miniprep following ligation of R1051P-hRyR2 plasmid shows recombination of DNA in some large colonies 81

Figure 3.4. Transfection efficiency of R1051-mutant hRyR2 in HEK293 cells transfected by Effectene is comparable to WT-hRyR2.. 82

Figure 3.5. Immunofluorescence analysis of HEK293 cells expressing WT or R1051-mutant hRyR2 indicates abnormal trafficking of R1051P and R1051C-hRyR2 85

Figure 3.6. Co-occurrence of eGFP fluorescence with the ER marker calreticulin is significantly reduced in cells expressing R1051P-hRyR2 86

Figure 3.7. Densitometry analysis of Western blots shows no significant difference in expression of R1051-mutant hRyR2 in HEK293 cells compared to WT-hRyR2 88

Figure 3.8. Densitometry analysis of phosphorylation at S2808 revealed no significant difference in phosphorylation of R1051-mutant hRyR2 compared to the WT 89

Figure 3.9. Proximity of P1 and P2 of the closest adjacent monomer in RyR1. 94

Chapter 4

Figures

Figure 4.1. Diagram of confocal microscope setup for live cell Ca^{2+} imaging. 98

Figure 4.2. Parameters measured from Ca^{2+} imaging data 103

Figure 4.3. Representative traces of spontaneous Ca^{2+} release events in HEK293 cells transfected with WT or R1051-mutant hRyR2 show different morphologies 105

Figure 4.4. Quantification of Ca^{2+} transients produced by HEK293 cells transfected with WT or R1051-mutant hRyR2 show significant differences between all mutants and the WT 107

Figure 4.5. Examples of aberrant Ca^{2+} release traces from HEK293 cells expressing WT or R1051-mutant hRyR2. 111

Figure 4.6. Representative example of caffeine-induced Ca^{2+} release in HEK293 cells expressing R1051-mutant hRyR2 or WT-hRyR2 114

Figure 4.7. HEK293 cells expressing R1051P and R1051H-hRyR2 have an impaired response to caffeine activation and a lower ER Ca^{2+} load.....115

Tables

Table 4.1. Median values for all Ca^{2+} imaging parameters in HEK293 cells show significant differences between WT-hRyR2 and R1051-mutant hRyR2 105
Table 4.2. Confidence intervals indicate that altered Ca^{2+} transient characteristics due to mutation at R1051 likely represent practical changes in hRyR2 function.....108
Table 4.3. HEK293 cells transfected with R1051-mutant hRyR2 show an increased number of Ca^{2+} transient abnormalities compared to WT-hRyR2 109
Table 4.4. The distribution of Ca^{2+} transient abnormalities is different in HEK293 cells transfected with R1051-mutant hRyR2 compared to WT-hRyR2 112

Chapter 5

Figures

Figure 5.1. Schematic of droplet interface bilayer device and setup on a TIRF microscope 132
Figure 5.2. Schematic of main steps of Gaussian Fitting Suite to analyse DIBs data 135
Figure 5.3. Alignment of electrophysiological and optical traces to estimate fluorescence equivalent to 1 channel 137
Figure 5.4. R1051P-hRyR2 populations exhibit novel Ca^{2+} flux behaviours not seen in WT-hRyR2 in DIB / TIRF.....140
Figure 5.5. R1051P-hRyR2 populations contain a comparable number of channels to WT-hRyR2 populations, but R1051C-hRyR2 and R1051H-hRyR2 populations are significantly larger 143
Figure 5.6. The distribution of Ca^{2+} release behaviours changes as estimated cluster size increases 145
Figure 5.7. The distribution of Ca^{2+} release behaviours from populations of WT and R1051-mutant-hRyR2 changes with cluster size 147
Figure 5.8. Relationship between estimated cluster size and channel activity or fluctuation of activity in WT and R1051P-hRyR2 populations recorded in DIBs 149
Figure 5.9. Relationship between applied voltage and estimated cluster size, channel activity, and behaviour in WT and R1051P-hRyR2 populations recorded in DIBs 156

Tables

Table 5.1. The distribution of Ca^{2+} release behaviours is different in R1051-mutant hRyR2 Ca^{2+} flux spots compared to WT-hRyR2 spots.....141
Table 5.2. Distribution of estimated minimum cluster size for all hRyR2 is comparable 143
Table 5.3. There is a significant association between Ca^{2+} release behaviour from hRyR2 and cluster size.....144
Table 5.4. The distribution of Ca^{2+} release behaviours as cluster size increases in R1051P-hRyR2 populations is different than in WT-hRyR2 populations.....146

Chapter 6

Figures

Figure 6.1. Example of different channels gating at the same P_O but with notable visible differences in behaviour. 163
Figure 6.2. Gating models of WT-hRyR2 at sub-activating, activating and saturating $[Ca^{2+}]_{cyt}$ from single channel recording 164
Figure 6.3. Schematic of cup and block system used in artificial lipid bilayer setup 169
Figure 6.4. Settings applied in QuB using idl/base function 172
Figure 6.5. Progressive building of gating model in QuB based on histograms and Maximum Log Likelihood for WT-hRyR2. 173
Figure 6.6. P_O, T_O and T_C of W-hRyR2 and R1051P-hRyR2 in 100 µM $[Ca^{2+}]_{cyt}$ were not significantly different 175
Figure 6.7. R1051P-hRyR2 and WT-hRyR2 show similar gating behaviours at sub-activating $[Ca^{2+}]_{cyt}$. 176
Figure 6.8. Gating models of WT-hRyR2 and R1051P-hRyR2 channels in saturating Ca^{2+} conditions are comparable. 178
Figure 6.9. Gating models of WT, R1051P and R1051H-hRyR2 at high P_O in contaminant $[Ca^{2+}]_{cyt}$ are comparable. 179
Figure 6.10. Modal gating results in changes to the P_O of WT and R1051P-hRyR2 channels over time 180

Appendix

Appendix I. Primer sequences for Sanger sequencing of full-length hRyR2. 204
Appendix II. Enhanced agarose gels showing bands below 1500bp following maxiprep 205
Appendix III. Western blotting of WT and R1051-mutant eGFP-hRyR2 expression in HEK293 cells 206
Appendix IV. Western blotting of phosphorylation at S2808 for WT and R1051-mutant hRyR2 expressed in HEK293 cells. 207
Appendix V. Example of stripped Western blot prior to assessing phosphorylation levels.. 208
Appendix VI. Normality testing of Ca^{2+} transient data from HEK293 cells expressing WT or R1051-mutant hRyR2 reveals data were non-normally distributed. 209
Appendix VII. Total internal reflection fluorescence microscopy allows eGFP fluorescence on individual hRyR2 channels to be visualised. 210
Appendix VIII. Laser path and filter setup used for TIRF microscopy in DIBs. 211
Appendix IX. Step size comparison can be used as a secondary classification for Ca2+ release behaviour from hRyR2 populations. 212
Appendix X. IF functions applied in Microsoft Excel to sort DIBs optical traces into categories. 213
Appendix XI. R1051P-hRyR2 populations contain a comparable number of channels to WT-hRyR2 populations, despite the appearance of very large clusters. 214
Appendix XII. Dwell times of each state in gating models of WT-hRyR2 and R1051P-hRyR2 channels were not significantly different 215
Appendix XIII. Frequency of each state in gating models of WT-hRyR2 and R1051P-hRyR2 channels were not significantly different 216

Abbreviations

2D	Two-dimensional
3D	Three-dimensional
AC	Adenylate cyclase
ADP	Adenosine diphosphate
AF	Atrial fibrillation
AM	Acetoxymethyl
AMP	Adenosine monophosphate
ANOVA	Analysis of variance
AP	Action potential
Apo-CaM	Ca^{2+}-free calmodulin
ARVD2/ARVC	Arrhythmogenic right ventricular cardiomyopathy/dysplasia
ATP	Adenosine triphosphate
β-AR	Beta adrenergic receptor
BCA	Bicinchoninic acid assay
BSA	Bovine serum albumin
BSolB	Bridging solenoid subunit B
BSolC	Bridging solenoid subunit C
Ca^{2+}	Calcium ion
Ca^{2+}-CaM	Ca^{2+}-bound calmodulin
$[Ca^{2+}]_{cyt}$	Cytosolic Ca^{2+} concentration
$[Ca^{2+}]_{SR}$	SR lumen Ca^{2+} concentration
CaM	Calmodulin
CaMKII	Ca^{2+} /calmodulin-dependent protein kinase II
cAMP	Cyclic adenosine monophosphate
cDMEM	Complete Dulbecco's Modified Eagle Medium
CHAPS	(3-((3-cholamidopropyl) dimethylammonio)-1-propanesulfonate) buffer
CICR	Calcium-induced calcium-release
CPVT	Catecholaminergic polymorphic ventricular tachycardia
CPVT1	Autosomal dominant CPVT, usually caused by RyR2 mutation
CPVT2	Autosomal recessive CPVT, usually caused by CSQ2 mutation

CPVT3	CPVT caused by mutation in *TECRL*
CPVT4	CPVT caused by mutation in *CALM1*
CPVT5	CPVT caused by mutation in *TRDN*
CRDS	Calcium Release Deficiency Syndrome
CRU	Ca^{2+} release unit
Cryo-EM	Cryo-electron microscopy
CSol	Core solenoid
CSQ2	Calsequestrin 2, cardiac isoform
CTD	C-terminal domain
DAD	Delayed afterdepolarisation
DCM	Dilated cardiomyopathy
dH_2O	Deionised water
ddH_2O	Double distilled water
DIB	Droplet interface bilayer
DMEM	Dulbecco's Modified Eagle Medium
DNA	Deoxyribonucleic acid
DPhPC	1,2-Diphytanoyl-sn-glycero-3-phosphocholine
dSTORM	Direct stochastic optical reconstruction microscopy
DTT	Dithiothreitol
E3DS	Exon-3 deletion syndrome
EAD	Early afterdepolarisation
EC	Excitation-contraction
ECG	Electrocardiogram
ECL	Enhanced chemiluminescence
EDTA	Ethylenediaminetetraacetic acid
eGFP	Enhanced green fluorescent protein
EGTA	Ethylene glycol tetraacetic acid
ER	Endoplasmic reticulum
EtBr	Ethidium bromide
F	Peak fluorescence signal intensity
F0	Basal fluorescence signal intensity
FCS	Foetal calf serum

FKBP	FK506-binding protein
FKBP12	FK506-binding protein 12kDa isoform
FKBP12.6	FK506-binding protein 12.6kDa isoform
GFP	Green fluorescent protein
GFS	Gaussian fitting suite
G_I	Stimulatory G-protein
GoF	Gain-of-function
GRK	G-protein receptor kinases
G_S	Inhibitory G-protein
HBS	HEPES buffered saline
HCM	Hypertrophic cardiomyopathy
HD1	Helical domain subunit 1
HD2	Helical domain subunit 2
HEK293	Human embryonic kidney cells 293
HEPES	4-(2-hydroxyethyl)-1-piperazineethanesulfonic acid buffering agent
HF	Heart failure
HGMD	Human Genome Mutation Database
HRP	Horseradish peroxidase
hRyR2	Human ryanodine receptor
IF	Immunofluorescence
iPSC	Induced pluripotent stem cells
JSol	Junctional solenoid
JUN	Junctin
JPH2	Junctophilin-2
KRH	Krebs Ringer HEPES buffer
LB	Luria Bertani
LB_{AMP}	Luria Bertani supplemented with ampicillin
LMNA	Lamin A/C
LoF	Loss-of-function
LQTS	Long QT syndrome
LTCC	L-type Ca^{2+} channel
mDMEM	Minimal Dulbecco's Modified Eagle Medium

MOPS	3-(N-morpholino)propane sulphonic acid buffer
MR_2	Muscarine receptor 2
NaB	Sodium butyrate
NTA	Nitrilotriacetic acid
NCX	Na^+/Ca^{2+} exchanger
NTD	N-terminal domain
PBS	Phosphate buffered saline
PC	L-Alpha-Phosphatidylcholine
PALM	Photoactivated localisation microscopy
PDB	Protein Database
PE	Phosphatidylethanolamine
PKA	Protein kinase A
PLB	Phospholamban
PLM	Phospholemman
P_O	Open probability
pRyR2	Porcine cardiac ryanodine receptor
PSG	Penicillin-streptomycin-glutamine
ROS	Reactive oxygen species
RT	Room temperature
RY	Ryanodine repeat
RyR	Ryanodine receptor
RyR1	Skeletal ryanodine receptor
RyR2	Cardiac ryanodine receptor
RyR3	Nervous tissue ryanodine receptor
SAN	Sinoatrial node
SCD	Sudden cardiac death
SDM	Site directed mutagenesis
SDS-PAGE	Sodium dodecyl sulphate-polyacrylamide gel electrophoresis
SERCa	Sarcoplasmic/endoplasmic reticulum Ca2+ ATPases
SERCa2a	Isoform of SERCa in cardiomyocytes
SMOD	Standard measure of difference
SOC	Super Optimal broth with Catabolite repression

SOICR	Store overload-induced Ca^{2+} release
SR	Sarcoplasmic reticulum
TAE	Tris, acetic acid, and EDTA buffer
TBS	Tris buffered saline
TBS-T	Tris buffered saline with Tween-20
TEM	Transmission electron microscopy
TIRF	Total internal reflection fluorescence microscopy
TM	Transmembrane
T_M	Melting temperature
TMD	Transmembrane domain
TnI	Troponin I
TRD1	Triadin
T-tubules	Transverse tubules
UV	Ultraviolet
VF	Ventricular fibrillation
VT	Ventricular tachycardia
WT	Wild type

Chapter 1

Introduction

1.1 Calcium signalling in the heart

Calcium ions (Ca^{2+}) are crucial second messengers in many cellular processes and regulate a wide range of functions including gene transcription, apoptosis, cell proliferation and muscle contraction (Berridge et al. 2000). At the most basic level, activation of these processes occurs when Ca^{2+} concentrations increase from 100 nM at rest up to 1 mM locally, and the diverse range of roles becomes possible due to variations in the speed, size and spatial patterning of Ca^{2+} signals, as well as interplay with other signalling pathways within the cell (Berridge et al. 2000). Owing to its role in muscle contraction, Ca^{2+} signalling also plays a vital role in generating the heartbeat, as Ca^{2+} transduces the electrical signal generated by the sinoatrial node (SAN) into the mechanical contraction of cardiomyocytes and the overall contraction of the heart.

1.1.1 Heart structure and cardiomyocyte contraction

The human heart consists of four chambers – two atria and two ventricles – enclosed in muscular tissue called the myocardium, all of which are surrounded by a protective double-walled sac called the pericardium. The myocardium contains cardiomyocytes which are cardiac-specific muscle cells containing contractile machinery that, on activation, results in contraction of the heart (**Figure 1.1**). Cardiac muscle is striated in appearance due to the cardiomyocytes being connected in a longitudinal pattern by intercalated discs, with each myocyte being approximately 50-100 µm long and 10-20 µm wide. Cardiomyocytes are surrounded by the sarcolemma, a specialised plasma membrane containing ion channels for transport of ions into and out of the cell. Within the cardiomyocyte are myofilaments, which form organised arrays called sarcomeres that constitute the smallest functional unit of striated muscles that align to form myofibrils. Each myofilament contains thick (myosin) and thin (actin) filaments (**Figure 1.1**), which interact to cause contraction of the myocyte.

During systole, the contraction phase, Ca^{2+} released from the sarcoplasmic reticulum (SR) binds to troponin C and troponin I on the thin filament, which causes a conformational change that reveals an active site for myosin binding, and displaces troponin I which, at rest, inhibits the myosin head. Hydrolysis of adenosine triphosphate (ATP) by ATPase on myosin then allows for the formation of cross bridges between the myosin head and the active site. Once bound, the myosin head bends and rotates in a ‘power stroke’, which pulls the myosin

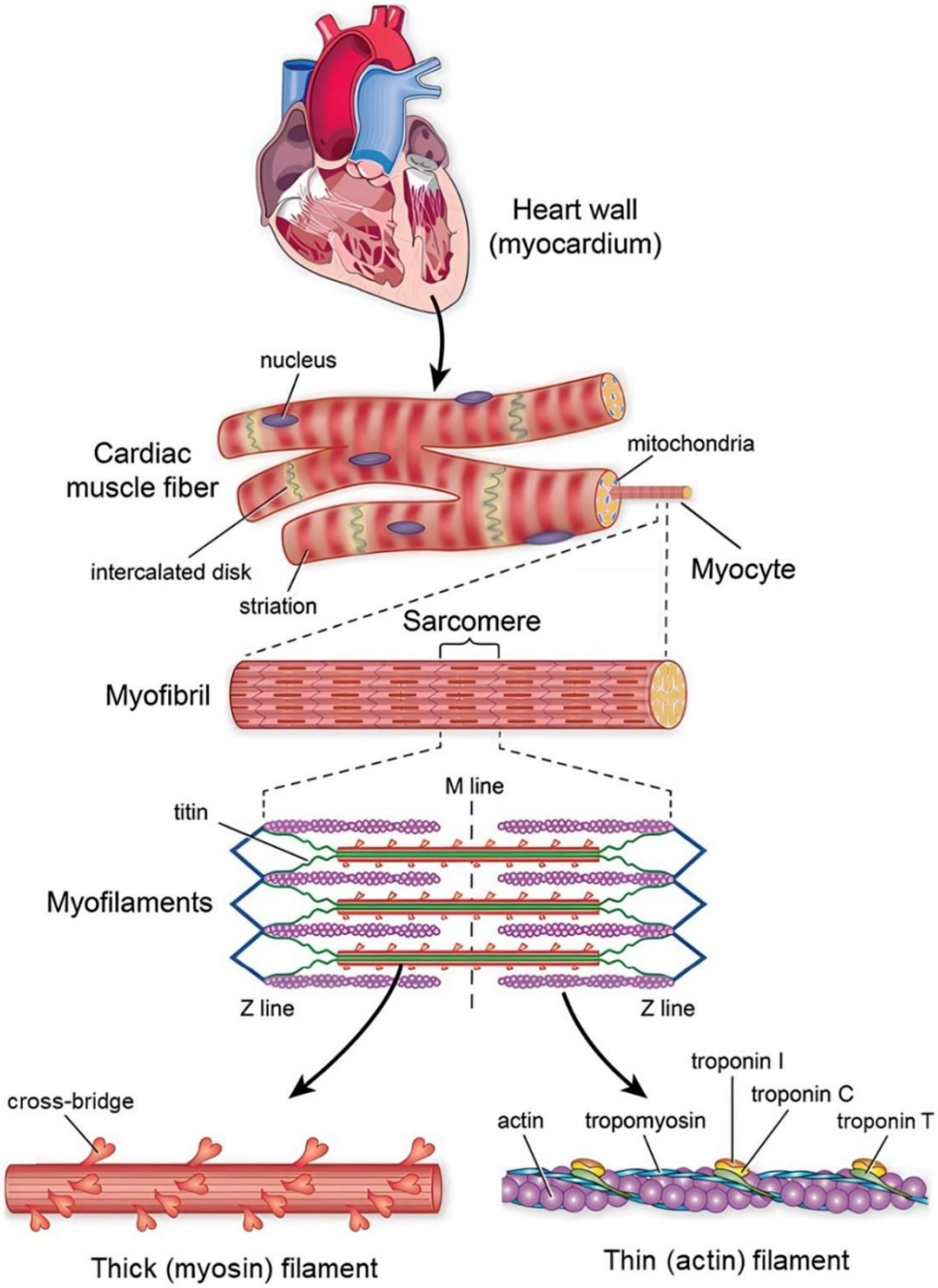

Figure 1.1. Structure of cardiac muscle. The myocardium is comprised of many muscle fibres that are made of myocytes connected via intercalated disks that facilitate signal transduction. Each myocyte contains structures called sarcomeres, which contain repeating thin actin filaments and thick myosin filaments; these thin and thick bands result in the striated appearance of cardiac muscle. The M line marks the centre of the sarcomere and attaches myosin filaments to each other; the Z line marks the ends of the sarcomere and attaches to the thin actin filaments and to myosin filaments via titin. Troponin T assists in binding tropomyosin to the actin filament. Figure taken from Golob et al. (2014).

head along the actin filament. The concerted contraction of myocytes results in contraction of the ventricular chambers which pumps blood from the heart to circulate around the body. Adenosine diphosphate (ADP) is released from the myosin head and a new ATP molecule binds, resulting in detachment of the cross bridge. As Ca^{2+} levels drop, it unbinds from troponin C and I and the cycle is then primed to repeat, allowing myosin to move along the actin filament provided there is sufficient Ca^{2+} and ATP. Lowered cytosolic Ca^{2+} is characteristic of the diastolic phase, during which the cardiomyocytes are at rest and the ventricular chambers of the heart can refill, primed for the next cycle of contraction.

1.1.2 The cardiac action potential

Excitation-contraction (EC) coupling is the process linking the action potential (AP) – the electrical stimulus for cardiac contraction – to the mechanical contraction and relaxation of cardiomyocytes that generate the heartbeat (Bers 2002). The electrical stimulus needed to generate an AP originates spontaneously from the SAN, the pacemaker of the heart. This stimulus results in a change in membrane potential that is propagated through the heart from the SAN to the atria, the atrioventricular node and finally to ventricular myocytes via gap junctions in the intercalated discs. The ventricular cardiac AP is summarised briefly below and illustrated in **Figure 1.2**:

- Phase 4 – Resting; membrane potential is stable at approximately -90mV.
- Phase 0 – Rapid depolarization; membrane potential quickly becomes positive (+40mV) due to fast influx of Na^+.
- Phase 1 – Early repolarization; inward Na^+ current is inactivated, and K^+ channels open causing K^+ efflux, reducing the membrane potential to 0mV.
- Phase 2 – Plateau; Influx of Ca^{2+} via voltage-gated L-type Ca^{2+} channels (LTCCs) balances K^+ efflux.
- Phase 3 – Repolarization; Ca^{2+} channels close but K^+ efflux continues, restoring membrane potential to -90mV.

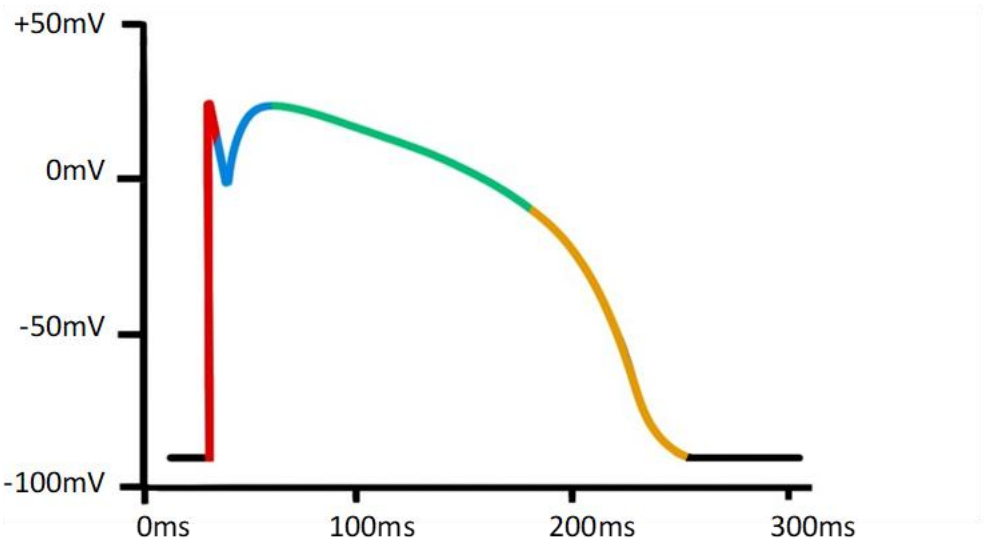

Figure 1.2. Phases of the cardiac action potential. There are five phases to the cardiac action potential. Phase 4 (black line) is the rest phase, followed by rapid depolarization in Phase 0 (red), slight repolarization in Phase 1 (blue) followed by a slower return to rest through Phase 2 (green) and 3 (yellow). One full cycle takes approximately 300ms. Figure adapted from Santana et al. (2010).

1.1.3 Excitation-contraction coupling

EC-coupling is a complicated and tightly regulated process involving many proteins in the cardiomyocyte; an overview is shown in **Figure 1.3**. It is dependent on specialised structures on the sarcolemma called transverse tubules (T-tubules); these are invaginations in the membrane that bring the sarcolemma into close range of the SR and where LTCCs concentrate at a region called the dyad. The T-tubules bring LTCCs into close apposition (~15nm) with cardiac ryanodine receptor (RyR2) channels on the SR membrane (Fabiato 1983; Bers 2002) in what is known as a couplon (Franzini-Armstrong et al. 1999). Couplons are also sometimes referred to as Ca^{2+} release units (CRUs), however this term is more commonly used to describe multiple clusters of RyR2 acting as one functional unit (also termed a 'supercluster') (Baddeley et al. 2009). During Phase 2 of the cardiac AP, LTCCs on the sarcolemma open due to changes in membrane potential, causing influx of Ca^{2+} into the cytosol (Bers 2006). This increases the concentration of Ca^{2+} ($[Ca^{2+}]$) at the dyad up to 10 µM, allowing Ca^{2+} to bind to high-affinity sites on RyR2 channels; this results in a conformation change in RyR2 causing it to open and release Ca^{2+} from the SR (Bers 2008). Release of Ca^{2+} from a single RyR2 channel increases local $[Ca^{2+}]$ and results in activation of

neighbouring channels, generating a Ca^{2+} 'spark' that propagates through the cell in a Ca^{2+} 'wave' to form a Ca^{2+} transient (Cheng et al. 1993; Bers 2002). This process is termed Ca^{2+} induced Ca^{2+} release (CICR) and is a critical stage in EC-coupling (Fabiato 1983; Bers 2002), as Ca^{2+} released from the SR goes on to bind to troponin C and facilitate the interaction of actin and myosin for muscle contraction.

Post-contraction, cardiomyocytes need to go through a diastolic phase to prepare for the next cycle of contractions, requiring a decrease in cytosolic $[Ca^{2+}]$ ($[Ca^{2+}]_{cyt}$) in order to dissociate Ca^{2+} from troponin C. This occurs via the sodium-calcium exchanger (NCX) exporting Ca^{2+} out of the cell in exchange for Na^{+}, and reuptake of Ca^{2+} into the SR by the sarcoplasmic/endoplasmic reticulum Ca^{2+}-ATPase (SERCa). Imbalances in Ca^{2+} flux in and out of the cytosol can disrupt normal functioning of the cell and are causative of arrhythmia.

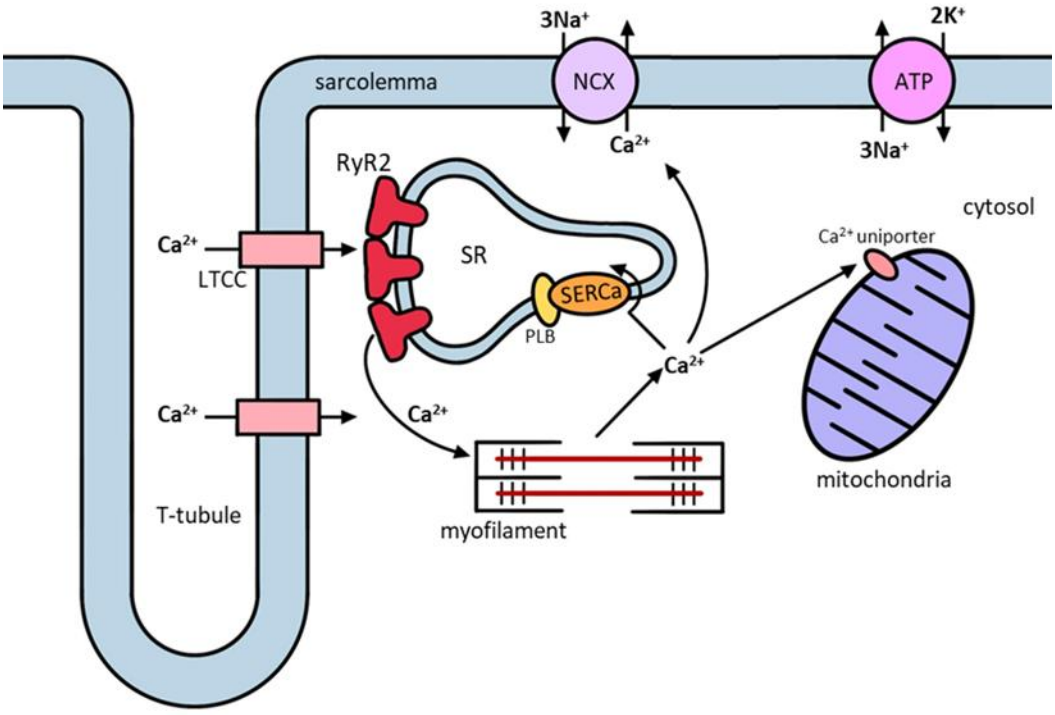

Figure 1.3. Schematic of EC-coupling within a cardiomyocyte. Fast inward current of Na^{+} during Phase 1 of the cardiac AP triggers depolarization which activates voltage-gated LTCCs. This increases the local concentration of Ca^{2+} in the vicinity of RyR2 channels on the SR membrane causing them to activate and release stored Ca^{2+}. This results in an overall increase in Ca^{2+} in the cytosol which results in contraction of the myofilaments. As the cell returns to rest, Ca^{2+} levels in the cytosol decrease due to reuptake into the SR by SERCa (bound to phospholamban (PLB)), uptake into the mitochondria, and export via NCX. The Na^{+}/K^{+} ATPase helps maintain the resting membrane potential by exporting $3Na^{+}$ for every $2K^{+}$ imported. Figure adapted from Bers (2002).

1.1.4 Beta-adrenergic pathway

During times of physical and emotional stress, blood pressure and heart rate rise to meet the increased metabolic demands that ensue; this is known as the fight-or-flight response. This involves stimulation of β-adrenergic receptors (β-AR) by catecholamines such as adrenaline and noradrenaline, which activate these G-protein coupled receptors and subsequently activate adenylate cyclase (AC) (**Figure 1.4**). AC catalyses formation of the secondary messenger cyclic adenosine monophosphate (cAMP), which is involved in many

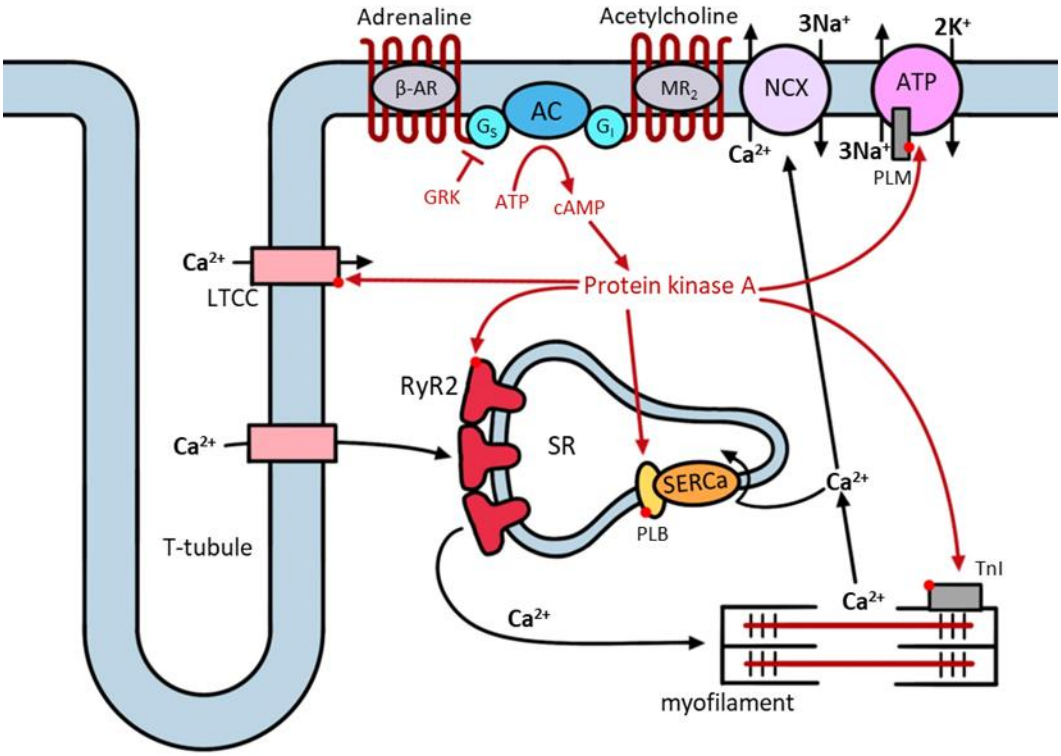

Figure 1.4. Schematic of β-adrenergic stimulation in cardiomyocytes. Catecholamines such as adrenaline and noradrenaline bind to and activate the β-AR during sympathetic stimulation. This triggers stimulatory G proteins (G_S) to activate AC which catalyses the formation of the second messenger cAMP from ATP; cAMP then activates protein kinase A (PKA). PKA phosphorylates many proteins in the cell including LTCCs, RyR2, PLB, phospholemman (PLM) and troponin I (TnI). This results in an overall increase in Ca^{2+} in the cytosol allowing it to bind to myofilaments for contraction; it is then exported via NCX or taken back up into the SR by SERCa. G-protein receptor kinase (GRK) phosphorylation of β-AR results in recruitment of arrestin, which inhibits the β-AR. The opposite effect is induced by binding of acetylcholine to the muscarine receptor (MR_2), resulting in activation of inhibitory G proteins (G_I) which inhibit AC and decrease cAMP production as part of the parasympathetic response. Figure adapted from Bers (2002) and El-Armouche and Eschenhagen (2009).

different signal transduction pathways and regulates processes including metabolism, gene expression and immune function. One of the ways that cAMP affects these processes is via activation of protein kinase A (PKA), a phosphotransferase enzyme whose activity is regulated by intracellular levels of cAMP. PKA phosphorylates many different proteins involved in EC coupling, including both LTCCs and RyR2. Phosphorylation of LTCCs increases influx of Ca^{2+} into the cell, and phosphorylation of RyR2 by PKA promotes channel opening. This results in increased Ca^{2+} release from the SR and increased contractility of cardiomyocytes, due to more Ca^{2+} being available to bind to the thin filament and facilitate cross-bridge formation (Catterall 2000; Marx et al. 2000). An overview of the β-adrenergic stimulation pathway is shown in **Figure 1.4**.

1.2 RyR2 as an ion channel

1.2.1 Ryanodine receptor isoforms

Ryanodine receptors (RyRs) are the largest known ion channels and are found in the endoplasmic reticulum (ER) or SR of excitable tissues throughout the body, acting as the main intracellular Ca^{2+} release channel. Three isoforms of ryanodine receptor are found in mammals; RyR1, RyR2, and RyR3. RyR1 is expressed primarily in skeletal muscle (Takeshima et al. 1989; Zorzato et al. 1990) and RyR3 mainly in the nervous tissue (Hakamata et al. 1992). RyR2 is predominantly expressed in the heart myocardium, however it is also abundant in the brain (hippocampus, cerebellum and cerebral cortex) and reproductive tissues (Lai et al. 1988; Nakai et al. 1990; Otsu et al. 1990; Marx et al. 2000). All three isoforms are expressed at lower levels throughout other tissues in the body, although their function outside their predominant regions is not well understood (Lanner et al. 2010). All three isoforms share approximately 66% sequence homology and thus maintain an overall similar structure and function (Hakamata et al. 1992). The majority of differences occur within three defined 'divergent regions', which correspond to binding sites for ligands and regulatory domains that may differentiate the function of each isoform, including variable Ca^{2+} and caffeine sensitivity (Sorrentino and Volpe 1993). Outside of these areas, sequence homology is upwards of 90% (Rossi and Sorrentino 2004).

The name ryanodine receptor is derived from the plant alkaloid, ryanodine, from *Ryania speciosa*. Ryanodine binds RyRs in their open conformation with high affinity and specificity,

locking it in a modified sub-conductance state (nanomolar concentrations) or a closed state (micromolar concentrations) (Tinker and Williams 1993; Tinker et al. 1996). This has made ryanodine a useful tool for identifying, isolating and studying RyRs, however it is also highly toxic given its ability to lock RyR channels in a modified state with a high open probability (P_O) but low conductance state, causing excess Ca^{2+} release and muscle contraction, or at higher concentrations complete paralysis (Tinker et al. 1996).

1.2.2 RyR2 structure

RyR2, like all isoforms of RyR, is a large, homotetrameric transmembrane ion channel, whose quaternary structure forms a quatrefoil shape with four-fold rotational symmetry that protrudes from the SR on the cytosolic side (Franzini-Armstrong et al. 1998) (**Figure 1.5A**). Each monomer consists of 4967 amino acids (human isoform), resulting in a tetramer of approximately 20,000 amino acids with a molecular weight of ~2.3MDa.

Due to its large size, elucidating the structure of RyR2 comes with many challenges and only cryo-electron microscopy (cryo-EM) studies have been able to resolve the structure of the channel in its entirety. Recent high resolution cryo-EM studies have resolved the structure of recombinant human RyR2 (hRyR2; R2474S-hRyR2 mutant) to 2.58 Å (Miotto et al. 2022), and multiple structures have achieved resolutions in the 3 to 5Å range in both the open and closed conformation and bound to a variety of modulators including FK506-binding protein 12.6kDa (FKBP12.6) and calmodulin (CaM) (Peng et al. 2016; Kobayashi et al. 2022; Miotto et al. 2022). These studies have clearly shown that each RyR2 monomer is formed of the following domains; N-terminal domain (NTD), SPRY1, SPRY2, SPRY3, P1 (also called RyR repeat (RY) 1&2 or clamp domain; future discussions will use the term P1), handle domain (also called junctional solenoid (JSol)), helical domain (HD1 and HD2, also called bridging solenoid (BSolB & BSolC)), P2 (also called RY3&4), central domain (also called core solenoid (CSol)), and channel domain (contains the transmembrane domain (TMD) and C-terminal domain (CTD)) (**Figure 1.5B**). All regions except the channel domain (which crosses the membrane and protrudes into the SR lumen) are found in the cytosolic portion of the protein. The central domain and NTD stack above the channel domain and occupy the central area of the tetramer. The other domains protrude outwards, with the handle domain and helical domains forming a bridge between SPRY1 / 2 / 3 and P1 on one side, and P2 on the other. There is some discrepancy between the nomenclature used by different

groups, with some calling the bridging solenoid the ‘central domain’; this study will use the nomenclature assigned by Peng et al (2016) which refers to the bridging solenoid as the ‘helical domain’ and the core solenoid as the ‘central domain’.

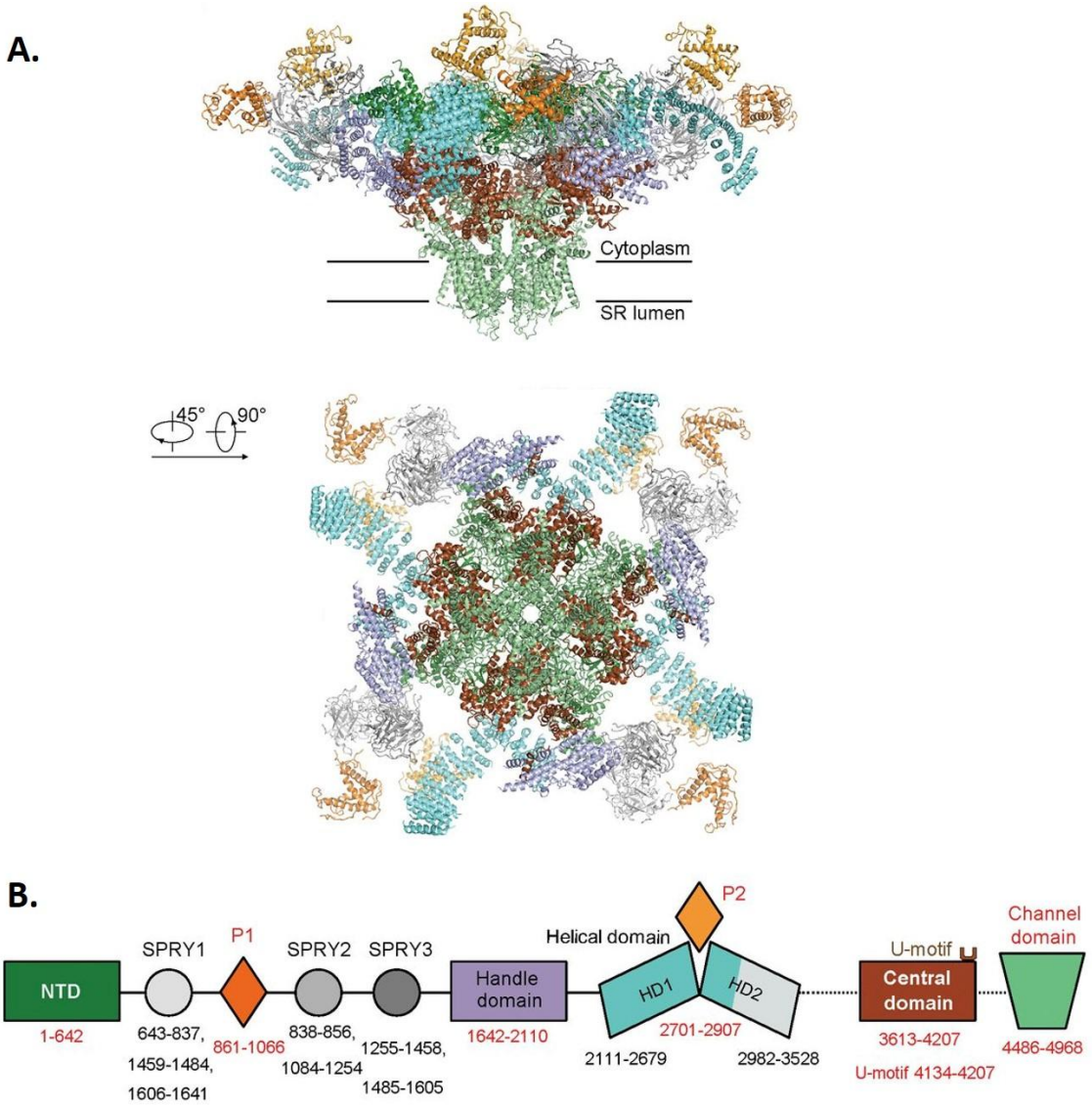

Figure 1.5. Structure of RyR2 in the closed state and schematic of domains. A. The structure of porcine RyR2 (pRyR2) in the closed state resolved to 4.2Å. The secondary structure is displayed and coloured according to the domains identified in **B. B**. The domain structure of an RyR2 monomer and their corresponding residues (porcine numbering); red numbering indicates confirmed boundaries. Figure adapted from Peng et al. (2016); Protein Database (PDB) accession code 5GO9 for pRyR2.

X-ray crystallography and cryo-EM have been used to resolve the structure of individual domains for both Wild Type (WT) and mutant RyR2, however due to the size of the ion channel there is no crystal structure available for the whole protein, with several unresolved loops present throughout the structure.

The main bulk of the protein sits on the cytosolic side of the SR, forming the characteristic 'mushroom' quatrefoil shape. Within this cytosolic region are binding sites for many regulators of RyR2, including FKBP12.6, CaM, and both high and low affinity Ca^{2+} sites needed for activation and to assist in termination of CICR (**Section 1.3.3**). The domains needed for interaction with adjacent RyR2s are also in the cytosolic domain, namely SPRY1 and P1 (with assistance from bound FKBP12.6; **Section 1.5.1**) (Cabra et al. 2016).

The transmembrane (TM) region is located close to the CTD in the 'channel domain' and contains six TM helices. These form the pore for ion movement and anchor the protein to the membrane; this is also the only luminal part of the protein (Peng et al. 2016). The ion channel selectivity filter is located within the TM pore and bears the amino acid motif GGGIGD, which is conserved in all RyR isoforms (Welch et al. 2004). A conformational change that takes place on activation of the channel by Ca^{2+} binding to high affinity sites is also required for ion transport (Peng et al. 2016). Activation shifts the constriction point from Ile4868 (rabbit RyR2; Ile4867 in human) in the closed conformation to Gln4864 (human Gln4863) in the open conformation (**Figure 1.6**) (Peng et al. 2016). The CTD itself lies on the cytosolic side of RyR2, buried in the central region.

1.2.3 Structural basis for RyR2 gating and permeation properties

The presence of the ion pore on its own is not sufficient to create the characteristic and essential gating activity that RyR2 possesses; this requires conformational changes to activate RyR2 and switch it from its closed to open conformation and vice versa (**Figure 1.6**). In the presence of activating Ca^{2+}, the S6 segments of the TM pore angle outwards, dilating the pore by approximately 8Å and shifting the constriction point from Ile4868 to Gln4864 to create a gate of approximately 4Å (**Figure 1.6B**) (Peng et al. 2016). At a larger scale, this shift presents as a downward (towards the SR) and clockwise (as viewed from the cytoplasm) twist in the SPRY1/2/3, P1/2 and helical domains, opposed by an upward and anticlockwise movement of the inner components, with the main structural changes occurring between the inner and outer parts (Peng et al. 2016).

Regarding selectivity, RyR2 is a cation specific ion channel with a moderate preference for divalent ions compared to monovalent ions (Tinker and Williams 1992; Gillespie et al. 2005), so while RyR2 carries many of the signatures of a Ca^{2+}-selective channel, it is not as strict in its preferences as other Ca^{2+} channels. This may be due to the rate at which Ca^{2+} must pass through the channel during EC coupling, with less selectivity helping speed up movement of ions from the SR lumen to the cytosol, and the relatively low concentration of other ions compared to Ca^{2+} meaning this is not a hindrance to its function as a Ca^{2+} channel. Its mild preference for divalent ions over monovalent is driven by charge/space competition; Ca^{2+} has a higher nuclear charge and smaller radius than K^{+} (or other monovalent cations) and is therefore preferred, and Ca^{2+} is also able to displace monovalent cations from the channel (Gillespie et al. 2005; Liu et al. 2021).

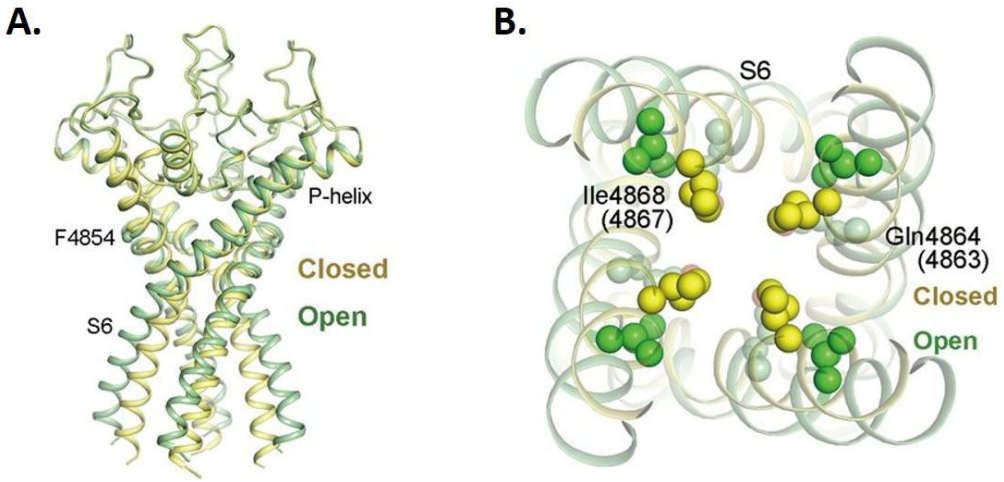

Figure 1.6. Structure of the RyR2 pore in the open and closed state. A. Overlay of the S6 bundle in the closed (yellow) and open (green) state, demonstrating the outward rotation of the pore upon opening of the channel; structures are aligned by the selectivity filter. **B.** Cytoplasmic view of the ion pore demonstrating the shifted constriction point from Ile4868 in the closed structure to Gln4864 in the open structure. Figure adapted from Peng et al. (2016); PDB accession codes 5GO9 (closed state) and 5GOA (open state) for pRyR2.

1.2.4 Ultrastructural arrangement and coupled gating of RyR2 clusters

In recent years, it has become increasingly clear that a key regulatory mechanism for Ca^{2+} handling in cardiomyocytes is the distribution of RyR2 within the SR. The need for grouping of RyR2s into spatially isolated clusters was initially proposed as a mechanism to prevent uncontrolled Ca^{2+} release via the positive feedback loop of CICR (Stern 1992). Later work

showed spatially and temporally isolated Ca^{2+} sparks, the summation of which would create a Ca^{2+} transient necessary for cardiomyocyte contraction and proposed that these would impose 'local control' over Ca^{2+} release based on the physical distance between groups of channels (Cheng et al. 1993; Cannell et al. 1995). It has since become apparent that RyR2s are organised into clusters of individual channels that serve to regulate Ca^{2+} release via allosteric communication and CICR (Marx et al. 2001; Sobie et al. 2006).

Initial studies estimated clusters to consist of approximately 100 tightly-packed channels (Franzini-Armstrong et al. 1999; Chen-Izu et al. 2006), however more recent studies utilising super-resolution microscopy techniques to resolve clusters to the single-molecule level have shown that they contain on average 15 channels (Baddeley et al. 2009; Macquaide et al. 2015; Munro et al. 2021). Initial studies showed that RyRs formed large 'checker-board' arrays with channels contacting each other via their corners (**Figure 1.7A**) (Yin and Lai 2000), however super-resolution has shown that in addition to the checker-board arrangement, a denser side-by-side organisation can be observed as well as more dispersed or isolated configurations (**Figure 1.7B**) (Wehrens et al. 2004b; Baddeley et al. 2009; Asghari et al. 2014; Hou et al. 2015; Asghari et al. 2020). The size and distribution of channels in a cluster has been directly linked to Ca^{2+} release in multiple studies, highlighting its importance as a regulator of RyR2 function. Smaller, sparsely packed clusters are reported to reduce Ca^{2+} spark frequency (Galice et al. 2018) but potentially increase 'silent' Ca^{2+} leak, where the amount of Ca^{2+} released is too low to contribute to sparks but is still implicated in the generation of arrhythmia (Wehrens 2007) and progression of heart failure (HF) (Kolstad et al. 2018; Dridi et al. 2020). On the other hand, densely packed clusters promote improved channel stability and reduced Ca^{2+} leak (Wehrens et al. 2004b; Asghari et al. 2020). These different organisations are dynamic and modified by multiple factors in the cell, including phosphorylation status (**Section 1.4.1**) and binding of FKBP12.6 (**Section 1.5.1**) and CaM (**Section 1.5.2**) to RyR2. Research has also shown that clusters within <100nm of each other can activate their neighbours via CICR, creating what is called a 'supercluster' or CRU (Sobie et al. 2006; Baddeley et al. 2009). This highlights the complexity of the clustering interaction and its importance in regulating Ca^{2+} release from RyR2.

The inter-tetramer interaction that facilitates clustering is believed to involve interaction of the SPRY1 and P1 domains of adjacent channels, as well as the accessory protein FKBP12.6

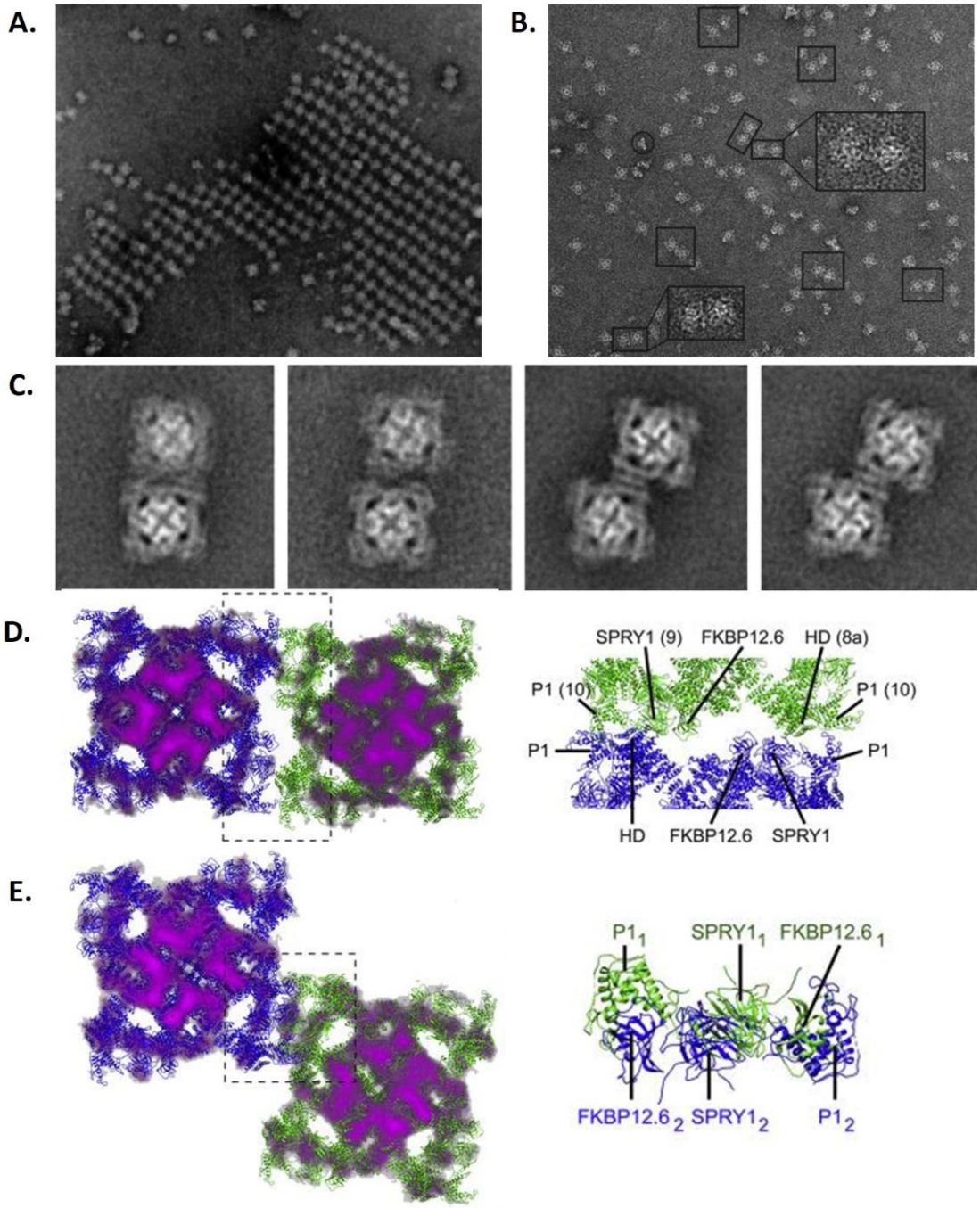

Figure 1.7. Clustering of RyR2 and the proposed interacting regions. A. Early research showing RyR3 forming large, structured arrays in a checker-board formation; the same arrangement was proposed for RyR2. **B**. Transmission electron microscopy (TEM) image of purified RyR2 on a carbon film demonstrating pairs of channels coupled together in a side-by-side and corner-to-corner arrangement. **C**. Averaged TEM images of paired RyR2 channels in the side-by-side (left two) and corner-to-corner (right two). **D**. Modelling of the side-by-side method of clustering showing the proposed domain interactions between P1, SPRY1 and the helical domain. **E**. Modelling of the corner-to-corner interaction showing the proposed interaction of P1, SPRY1 and FKBP12.6; this indicates interatomic clashes between SPRY1-SPRY1 and P1-FKBP12.6. Figures adapted from Yin and Lai (2000) and Cabra et al. (2016).

(**Figure 1.7C, D** and **E**) (Cabra et al. 2016). Modelling suggests that there is a degree of interatomic clashing between interacting domains in the checker-board arrangement that may require domain rearrangement to create a tight interaction (**Figure 1.7E**) (Cabra et al. 2016). It is also suggested that dissociation of one FKBP12.6 molecule per interaction may be required to facilitate this tight interaction (Cabra et al. 2016), although the role of FKBP12.6 in RyR2 is not fully understood (**Section 1.5.1**). Recent studies have shown that saturation of RyR2 with FKBP12.6 (and / or FKBP12) results in reduced cluster size and causes a shift towards the more densely packed side-to-side configuration (Asghari et al. 2020). The role of FKBP12.6 in RyR2 regulation as a whole is discussed in more detail in **Section 1.5.1**.

As well as regulating Ca^{2+} release by isolating groups of RyR2s, clustering is also proposed to allow for coupled gating of channels, where two or more channels gate simultaneously (Marx et al. 2001; Gaburjakova and Gaburjakova 2010; Porta et al. 2012). This has been shown to promote concerted opening and closing of channels in a cluster and result in prolonged open and closed periods compared to single channels (Marx et al. 2001). This is proposed to stabilise RyR2 and prevent silent Ca^{2+} leak by preventing individual channels from reopening as cytosolic Ca^{2+} concentration decreases, resulting in termination of Ca^{2+} release despite the positive feedback loop of CICR (Marx et al. 2001; Chen et al. 2009). Coupled gating of up to 4 RyR channels (RyR1 and RyR2) has been demonstrated in planar lipid bilayers (Marx et al. 2001; Ondrias and Mojzisová 2001; Gaburjakova and Gaburjakova 2008; Gaburjakova and Gaburjakova 2010; Porta et al. 2012). It is believed to rely on allosteric communication between channels (Marx et al. 2001; Sobie et al. 2006; Chen et al. 2009) however there is no direct evidence for this at present, and some suggest that the apparent effect of coupled gating is simply a function of CICR (Cannell et al. 2013; Gillespie and Fill 2013). Accessory proteins and other regulators of RyR2 are also implicated in coupled gating, with Mg^{2+} and ATP purported to be required for coupled gating (Porta et al. 2012) along with FKBP12.6 (Marx et al. 2001) although this has been disputed (Hu et al. 2005) and is likely complicated both by the unclear role of FKBP12.6 in RyR2 regulation (**Section 1.5.1**) and the complicated nature of clustering dynamics (Asghari et al. 2014; Asghari et al. 2020).

1.3 Regulation of RyR2 by ions and small molecules

1.3.1 Activation of RyR2 by cytosolic Ca^{2+}

The main regulator of RyR2 is Ca^{2+}, from both the cytosolic and luminal side of the SR membrane. During diastole, $[Ca^{2+}]_{cyt}$ is approximately 100 nM; RyR2 is largely inactive at this concentration and the P_O is very low (Laver 2007; Mukherjee et al. 2012; Laver 2018). Following membrane depolarization and the rapid influx of Ca^{2+} into the cytosol via LTCCs, Ca^{2+} binds to high-affinity sites on the cytosolic face of RyR2 resulting in an increase in P_O, until RyR2 is maximally activated at approximately 100 µM (Laver 2018). In single channel experiments, the largest increase in P_O (100-fold increase) was observed between 100 nM and 1 µM (Mukherjee et al. 2012).

Activation of RyR2 by cytosolic Ca^{2+} is facilitated by binding of Ca^{2+} to the *A*-site (denoting 'activation') in the central domain (Fessenden et al. 2001; Li and Chen 2001) (**Figure 1.8**). The location of the site was predicted due to the mutation E3987A reducing channel activation, suggesting this region may be involved in cytosolic Ca^{2+} activation; the corresponding mutation in RyR1 (E4032A) also reduces channel activation (Fessenden et al. 2001; Li and Chen 2001). Modelling has shown that the Ca^{2+} binding site on RyR1 also includes residues E3893, E3967, and T5001, with E4032 likely contributing to the structural stability of the site (des Georges et al. 2016). This is in the central domain and has been corroborated by site directed mutagenesis (des Georges et al. 2016; Murayama et al. 2016; Xu et al. 2018).

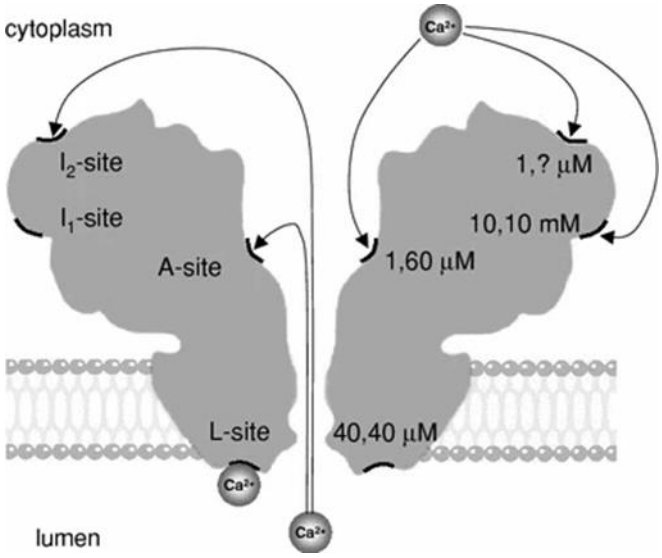

Figure 1.8. Proposed locations of binding sites for Ca^{2+} and divalent cations on RyR2. Three cytoplasmic sites and one luminal site have been reported on RyR2 and are believed to bind Ca^{2+} or other divalent cations such as Mg^{2+}. The *A*-site is the high-affinity activating site located in the central domain, not far from the exit of the ion pore (des Georges et al. 2016; Murayama et al. 2016; Xu et al. 2018).Two inhibitory sites are also found on the cytoplasmic domain although their precise locations are unknown; the low affinity *I1*-site is proposed between residues 1873 and 1903, and the high affinity *I2*-site (Laver 2006; Laver 2007). The *L*-site is the luminal activating site and is believed to centre on E4872 (Chen et al. 2014). The numbers indicated on the right side of the diagram indicate the affinity of Ca^{2+} (left) and Mg^{2+} (right) for each site. Figure taken from (Laver 2009).

1.3.2 Luminal Ca^{2+} as an activator of RyR2

Luminal Ca^{2+} is also involved in activation of RyR2 (Fabiato 1985a; Sitsapesan and Williams 1994; Laver 2007), evident because Ca^{2+} is released from the SR once luminal [Ca^{2+}] reaches a critical threshold (termed store-overload induced calcium release (SOICR) (Jiang et al. 2005). One hypothesis, termed the 'feed-through' hypothesis, is that luminal Ca^{2+} activates RyR2 by passing through the open pore and binding to cytosolic Ca^{2+} sites (Tripathy and Meissner 1996; Xu and Meissner 1998), and that removing cytosolic Ca^{2+} and increasing luminal Ca^{2+} does not result in activity, suggesting no luminal Ca^{2+} sites (Xu and Meissner 1998). However, other research has pointed to a separate luminal Ca^{2+} site and more independent activation by luminal Ca^{2+} (Laver 2007). Research in the absence of cytoplasmic Ca^{2+} has provided evidence of a luminal Ca^{2+} site (*L*-site) that on binding Ca^{2+} triggers short channel openings that facilitate feed-through of Ca^{2+} to the cytosolic *A*-site to stabilise and further activate the channel (Laver 2007) (**Figure 1.8**). While the location of the *L*-site has not been resolved via cryo-EM, mutagenesis of E4872A within the S6 segment of the

transmembrane helix abolished luminal Ca^{2+} activation without greatly impacting cytosolic activation, suggesting luminal and cytosolic activation are linked but not inter-dependent on each other (Chen et al. 2014).

1.3.3 Termination of CICR

Activation of RyR2 via CICR is a well-characterised process and functions as a self-regenerating positive-feedback loop, however termination of Ca^{2+} release from the SR is less well understood. Several mechanisms have been proposed which may act individually or in combination to terminate CICR, in addition to the potential contribution of coupled gating as described above (**Section 1.2.4**).

Studies suggested that increases in $[Ca^{2+}]_{cyt}$ can inactivate RyR1 and RyR2 due to binding to a low-affinity inhibition site on the cytosolic domain (named the I_1-site (Laver et al. 1995; Laver 2007) resulting in a decrease in channel P_O at $[Ca^{2+}]_{cyt}$ above 100 µM (Fabiato 1985b; Mukherjee et al. 2012). Other divalent cations may also bind to I_1 to reduce channel P_O, and an additional high-affinity Ca^{2+}-binding inactivating site (I_2-site) has also been proposed on the cytosolic domain (Laver 2007) (**Figure 1.8**). Luminal $[Ca^{2+}]$ is also reported to be important in CICR termination (Fabiato 1985b; Terentyev et al. 2002; Gyorke and Terentyev 2007) and research has shown there is a critical threshold $[Ca^{2+}]_{SR}$ below which CICR is terminated (Zima et al. 2008). This could occur either via decreased activation of RyR2 by reduced binding of Ca^{2+} to the *L*-site, or by reduced Ca^{2+} flux through RyR2 leading to decreased local $[Ca^{2+}]_{cyt}$ preventing regenerative CICR between nearby channels (Sato and Bers 2011; Laver et al. 2013). This latter process is termed 'induction decay' and is essentially a product of CICR depleting the SR gradually, leading to CICR termination (Laver et al. 2013).

Time-dependent termination of CICR has also been proposed, initially termed adaptation, that suggests RyR2 adapts to constant Ca^{2+} concentrations with a decrease in P_O that can be restored by addition of a greater Ca^{2+} stimulus (Györke and Fill 1993). This was proposed to occur due to the channel adapting over time rather than due to Ca^{2+}-dependent inactivation (Györke and Fill 1993), however the timescales involved in this mechanism are too extended to account for the quick termination of CICR observed in cells (Winslow and Greenstein 2013) and it is now proposed that time-dependent inactivation and Ca^{2+}-dependent

inactivation may function together to terminate CICR (Györke 1999; Zahradníková and Zahradník 1999; Lee and Keener 2008).

Stochastic attrition is mechanism of CICR termination that describes spontaneous closings of RyR2 that interrupt the positive-feedback look of CICR and in turn cause it to cease (Stern 1992). This mechanism is proposed to be sufficient for terminating Ca^{2+} release in smaller groups of independently acting RyR2s (<10 channels), however larger clusters present an issue in that the probability of enough channels spontaneously closing at any one time to effectively induce termination of CICR is low (Stern 1992; Laver et al. 2013). The issue with stochastic attrition in larger clusters could be somewhat mitigated by allosteric communication between channels causing them to gate cooperatively (Marx et al. 2001; Sobie et al. 2006), however this mechanism of CICR termination remains more viable for groups of <10 RyR2s (Stern 1992; Sobie et al. 2002).

Finally, a mechanism termed pernicious attrition suggests that Ca^{2+} release from RyR2s will terminate because of stochastic closing of individual RyR2s, leading to a more gradual decrease in local $[Ca^{2+}]_{cyt}$ until it is insufficient to sustain CICR (Gillespie and Fill 2013). This is distinct from stochastic attrition as it does not involve the simultaneous closing of all channels, but instead relies on the Ca^{2+} current reducing by a small amount that prevents activation of other channels leading to termination of Ca^{2+} release (Yonkunas et al. 2012; Gillespie and Fill 2013). Collectively, the termination of CICR is still not well defined, however it is likely that a combination of the above regulatory mechanisms contributes to ending the positive feedback loop of CICR.

1.3.4 Activation and inhibition by ATP and Mg^{2+}

In addition to Ca^{2+}, Mg^{2+} and ATP have both been identified as important regulators of RyR2 function and are found in the cytosol predominantly in the ATP-Mg^{2+} complex, thus their levels are co-dependent. ATP is known to activate RyR2, whereas Mg^{2+} acts as an inhibitor. ATP binding RyR2 potentiates activation of the channel by stabilising the open conformation in the presence of Ca^{2+} (Xu et al. 1996; Kermode et al. 1998; Laver 2007); ADP and AMP also increase RyR2 activation by this mechanism but to a lesser extent (Kermode et al. 1998). During diastole, cardiomyocytes contain ~1 mM free Mg^{2+} (Godt and Maughan 1988) and this acts as a competitive inhibitor of Ca^{2+} binding at the A-site of RyR2 (Smith et al. 1986) while $[Ca^{2+}]_{cyt}$ is low (Rousseau et al. 1987); Mg^{2+} can also bind to the L-site and inhibit RyR2

activation by preventing Ca^{2+} binding here (Laver and Honen 2008) and the I_1-site to provide direct inhibition of RyR2 (Laver et al. 1997).

1.4 Post-translational modifications of RyR2

1.4.1 Phosphorylation of RyR2 by PKA and CaMKII

Phosphorylation of RyR2 takes place during the 'fight-or-flight response' when β-adrenergic receptors are stimulated by adrenaline (epinephrine) following physical or emotional stress, resulting in increased cAMP production and activation of PKA (**Section 1.1.4**) (Bers 2002). Following this, LTCCS are activated by PKA phosphorylation resulting in increased Ca^{2+} influx, and PLB phosphorylation reduces inhibition of SERCa resulting in an increase of reuptake into the SR and causing faster myocyte relaxation (Bers 2006; Halls and Cooper 2011). As well as phosphorylation by PKA, RyR2 is also acted upon by Calmodulin Kinase II (CaMKII) and several other serine/threonine kinases, although PKA and CaMKII are considered the most important in its regulation. A 'hotspot' region for RyR2 phosphorylation exists on an exposed region centred on S2808 and S2814 in the P2 domain (also known as RY3&4) (**Figure 1.9**), which is located close to the P1 and SPRY1 domain of the adjacent monomer (Yuchi et al. 2012). PKA phosphorylation in RyR2 predominantly occurs at two sites; S2808 (which may also be phosphorylated by CaMKII) and S2030, a PKA-specific site (Marx et al. 2000; Xiao et al. 2005; Wei et al. 2023). Hyperphosphorylation at S2808, as is observed in some cases of HF, was initially believed to destabilise the closed state of the channel by causing dissociation of the stabilising accessory protein, FKBP12.6, resulting in increased channel P_O and Ca^{2+} leak (Marx et al. 2000; Wehrens et al. 2006). These findings have been disputed on multiple fronts, both in terms of the contribution of phosphorylation to HF, as well as its impact on FKBP12.6 binding. Regarding HF, initial research by the Marks group indicated that there was an approximately 4x increase in PKA phosphorylation in human and canine failing hearts (Marx et al. 2000), and several other papers from the group have supported this finding (Wehrens et al. 2006; Shan et al. 2010b; Shan et al. 2010a; Miotto et al. 2024). However, multiple other studies have demonstrated limited or no effect of PKA phosphorylation as a causative mechanism in HF, including the role of S2808 phosphorylation being relevant only to some forms of HF (specifically ischemic HF with

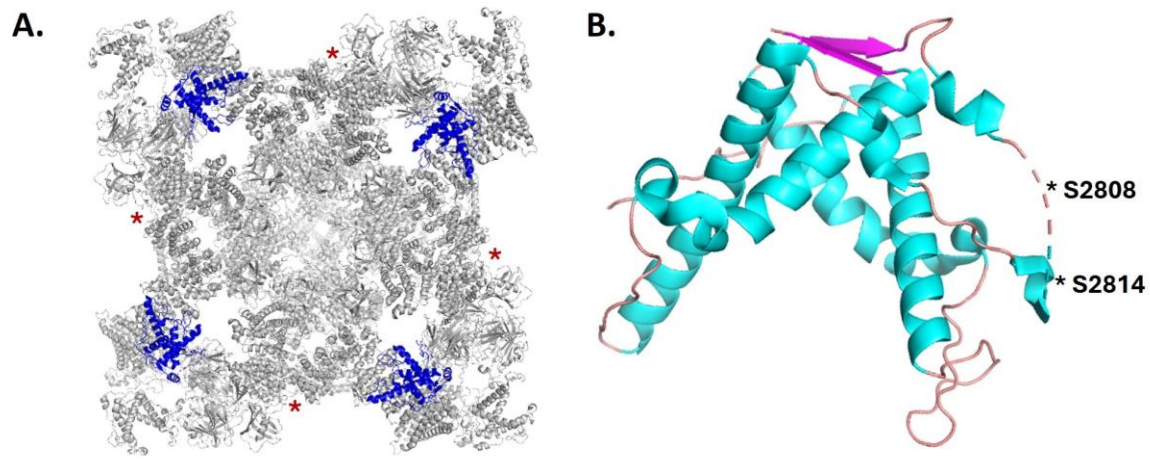

Figure 1.9. Location of the phosphorylation hotspot in the P2 domain and the main phosphorylation sites. A. Location of the P2 domain (blue) on the corner of each RyR2 monomer as viewed from the cytosol; S2030 is not located in the P2 domain and is found in the handle (approximate location indicated by red asterisk (*)). **B**. Structure of the P2 domain from cryo-EM studies demonstrating the clamp shape of the P2 domain and the approximate location of the main phosphorylation sites on an unresolved flexible loop. Models produced in PyMOL (Schrödinger and DeLano 2020) using PDB accessions 7U9Q (**A**) and 4ERT (**B**).

reduced ejection fraction) (Chen-Izu et al. 2007; Ather et al. 2013; Dobrev and Wehrens 2014), and others finding no effect at all (Benkusky et al. 2007; MacDonnell et al. 2008; Zhang et al. 2012; Houser 2014; Alvarado et al. 2017). There is also evidence to suggest that basal phosphorylation at S2808 is high even in healthy hearts with limited increase in HF (Xiao et al. 2005; Carter et al. 2006a; Benkusky et al. 2007; Huke and Bers 2008). FKBP12.6 dissociation due to PKA hyperphosphorylation is equally disputed. The original study and subsequent research by the Marks group shows significant dissociation of FKBP12.6 following PKA hyperphosphorylation, which is in turn proposed to destabilise the channel and increase P_O (Marx et al. 2000; Wehrens et al. 2003; Wehrens et al. 2006). However other groups have indicated that FKBP12.6 binding is unaffected by S2808 phosphorylation (Jiang et al. 2002b; Stange et al. 2003; Guo et al. 2010; Shan et al. 2010a; Asghari et al. 2020) and there is also debate as to whether FKBP12.6 stabilises the channel in the first place (**Section 1.5.1**). S2030 is also phosphorylated by PKA, however there are conflicting opinions about which site is the 'major' PKA site. Early research into this site suggested it is the major PKA site during the β-adrenergic response (Xiao et al. 2006; Potenza et al. 2019), while more recent studies have found that it modulates CaM-dependent termination of Ca^{2+} release

(Wei et al. 2023). It remains that the role of PKA phosphorylation and hyperphosphorylation in RyR2 regulation is highly contentious, and it may be that a combination of factors along with PKA phosphorylation at S2808 and / or S2030 are responsible for altered Ca^{2+} release from RyR2.

CaMKII, activated by Ca^{2+}-bound CaM (Ca^{2+}-CaM) , phosphorylates RyR2 predominantly at the S2814 site and has been shown to increase channel P_O resulting in Ca^{2+} leak (Wehrens et al. 2004b; Curran et al. 2007). Increased phosphorylation at S2814 has been reported in both HF (Chen-Izu et al. 2007; Fischer et al. 2014) and dilated cardiomyopathy (DCM) (Fischer et al. 2014), and reportedly causes a conformational change in RyR2 that promotes Ca^{2+} leak and CaM disassociation (Uchinoumi et al. 2016). While there are many other factors that contribute to these pathological effects on RyR2 including PKA phosphorylation, binding of accessory proteins (**Section 1.5**), and other post-translational modifications (**Section 1.4.2**), some argue that CaMKII phosphorylation at S2814 is both the major contributor HF (Chen-Izu et al. 2007) and the major phosphorylation site following the β-adrenergic response (Baier et al. 2021). While it appears that phosphorylation by both PKA and CaMKII has a role in Ca^{2+} leak, there is still a great degree of uncertainty regarding their contribution and mechanism of action. In all likeliness, a combination of the two kinases along with other post-translational modifications and accessory protein interactions likely contribute to Ca^{2+} leak and RyR2 dysfunction in disease.

1.4.2 Oxidative Modification of RyR2: Reactive oxygen species, *S*-Nitrosylation and *S*-Glutathionylation

RyR2 is highly sensitive to redox modification and oxidative stress (Zima and Blatter 2006), during which reduced free thiol residues on cysteines can be modified to di-sulfide bonds or act as targets for *S*-nitrosylation or *S*-glutathionylation. In RyR2 there are estimated to be 84 cysteine residues in a reduced free thiol state available for modification, out of a total of 356 cysteine residues (Xu et al. 1998). Oxidative conditions lead to an increased P_O in RyR2, with elevated concentrations of reactive oxygen species (ROS) implicated in altered RyR2 function which has been shown to contribute to depletion of SR Ca^{2+} load and generation of arrhythmias (Yan et al. 2008; Prosser et al. 2011; Bovo et al. 2012; Nikolaienko et al. 2023), as well as dissociation of regulatory CaM (Ono et al. 2010). During oxidative stress, ROS act on RyR2 to form sulfenic, sulfinic or sulfonic acid products on free thiols. Reduced

glutathione protects against ROS by scavenging free radicals and binding to sulfenic acid to produce S-glutathiolynation of RyR2; this is a reversible process that acts to protect RyR2 from ROS (Zima and Mazurek 2016).

The role of *S*-nitrosylation in RyR2, in which nitric oxide is added onto free thiols (Lima et al. 2010), is less clear. Some studies show that *S*-nitrosylation activates RyR2 (Zima and Blatter 2006; Gonzalez et al. 2009), however hyponitrosylation has been demonstrated to increase oxidation by ROS which in turn leads to Ca^{2+} leak and arrhythmogenesis (Gonzalez et al. 2010). *S*-nitrosylation is also considered to have a cardioprotective effect on many other cardiac and Ca^{2+} handling machinery (Zhang et al. 2005; Rassaf et al. 2014); it therefore appears that a fine balance must be struck in the cell to regulate RyR2 modification by ROS and nitrosylation.

1.5 Regulation by accessory proteins

1.5.1 Regulation by FKBP12 and FKBP12.6

The FK506 binding proteins FKBP12 (12kDa isoform, also known as calstabin) and FKBP12.6 (12.6kDa isoform, also known as calstabin2) are immunophilins that bind the immunosuppressants FK506 and rapamycin, and they also bind RyR2 and regulate its function (**Figure 1.10**) (Timerman et al. 1993; Timerman et al. 1996; Zissimopoulos and Lai 2005). FKBP12 and FKBP12.6 share 85% sequence homology, but the binding affinity of FKBP12 for RyR2 is far lower than FKBP12.6, believed to be due to a conformational change that alters the hydrophobic binding pocket of the accessory protein (Deivanayagam et al. 2000), however the exact mechanism of this difference is unconfirmed. While both isoforms are expressed in the heart, FKBP12 is expressed at a much higher level than FKBP12.6, however almost all FKBP12.6 found in the heart is bound to RyR2 despite only 20% of RyR2s being bound to FKBP12.6 (Jeyakumar et al. 2001; Guo et al. 2010). This suggests that, while the affinity of FKBP12.6 is much higher, the greater amount of FKBP12 present in the heart may mean that it occupies a greater proportion of binding sites simply due to abundance, which brings into question which isoform is the most physiologically relevant (Gonano and Jones 2017; Richardson et al. 2023). Both FKBP12 and FKBP12.6 bind RyR2 in a ratio of 4 FKBP to 1 tetramer (Timerman et al. 1993; Timerman et al. 1996; Zissimopoulos et al. 2012)

with the binding site located adjacent to SPRY1 in RyR2 (Zissimopoulos and Lai 2005; Yuchi et al. 2015; Peng et al. 2016).

The exact roles of both FKBP12 and FKBP12.6 are not well defined in the literature, and there is much discussion about their contribution to RyR2 regulation. FKBP12 is generally understood to be an activator of RyR2, sensitising the channel to cytosolic Ca^{2+} and increasing SR Ca^{2+} release (Venturi et al. 2014; Galice et al. 2018; Richardson et al. 2023), but having an opposite stabilising effect on RyR1 (Brillantes et al. 1994). Activation is believed to occur in a biphasic manner, with lower concentrations of FKBP12 resulting in potent activation, whereas at higher concentrations more binding sites become occupied resulting in inhibition, potentially due to changes in interdomain interactions (Richardson et al. 2023). The role of FKBP12.6 is less well defined, and while it is generally accepted as an important regulator of RyR2, its exact mechanism of function is not well understood and there is much disagreement about how it regulates RyR2 and whether it is needed at all for normal function. One aspect of FKBP12.6's role in RyR2 regulation is stabilisation of the closed state of the channel, which was first shown to reduce channel P_O in single channel recordings (Marx et al. 2000) and has since been backed up by several other studies (Prestle et al. 2001; Yano et al. 2003; Guo et al. 2010; Chi et al. 2019). The mechanism of stabilisation is unclear, but it is proposed that FKBP12.6 binding might result in tilting of the handle domain on the cytosolic face of RyR2 outwards, which promotes closing of the ion pore (Chi et al. 2019). Others disagree with this view, with some research showing no stabilisation of RyR2 by FKBP12.6 (Timerman et al. 1996; Barg et al. 1997), no altered binding of FKBP12.6 in mutants (George et al. 2003a; Zissimopoulos et al. 2009), and no effect of FKBP12.6 on RyR2 activation by Ca^{2+} (Xiao et al. 2007b; Guo et al. 2010), although termination of Ca^{2+} release may be impacted (Zhang et al. 2016). A different argument for the apparent stabilisation is that, due to the higher affinity of FKBP12.6 for RyR2 than FKBP12, it out-competes FKBP12 and removes its activating effect which therefore mimics stabilisation by the larger isomer (Galfré et al. 2012a). This highlights the complicated nature of RyR2 regulation by FKBP12 and FKBP12.6, and it is likely that a balance of binding of the two isoforms is responsible for its regulation (Gonano and Jones 2017).

There is also the question of whether S2808 hyperphosphorylation impacts FKBP12.6 binding. As already discussed in **Section 1.4.1**, S2808 hyperphosphorylation by PKA is

proposed to dissociate FKBP12.6 and result in increased Ca^{2+} leak, as well as contribute to the progression of HF (Marx et al. 2000; Wehrens et al. 2006; Dridi et al. 2020), however this interpretation does not have the support of many other groups (Jiang et al. 2002b; Stange et al. 2003; Guo et al. 2010; Shan et al. 2010a; Asghari et al. 2020). The FKBP12.6 binding site is also not in close proximity to the phosphorylation site in the P2 domain (Miotto et al. 2022), so it is unclear how the two might be linked. Taking all of these findings into account, there is no clear conclusion as to the effect of S2808 hyperphosphorylation on FKBP12.6 binding, or the role of FKBP12.6 in RyR2 regulation as a whole.

FKBP12.6 is also believed to play an important role in the inter-tetramer interaction during clustering (**Section 1.2.4**), further complicating the role of FKBPs in the stabilisation of RyR2. FKBP12.6 bound to RyR2 adjacent to the SPRY1 domain contacts P1 on the adjoining tetramer during the checker-board arrangement of channels, but is not thought to be involved in the side-to-side arrangement (Cabra et al. 2016). Whether FKBP12 also functions in a similar way is unclear, however both isoforms bind at the same binding site and share a largely similar structure, with the main exception being in the binding domain. Single molecule imaging has revealed that saturation with either FKBP pushes RyR2 to enter the side-to-side arrangement, which results in more densely-packed clusters which are associated with less Ca^{2+} leak, likely due to steric hindrance of adjacent channels (Asghari et al. 2014; Asghari et al. 2020). This somewhat supports the idea that FKBP12.6 binding increases channel stability as a function of clustering, but not as an effect on the single channel. The same study indicated that this effect was negated by phosphorylation, but that this didn't result in FKBP dissociation and simply reversed its effects (Asghari et al. 2020).

Ultimately, while both FKBP12.6 and FKBP12 are often considered to be important regulators of RyR2 function, there is no consensus on the role of either isoform in RyR2 regulation. The inconsistencies in experimental results do not strongly support a requirement for FKBP12.6 binding for normal RyR2 function, but equally there is substantial evidence that it is somehow involved in its regulation. The potential contribution of FKBPs in the generation of disease is discussed in Section **1.6.2.1**.

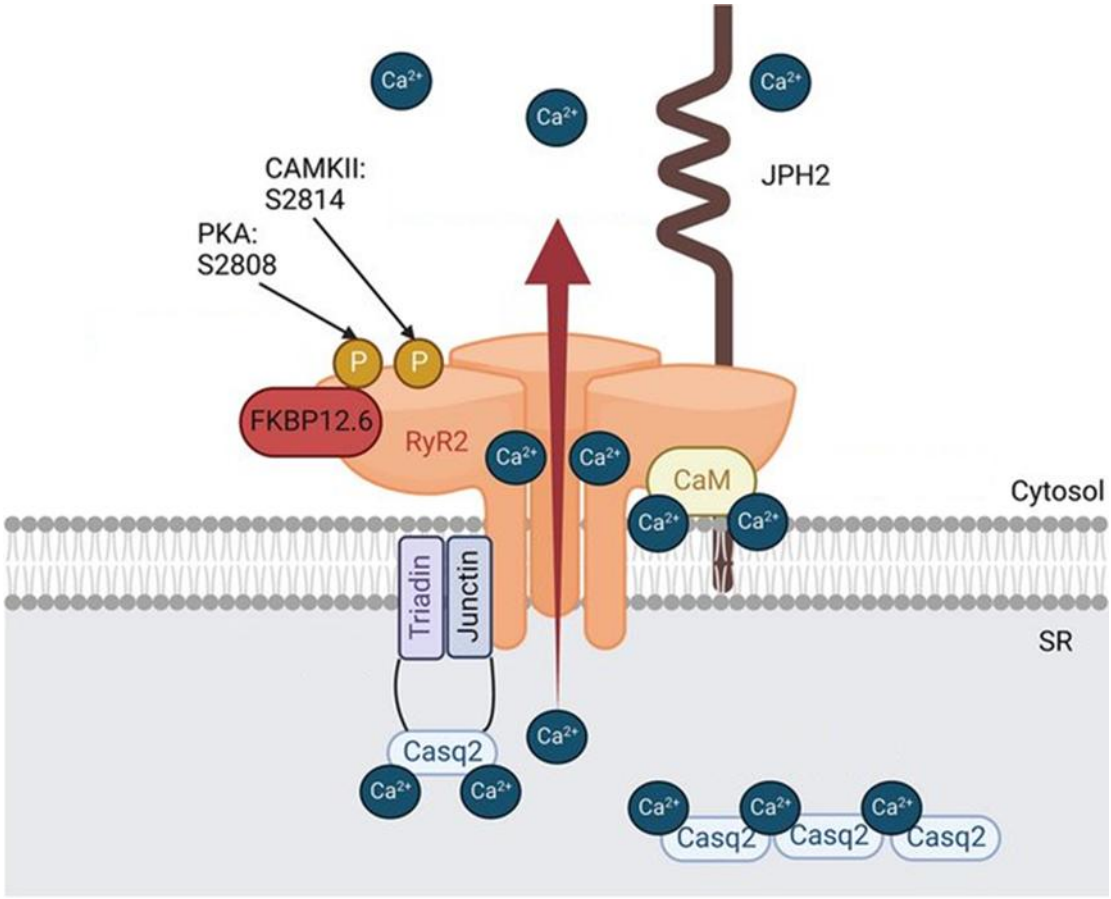

Figure 1.10. Schematic of binding sites for main regulatory accessory proteins of RyR2. The approximate accessory protein binding sites and primary phosphorylation sites for RyR2 are illustrated. As RyR2 is a tetramer, there are multiple binding sites on each channel for these regulatory factors, however under physiological conditions not all binding sites may be occupied. Figure adapted from Keefe et al. (2023).

1.5.2 Regulation by Calmodulin and EF-hand proteins

CaM is a ubiquitously expressed ~17kDa intracellular Ca^{2+} sensor that directly binds to RyR2 (**Figure 1.10**) to regulate its function, as well as modulating it through CaMKII and its action on other proteins (Samsó and Wagenknecht 2002; Tang 2002; Bers 2004). It contains 4 Ca^{2+} binding sites, two on each EF-hand motif (Peterson et al. 1999; Fruen et al. 2000) and binds to RyR2 in both its non-Ca^{2+} bound (apo-CaM) and Ca^{2+}-bound form (Ca^{2+}-CaM) (Balshaw et al. 2001). Ca^{2+} binding to CaM induces a conformational change in the protein which alters its effect on RyR2 and affects its binding site (Samsó and Wagenknecht 2002), although both forms bind in the same space between the handle, central and helical domain centred on residues 3581 to 3612 on RyR2 (based on research in RyR1) (Yamaguchi et al. 2003; Gong et al. 2019). Ca^{2+}-CaM binding to RyR2 inhibits channel opening (Balshaw et al. 2001) by

desensitising the channel to cytosolic Ca^{2+} (Yamaguchi et al. 2003) and it can also terminate SOICR (Tian et al. 2013). The effect of apo-CaM is less well defined, with some studies showing it has an inhibitory effect (Balshaw et al. 2001) or no effect on function (Fruen et al. 2000). This is distinctly different from both RyR1 and RyR3, as while RyR2 appears to be inhibited by CaM at all $[Ca^{2+}]_{cyt}$, RyR1 and RyR3 are activated in the nanomolar (<1 μM) range and only inhibited in the micromolar (>1 μM) range (Yamaguchi et al. 2003). CaM also affects RyR2 function by activating CaMKII during systole, which allows CaMKII to go on to phosphorylate RyR2 and increase its activity (Wehrens et al. 2004; Curran et al. 2007). This shows an opposite action of CaM versus CaMKII, and phosphorylation by CaMKII has been shown to be an important factor in the potency of CaM inhibition (Uchinoumi et al. 2016). Overall, CaM plays an important regulatory role in RyR2 function in both its activation and inhibition, and dysregulation of CaM is associated with arrhythmogenesis (Chazin and Johnson 2020).

CaM is not the only EF-hand protein to regulate RyR2, with both sorcin and S100A1 able to bind to the channel and regulate its Ca^{2+} release. Sorcin is a ~21kDa protein containing 5 EF-hand motifs that, upon binding Ca^{2+}, moves towards the T-tubules where it associates with RyR2 (Ilari et al. 2015) and inhibits channel activity (Meyers et al. 1995; Farrell et al. 2003; Meyers et al. 2003), with knock-out of sorcin resulting in arrhythmogenesis (Chen et al. 2018). The role of S100A1 in RyR2 regulation is less well defined, as this ~10kDa protein that binds at the same site as CaM (Prosser et al. 2008) has been shown to both activate (Most et al. 2003; Kettlewell et al. 2005) and inhibit (Völkers et al. 2007; Yamaguchi et al. 2013) RyR2 in different studies.

1.5.3 Regulation by Calsequestrin-2, Junctin and Triadin

Calsequestrin-2 (CSQ2) is a low-affinity Ca^{2+} binding protein that acts as the main Ca^{2+} buffer in the SR, maintaining free $[Ca^{2+}]_{SR}$ at ~1 mM (Gyorke and Terentyev 2007). In the SR lumen, CSQ2 exists as a monomer at low $[Ca^{2+}]_{SR}$ and then dimerises as the Ca^{2+} content increases, eventually forming into a linear polymer which creates areas of negative charge between each pair of dimers; this attracts more Ca^{2+} ions and increases its capacity to buffer Ca^{2+} (Park et al. 2003; Titus et al. 2020). CSQ2 also binds RyR2 via association with the SR membrane proteins triadin (TRD1) and junctin (JUN) to form a quaternary protein complex (**Figure 1.10**) (Liu and Pessah 1994; Guo and Campbell 1995; Györke et al. 2004). This

protein complex acts as a luminal Ca^{2+} sensor on RyR2 and is believed to have both a direct and indirect effect on RyR2 function (Gyorke and Terentyev 2007; Sibbles et al. 2022). At low $[Ca^{2+}]_{SR,}$ CSQ2 associates with RyR2 via TRD1 and JUN or via direct binding and inhibits Ca^{2+} release by buffering Ca^{2+} in its vicinity, whereas as higher concentrations CSQ2 dissociates which increases channel activity (Beard et al. 2002; Györke et al. 2004; Fan et al. 2008; Handhle et al. 2016). JUN and TRD1 are both integral membrane proteins in the SR and serve as anchors for the interaction of CSQ2 and RyR2, but they also activate RyR2 on their own (Györke et al. 2004). JUN however appears to have a dual role, acting as an activator at low $[Ca^{2+}]_{SR}$ but an inhibitor at high $[Ca^{2+}]_{SR}$ (Altschafl et al. 2011). The importance of these accessory proteins and their regulatory role in RyR2 function is highlighted by their role in disease, with both CSQ2 and TRD1 mutations associated with the generation of arrhythmia (discussed more in **Section 1.6.2**).

1.5.4 Regulation by Junctophilin-2

Junctophilin-2 (JPH2) is a ~100kDa protein that is anchored to the SR via its transmembrane domain, and its cytoplasmic domain forms non-covalent interactions with the plasma membrane (**Figure 1.10**) (Takeshima et al. 2000). This tethers the two membranes together and is necessary for the formation of T-tubules, which brings RyR2 close to LTCCs to facilitate CICR during EC-coupling (Takeshima et al. 2000; Pritchard et al. 2019). Genetic knockout of JPH2 has been shown to be embryonically lethal (Takeshima 2000) and knockdown resulted in HF and increased distance between the plasma membrane and SR (van Oort et al. 2011) which reflects data showing JPH2 downregulation in HF models (Wu et al. 2012; Reynolds et al. 2016). There is also a direct interaction between JPH2 and RyR2 that may impact channel activity and regulate RyR2 cluster structure. Single channel studies have shown reduced JPH2 expression results in increased channel P_O (Wang et al. 2014), whereas a decrease in P_O was observed when a JPH2-derived peptide was added to single channels (Beavers et al. 2013). The effect of JPH2 knockdown on Ca^{2+} sparks has also been investigated with most studies showing increased frequency and duration of sparks indicating increased Ca^{2+} release (Cheng et al. 1993; van Oort et al. 2011; Wang et al. 2014), although this is not universally accepted (Munro et al. 2016). Super-resolution microscopy has demonstrated a high degree of colocalization between JPH2 and RyR2 in clusters and increased cluster size with JPH2 overexpression (Munro et al. 2016), as well as loss of JPH2

being implicated in remodelling of the dyad in HF (Sheard et al. 2022). This reveals that JPH2 is an important regulatory factor for RyR2 both due to direct interaction with clusters and in facilitating CICR through the T-tubule structure.

1.6 Dysregulation of RyR2 and its role in arrhythmias and cardiomyopathies

1.6.1 RyR2-associated diseases

Given the essential role of RyR2 in EC-coupling, dysregulation of this ion channel is associated with cardiac dysfunction, including HF, triggered arrhythmias and cardiomyopathies. These conditions are referred to as cardiac ryanodinopathies (or ryanopathies) and some of the most prominent include the genetic disorders catecholaminergic polymorphic ventricular tachycardia (CPVT) and arrhythmogenic right ventricular dysplasia (ARVD2). These arise from distinct mutations in RyR2 and to date more than 300 missense mutations associated with arrhythmia have been identified in RyR2, many of which result in channel destabilisation, increased activity and Ca^{2+} leak (Olubando et al. 2020). Several of the most prominent disorders associated with RyR2 are discussed in more detail in the following sections. It is important to note that, in a clinical context, the term 'mutation' is often reserved for variants classified as pathogenic based on multiple factors including population data, clinical reports, computational data, and functional studies. In this research, however, the term 'mutation' or 'mutant' will be used to refer more broadly to changes to genetic material, regardless of pathogenicity.

1.6.2 Catecholaminergic polymorphic ventricular tachycardia

CPVT is an inherited arrhythmogenic disease that is associated with sudden cardiac death (SCD) (Jiang et al. 2002a; Thomas et al. 2004; Miotto et al. 2022). The most common genetic subtypes of CPVT are the autosomal dominant CPVT1 variant and the autosomal recessive CPVT2 variant. Approximately 70% of CPVT1 cases are caused by mutation of RyR2 with at least 170 RyR2 gain-of-function (GoF) mutations implicated in CPVT1 (Olubando et al. 2020; Priori et al. 2021). CPVT2 is associated with mutation of the *CASQ2* gene encoding CSQ2 (Lahat et al. 2001; Eldar 2003), although there is recent evidence to suggest CSQ2 mutation can also cause autosomal dominant CPVT (Ng et al. 2020). There are also several rarer genetic variants; CPVT3, CPVT4 and CPVT5, that are linked to mutations in the genes *TECRL*

(encoding trans-2,3-enoyl-CoA reductase-like protein), *CALM1* (encoding CaM), and *TRDN* (encoding TRD1), respectively (Nyegaard et al. 2012; Roux-Buisson et al. 2012; Garcia-Elias and Benito 2018). All future references to CPVT refer to CPVT1 unless otherwise stated.

CPVT is estimated to affect ~1:10,000 people and symptom onset is primarily during childhood in otherwise healthy patients, although later onset has been observed. The presentation of CPVT is heterogeneous with the same genotype often appearing phenotypically distinct in different patients, although the basic characteristics are the same. It is characterised by syncopal episodes in response to β-adrenergic stimulation due to physical or emotion stress, which results in delayed afterdepolarisations (DADs) (**Figure 1.11**) resulting in polymorphic or bidirectional ventricular tachycardia (VT) which can deteriorate to ventricular fibrillation (VF) and in some cases SCD (Priori et al. 2002). This occurs in the absence of structural alterations to the heart which distinguishes it from ARVD2 (**Section 1.6.3**). Due to the stress-induced nature of CPVT, electrocardiograms (ECGs) conducted at rest in individuals with CPVT do not display abnormalities, so exercise stress testing is conducted to generate the β-adrenergic stimulation needed to diagnose the condition (Priori et al. 2002). The first signs of CPVT are therefore often repeated syncopal episodes, or in some instances, SCD.

Most CPVT-linked RyR2 mutations are missense mutations that result in channel GoF, and the majority are located in one of four 'hotspot' domains (**Figure 1.12**) (George et al. 2007; Olubando et al. 2020). These hotspots all fall in highly conserved regions of RyR2 and are located as follows; hotspot I – residues 77-466 in the NTD, 10.7% of mutations; hotspot II – residues 2246-2534 in the helical domain, 14.7%; hotspot III – residues 3778-4201 in the central domain, 21.5%; and hotspot IV – residues 4497-4959 in the channel domain, 21.2% (**Figure 1.12A**) (Olubando et al. 2020). The remaining mutations are located outside of these regions and are largely classified as benign or of uncertain significance (**Figure 1.12B**), however this may be due to many studies focussing on characterising mutations in the hotspot domains due to their perceived increased likelihood of pathogenicity, despite no definitive link between mutation location and the severity of CPVT phenotypes (Olubando et al. 2020; Fowler and Zissimopoulos 2022).

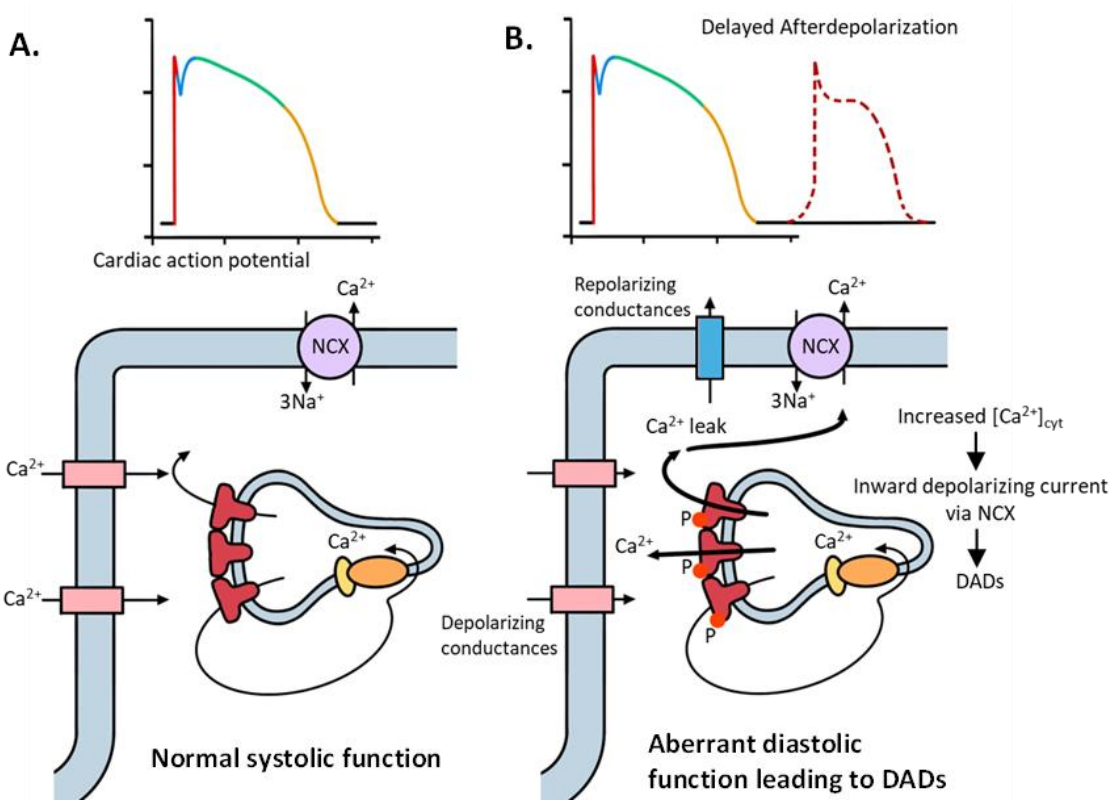

Figure 1.11. Diagram of normal systolic function vs aberrant diastolic function contributing to DADs. A. During systole, LTCCs activate and Ca^{2+} enters the cell, activating RyR2 and triggering CICR which increases cytosolic Ca^{2+} and initiates cardiomyocyte contraction. **B**. Increased spontaneous Ca^{2+} release during diastole due to Ca^{2+} leak (affected by hyperphosphorylation (P) of RyR2, dissociation of stabilising accessory proteins, or other mechanisms of RyR2 dysfunction) increases cytosolic Ca^{2+} which is pumped out via NCX. This causes an inward depolarizing Na^{+} current which triggers DADs. Figure adapted from Nattel et al. (2018).

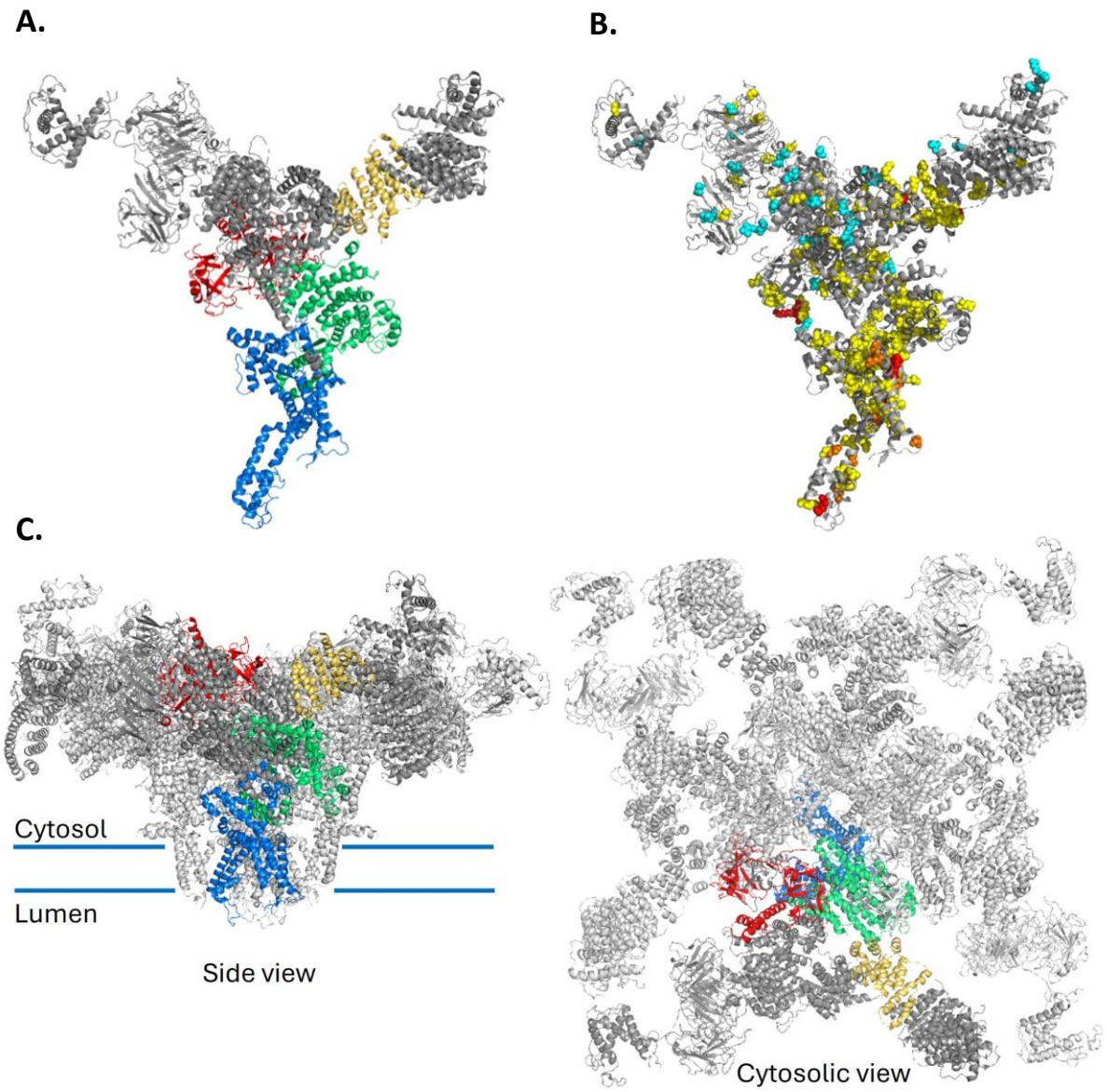

Figure 1.12. Location of disease-associated mutations and hotspot domains in RyR2. A. The location of the four mutation hotspot domains in the RyR2 monomer; hotspot I residues 77-466 = red, hotspot II residues 2246-2534 = yellow, hotspot III residues 2778-4201 = green, hotspot IV residues 2297-4959 = blue. **B**. The location of 326 CPVT-associated mutations on a single RyR2 monomer, classified by their pathogenicity based on the study by Olubando et al. (2020); cyan = benign, yellow = unknown significance, orange = likely pathogenic, red = pathogenic. Comparing **A** and **B** reveals that most pathogenic or likely pathogenic mutations occur in one of the hotspot domains, and most mutations classified as benign occur outside of these regions. **C**. Relative position of the hotspot domains in the RyR2 tetramer. Models produced in PyMOL using PDB accession 5GOA.

1.6.2.1 Mechanisms of dysfunction in CPVT

With so many CPVT-linked RyR2 mutations identified, the breadth of phenotypes reported in patients, and the size and complexity of RyR2 structure and function, it is improbable that all mutations cause dysfunction by a single mechanism. However, three main mechanisms have been proposed for the pathogenically altered Ca^{2+} release from GoF CPVT-linked RyR2 mutations. While the molecular changes responsible for CPVT differ for each mechanism, all hinge on dysfunction of RyR2 that results in increased SR Ca^{2+} release that contributes to the generation of arrhythmia.

The first mechanism involves FKBP12.6 dissociation and is proposed to destabilise the RyR2 channel and increase Ca^{2+} leak (Marx et al. 2000). This theory suggests that mutations in RyR2 affect FKBP12.6 binding and therefore reduce its binding to the channel; it also suggests that hyperphosphorylation by PKA increases the dissociation of FKBP12.6 (Marx et al. 2000). As discussed in **Section 1.4.1**, hyperphosphorylation of RyR2 at S2808 by PKA is a controversial subject and many don't agree that this is implicated in disease (Benkusky et al. 2007; MacDonnell et al. 2008; Zhang et al. 2012; Houser 2014; Alvarado et al. 2017), and equally there is little agreement that CPVT mutations alter FKBP12.6 binding, or whether FKBP12.6 is required for normal RyR2 function (**Section 1.5.1**) (Timerman et al. 1996; George et al. 2003a; Xiao et al. 2007b; Zissimopoulos et al. 2009; Galfré et al. 2012). This theory can be broadened to include dysfunctional binding of other accessory proteins such as CaM or JPH2 (Nakamura et al. 2019; Yin et al. 2021; Fowler and Zissimopoulos 2022), but on its own there is limited evidence to suggest that altered FKBP12.6 binding is a main causative factor in CPVT.

The second mechanism suggests that CPVT mutations alter interdomain interactions between the N-terminal and helical domain resulting in 'domain unzipping', which destabilises the closed state of the channel and increases sensitivity to Ca^{2+}, leading to diastolic Ca^{2+} leak (Ikemoto 2002; Oda et al. 2005; Uchinoumi et al. 2010a). This mechanism of unzipping is also extended to other inter- and intradomain interactions, including unzipping of the NTD itself (Seidel et al. 2015), the NTD and central domain (Yin et al. 2021) and an area termed the 'interacting' or I-domain (residues 3722-4610) which facilitates interaction of the transmembrane and cytoplasmic regions of RyR2 (Tateishi et al. 2008). These areas have been identified as candidates for domain unzipping using synthetic

peptides that mimic one of the interacting 'zipped' domains; WT peptides competitively bind the corresponding domain leading to unzipping of RyR2, which indicates that the WT protein forms a tight interaction. Mutant peptides that fail to bind and do not induce unzipping indicate mutations that disrupt the interdomain interaction and could cause dysfunction (Oda et al. 2005; Yang et al. 2006; Tateishi et al. 2008; Uchinoumi et al. 2010a; Suetomi et al. 2011). Several mutations have been linked to this specific mechanism of dysfunction including R2474S (Yang et al. 2006; Uchinoumi et al. 2010a), R176Q and N4104K (Tateishi et al. 2008), whereas the S2246L mutation has been proposed to increase the strength of interdomain interactions (Suetomi et al. 2011).

The third proposed mechanism of dysfunction is increased Ca^{2+} sensitivity leading to increased activity and Ca^{2+} leak (Li and Chen 2001; Jiang et al. 2004; Xiao et al. 2016). This is identified in multiple CPVT mutations and includes increased sensitivity to cytosolic Ca^{2+} (Li and Chen 2001; Fernández-Velasco et al. 2009; Xiao et al. 2016), luminal Ca^{2+} (Jiang et al. 2004; Jiang et al. 2005; Jones et al. 2008) or both luminal and cytosolic Ca^{2+} (Liu et al. 2013; Uehara et al. 2017). While it is clear that some mutations do impact cytosolic Ca^{2+} sensitivity, some propose that changes to luminal Ca^{2+} sensitivity constitute the predominant mechanism of dysfunction by increasing the propensity for SOICR. In this scenario, enhanced luminal Ca^{2+} sensitivity reduces the threshold for SOICR and leads to spontaneous diastolic Ca^{2+} release (**Figure 1.13**) (Jiang et al. 2004). SOICR is the spontaneous release of Ca^{2+} from the SR when a critical threshold is reached, and is often accompanied by a decreased SR Ca^{2+} store load as a result of increased channel activity (Jiang et al. 2004; Jiang et al. 2005). This was first observed in human embryonic kidney cells (HEK293) expressing CPVT-mutant RyR2 which were seen to have an increased propensity for Ca^{2+} release, a reduced response to caffeine (which is used as an indicator of store load), as well as increased P_O in response to luminal Ca^{2+} in single channel studies compared to the WT (Jiang et al. 2004; Jiang et al. 2005). The response to cytosolic Ca^{2+} however was shown to be comparable in [^{3}H]-ryanodine binding assays, an experiment that uses the binding of radiolabelled ryanodine to open RyR2 channels as a measure of channel function (Jiang et al. 2004; Jiang et al. 2005), and many CPVT-associated mutants have demonstrated no difference in cytosolic Ca^{2+} sensitivity in single channel experiments (Jiang et al. 2005; Tester et al. 2007).

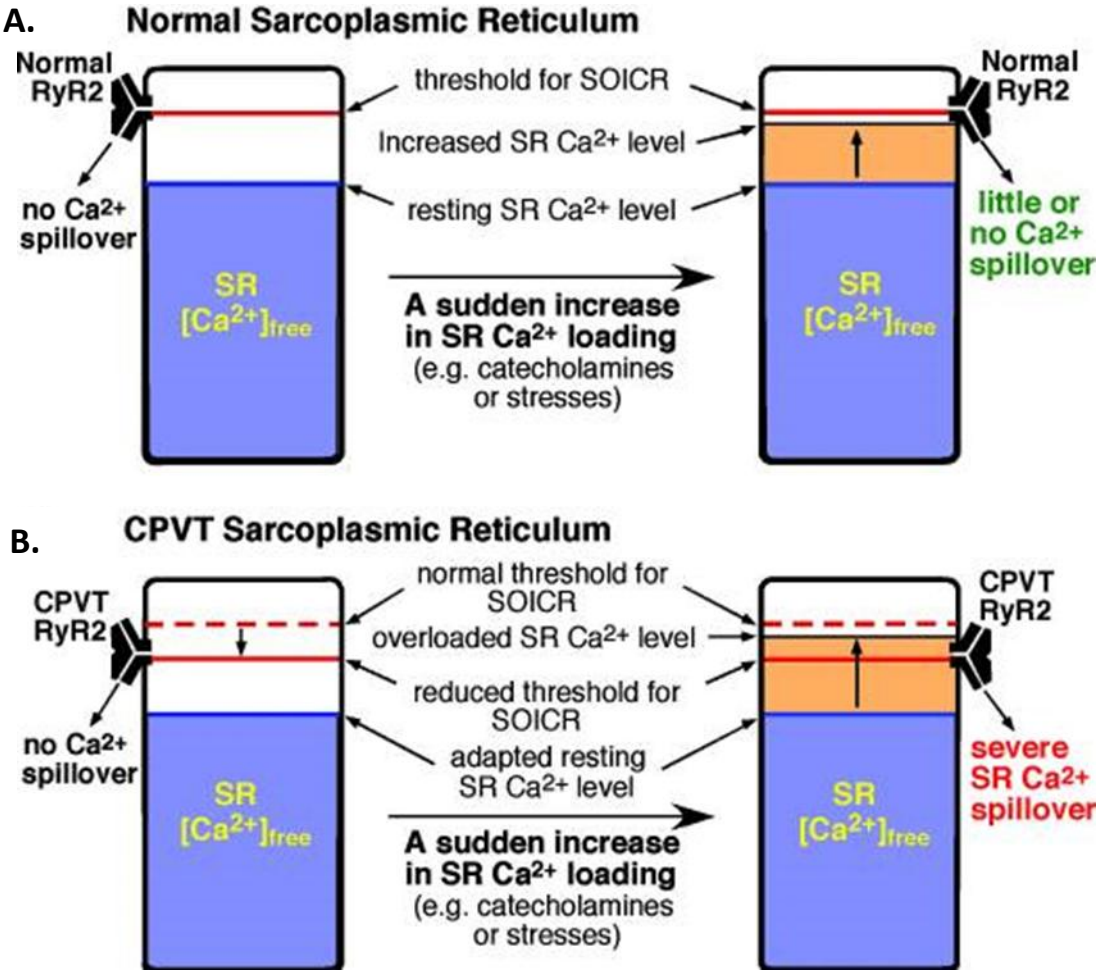

Figure 1.13. Proposed mechanism of SOICR dysfunction in CPVT-RyR2 mutants. Schematic representation of normal SR SOICR function (**A**) compared to the proposed effect of CPVT-linked RyR2 mutations on SOICR (**B**). Under normal circumstances, the difference between the SR $[Ca^{2+}]_{free}$ level (blue shading) and threshold for SOICR (red line) is sufficient such that sudden large increases in Ca^{2+} (orange shading) due to β-adrenergic stimulation do not breach the threshold, resulting in little to no Ca^{2+} leak from the SR. CPVT-linked RyR2 mutations are proposed to cause a decreased threshold for SOICR, as well as potentially altering the resting SR $[Ca^{2+}]_{free}$ level, causing increases in Ca^{2+} to result in Ca^{2+} leak from the SR which can trigger DADs and triggered arrhythmias. Figure taken from Jiang et al. (2004).

While these three mechanisms have been proposed as primary mechanisms of dysfunction, the appearance of one does not exclude a secondary contributing cause of CPVT and it is unlikely that there is one unifying mechanism to describe the effect of mutation. For example, the R2474S mutation causes domain unzipping that is followed by CaM dissociation (Uchinoumi et al. 2010a), and R420Q weakens the interaction with JPH2 and causes unzipping of the NTD and central domain (Yin et al. 2021). There is also the

possibility of additional mechanisms of dysfunction given only a small proportion of RyR2 mutations have been characterised (Olubando et al. 2020). It is likely that combination of these mechanisms and other aspects of dysfunctional channel activity all contribute to the breadth of CPVT phenotypes.

1.6.2.2 Treatment of CPVT

The first line of treatment for CPVT is often non-selective β-blockers such as propranolol or nadolol (Mazzanti et al. 2022) which counteract β-adrenergic stimulation (Priori et al. 2002), however this does not work for all patients (Hayashi et al. 2009) and without effective treatment, the mortality rate of CPVT patients is 30-50% by 35 years old (Hayashi et al. 2009; Tester et al. 2012; Kapplinger et al. 2018). This highlights the multifaceted nature of RyR2 dysfunction (**Section 1.6.2.1**) and the significant need for improved treatment options, several of which are explored below.

Flecainide is a sodium channel blocker that has antiarrhythmic effects and has been used in the treatment of AF and VT (Anderson et al. 1989) and has since been suggested to block Ca^{2+} release from RyR2 (Watanabe et al. 2009; Hilliard et al. 2010; Hwang et al. 2011; Kryshtal et al. 2021), however its mechanism of action in CPVT is highly debated. The evidence for an effect of flecainide on RyR2 includes a reduction in the rate of spontaneous Ca^{2+} waves in CSQ2-knockout cardiomyocyte models of CPVT2 (Watanabe et al. 2009; Hilliard et al. 2010; Hwang et al. 2011) and reduction in P_O due to flecainide addition in single channel recordings (Hilliard et al. 2010; Kryshtal et al. 2021). This has been disputed by studies that have shown flecainide only blocks cation movement through RyR2 in the cytosolic to luminal direction but not in the physiological direction (Bannister et al. 2015; Bannister et al. 2016), and that while flecainide can reduce the rate of Ca^{2+} waves, this is due to an effect on NCX rather than RyR2 (Sikkel et al. 2013). Despite this controversy, flecainide does appear to have a therapeutic effect and remains a potential treatment option for CPVT patients who are resistant to β-blocker treatment, regardless of its mechanism of action (Lieve et al. 2016; Wang et al. 2019; Benitah and Gómez 2021).

Dantrolene is a skeletal muscle relaxant used to treat malignant hyperthermia due to RyR1 mutations (Muehlschlegel and Sims 2009), but is also reported to have an antiarrhythmic effect on RyR2 (Kobayashi et al. 2009; Kobayashi et al. 2010). It has been shown to reduce RyR2 hyperactivity in several CPVT models, including reducing Ca^{2+} spark frequency in the

R2474S (Kobayashi et al. 2010) and S406L mutants (Jung 2012), and it also rescued an arrhythmogenic phenotype in HF cardiomyocytes (Maxwell et al. 2012; Nofi et al. 2020; Schmeckpeper et al. 2023; Yano et al. 2023), but has limited effect in healthy hearts (Paul-Pletzer et al. 2005). Dantrolene binds to RyR2 at residues 601-620 (rabbit RyR2) and exerts its inhibitory effects by stabilising inter-domain interactions (Seidel et al. 2015; Kajii et al. 2020; Uchinoumi et al. 2025). There is also evidence that dantrolene treatment is only effective for some mutants, with mutations in the channel domain (containing the TMD and CTD, aligning with hotspot cluster 4 and the end of cluster 3) appearing less affected (Penttinen et al. 2015). CaM and FKBP12.6 are also implicated in the efficacy of dantrolene. Single channel studies have shown that CaM is required for dantrolene inhibition of both RyR1 and RyR2, possibly due to causing a conformational change that alters the dantrolene binding site (Nishimura et al. 2015; Oo et al. 2015). FKBP12.6 dissociation by PKA phosphorylation or rapamycin also reduced the inhibitory effect of dantrolene in single channel studies but was rescued by addition of exogenous FKBP12.6 (Walweel et al. 2023a).

Rycals are stabilising small-molecule drugs that bind RyRs adjacent to the ATP binding site (Melville et al. 2022) and have been shown have an antiarrhythmic effect (Wehrens et al. 2004a; Lehnart et al. 2006; Miotto et al. 2022). Rycals are proposed to stabilise RyR2 by altering its conformation from a 'primed' state (an intermediate conformation in which the cytoplasmic domain shifts downwards and outwards) from which it can open into the closed state, and by preventing dissociation of stabilising FKBPs (Miotto et al. 2022). Several rycal molecules exist and have shown efficacy in reducing Ca^{2+} leak to different degrees. K201 (aka JTV-519) was the first rycal developed and reduced Ca^{2+} leak in canine models of HF, however it was found to block other channels in addition to RyRs (Yano et al. 2003). S107 is an RyR-specific rycal that has been shown to reduce diastolic Ca^{2+} release from RyR2 in atrial myocytes in the presence of FKBP12.6 (Shan et al. 2012), prevent VT and SCD (Lehnart et al. 2008) and prevent dissociation of FKB12 in RyR1 (Bellinger et al. 2008). ARM210 is a second generation rycal with improved binding that has reversed the primed structure of phosphomimetic S2808D RyR2 and the CPVT linked mutants R2474S (Miotto et al. 2022), R420Q and R420W (Miotto et al. 2024). This molecule is now undergoing clinical trials in patients with both RyR1 and RyR2-related myopathies (Marks 2023). These results, while promising, are controversial due to the highly debated role of FKBP12.6 in RyR2 function

(**Section 1.5.1**), however if they confer reduced Ca^{2+} leak then they remain a viable future treatment option for CPVT regardless of mechanism.

1.6.3 Arrhythmogenic right ventricular dysplasia

ARVD2 (also called arrhythmogenic right ventricular cardiomyopathy (ARVC)) is an inherited arrhythmogenic condition that can arise from RyR2 mutation and presents much like CPVT with exercise-induced VT. However, unlike in CPVT, patient hearts with ARVD2 display fatty and fibro-fatty replacement of cardiomyocytes (Rampazzo et al. 1995; Basso et al. 1996). Several ARVD2-linked mutations have been identified in RyR2. R176Q, L433P, N2386I and T2504M were the first 4 identified (Tiso 2001) and resulted in RyR2 GoF, with the exception of L433P which showed a reduction-of-function phenotype (Thomas et al. 2004). R420W (Nishio et al. 2006), Y2392C (Bauce et al. 2002; Tiso et al. 2002), A77V (d'Amati et al. 2005) are also implied to cause fatty replacement in the myocardium and dysfunctional Ca^{2+} release that is corrected by treatment with β-blockers (Sleiman et al. 2022), and many more have been identified in genetic screening as potential causative mutations for ARVD2 (Roux-Buisson et al. 2014). Despite evidence that these mutations can result in the characteristic fibro-fatty replacement of cardiomyocytes (Tiso 2001; Bauce et al. 2002; d'Amati et al. 2005; Nishio et al. 2006; Del Duca et al. 2024) there is still some disagreement as to whether they cause ARVD2 or CPVT (Jiang et al. 2005; Priori and Napolitano 2005; Ohno 2016) and several studies have found no evidence of fatty-fibrous tissue in R176Q (Kannankeril et al. 2006; Mathur et al. 2009) or R420W mouse models (Okudaira et al. 2014).

1.6.4 Loss-of-function RyR2 diseases

While RyR2 dysfunction is most commonly associated with channel GoF, several loss-of-function (LoF) mutations have been identified that reduce channel activity (Thomas et al. 2004; Jiang et al. 2007; Zhao et al. 2015; Fujii et al. 2017; Roston et al. 2017). This has been attributed to decreased luminal or cytosolic Ca^{2+} sensitivity and can result in decreased caffeine sensitivity and an increase in the threshold for SOICR (**Figure 1.14**), leading to reduced Ca^{2+} leak, but contributing to the generation of early afterdepolarizations (EADs) (Thomas et al. 2004; Jiang et al. 2007; Fujii et al. 2017; Roston et al. 2017; Li et al. 2021; Sun et al. 2021; Zhong et al. 2021). The resulting phenotype of an LoF varies, however in some cases it presents as CPVT or ARVD2 with syncope or SCD that can be adrenergically stimulated (Roston et al. 2017; Sun et al. 2021; Zhong et al. 2021). Other LoF mutations

show little to no response to β-adrenergic stimulation and cannot be detected by exercise stress testing (Li et al. 2021; Sun et al. 2021). This has resulted in identification of a novel ryanodinopathy termed Calcium Release Deficiency Syndrome (CRDS) that has a distinct arrhythmogenic mechanism compared to CPVT and is predominantly associated with mutations in hotspot IV (residues 4497-4959) that are insensitive to catecholaminergic stimulation (Sun et al. 2021).

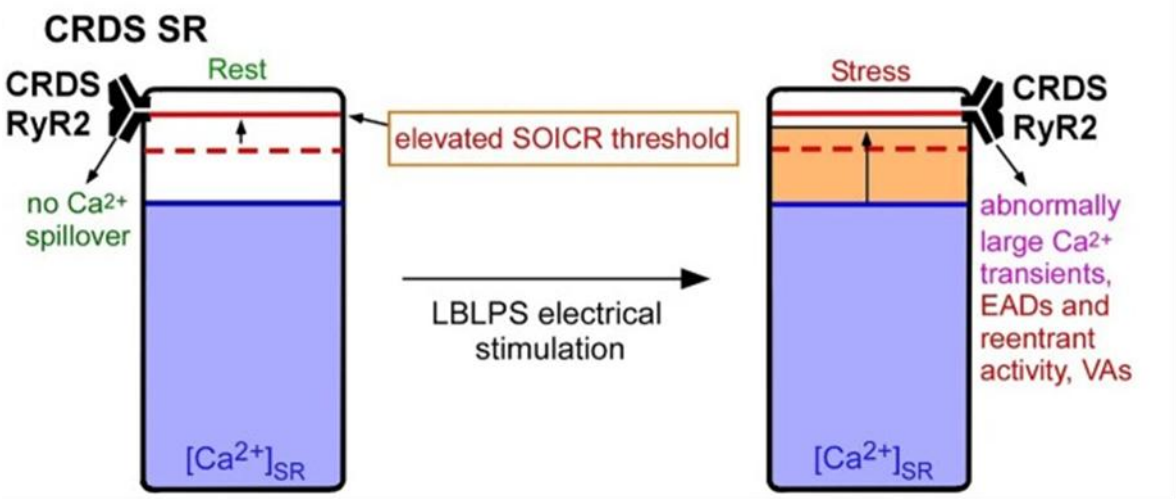

Figure 1.14. Changes to SOICR threshold in CRDS RyR2 mutations. CRDS increases the threshold for activation of SOICR due to decreased sensitivity to luminal Ca^{2+}. This leads to increased SR Ca^{2+} load upon long-burst, long-pause, short-coupled (LBLPS) electrical stimulation and reduced diastolic Ca^{2+} release. Figure taken from Steinberg et al. (2023).

1.6.5 RyR2 in heart failure

HF is a leading cause of death worldwide and is a chronic disease in which both systolic and diastolic cardiac function deteriorate over time. In HF, β-adrenergic stimulation is dysregulated due to stress, which over time results in desensitization and downregulation of receptors, requiring progressively greater stimulation to generate a normal cardiac output (Schwinger 2021). HF can present with either a reduced ejection fraction or a preserved ejection fraction; a reduced ejection fraction is generally associated with cardiac injury or hypertension, resulting in altered cardiac function (Schwinger 2021). At the cellular level, the expression and function of many EC-coupling proteins is altered in HF including SERCa, LTCCs, NCX and RyR2 (Hasenfuss et al. 1994; Schröder et al. 1998; Chen et al. 2002; Hasenfuss and Pieske 2002) and Ca^{2+} homeostasis is disrupted (Bers 2006). This includes increased Ca^{2+} transient duration and decreased amplitude caused by reduced SR Ca^{2+}

content, increased Ca^{2+} leak due to increased RyR2 activity, and the generation of DADs (Hasenfuss and Pieske 2002; Janse 2004; Pogwizd 2004; Bers 2006). Structural remodelling is also observed in HF, including loss of T-tubules which impacts CICR propagation (Guo et al. 2013; Jones et al. 2018), loss of contractile machinery and remodelling of the extracellular matrix which increases the stiffness of the myocardium (Schaper et al. 2002; Segura et al. 2014; Schwinger 2021).

Regarding altered Ca^{2+} homeostasis, the increased Ca^{2+} transient duration and decreased amplitude seen in HF is a product of increased Ca^{2+} efflux from the cell via NCX, decreased SERCa expression, and altered RyR2 function, leading to reduced SR Ca^{2+} load (Bers 2006). Increased activity of RyR2 leading to Ca^{2+} leak has long been implicated in the progression of HF (Fischer et al. 2014; Uchinoumi et al. 2016; Eisner et al. 2017; Walweel et al. 2017a; Dries et al. 2018) and is regulated by multiple factors, including phosphorylation (**Section 1.4.1**), FKBP12.6 binding (**Section 1.5.1**), and altered clustering of channels (**Section 1.2.4**). While these mechanisms all individually contribute to HF they are also interlinked, with the possibility that PKA hyperphosphorylation results in FKBP12.6 dissociation (Marx et al. 2000) which shifts clusters into a less dense arrangement (Asghari et al. 2020), all of which increase Ca^{2+} leak. This then increases the propensity for triggered activity such as DADs and EADs that can deteriorate into VT and VF (Janse 2004; Pogwizd 2004; Venetucci et al. 2007a). Collectively, it is the interplay of multiple EC-coupling proteins that contribute to the progression of HF, however RyR2's role is central to this and to controlling Ca^{2+} flux from the SR.

1.6.6 Dilated Cardiomyopathy

Dilated cardiomyopathy (DCM) is characterised by dysfunctional and enlarged ventricles (typically the left) with reduced contractility (Lipshultz et al. 2003). It is genetically determined in up to 50% of cases (Bozkurt et al. 2016; McKenna et al. 2017), most of which occur due to mutation in the genes encoding titin, myosin 7, troponin T, phospholamban (PLB) and lamin A/C (LMNA) (Schultheiss et al. 2019). RyR2 mutation has been noted as a genetic cause in several studies, specifically in cases of exon-3 deletion syndrome (E3DS) which is a rare ryanodinopathy that causes an in-frame deletion of 35 amino acids in exon 3 that results in a mixed tachycardic-bradycardic phenotype (Bhuiyan et al. 2007; Campbell et al. 2015; Dharmawan et al. 2019). Genetic testing has also identified several RyR2 missense

mutations in DCM patients (Pugh et al. 2014; Walsh et al. 2017), although no further testing has been performed to confirm the potential impact of these mutations, and as such DCM appears to remain a rare consequence of RyR2 mutation.

A central mechanism in the genesis and progression of DCM is dysfunctional contraction which arises from decreased myocyte contractility, which can be due to abnormal Ca^{2+} handling (Haghighi et al. 2004; Robinson et al. 2007; Liu et al. 2015; Rowe et al. 2017; Law et al. 2020; Pioner et al. 2020; Wang et al. 2025). These changes trigger cardiac remodelling via several mechanisms including the calcineurin / nuclear factor of activated T-cells (NFAT) pathway (Schulz and Yutzey 2004) and via CaM / CaMKII (Zhang and Brown 2004). Several studies have sought to determine the changes to Ca^{2+} handling that might precede DCM and a common phenotype is decreased SR Ca^{2+} store load and decreased Ca^{2+} transient amplitude (Sun et al. 2012; Liu et al. 2015; Dridi et al. 2021). This has been observed in a rat model of DCM-linked PLB mutation (R25C-PLB) which decreased SR Ca^{2+} load and Ca^{2+} transient amplitude, and increased RyR2 phosphorylation and Ca^{2+} leak (Liu et al. 2015). A mouse model of muscular dystrophy-associated DCM caused by mutation in LMNA (H22P-LMNA) also resulted in increased Ca^{2+} leak, increased phosphorylation at S2808 in RyR2, decreased SR store load, and dissociation of FKBP12.6 (Dridi et al. 2021). An induced pluripotent stem cell (iPSC) model of familial DCM caused by mutation of troponin T also reduced store load and Ca^{2+} transient amplitude (Sun et al. 2012). E3DS in RyR2 did not alter the store load, but increased the propensity for SOICR and the amplitude of SOICR-induced transients by reducing the threshold for activation and termination of Ca^{2+} release (**Figure 1.15**) (Tang et al. 2012). Not only do many of these behaviours increase the likelihood of DADs (Tang et al. 2012; Dridi et al. 2021), but they deregulate cytosolic Ca^{2+} which impairs contraction and contributes to DCM.

1.6.7 Hypertrophic Cardiomyopathy

Hypertrophic cardiomyopathy (HCM) is characterised by thickening of the ventricle wall (typically the left ventricle), fibrosis and diastolic dysfunction (Smania 2025). It is commonly caused by genetic mutation of sarcomeric proteins with 70% of cases linked to mutations in the genes encoding myosin heavy chain 7 and myosin-binding protein (Maron et al. 2012), however a small number of RyR2 mutations have been implicated in HCM through genetic

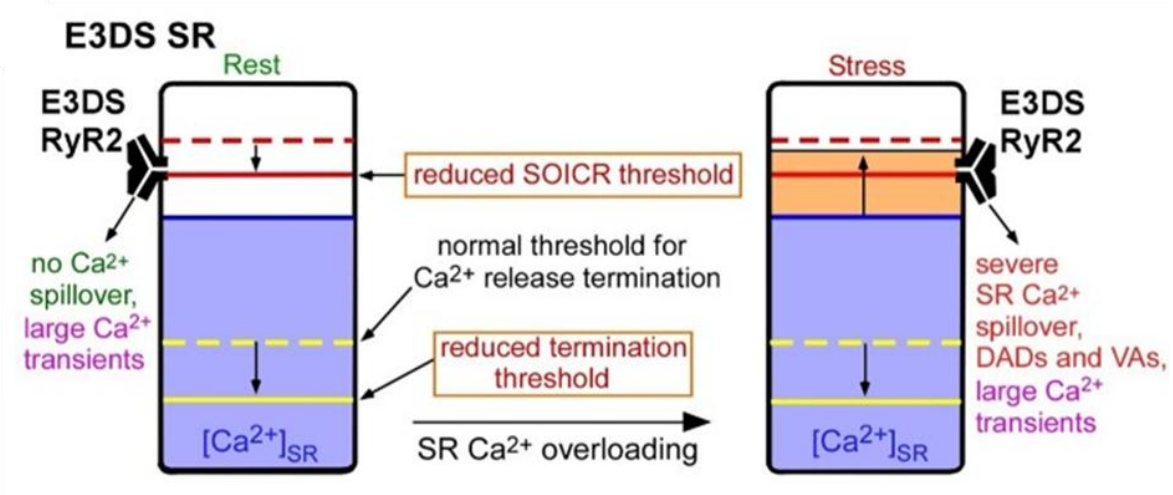

Figure 1.15. Changes to SOICR threshold in E3DS RyR2 mutations. E3DS results in deletion of 35 amino acids in exon 3 and causes a reduced threshold for activation of SOICR and a reduced threshold for termination of SOICR. This results in increased Ca^{2+} leak and prolonged Ca^{2+} transients with greater fractional $Ca^{2=}$ release. Figure taken from Steinberg et al. (2023).

testing (Fujino et al. 2006; Landstrom and Ackerman 2012; Lopes et al. 2015; Walsh et al. 2017; Alvarado et al. 2019). The mechanisms involved in HCM operate via many of the same pathways as DCM including via the calcineurin / NFAT pathway and CaMKII, but in general their effects are opposites, with HCM involving increased contractility compared to hypocontractility in DCM (Schulz and Yutzey 2004; Zhang and Brown 2004; Robinson et al. 2007; Tang et al. 2012).

T1107M was the first RyR2 mutation linked to HCM, identified in patients with asymmetrical left ventricular hypertrophy which was accompanied by VF (Fujino et al. 2006). A cell model of the mouse equivalent mutation A1107M was shown to increase the termination threshold for Ca^{2+} release from the SR meaning Ca^{2+} release terminated at a higher store load than the WT (Tang et al. 2012). This was accompanied by no change in the threshold for Ca^{2+} release and no change in store load, resulting in an overall decrease in fractional Ca^{2+} release, which is a hallmark of HCM (Tang et al. 2012). A second mutation in the same domain (SPRY2), P1124L, was also identified in a patient with HCM and a mouse model of this mutation resulted in both arrhythmia and HCM (Alvarado et al. 2019). However, this resulted in a reduced termination threshold for Ca^{2+} release and decreased sensitivity to cytosolic Ca^{2+} indicating a luminal GoF but a cytosolic LoF that resulted in an overall increase in fractional release (Alvarado et al. 2019). This is contrary to the usual changes to Ca^{2+}

release in HCM, but it was posited that increased CaM expression might be an important factor in the development of hypertrophy in P1124L mice, and that cytosolic LoF drives HCM whereas luminal GoF drives the arrhythmia phenotype (Alvarado et al. 2019).

1.7 Project Rationale

Given the vast number of hRyR2 mutations that have been implicated in disease, it is unsurprising that many remain uncharacterised simply due to the resources required to investigate each one. This is particularly noticeable for mutations located outside the hotspot regions, many of which are classified as variants of uncertain significance (VUS) with no real indication as to their pathogenicity or mechanism of dysfunction. This includes the areas involved in the clustering interaction – P1 and SPRY1 – where several VUS mutations associated with cardiomyopathies and / or arrhythmias are found. This is a structurally significant part of RyR2 due to the importance of clustering as a regulatory mechanism, but little is known about mutations in this region. Notably, two HCM-associated mutations, T1107M and P1124L, are found in SPRY2 which is adjacent to P1 and SPRY1. This highlights a potentially interesting and largely unexplored region of RyR2 in which to investigate disease-linked mutations from both a structural and functional perspective.

1.7.1 Mutation at Arginine 1051 in the P1 domain

Three missense mutations that fall into this category are found at R1051 in the P1 domain; R1051P, R1051C and R1051H, which have been linked to CPVT (all variants) (Marjamaa et al. 2009; Landrum et al. 2016, ClinVar accessions VCV000201235.30 and VCV000043765.41), HCM (R1051C) (Lopes et al. 2015), and DCM (R1051H) (Pugh et al. 2014; Walsh et al. 2017) through genetic testing. Multiple other mutations linked to cardiac conditions have been identified in the P1 domain through genetic screening and the vast majority are classified as VUS; notably, none are classified as pathogenic based on *in silico* analyses nor have functional characterisations been performed (Stenson et al. 2003; Landrum et al. 2016). Mutations in P1 are most commonly associated with CPVT (Marjamaa et al. 2009; Medeiros-Domingo et al. 2009; Giudicessi et al. 2019), however there are also several that have been genetically linked to cardiomyopathies (Haas et al. 2015; Walsh et al. 2017) and sudden infant death (Tester et al. 2007). In addition to their role in disease, the R1051 mutations are

of interest due to the involvement of the P1 domain in the clustering interaction, where it is proposed to interact directly with adjacent tetramers (Cabra et al. 2016). Mutations at R1051 are therefore interesting from a clinical standpoint as well as structural one, making them a prime candidate for characterisation.

1.7.2 Structure of the P1 domain

The P1 domain consists of residues 861 to 1066 (human numbering) and contains two interconnected domains (repeat 1 & 2) that form a 'C'-shaped clamp on each corner of the RyR2 tetramer (**Figure 1.16A**) (Peng et al. 2016). While no high-resolution structure is available for the P1 domain of RyR2 (highest available is 2.58Å from cryo-EM (Miotto et al. 2022)), the crystal structure of P1 in rabbit RyR1 (residues 862-1054) has been resolved to 1.5Å and shows that both repeats contain two α-helices and a short single stranded C-terminus β-sheet, and repeat 2 contains an additional 3-stranded β-sheet; the two repeats are connected via an unstructured 30-amino acid loop (Yuchi et al. 2015) (**Figure 1.16B**). The sequence homology between P1 in human RyR1 and hRyR2 is 74% (**Figure 1.16C**), so while there are minor structure differences between the two, the general structure of the clamp domain as seen in cryo-EM structure appears comparable to that of RyR1 (**Figure 1.16B**) (Yuchi et al. 2015; Peng et al. 2016; Bauerová-Hlinková et al. 2020). R1051 is located in the centre of the second α-helix in repeat 2 based on both the crystal structure of P1 in RyR1 and the RyR2 cryo-EM (Yuchi et al. 2015; Peng et al. 2016). This residue is highly conserved in RyR2 across species and is conserved in RyR3, however the equivalent residue in RyR1 is a cysteine (**Figure 1.16C**) (Marjamaa et al. 2009).

P1 is proposed to form one of the main contact points for the inter-tetramer interaction during clustering of RyR2 channels, contacting either the P1 domain on adjacent channels (side-by-side interaction), FKBP12.6 or the helical domain (corner-to-corner / checker-board interaction) (**Figure 1.7D** and **E**) (Yin and Lai 2000; Zalk et al. 2015; Cabra et al. 2016). This, along with the SPRY1 domain and the accessory protein FKBP12.6, allows RyR2 to form clusters of multiple channels as a way to regulate Ca^{2+} release and potentially facilitate coupled gating between channels (**Section 1.2.4**). Modelling also suggests that, in addition to the potential need for FKBP12.6 dissociation, some domain rearrangement in P1 may be required to facilitate a tight corner-to-corner clustering interaction (Cabra et al. 2016). How this might present is unclear, but it is known that this domain undergoes dynamic changes

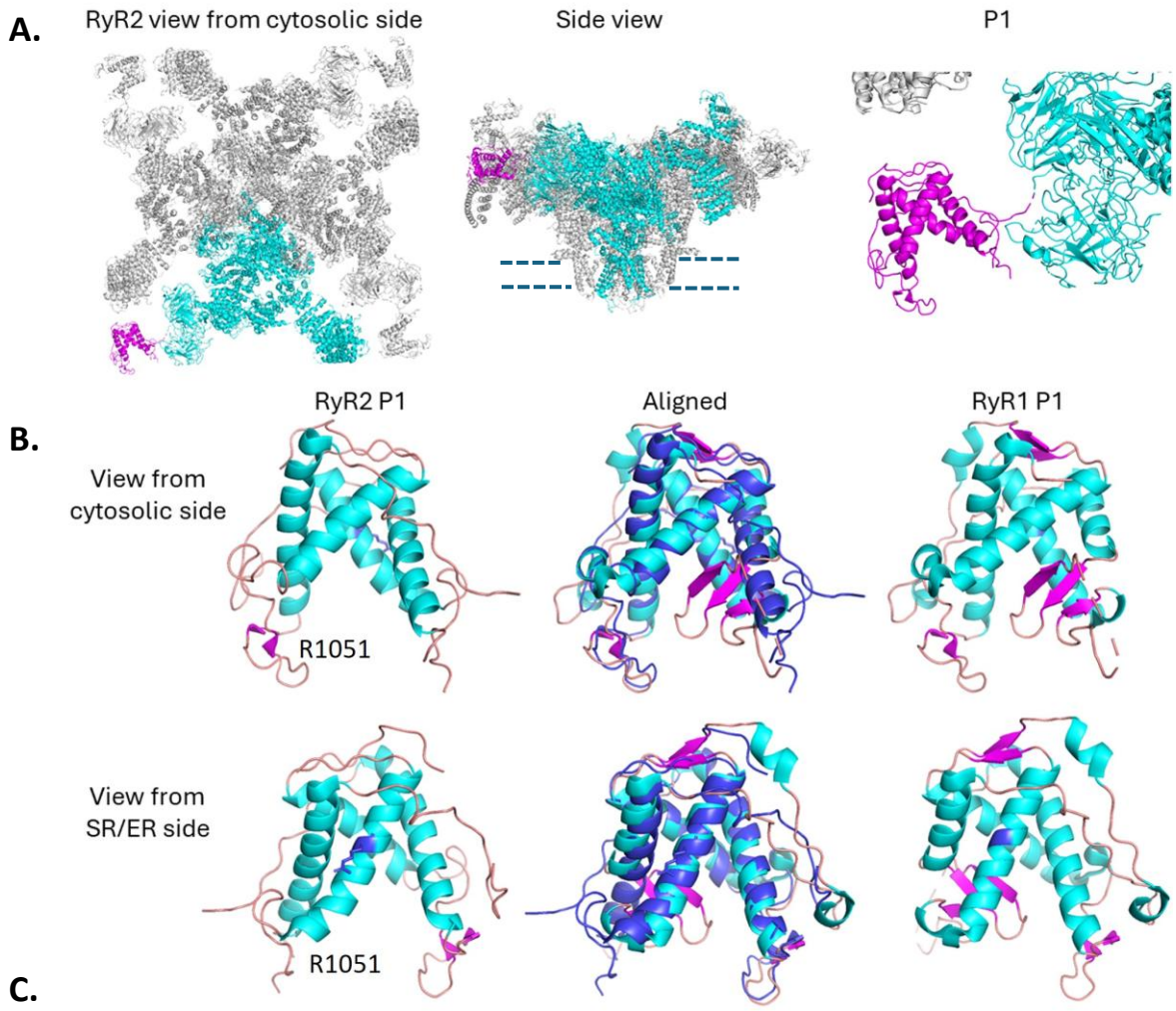

C.

```
hRyR1   IVLPPHLERIREKLAENIHELWALTRIEQGWTYGPVRDDNKRLHPCLVDFHSLPEPERNYNLQMSG   930
        |||||||||||||||||||||| + +|| || |||||||||| |||||+|  ||| |||||||||
hRyR2   IVLPPHLERIREKLAENIHELWVMNKIELGWQYGPVRDDNKRQHPCLVEFSKLPEQERNYNLQMSL   941

hRyR1   ETLKTLLALGCHVGMADEKAEDNLKKTKLPKTYMMSNGYKPAPLDLSHVRLTPAQTTLVDRLAENG   992
        ||||||||||||||++|| ||| +|| |||| | +++|||||+||| ++|||+|  +||+||||
hRyR2   ETLKTLLALGCHVGISDEHAEDKVKKMKLPKNYQLTSGYKPAPMDLSFIKLTPSQEAMVDKLAENA  1003

hRyR1   HNVWARDRVGQGWSYSAVQDIPARRNPRLVPYRLLDEATKRSNRDSLCQAVRTLLGYGYNIE       1054
        ||||||||+ |||+|   ||+  ||||||||| |||+ ||+||+||| +|||||||||||+|
hRyR2   HNVWARDRIRQGWTYGIQQDVKNRRNPRLVPYTLLDDRTKKSNKDSLREAVRTLLGYGYNLE       1065
```

Figure 1.16. Location and structure of the P1 domain in RyR2 and RyR1. A. Location of P1 (pink) in one monomer (cyan) of the hRyR2 tetramer as viewed from the cytosol towards the membrane, side view (SR membrane denoted by dashed lines, cytosolic domain at top), and a close-up of P1 and adjacent domains. **B.** Alignment of P1 domain in RyR2 and RyR1; in aligned structure RyR2 is indicated by dark blue. The alignment demonstrates that the structure from the RyR2 cryo-EM is largely comparable to the X-ray crystallography structure of RyR1, except for β-sheets and several smaller helices that are not resolved in the RyR2 structure. **C.** Alignment of hRyR1 and hRyR2; | indicates conserved residue, + indicates conservative changes, absence of symbol indicates non-conservative changes; the residue change from RyR1 to RyR2 is indicated in yellow. RyR2 structure – PDB accession 5GOA (Peng et al. 2016). RyR1 P1 structure – PDB accession 5C30 (Yuchi et al. 2015).

as the channel shifts from a closed to an open state involving a downward and rotational shift (Efremov et al. 2015; Yuchi et al. 2015; Peng et al. 2016), so it is possible that it undergoes additional conformational shifts during clustering. Mutations in P1, including R1051, may therefore impair any rearrangement in addition to affecting interaction with adjacent tetramers.

1.7.3 R1051P

The R1051P-hRyR2 mutation was first identified in a study of patients experiencing premature ventricular contractions with a family history of syncopal episodes and sudden death, where it was found in a patient presenting with CPVT and subsequently in one additional family member (Marjamaa et al. 2009). The patient had a history of syncopal episodes from the age of 30, and had minor left ventricular hypertrophy but not sufficient to warrant an HCM diagnosis (Marjamaa et al. 2009). The patient's son also carried the R1051P mutation and showed characteristics of CPVT from adolescence in the absence of any hypertrophy (Marjamaa et al. 2009). The patients' zygosity is unconfirmed but is presumed heterozygous based on the available genetic information. No other reports of R1051P are noted in the literature, and the variant is not reported in the ClinVar database (Landrum et al. 2016), although it is reported on the Human Genome Mutation Database (HGMD) (Stenson et al. 2003).

In silico analyses give contradictory predictions for the pathogenicity of R1051P ranging from tolerated to strongly pathogenic (**Table 1.1**). Based solely on the amino acid substitution, proline is a non-conservative substitution that is likely to disrupt the local secondary structure of the P1 domain as it is known as a helix breaker (Imai and Mitaku 2005; Melnikov et al. 2016; Bauerová-Hlinková et al. 2020). This is due to its unique structure in which the side chain covalently attaches to the amino group creating a rigid cyclical pyrrolidine ring; this also means there is no hydrogen on the amino group, preventing proline from forming hydrogen bonds with other amino acids in the backbone and introducing a kink into α-helices (Imai and Mitaku 2005; Melnikov et al. 2016). As R1051 is located in the centre of one of four α-helices in the P1 domain, it is probable that mutation to a proline would impact the secondary structure which may then impact the domain's ability to function correctly, whether that be during clustering or domain rearrangement. Due to the potential detrimental effect of proline on protein structure, it

was hypothesised that R1051P would be the most likely mutation to cause disruption to RyR2 function.

Table 1.1. In silico predictions of pathogenicity for all identified R1051-hRyR2 missense mutations. Computational predictions vary in their expected pathogenicity of different variants, and as such multiple tools were consulted (a PolyPhen-2 score could not be obtained for R1051G). AlphaMissense, PolyPhen-2 and REVEL all use a score of 1 to indicate pathogenic mutations and 0 to indicate benign/tolerated; SIFT indicates tolerated mutations by a score of 1, and pathogenic mutations by a score of 0. AlphaMissense, Polyphen-2 and SIFT are all individual tools for predicting pathogenicity based on sequence and structural predictions; REVEL is an ensemble tool that combines scores from 13 individual algorithms (including SIFT and PolyPhen-2) as a measure of pathogenicity. Scores were obtained via SpliceAI Lookup (https://spliceailookup.broadinstitute.org/) and supplemented by scores from the relevant tools where SpliceAI did not provide a score (AlphaMissense - (Tordai et al. 2024), PolyPhen-2 (Adzhubei et al. 2010), SIFT (Sim et al. 2012), REVEL (Ioannidis et al. 2016)).

	AlphaMissense	PolyPhen2	SIFT	REVEL
R1051P	0.9982	0.833	0.258	0.87
	Strong pathogenic	Possibly damaging	Tolerated	Moderately pathogenic
R1051C	0.5871	0.905	0.37	0.678
	Indeterminate	Possibly damaging	Tolerated	Mildly pathogenic
R1051H	0.5039	0.876	0.3	0.716
	Indeterminate	Possibly damaging	Tolerated	Mildly pathogenic
R1051L	0.8767	0.012	0.37	0.666
	Supports pathogenic	Supports benign	Tolerated	Mildly pathogenic
R1051G	0.8832		0.435	0.716
	Supports pathogenic		Tolerated	Mildly pathogenic

1.7.4 R1051C

R1051C was first identified in a large-scale genetic screening of HCM patients (Lopes et al. 2015) and has since been identified in a patient suffering from an unspecified congenital cardiac defect (Hauser et al. 2018), and has also been linked to CPVT (Landstrom et al. 2017a). The zygosity of these patients is unconfirmed, but all genome database entries for R1051C report the variant in the heterozygous state. The total allele frequency of R1051C as recorded in the gnomAD database (variant ID 1-237550628-C-T) (Karczewski et al. 2020) is 0.000064, with some indications that this allele may be too frequently occurring to

represent a pathogenic disease mutation (Landstrom et al. 2017a). R1051C is listed in the ClinVar (accession VCV000201235.30) and HGMD databases as a VUS. *In silico* predictions for pathogenicity range from likely tolerated to possibly damaging (**Table 1.1**). The amino acid substitution in R1051C is non-conservative as it replaces the basic side chain of arginine with the non-polar, sulphur-containing side chain of cysteine. The consequences for the local secondary structure of the α-helix are likely to be less detrimental than in the R1051P mutation as cysteine should not greatly interrupt the secondary structure of the helix. However, it is still prone to changing the interactions that can form, including the potential formation of disulfide bonds with nearby cysteine residues that could restrict movement of the domain. However, while R1051 is a highly conserved residue in RyR2, the equivalent amino acid in RyR1 is a cysteine which might indicate that it is tolerated at this position.

1.7.5 R1051H

R1051H is listed in both ClinVar and the HGMD and has been identified by genetic screening in a patient with DCM (Pugh et al. 2014; Walsh et al. 2017) and suspected-CPVT (Kapplinger et al. 2018). The DCM patient also harboured 6 other mutations in DCM-associated genes, including genes encoding titin (2 mutations), vinculin, laminin subunit alpha 4, LIM binding domain 3, and RNA-binding motif protein 20, and was heterozygous for the R1051H variant in hRyR2. The total allele frequency of R1051H was 0.00022 as reported in ClinVar; this is higher than the expected frequency of pathogenic RyR2 mutations (Landrum et al. 2016, ClinVar acession VCV000043765.41). *In silico* predictions of pathogenicity for R1051H ranged from tolerated to possibly pathogenic (**Table 1.1**). Histidine is a conservative amino acid substitution due to its basic side chain, however histidine is a less interactive residue than arginine which may reduce the number of interactions it can form (Muller et al. 2019), which could impact the function of the P1 domain.

1.7.6 R1051L and R1051G

More recently, two additional substitutions at R1051 have been detected; R1051L and R1051G. Both missense mutations were identified by genetic testing and linked to CPVT (ClinVar accession VCV001993717.3 and VCV003070716.1, respectively) and are not present in population databases, nor in the literature. *In silico* predictions for R1051L and R1051G range from tolerated to mildly pathogenic (**Table 1.1**). R1051L is a non-conservative amino acid substitution as leucine is an aliphatic branched chain amino acid. R1051G is also a non-

conservative amino acid substitution as glycine is an aliphatic amino acid with a single hydrogen as its side chain. While neither substitution is likely to make drastic changes to the secondary structure of the local region like proline, they are prone to altering the interactions formed due to the loss of the basic properties of arginine.

1.8 Project hypotheses and aims

This project aims to provide the first functional characterisation of R1051P, R1051C and R1051H mutations in hRyR2. These mutations have been identified as potentially disease causing in a range of cardiac conditions including CPVT, HCM and DCM, and therefore they represent a potential broad range of conditions arising from mutations at a singular residue. The pathogenicity of these mutants is uncertain, therefore functional characterisation will assist in understanding how they might contribute to disease and by what mechanism this may occur. These mutations are particularly of interest as they occur outside the mutation hotspot domains of RyR2 and are found in the P1 domain, which is proposed to interact during the clustering interaction. It is hypothesised that the R1051 mutants will alter Ca^{2+} release from RyR2, and that this may result from a change to the clustering interaction. It is proposed that R1051P-hRyR2 will have the most damaging effect on hRyR2 function due to its properties as a helix breaker. To test this hypothesis the main aims of the project are as follows;

- Engineer recombinant R1051-mutant hRyR2 and express in HEK293 cells; this will provide a suitable system for functional characterisation in whole cells and for overexpression for solubilisation and purification of mutant hRyR2. Expression will use a homozygous model which will result in the formation of homotetramers containing only WT or mutant-hRyR2. While co-transfection of R1051-mutants with the WT would more closely mimic the heterozygous genotype of patients, this would result in a heterogenous population of channels including WT homotetramers, mutant homotetramers, and heterotetramers which could complicate the interpretation of functional data. A homozygous approach will allow the impact of R1051-mutation to be assessed more directly.
- Characterise R1051-mutant hRyR2 function at the whole cell level. This will include live cell Ca^{2+} imaging in HEK293 cells transfected with R1051-mutant hRyR2 to assess whether mutation impacts spontaneous Ca^{2+} release from RyR2. Whole cells will also

be assessed by immunofluorescence to determine whether R1051-mutant hRyR2 is trafficked correctly within the cell, and expression levels of mutant hRyR2 will be investigated by Western Blotting.

- Droplet interface bilayers (DIB) and total internal reflection microscopy (TIRF) will be used to assess Ca^{2+} release from populations of R1051-mutant hRyR2. This will allow Ca^{2+} release dynamics to be assessed in a minimal system and correlated to cluster size, which should reveal whether R1051-mutants impact the ability of channels to form clusters and whether this alters Ca^{2+} release from hRyR2 on a population level.
- Solubilised and purified R1051-mutant hRyR2 will be incorporated into artificial lipid bilayers to assess the gating of single channels in a minimal system. This will reveal whether the gating mechanics of mutant hRyR2 differs from the WT under diastolic (nominally ~0 nM $[Ca^{2+}]_{cyt}$) and systolic (100 mM $[Ca^{2+}]_{cyt}$) conditions in the absence of other regulatory factors and will reveal basal dysfunction of the channels.

Chapter 2

Materials and methods

2.1 Materials List

2.1.1 General laboratory reagents, chemicals and equipment

All reagents and chemicals were analytical grade and purchased from Sigma Aldrich or Thermo Fisher Scientific, unless otherwise noted. Reagents and buffers were prepared using deionised water (dH_2O) or autoclaved deionised water (ddH_2O) for molecular biology or cell culture applications and stored as per the manufacturer's instructions. Where necessary, solutions were filter sterilised using a 0.22 µM Millex® syringe filter (Millipore) (indicated in methods). All pH readings were taken using the Mettler Toledo FiveEasy Plus pH kit and adjusted using 1 M/10 M HCl or 1 M/10 M KOH unless otherwise noted.

2.1.2 Site directed mutagenesis

- Forward and reverse primers (Eurofins) - designed specifically for R1051 site (see **Section 2.2.1**).
- QuikChange II XL Site-Directed Mutagensis kit (Agilent).
    - 10x Reaction Buffer – proprietary formula.
    - QuikSolution reagent – proprietary formula, used to improve linear amplification.
    - PfuUltra High-Fidelity DNA Polymerase – 2.5 units/µL
    - dNTP mix – proprietary formula.
    - DpnI restriction enzyme – 10 units/µL.
- Nuclease free water – deionised and filtered water containing no DNases or RNases to prevent degradation of DNA or RNA in samples.

2.1.3 Cloning

- pSL1180 plasmid containing *SpeI/SanDI* fragment of hRyR2 (Obtained from Dr N L Thomas (Thomas et al. 2004)).
- pcDNA3-eGFP-hRyR2 plasmid (Obtained from Dr C H George (George et al. 2003a; George et al. 2003b)).
- GeneJet Gel Extraction Kit (Thermo Fisher Scientific).
    - Binding Buffer – contains guanidinium thiocyanate, proprietary formula.
    - Wash Buffer – diluted 1:5 with 96-100% ethanol, proprietary formula.
    - Elution Buffer – 10 mM Tris-HCl, pH 8.5.
- Rapid DNA Ligation Kit (Roche Applied Science).

- T4 DNA Ligase.
- 5x T4 DNA Ligase Buffer – 250 mM Tris-HCl (pH 7.6), 50 mM $MgCl_2$, 5 mM ATP, 5 mM DTT, 25% (w/v) polyethylene glycol-8000.

2.1.4 Transformation and propagation

- XL10-Gold cells (Agilent) – Competent *Escherichia coli* cell line used for ligation products.
- MAX Efficiency™ Stbl2™ cells (Thermo Fisher Scientific) – Competent *E. coli* cell line used for general propagation of hRyR2 plasmid DNA.
- Super Optimal broth with Catabolite repression (SOC) medium - 2% tryptone, 0.5% yeast extract, 10 mM NaCl, 2.5 mM KCl, 10 mM $MgCl_2$, 10 mM $MgSO_4$, and 20 mM glucose.
- Luria Bertani (LB) broth - 10 g/L tryptone, 5 g/L yeast extract, 5 g/L NaCl, autoclaved, and ampicillin added before use.
- LB_{AMP} agar plates – LB broth supplemented with 15 g/L agar, autoclaved, and ampicillin added before setting.
- Ampicillin 100 mg/mL stock – filter sterilised and stored at -20°C. Working concentration 100 µg/mL.

2.1.5 Miniprep – small-scale plasmid isolation

- QIAprep® Spin Miniprep Kit (Qiagen).
  - Buffer P1 – Resuspension buffer - 50 mM Tris-Cl, pH 8.0, 10 mM ethylenediaminetetraacetic acid (EDTA), 100 µg/ml RNase A.
  - Buffer P2 – Lysis buffer - 200 mM NaOH, 1% sodium dodecyl sulphate (SDS) (w/v).
  - Buffer N3 – Neutralisation buffer - 4.2 M guanidine hydrochloride, 0.9 M potassium acetate, pH 4.8.
  - Buffer PE – Wash buffer - 80 mM NaCl, 8 mM Tris-HCl, pH 7.5. Ethanol (96-100%) added 4:1 before use.

2.1.6 Maxiprep – large-scale plasmid isolation

- HiSpeed® Maxi Prep Kit (Qiagen).
  - Buffer P1 - Resuspension buffer - 50 mM Tris-Cl, pH 8.0, 10 mM EDTA, 100 µg/mL RNase A.

- Buffer P2 - Lysis buffer - 200 mM NaOH, 1% SDS (w/v).
- Buffer P3 – Neutralisation buffer - 3.0 M potassium acetate, pH 5.5.
- Buffer QBT – Equilibration buffer - 750mM NaCl, 50 mM 3-(N-morpholino)propane sulphonic acid (MOPS buffer), pH 7.0, 15% isopropanol (v/v), 0.15 % Triton®-X-100 (v/v).
- Buffer QC – Wash buffer - 1.0 M NaCl, 50 mM MOPS, pH 7.0, 15% isopropanol (v/v).
- Buffer QF – Elution buffer - 1.25 M NaCl, 50 mM Tris-Cl, pH 8.5, 15% isopropanol (v/v).

2.1.7 Restriction digest

- All restriction enzymes were from the FastDigest range by Thermo Fisher Scientific and were used with the optimised 10x FastDigest Buffer provided.
  - *BcuI* – isoschizomer of *SpeI* for double restriction digest.
  - *KflI* – isoschizmer of *SanDI* for double restriction digest.
  - *BglI* – for verification of maxipreps.
  - *EcoRI* – for verification of ligation, minipreps and maxipreps.
  - *HindIII* – for verification of maxipreps.

2.1.8 Agarose gel electrophoresis

- Agarose (Bio-Rad) – high purity
- 50x TAE buffer – 2 M Tris, 2 M glacial acetic acid, 50 mM EDTA. Diluted to 1x in dH_2O for use.
- Ethidium bromide (EtBr) – stock 10 mg/mL; working concentration 0.1 µg/ml.
- 2x DNA loading buffer – 50% (v/v) glycerol, 50% 1x TAE buffer, Orange-G loading dye (Sigma) added to the desired detection colour.
- Gel cast, combs, tank and power pack were all purchased from Bio-Rad.

2.1.9 Mammalian Cell Culture

- Dulbecco's Modified Eagle Medium (DMEM), high glucose (Thermo Fisher Scientific) – primary constituents are sodium chloride 6.4 g/L, sodium bicarbonate 3.7 g/L, L-Glutamine 5.84 g/L, D-Glucose 4.5 g/L, and Phenol Red 15 mg/L (referred to as minimal DMEM (mDMEM)).

    - Before use, mDMEM was supplemented with 10% (v/v) heat-inactivated foetal calf serum (FCS) and 2% (v/v) 100 µg/mL penicillin-streptomycin-glutamine (PSG) (filter sterilised) to form complete DMEM (cDMEM).
- Phosphate buffered saline (PBS) – pH 7.4.
- Trypsin-EDTA (0.25%) phenol red – filter sterilised.

2.1.10 Effectene® transfection

- Effectene® Transfection Reagent Kit (Qiagen) – contains proprietary formulas.
    - Effectene® Transfection Reagent - non-liposomal, lipid-based reagent.
    - Enhancer – for DNA condensation.
    - Buffer EC – for DNA condensation.
- 35mm glass-bottomed dish (10mm glass diameter), poly-D-lysine coated (Mattek).
- 6 well plastic cell culture dishes.

2.1.11 $CaPO_4$ transfection

- $CaCl_2$ – pH 7, sterile, 1 M stock stored at -20°C.
- 2x HEPES Buffered Saline (HBS) – 280 mM NaCl, 10mM NaCl, 10 mM KCl, 1.5 mM Na_2HPO_4, 10 mM glucose, 50 mM HEPES, pH 7.05, filter sterilised and stored in aliquots at -20 °C.
- Sodium butyrate (NaB) – 1 M stocks stored at -20 °C, filter sterilised.

2.1.12 Preparation of cell homogenate

- Homogenisation buffer – 20 mM Tris, 1 mM EDTA pH 7.4, Protease and Phosphatase Inhibitor Mini Tablets (Pierce; 1 tablet per 10 mL), 1 % (v/v) Triton®-X-100.

2.1.13 Preparation of mixed membranes

- Hypo-osmotic buffer – 20 mM Tris, 1 mM EDTA pH 7.4, Protease Inhibitor Tablets (Roche; 1 tablet per 50 mL).
- Protein resuspension buffer – 400 mM sucrose, 10 mM HEPES, pH 7.2, Protease Inhibitor Tablets (Roche; 1 tablet per 50 mL).

2.1.14 Protein Quantification

- Pierce™ BCA Assay Kit.
    - BCA Reagent A – proprietary formula containing bicinchoninic acid and sodium bicinchoninate.

- BCA Reagent B – proprietary formula containing copper sulphate.
- Albumin Standard ampule – 2 mg/mL.

2.1.15 Solubilisation and purification

- 3-((3-cholamidopropyl) dimethylammonio)-1-propanesulphonate (CHAPS) – non-denaturing zwitterionic detergent.
- L-Alpha-Phosphatidylcholine (PC) (Merck) – from soybean.
- Gradient buffer – 300 mM NaCl, 25 mM Tris, 50 mM HEPES buffer, 0.3 mM ethylene glycol tetraacetic acid (EGTA), 0.1 mM $CaCl_2$, 0.3% CHAPS/PC mixture, 2 mM DTT, made up with dH_2O, Protease Inhibitor Tablets (Roche; 1 tablet per 50 mL).
- Sucrose solutions – 5%, 25% and 40% (w/w) made up in gradient buffer.
- High-salt solubilisation buffer – 1 M NaCl, 0.15 mM $CaCl_2$, 0.1 mM EGTA, 25 mM PIPES, 0.6% CHAPS/PC mixture, 2 mM DTT, made up with dH_2O, pH 7.4, 1:1000 Protease Inhibitor Cocktail (Sigma).

2.2 Methods

2.2.1 Site Directed Mutagenesis of SpeI/SanDI Cassette

As the full-length hRyR2 plasmid is too large to be amplified reliably, a cassette-based mutagenesis strategy was employed (**Figure 2.1**) using a ~5.5kb fragment of the hRyR2 coding sequence which had been previously sub-cloned into the pSL1180 plasmid. This fragment is isolated by restriction digest using *SpeI* and *SanDI* restriction enzymes (of which only one restriction site of each is found in the pcDNA3-eGFP-hRyR2 plasmid) and is therefore referred to as the *SpeI/SanDI* fragment; *SpeI* recognises the sequence 5'-ACTAGT in the plasmid vector immediately upstream of the hRyR2 sequence; *SanDI* recognises the sequence 5'-GGGACCC ~5.5kb into the hRyR2 sequence. Following site-directed mutagenesis (SDM) to introduce the required point mutations, this fragment can then be re-ligated into the full-length hRyR2 plasmid to produce the desired mutant. To introduce the point mutation into the cassette, forward and reverse primers were designed overlapping the mutation site (manufactured by Eurofins) to incorporate the desired base changes (**Table 2.1**). Analysis showed a relatively high GC content which could adversely affect primer annealing, however this was mitigated using the high fidelity PfuUltra HF DNA polymerase which is designed to work with GC-rich sequences.

Primers were used with the QuikChange II XL Site-Directed Mutagenesis Kit (Agilent) to introduce the point mutation into the template in the following reaction; 35.5 µL nuclease free water, 5 µL 10x buffer, 1.5 µL template DNA, 1.5 µL forward primer, 1.5 µL reverse primer, 1 µL dNTP, 1 µL Quik Solution and 1 µL PfuUltra HF DNA Polymerase. Thermal cycling conditions are presented in **Table 2.2**. Thermal cycling products were treated with DpnI (1 µL) for 1 hour at 37^{o}C for 1 hour to remove methylated template DNA before transformation.

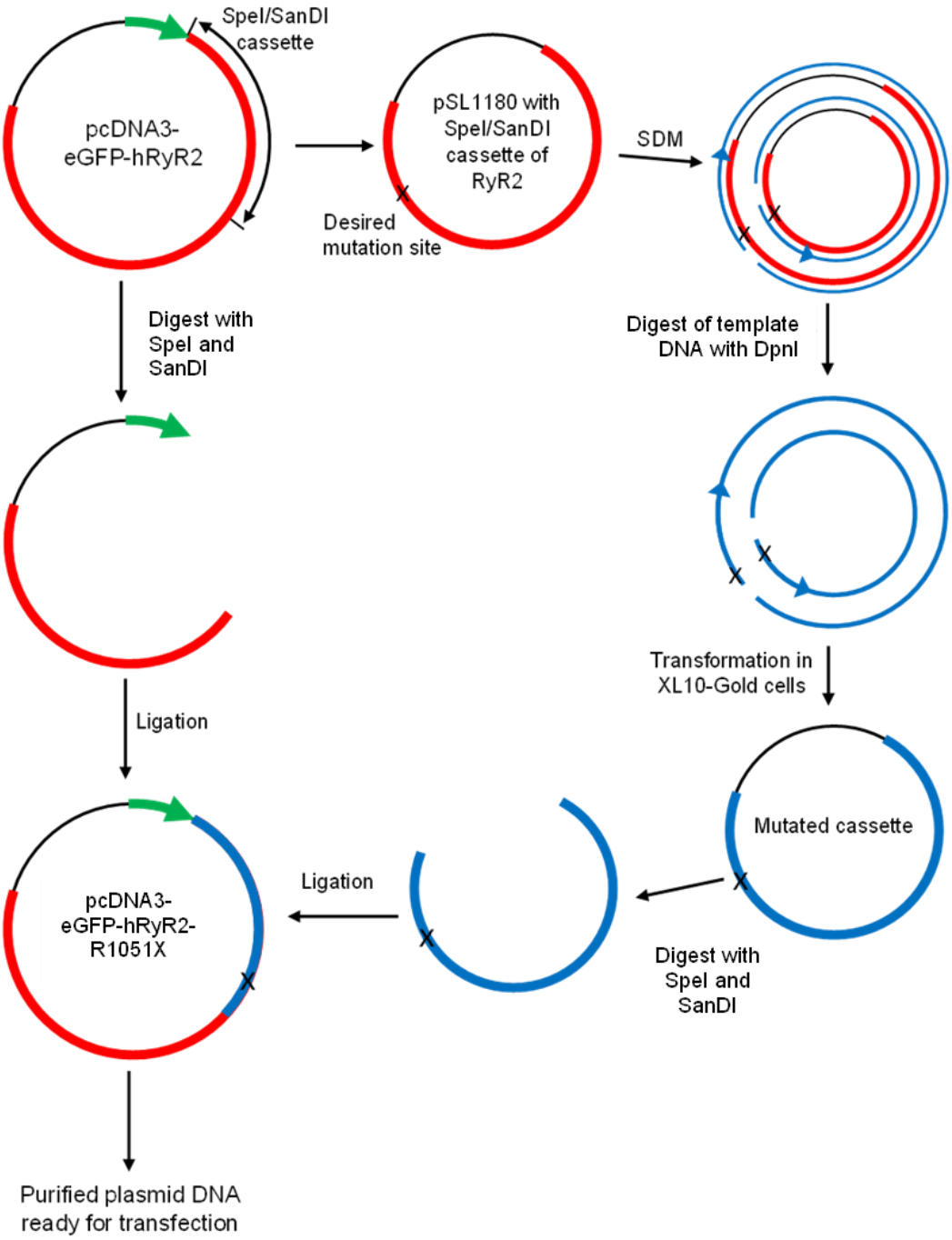

Figure 2.1 Schematic demonstrating the cassette-based site-directed mutagenesis strategy and ligation into the full-length pcDNA3-eGFP-hRyR2 construct with R1051-mutation. The *SpeI/SanDI* cassette from pcDNA3-eGFP-hRyR2 ligated in the pSL1180 plasmid was subjected to SDM using specific primers to introduce an amino acid substitution at R1051 (to proline (R1051P), cysteine (R1051C), or histidine (R1051H), denoted 'X' on the diagram). Post-SDM, the pSL1180-*SpeI/SanDI* plasmid and pcDNA3-eGFP-hRyR2 plasmid were subjected to double restriction digest by *BcuI* and *KflI* (isoschizomers of *SpeI* and *SanDI*) and ligated to form the full-length mutated hRyR2 plasmid for transfection. The cassette-based method was chosen due to the large size of the pcDNA3-eGFP-hRyR2 plasmid making it unsuitable for SDM.

Table 2.1 Oligonucleotide primers for site-directed mutagenesis for R1051-mutant hRyR2. Primers were used in combination with the cassette-based SDM strategy illustrated in **Figure 2.1** and are displayed in the 5' to 3' direction. Grey highlighted sections indicate the target codon; the bold red letters indicate the nucleotide that was altered from the WT-hRyR2 sequence.

	Direction	Sequence	Length	GC %	T_M
R1051P	**Forward**	CCAACAAGGACAGCCTCC**C**CGAGGCTGTGCGCACG	35	68.6	>75
	Reverse	CGTGCGCACAGCCTCG**G**GGAGGCTGTCCTTGTTGG	35	68.6	>75
R1051C	**Forward**	CCAACAAGGACAGCCTC**T**GCGAGGCTGTGCGCACG	35	65.7	>75
	Reverse	CGTGCGCACAGCCTCGC**A**GAGGCTGTCCTTGTTGG	35	65.7	>75
R1051H	**Forward**	CCAACAAGGACAGCCTCC**A**CGAGGCTGTGCGCACG	35	65.7	>75
	Reverse	CGTGCGCACAGCCTCG**T**GGAGGCTGTCCTTGTTGG	35	65.7	>75

Table 2.2. Thermal cycling conditions for site-directed mutagenesis. SDM was performed using the QuikChange II XL kit (Agilent). The extension time was calculated using a guide of 1 minute per kb of plasmid; the *SpeI/SanDI* cassette was 8.6kb.

Cycles	Stage	Temperature (°C)	Time
1 cycle	Denaturation	95	1 minute
18 cycles	Denaturation	95	50 seconds
	Annealing	60	50 seconds
	Extension	68	9 minutes
1 cycle	Extension	68	7 minutes

2.2.2 Cloning of R1051P eGFP-hRyR2

SpeI/SanDI fragments were excised from the mutated pSL1180 plasmid and the WT pcDNA3-eGFP-hRyR2 plasmid by double restriction digest (**Section 2.2.6**) before loading onto an agarose gel for separation (**Section 2.2.7**). Visualisation using a UV transilluminator allowed the required bands (5.5kb *SpeI/SanDI* cassette and 15.8kb pcDNA3-eGFP-hRyR2) to be excised using a scalpel. Gel slices were processed individually to purify the plasmid fragments using the GeneJET Gel Extraction Kit (Thermo) according to the manufacturer's instructions. Briefly, the excised gel slices were placed in a 1.5 mL tube and weighed, then Binding Buffer was added in a 1:1 ratio (volume:weight) and the mixture incubated at 50^{o}C until the gel slice dissolved. The tube was inverted to mix, vortexed and then loaded onto the GeneJET purification column. For the pcDNA3-eGFP-hRyR2 slice, an additional volume of ddH_2O equal to the volume of Binding Buffer used was added and mixed with the solution prior to loading onto the column. Columns were centrifuged at 13,000 x *g* (applies to all centrifugation steps during gel extraction) for 1 minute and the flow-through discarded, then 700 µL Wash Buffer was added to the column, centrifuged at for 1 minute, and the flow-through discarded, followed by an additional 1-minute centrifugation to dry the column. The column was transferred to a clean collection tube and 50 µL Elution Buffer added and centrifuged for 1 minute to collect the purified extraction products.

Extraction products (5 µL) were run on a 1% agarose gel (**Section 2.2.7**) to estimate yield before ligating using the Rapid DNA Ligation Kit (Roche Applied Science). Briefly, a 1:3 molar ratio of vector to insert (50 ng vector (15.79kb) to 52 ng insert (4.55kb)) was mixed with DNA Dilution buffer and T4 DNA Ligation buffer according to the manufacturer's instructions, along with 1 µL T4 DNA Ligase and mixed gently, then incubated for 16 hours at 4^{o}C before transformation into XL10-Gold cells.

2.2.3 Transformation and propagation of WT and mutant RyR2

Due to the large size (21,229 bp) and fragility of the hRyR2 plasmid it is not possible to store long term in glycerol stocks and instead it must be transformed and propagated each time from plasmid stocks. This requires using supercompetent cell lines for transformation, and the established protocol has been optimised to accommodate the challenges of working with the hRyR2 plasmid. The protocol largely follows that of a normal bacterial transformation, however bacterial culture must generally be carried out at 30°C rather than

37°C to minimise the likelihood of recombination, and colonised agar plates cannot be stored at 4°C.

Two different competent *E. coli* cell lines were used for transformation; XL10-Gold – a cell line designed for cloning large or ligated inserts, used here for transformation of ligation products; and MAX Efficiency Stbl2 – a cell line designed for propagation of unstable constructs, used here for general propagation due to its higher yield.

The general protocol for transformation was as follows; differences between the two cell lines are noted. XL10-Gold cells were pre-treated with 2 µL beta-mercaptoethanol for 10 minutes before transformation. Plasmid DNA was diluted to 1-10 ng/µL and 2 µL was added to thawed cells (50 µL for Stbl2, or 45 µL for XL10-Gold) and incubated on ice for 30 minutes prior to heat-shock treatment at 42°C for 30 seconds (XL10-Gold) or 25 seconds (Stbl2) before incubation on ice for 2.5 minutes. SOC medium (500 µL) was added to cells which were subsequently incubated at 37°C, 150 rpm for 1 hour in an orbital shaker. After incubation cells were plated on LB_{Amp} agar plates and incubated for at least 24 hours at 30°C. Colonies were picked from plates and transferred into 5 mL LB_{Amp} broth for an 18-hour incubation at 30°C, 150 rpm.

2.2.4 Miniprep of plasmid DNA

Following incubation of overnight cultures, 3 mL was taken off for small-scale plasmid DNA isolation, and an additional 6 mL LB_{AMP} broth added to cultures to continue growing throughout the day (~5 hours) in preparation for seeding into large scale cultures. Plasmid DNA isolation was carried out using the Qiagen Spin Miniprep Kit according to the manufacturer's instructions; all centrifugation steps were carried out at ~17,900 *x g*. Bacterial overnight culture (1.5 mL) was pelleted by centrifugation for 1 minute at room temperature (RT) and the supernatant removed, then the remaining 1.5 mL culture was added onto the pellet and centrifuged a second time. The pellet was resuspended in 250 µL Buffer P1 and then 250 µL Buffer P2 added and mixed by inversion until the solution became clear. The solution was incubated for 5 minutes at RT before adding 350 µL Buffer N3 and mixing by inversion and centrifuging for 10 minutes at 4°C. The resulting supernatant was pipetted onto a QIAprep spin column and centrifuged for 1 minute and the flow through discarded. The column was washed with 500 µL Buffer PB, centrifuged for 1 minute and the flow through discarded, then washed again with 750 µL Buffer PE. After addition of Buffer

PE, the column was centrifuged for 1 minute, the flow through discarded, and centrifuged for a further minute to remove residual wash buffer. The column was placed into a 1.5 mL tube and the plasmid DNA eluted by adding 50 µL ddH_2O to the column, letting stand for 1 minute, then centrifuging for 1 minute. Purified plasmids were verified by restriction digest using *EcoRI* and agarose (1%) gel electrophoresis (**Section 2.2.6** and **Section 2.2.7**).

2.2.5 Maxiprep of plasmid DNA

Following verification of plasmid DNA by miniprep, large-scale cultures were inoculated with bacterial culture (from the small-scale overnight cultures that had grown for ~5 hours while the miniprep was performed) at a dilution of 1:100 in LB_{AMP} broth. Cultures were then incubated at 30°C, 150rpm in an orbital shaker for 18-21 hours to grow. Cultures (total volume 1 L per maxiprep; grown as 5 x 200 mL, or 2 x 400 mL and 1 x 200 mL) were pelleted by centrifugation for 15 minutes at 4°C, 6500 x *g* after which the supernatant was removed and the plasmid DNA purified using the Qiagen HiSpeed Plasmid Kit following the manufacturer's instructions. Pellets were resuspended in 10 mL Buffer P1 per 200 mL of culture, then an equivalent volume Buffer P2 (i.e. 10 mL of buffer P2 if 10 mL of buffer P1 was used for resuspension) added and the solution mixed by inversion 5 times then incubated for 5 minutes at RT. After incubation, an equivalent volume of Buffer P3 (chilled) was added and mixed 5 times by inversion before pouring the lysate into a prepared QIAfilter Cartridge and incubating for 10 minutes at RT. During incubation, a HiSpeed Tip was equilibrated with 10 mL Buffer QBT and allowed to flow through the resin. A plunger was inserted into the QIAfilter Cartridge and the lysate filtered onto the HiSpeed Tip using constant pressure and allowed to run through. Once the lysate had filtered through, the HiSpeed Tip was washed with 60 mL Buffer QC before placing above a collection tube and eluting the DNA using 15 mL Buffer QF. After elution the DNA was precipitated by addition of 10.5 mL isopropanol, mixing by inversion, and incubating for 5 minutes at RT. A QIAprecipitator Module (filter) was attached to the nozzle of a 30 mL syringe with the plunger removed, and after incubation the eluate-isopropanol mixture was poured into the syringe and filtered through using constant pressure. The QIAprecipitator was detached and the plunger removed before reattaching the QIAprecipitator and adding 2 mL 70% (v/v) ethanol which was filtered through using the plunger to wash the DNA. The QIAprecipitator and plunger were removed and reattached again, then the plunger used to push air through

the filter to dry it; this was repeated 3 times. The QIAprecipitator was removed and attached to a 5 mL syringe with the plunger removed, before adding 500 µL warmed DNAse-free water, inserting and depressing the plunger to elute the plasmid DNA into a clean 1.5 mL tube.

An aliquot of purified plasmid DNA was taken and diluted 1:50 with dH_2O to be quantified using the BioMate 3S Spectrophotometer (Thermo). Plasmid DNA was checked again for recombination by visualisation of restriction digest products on a 1% agarose gel using *EcoRI, BglII,* and *HindIII* (**Section 2.2.6** and **Section 2.2.7**).

2.2.6 Restriction digest

Restriction digests were performed as both a verification step for confirming the integrity of plasmid DNA and during cloning to produce the *SpeI/SanDI* fragment for SDM. All enzymes were purchased from Thermo Fisher Scientific and used according to the manufacturer's instructions with regards to buffering; incubation times were adjusted as necessary and noted below.

For verification of eGFP-hRyR2 plasmid DNA, restriction digests were set up to produce a distinct 'fingerprint' that was compared to a visual representation of full-length hRyR2 digestion by the same enzymes using the NEBcutter® online tool (https://nc3.neb.com/NEBcutter/). Three restriction enzymes were chosen to identify full-length hRyR2 after the maxiprep stage of plasmid propagation; *BglI, EcoRI* and *HindIII* (*EcoRI* alone was used on its own to verify the plasmid after ligation and for all minipreps). For verification after miniprep and ligation, samples were prepared by mixing 1 µL FastDigest *EcoRI* Enzyme, 2 µL 10X FastDigest Buffer and 17 µL miniprep sample. After maxiprep and DNA quantification, samples were prepared by mixing 1 µL FastDigest Enzyme, 2 µL 10X FastDigest Buffer, 1 µg plasmid DNA and made up to 20 µL with dH_2O (one sample was used for each restriction enzyme). Restriction digests were then performed by incubating samples at 37^oC for 20 minutes before mixing 1:1 with 2x Orange-G loading dye and loading onto a 1% agarose gel.

Isolation of the *SpeI/SanDI* fragment from the pSL1180 plasmid and of the corresponding fragment from the full-length pcDNA3-eGFP-hRyR2 plasmid for ligation was performed by double restriction digest. The restriction enzymes *BcuI* (isoschizomer of *SpeI*) and *KflI*

(isoschizmer of *SanDI*) were chosen as they were available in FastDigest format from Thermo Fisher Scientific. Samples were prepared by mixing 0.5 µL FastDigest *BcuI* Enzyme, 0.5 µL FastDigest *KflI* Enzyme, 2 µL 10X FastDigest Buffer, 1 µg plasmid and made up to 20 µL using ddH_2O. Samples were incubated at 37^{o}C for 4 hours to ensure complete digestion at both sites, then were loaded onto an agarose gel for electrophoresis before excision and gel extraction for ligation (**Section 2.2.2**)

2.2.7 Agarose gel electrophoresis

Agarose gel electrophoresis is used to separate DNA fragments based on their molecular weight and was used during several stages of research. A 1% (w/v) agarose gel was prepared by adding agarose to 1x TAE buffer and warming to dissolve in a microwave. Once cooled to approximately 50^{o}C, EtBr was added to a concentration of 0.1 µg/mL to allow for visualisation of the DNA and the mixture poured into a gel cast with comb and allowed to set. The gel was placed into a BioRad gel tank and submerged in 1x TAE buffer. Following restriction digest (**Section 2.2.6**) samples were prepared by adding equal volumes sample and 2x Orange-G loading dye before loading into the gel wells. Gels were run at 100V for approximately 45 minutes – 1 hour, or until the dye front reached the end of the gel. Gels were imaged using the G:BOX Chemi XX6 gel documentation system (Syngene), set to detect EtBr fluorescence.

2.2.8 Mammalian cell culture and routine maintenance

Expression of eGFP-hRyR2 was carried out in the immortalised cell line HEK293, a cell type that does not endogenously express RyRs. HEK293s were cultured in T75 tissue culture flasks containing Dulbecco's Modified Eagle Medium (DMEM) supplemented with 10% (v/v) FCS and 2% (v/v) PSG to create complete DMEM (cDMEM). Cells were kept in a humid cell culture incubator at 37°C, 5% CO_2 and passaged when the monolayer approached full confluence (approximately 90%) to maintain cell health. During passaging, media was removed, and the cells washed with PBS before detaching using 1 mL trypsin. Once detached, 10 mL cDMEM was added to inactivate the trypsin and cells were centrifuged at 1000 x *g* for 5 minutes to form a pellet. After pelleting the supernatant was removed and the pellet gently resuspended in 10 mL cDMEM before a proportion of cells were re-seeded into new T75 flasks.

2.2.9 Effectene transfection of HEK293 cells with WT or mutant eGFP-hRyR2 plasmid DNA

Transfection for live cell imaging and immunofluorescence (IF) used Effectene® Transfection Reagent (Qiagen). This method was chosen as the non-liposomal lipid formula produces a high transfection efficiency and has low cytotoxicity as it uses only small amounts of DNA, making it more suitable for imaging live cells compared to other transfection reagents that may impact cell survival, such as calcium phosphate ($CaPO_4$), as well as maintaining normal trafficking for IF.

Seeding of cells following routine culture to 70-100% confluence was different for live cell Ca^{2+} imaging (**Section 4.2.2**) and IF (**Section 3.2.2**); the Effectene reagent was made up as follows for both live cell imaging and IF; volumes are sufficient for 7 coverslips (live cell Ca^{2+} imaging) or 1 well (IF). Plasmid DNA (0.8 µg) was made up to 100 µL with Buffer EC and then 6.4 µL Enhancer added, vortexed for 10 seconds and incubated at RT for 5 minutes. Effectene (20 µL) was added, vortexed for 10 seconds and incubated at RT for 10 minutes before cDMEM (600 µL) was added and mixed by pipetting up and down twice. The mixture was then added dropwise to each coverslip meniscus (100 µL) for live cell imaging, or adding all of the reaction mixture to a single well (IF) and returning them to the incubator for at least 18 hours, after which dishes were flooded with 2 mL cDMEM.

2.2.10 $CaPO_4$ transfection of HEK293 cells with WT or mutant eGFP-hRyR2 plasmid DNA

$CaPO_4$ transfection was used for the preparation of cell homogenate for Western blotting and for preparation of mixed membranes for solubilisation and purification. This method has a higher cytotoxicity than Effectene, however the total protein expression is much higher when using $CaPO_4$ and ensures sufficient protein for purification.

HEK293 cells ($1.5x10^6$) were seeded in 10cm diameter petri dishes with 10 mL cDMEM and incubated at 37°C, 5% CO_2 for 24 hours prior to $CaPO_4$ transfection; 10 to 15 petri dishes were used for each construct. Plasmid DNA (12 µg/dish) was mixed with $CaCl_2$ solution pH 7 (1 M, final concentration 124 mM) and ddH_2O to a volume of 500 µL. The solution was added dropwise to 500 µL warmed 2x HBS (pH 7.05) while continuously vortexing and incubated for 20 minutes at RT to allow a precipitate to form. The solution was vortexed and 1 mL added dropwise per plate before incubation at 37°C, 5% CO_2 for 24 hours. Media was replaced with cDMEM containing 2 mM NaB to upregulate expression then incubated for a further 24 hours at 37°C, 5% CO_2. After incubation cells were checked for expression using a

Zeiss fluorescence microscope to assess eGFP fluorescence and estimate transfection efficiency (needed to exceed 25% for to ensure sufficient yield following solubilisation and purification). Cells were then harvested using a cell scraper and pelleted by centrifugation at 1000 x *g* for 5 minutes before storing at -80°C.

2.2.11 Preparation of cell homogenate from transfected HEK293 cells for Western blotting

Cell homogenate was used for Western blotting to determine expression levels of R1051-mutant eGFP-hRyR2 compared to the WT and to assess phosphorylation levels (**Chapter 3**). Frozen $CaPO_4$-transfected cells were thawed and resuspended in hypo-osmotic buffer (50 µL per million cells) on ice to cause them to rupture. Cells were then passed through a 23G needle 20-25 times to homogenise them and then subjected to 5 rounds of freeze-thaw using liquid nitrogen and a sonicator waterbath. This was followed by centrifugation at 1,000 x *g* for 5 minutes at 4°C to pellet the nuclei. The supernatant, containing cell homogenate, was removed and aliquoted into suitable volumes and snap-frozen in liquid nitrogen before storing at -80°C. Protein quantification of samples was carried out using a BCA assay (**Section 2.2.13**).

2.2.12 Preparation of mixed membrane microsomal fractions from transfected HEK293 cells for solubilisation and purification

As RyR2 is a membrane protein, it is necessary to isolate the membrane from other cellular components prior to solubilisation and purification of RyR2. Following $CaPO_4$ transfection, cells stored at -80°C were thawed and resuspended in hypo-osmotic buffer at a concentration of $1x10^6$ per mL. After resuspension, cells were kept on ice and homogenised by passing through a 23G needle ~20 times. Unbroken cells and nuclei were removed using low-speed centrifugation at 1500 x *g*, 4°C for 10 minutes. The supernatant was removed into Beckman Ultra-Clear 38.5 mL open top centrifuge tubes for a high-speed spin to produce microsomal material; 10% of the total volume of supernatant was removed to a different tube and balanced with hypo-osmotic buffer for use in a protein assay after centrifugation. The supernatant was centrifuged at 100,000 x *g*, 4°C for 1 hour in a Beckman Optima Ultracentrifuge to produce pellets containing microsomal material. After spinning, the supernatant was discarded and pellets kept on ice while the small pellet was resuspended using a dounce homogeniser in 500 µL resuspension buffer. This small pellet

was used to estimate protein concentration by BCA protein assay (**Section 2.2.13**). Pellets kept on ice were later solubilised using the known protein concentration (**Section 2.2.14**).

2.2.13 Protein assay for quantification of protein concentration

Protein quantification was used to estimate the total protein concentration in cell homogenate and microsomal fractions for use in Western blotting and for protein solubilisation and purification, respectively. The BCA assay system (Pierce) was chosen as the colorimetric reaction provides quick and easy protein quantification based on reduction of Cu^{2+} to Cu^{+} by the peptide bonds of proteins, where the amount of Cu^{2+} reduced is proportional to the protein concentration.

The method followed was based on the manufacturer's instructions for a microplate BCA assay. Briefly, sample dilutions (1:50, 1:100, 1:200) and protein standards (bovine serum albumin (BSA), 5 – 250 µg/µL) were prepared and 100 µL of each added in duplicate to the wells of a clear, flat-bottomed, 96-well plate. Working reagent was prepared by adding 50 parts BCA Reagent A to 1 part BCA Reagent B and mixing; 100 µL of working reagent was then added to each well and mixed by pipetting up and down, before covering the plate and incubating at 37°C for 30 minutes to allow the assay to develop. Absorbance readings were taken at 562nm using the Tecan Infinite 200Pro plate reader. A standard curve of protein concentration vs absorbance was plotted and the sample protein concentration calculated using the polynomial (order 2) trendline equation of the standard curve. A polynomial line was chosen in place of a linear standard curve as this produces a better fit and therefore a more accurate protein concentration reading of samples. The total protein concentration of transfected cells varied based on expression but was calculated in the region of 1.2 to 2.6 µg/µL; total protein concentration of untransfected HEK293 cells ranged from 0.9 to 1.4 µg/µL, but in all cases the total protein concentration of transfected cells was higher than untransfected cells from the same preparation batch.

2.2.14 Solubilisation and purification via sucrose density centrifugation of hRyR2 from microsomal material

To purify RyR2 from the mixed membranes requires solubilisation of the protein using a detergent-lipid mixture followed by separation by sucrose density centrifugation, which separates proteins by density. The detergent-lipid stock mixture was made up as a 10% CHAPS and 5% phosphatidylcholine (PC) w/v mixture (CHAPS/PC) in dH_2O and left overnight

on a roller at 4°C to form a suspension. This was then added at a concentration of 0.3% in the gradient buffer and 0.6% in the solubilisation buffer. The concentration of detergent is based on extensive optimisation to ensure sufficient solubilisation while preventing denaturation of channels, to obtain a high yield and functional protein (Mukherjee 2014).

Before solubilising the protein, continuous sucrose gradients were prepared for the sucrose density centrifugation. To make the gradients, 5%, 25% and 40% (w/w) sucrose solutions were made in gradient buffer. A gradient maker and pump were used to create a gradient in Beckman Ultra-Clear 38.5 mL open top centrifuge tubes by dilution of the 25% sucrose with the 5% sucrose, on a cushion of 40% sucrose. Tubes were handled gently to prevent disturbing the gradient and were kept chilled at 4°C until the protein was ready to be loaded onto them; gradients were not stored overnight and were made on the day of purification.

Following the estimation of protein concentration by BCA assay, the remaining pellets were resuspended at a concentration of 2.5 mg/mL in high-salt solubilisation buffer containing 0.6% CHAPS/PC and left to solubilise for 1 hour at 4°C while stirring. The solution was transferred to a 1.5 mL tube and centrifuged at 16,000 x *g* for 30 minutes at 4°C before the supernatant was gently loaded onto the gradients and centrifuged at 100,000 x *g* for 18 hours at 4°C.

The following day, the gradient was carefully collected in 1.5 mL fractions from the top, and the density of sucrose fractions measured with a refractometer. Based on previous research (Mukherjee et al. 2012) hRyR2 is expected to be found at 28-30% sucrose; all fractions between 26% and 32% sucrose were frozen in dry ice and stored at -80°C.

Chapter 3

Generation of R1501-mutant hRyR2 constructs and their expression in HEK293 cells

3.1 Introduction

3.1.1 Engineering recombinant hRyR2 mutations and transfection into a suitable cell system

To date, more than 300 missense variants of hRyR2 have been identified (Olubando et al. 2020) yet only a small number have undergone significant functional characterisation and often these are the mutations associated with the most severe phenotype. The mutants of interest in this study, R1051P, R1051C, and R1051H, are some of the many disease-associated hRyR2 mutations that are classified as of uncertain-significance that have not undergone any characterisation, and this study aims to provide the first experimental data for these mutants. As no animal models exist carrying these mutations and patient data is limited, it was decided to engineer recombinant mutant hRyR2 that could then be expressed in a mammalian cell system as a means to assess function. This approach has long been used to generate hRyR2 mutants (Jiang et al. 2002a; Jiang et al. 2004; Thomas et al. 2004; Thomas et al. 2005), providing precise control over the mutation introduced as well as the ability to use tags such as eGFP (George et al. 2003a) that open up new avenues to assess hRyR2 function.

While the engineering of hRyR2 mutants is not new it is still a complicated process, predominantly due to the large size of the hRyR2 plasmid. At ~21kb, the high molecular weight of the plasmid makes it both fragile and prone to recombination, and as such the methods used for SDM and transformation/propagation must be highly optimised. This includes the use of a cassette-based mutagenesis strategy in which a fragment of the plasmid containing the mutation site is excised from the full-length plasmid and ligated into a smaller plasmid for SDM (**Figure 2.1**), as well as the use of super-competent bacterial cell lines for propagation (**Section 2.2.3**).

Once the mutants have been generated and expressed, there are then a multitude of techniques that can be used to assess their mechanisms of dysfunction. The three main techniques that will be used to assess their function in this study are live cell Ca^{2+} imaging (**Chapter 4**), DIBs (**Chapter 5**) and single channel analysis in artificial lipid bilayers (**Chapter 6**), however prior to carrying out these experiments it must first be confirmed that the recombinant mutant hRyR2 can be expressed in an appropriate cell system. For this research, the cell system of choice was HEK293 cells which are a commonly used due to

their easy maintenance and high yield of recombinant protein expression (Viero et al. 2012; Tan et al. 2021).

3.1.2 HEK293 cells as a system for recombinant hRyR2 expression

Ca^{2+} signalling in the cell is affected by a vast number of different proteins, which when trying to assess the contribution of RyR2 to whole cell Ca^{2+} release can lead to difficulty in interpreting results, and as such RyR2 function must be isolated as best as possible. Many cell lines can be used for recombinant expression of RyR2, however those that express other isoforms of RyR or accessory proteins that bind RyR2 do not present an ideal system as these factors would influence Ca^{2+} release; therefore, an RyR2-deficient cell line is most appropriate. HEK293 cells do not endogenously express RyR2 or other isoforms of RyR (Chen et al. 1997) and can be transfected with RyR2 cDNA to express homotetrameric channels. This presents a good system for the expression of RyR2 to assess channel function (Chen et al. 1997; Jiang et al. 2005) or as a vehicle for overexpression of recombinant RyR2 for solubilisation and purification of channels for use in single channel experiments (Chen et al. 1997; Thomas and Smart 2005; Mukherjee et al. 2012). HEK293 cells do not contain the intracellular contractile machinery of cardiomyocytes, however studies have shown that they demonstrate comparable functional data on Ca^{2+} oscillations due to SOICR (**Section 1.6.2.1** and **Section 4.1.3**) (Jiang et al. 2004; Thomas et al. 2004; Kong et al. 2008). This makes them a suitable system for assessing whole cell Ca^{2+} release, expression levels, and localisation, as well as a system to express protein for solubilisation and purification.

3.1.3 Chapter Aims

R1051P, R1051C and R1051H hRyR2 have all been linked to arrhythmia or cardiomyopathy, however currently there is no experimental data available and as such characterising them is necessary to determine whether they are functionally heterogeneous from WT-hRyR2. Prior to carrying out characterisation, the mutant hRyR2 plasmids must first be engineered and propagated to produce the necessary DNA for transfection. Once engineered, the constructs can then be expressed in a mammalian cell system to assess their basic functionality, including localisation and expression, prior to more rigorous functional characterisation. This chapter focuses on the generation and primary characterisation of these mutants to determine whether they can be expressed in HEK293 cells and if they localise to the ER. The aims of this chapter are as follows;

- Engineer mutant hRyR2 using SDM and super-competent *E. coli* cell lines and verify successful incorporation of the desired mutations using Sanger sequencing.
- Determine whether R1051P, R1051C and R1051H hRyR2 are located in the same cellular compartment as WT-hRyR2 using IF, and therefore whether any dysfunction may be related to incorrect cellular trafficking.
- Assess protein expression levels of R1051P, R1051C and R1051H hRyR2 constructs compared to the WT-hRyR2 by Western Blotting to determine whether any changes in function can be attributed to changes in expression level. In addition, assess phosphorylation at S2808 to determine any difference in phosphorylation at this site.

3.2 Materials & Methods

3.2.1 Materials

3.2.1.1 Immunofluorescence Antibodies, Reagents and Buffers

All reagents for cell culture are as described in **Section 2.1.9**.

- Alexa Fluor® 647 Anti-Calreticulin antibody [EPR3924] (ab196159) (Abcam). Rabbit monoclonal antibody used for IF as an ER marker; diluted 1:150 with PBS.
- Paraformaldehyde – 4% (v/v) in PBS
- Triton-X – 0.1% (v/v) in PBS
- Fluorsave Reagent (Calbiochem)
- Leica SP5 confocal microscope (Leica Microsystems) – used with 100x oil immersion objective

3.2.1.2 SDS-PAGE

- 2x Laemmli sample buffer - 0.5M Tris (pH 6.8), 10 % (w/v) SDS, 10 % (v/v) glycerol, 0.5 % (w/v) bromophenol blue, 5% (v/v) β-mercaptoethanol as a reducing agent
- 4–15% Mini-PROTEAN® TGX™ Precast Protein Gels (BioRad)
- Precision Plus Protein Kaleidoscope marker (BioRad)
- Mini-PROTEAN Electrophoresis Tank (BioRad)

3.2.1.3 Western Blotting Antibodies, Reagents and Buffers

- Anti-GFP Antibody (B-2) sc-9996 (Santa Cruz Biotechnology) - Mouse monoclonal primary antibody used to detect hRyR2 via the eGFP tag for Western blotting; 1:5000 dilution.
- Alpha Tubulin Monoclonal Antibody (1E4C11) (Thermo Fisher) - Mouse monoclonal primary antibody used to detect α-tubulin as a loading control for Western Blotting; 1:10,000 dilution.
- Rabbit Anti-Mouse IgG H&L (conjugated to horseradish peroxidase (HRP)) ab6728 (Abcam) - Secondary antibody for Western blotting; 1:10,000 dilution.
- Goat Anti-Rabbit IgG H&L (HRP) ab6721 (Abcam) - Secondary antibody for Western blotting; 1:10,000 dilution.
- RYR2 antibody (pSer2808) (Antibodies Online) - Phospho-specific antibody for detecting phosphorylation at S2808 on hRyR2; 1:1000 dilution.

- Tris-buffered Saline with Tween (TBS-T) – 20 mM Tris, 150 mM NaCl, pH adjusted to 7.6, before addition of 1 ml/L Tween-20.
- Enhanced Chemiluminescence Substrate (ECL) (Pierce) – includes luminol enhancer and peroxide solution, mixed at a 1:1 ratio immediately prior to imaging.
- G:BOX Chemi XX6 gel documentation system (Syngene).
- Blot stripping buffer - 50 mM Tris/HCl, pH 6.8, 2% SDS, 0.1 M β-mercaptoethanol, made up with dH_2O.

3.2.2 Immunofluorescence analysis

Following routine culture, HEK293 cells were seeded into 6 well plates at a density of $8x10^5$ cells per well and cDMEM added to a total volume of 2 mL before incubation at 37°C, 5% CO_2 for 24 hours. Cells were transfected with each hRyR2 construct using Effectene Transfection Reagent (Qiagen) prepared as in **Section 2.2.9** and the entirety of the reaction mixture added to the cells with fresh cDMEM. After 24 hours, cells were washed in PBS, detached using trypsin and resuspended in cDMEM to a density of $8x10^5$ cells/mL, before 150 µL was added in a meniscus to a poly-lysine coated coverslip and incubated at 37°C, 5% CO_2 for 24 hours. Cells were washed 3 times with PBS and fixed in 4% (v/v) paraformaldehyde in PBS for 10 minutes at RT in the dark. Cells were washed again with PBS and rehydrated in PBS for at least 24 hours at 4°C.

After rehydration, cells were washed with PBS and permeabilised using 0.1% (v/v) Triton-X in PBS for 30 minutes at RT in the dark, then washed with PBS. Cells were incubated in 10% (v/v) FCS in PBS for 30 minutes at RT in the dark, then washed with PBS. After washing, cells were incubated with an anti-calreticulin antibody (ab196159, 1:150 dilution in PBS) in a 150 µL meniscus for 90 minutes at RT in the dark. Cells were washed 3 times for 10 minutes in PBS in the dark, then washed in distilled water and mounted on a slide using one drop of Fluorsave and allowed to dry for 30 minutes before storing at 4°C.

Cells were imaged using an SP5 confocal microscope (Leica) and a 100X oil immersion objective. Detection of eGFP fluorescence was carried out using the argon laser, set to excite at 488nm and detect between 500nm and 570nm (the 'green' channel); detection of the anti-calreticulin antibody used the HeNe633nm laser with excitation set to 633nm and detection between 640nm and 700nm (the 'red' channel). Spectral bleed-through was assessed by turning off the 633nm laser and imaging a sample with the 488nm laser only.

Emission was monitored in the 'red' channel to determine whether any fluorescent signal was detected; this revealed no spectral overlap. Files were saved as .lif files before analysis in the FIJI analysis suite (Schindelin et al. 2012). The co-occurrence of eGFP and anti-calreticulin antibody fluorescence was calculated using the Coloc2 plugin (https://github.com/fiji/Colocalisation_Analysis) in FIJI (Schindelin et al. 2012). This calculated the thresholded Manders Overlap Coefficient value (Manders et al. 1993) for green-to-red pixels; this is the most biologically relevant comparison as this indicates where hRyR2 expression co-localises with calreticulin. A coefficient closer to 1 is indicative of a high co-occurrence of the two signals; for example a coefficient of 1 for green-to-red would indicate that all green fluorescence (eGFP-hRyR2) occurs in an area that also shows red fluorescence (Alexa Fluor® 647 anti-calreticulin antibody); but a coefficient of 0.5 would indicate that there are areas of green fluorescence that have no red fluorescence.

3.2.3 Sodium Dodecyl Sulphate Polyacrylamide Gel Electrophoresis (SDS-PAGE)

Prior to Western Blotting for expression levels, cell homogenate samples were run on an SDS-PAGE gel to separate proteins out by size. Samples were prepared by adding a volume equivalent to 100 µg total protein (determined by BCA Assay; **Section 2.2.13**) in a ratio of 1:1 with 2x Laemmli sample buffer and heating at 42°C for 20 minutes. Samples were loaded into a 4-15% (v/v) precast polyacrylamide gel (BioRad) along with Precision Plus Protein Kaleidoscope marker (BioRad). This gel is suitable for resolving hRyR2 (MW 565kDa) and should produce a band at the top of the gel. The gel was run at 100V until the sample entered the gel, then increased to 150V for the remaining running time.

3.2.4 Western Blotting for Protein Expression

After separating the cell homogenate using SDS-PAGE, proteins were transferred to a PVDF membrane using the iBLOT™ 2 Gel Transfer Device (Invitrogen) following the manufacturer's instructions. The gel was transferred at 25V for 6 minutes.

Immediately after transfer, the PVDF membrane was incubated in 5% (w/v) blocking solution (5% dried skimmed milk powder in TBS-T) solution for 1 hour at RT on a rocker. For detection, 1% (w/v) blocking solution was supplemented with two primary antibodies; mouse monoclonal to eGFP (to detect the eGFP tag on hRyR2; sc-9996 (SantaCruz)) was added at a concentration of 1:5000, and rabbit monoclonal to α-tubulin (1E4C11 (Abcam), internal loading control) was added at a concentration of 1:10,000. Membranes were

incubated in the primary antibody solution for 2 hours at RT on a rocker, or overnight at 4°C. Membranes were then washed 3 times for 5 minutes each in 1% (w/v) blocking solution on a rocker to remove excess unbound antibody. HRP-conjugated secondary antibodies (rabbit anti-mouse IgG (ab6728) and goat anti-rabbit IgG (ab6721) (Abcam)) were added to 1% (w/v) blocking solution at a concentration of 1:10,000 each and membranes incubated in the solution for 90 minutes at RT on a rocker. Membranes were then washed 5 times for 5 minutes each in TBS-T on a rocker to remove excess antibody and blocking solution.

Proteins were visualised by applying ECL (Pierce) to the membrane, which reacts with the HRP conjugated to the secondary antibodies and oxidises luminol, resulting in light emission at 425nm. Images were captured using the G:BOX Chemi XX6 gel documentation system (Syngene) with a 10-30 second exposure time and analysed by densitometry using ImageJ in FIJI (Schindelin et al. 2012). Briefly, the intensity of individual bands indicating hRyR2 expression was calculated by the software based on pixel intensity and subtracted from the background intensity. This was then expressed as a proportion of the intensity of the loading control (α-tubulin). This was performed individually for both the 565kDa band and the 400kDa band (corresponding to a calpain cleavage product commonly seen when assessing RyR2 by Western analysis (Viero et al. 2012; Zissimopoulos et al. 2013)), and the two bands combined.

3.2.5 Assessing phosphorylation at S2808 via Western Blotting

To assess phosphorylation at S2808, blots were first probed for eGFP-hRyR2 expression and then stripped of antibody and re-probed with an antibody raised to the phosphoserine S2808 epitope. This allows for phosphorylation to be expressed as a proportion of hRyR2 expression, with the eGFP-hRyR2 signal essentially acting as the loading control as phosphorylation levels are inherently tied to the total amount of hRyR2 expressed.

Blots were assessed for hRyR2 expression as in **Section 3.2.4** and then placed in a tube with 50 mL pre-warmed stripping buffer containing β-mercaptoethanol and incubated in a 50°C waterbath for 10 minutes in a fume cupboard. Blots were washed in TBS-T 3 times for 5 minutes each and then re-examined by applying ECL to the membrane and visualising as described in **Section 3.2.4** to check no signal from the HRP conjugated antibodies used in **Section 3.2.4** were visible. Blots were then washed with TBST-T solution 3 times for 5 minutes each and then blocked in 5% (w/v) TBST-T blocking solution for 1 hour. The

phospho-specific S2808 antibody (ABIN2744161, Antibodies Online) was added to 1% (w/v) TBST-T at a concentration of 1:1000 and incubated overnight at RT on a rocker. Blots were then washed and imaged as in **Section 3.2.4** to create an image of phosphorylation levels at S2808.

3.3 Results

3.3.1 Generation of R1051-mutant hRyR2 constructs was successful

R1051P, R1051C and R1051H-hRyR2 were successfully engineered and cloned via insertion of a mutated *SpeI/SanDI* cassette into the pcDNA3-eGFP-hRyR2 plasmid (**Section 2.2.1** and **Section 2.2.2**). Restriction digest verified that the full-length plasmid had not recombined by producing the predicted fingerprint pattern of hRyR2 digestion (**Figure 3.1**). Sanger sequencing was used to confirm the integrity of the restriction boundaries, and the site of mutagenesis in each of the final constructs (**Figure 3.2**; primer sequences in **Appendix I**).

One of the biggest challenges in cloning and propagating large constructs like pcDNA3-eGFP-hRyR2 is recombination, and many steps of the method have been optimised to minimise the chance of this occurring, including reducing the temperature of incubation and the choice of cell line. This did not completely avoid issues with recombination, as it was noted following transformation of the R1051P-hRyR2 ligation product into XL10-Gold supercompetent *E. coli* that colony size was heterogeneous; this can be an indicator of recombination. Therefore, both and small and large colonies were picked to increase the likelihood of selecting colonies that represented successfully ligated plasmids without recombination. Restriction digest with *EcoRI* following miniprep (**Section 2.2.4** and **Section 2.2.6**) of these colonies revealed recombination of plasmid DNA in several of the larger colonies, but all smaller colonies produced a successful digest indicating full-length pcDNA3-eGFP-hRyR2 (**Figure 3.3**). This heterogeneity in colony size was also observed in R1051C and R1051H constructs, so for all future ligations only smaller colonies were selected which yielded a high success rate. Following transformation into MAX Efficiency Stbl2 cells for large scale culture it was also noted that cultures containing the R1051P construct, but not R1051C or R1051H, grew at a slower rate than those with WT-hRyR2 construct. In an attempt to optimise the yield of plasmid without promoting recombination, the optical density (absorbance at 600nm (OD600) as a measure of cell growth) of cultures was checked every 30 minutes post 16-hours of incubation, with cells harvested when the culture reached an OD600 of 1 (experience within the group has demonstrated this is the optimal OD to balance yield and recombination). This was achieved at ~21-22 hours post-inoculation for cultures containing R1051P, but 16-18 hours for WT, R1051C and R1051H. With these

adjustments, all pcDNA3-eGFP-hRyR2 plasmids were successfully propagated multiple times with a consistent yield.

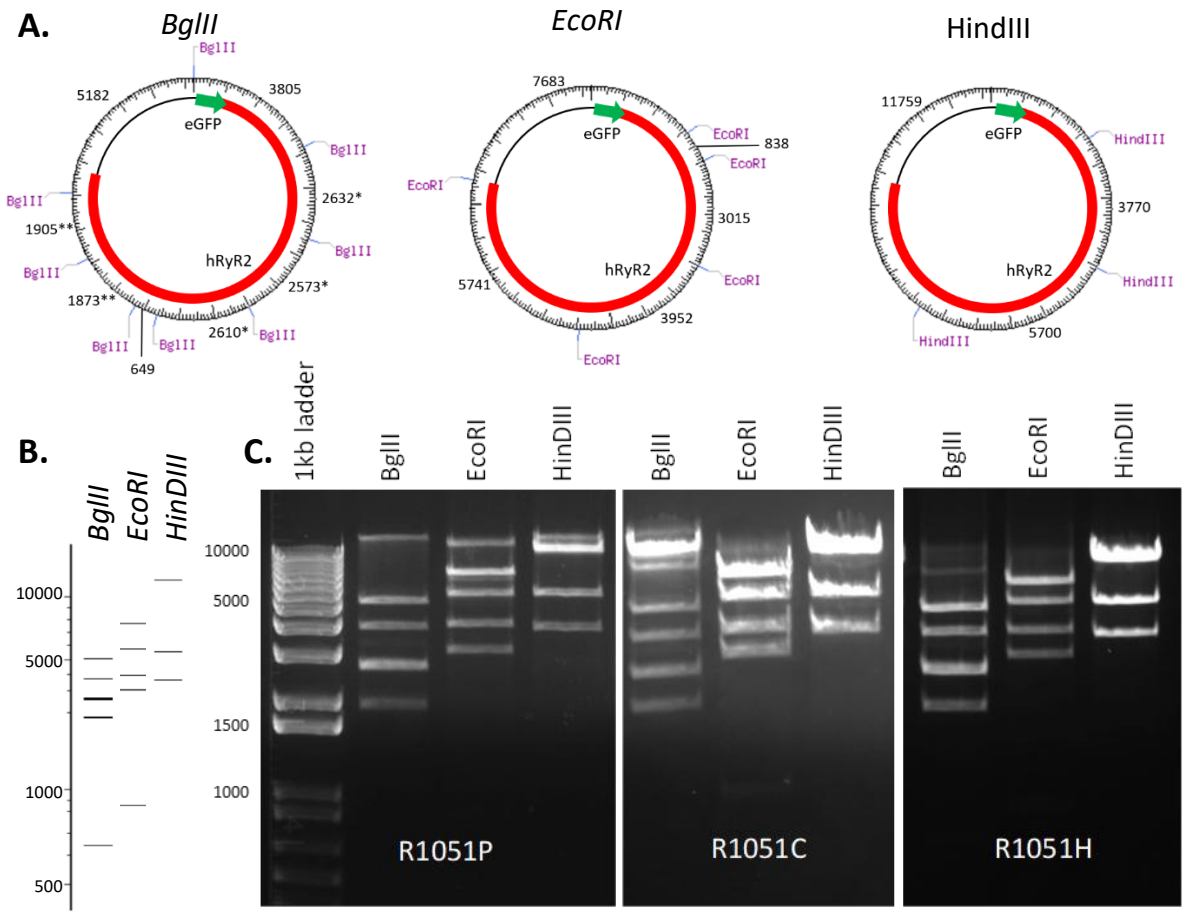

Figure 3.1 Restriction digest of WT, R1051P, R1051C and R1051H-hRyR2 following maxiprep indicate the expected fingerprint pattern of full-length hRyR2. A. Map showing pcDNA3-eGFP-hRyR2 plasmid and the restriction sites for each of the restriction enzymes (*BglII, EcoRI* and *HindIII*) used to identify full-length hRyR2 (generated by NEB Cutter (**Section 2.2.6**)); asterisks indicate bands that are too similar in molecular weight and cannot be separated on the gel, presenting as one band. **B**. Predicted positive digest pattern of full-length pcDNA3-eGFP-hRyR2 plasmid with the chosen restriction enzymes (obtained from NEB Cutter); fewer bands are visible than the total number of fragments produced as shown in **A** due to bands of similar size overlapping. **C**. Restriction digest of all three R1051-mutant-hRyR2 constructs following maxiprep produced positive fingerprints indicating full-length pcDNA3-eGFP-hRyR2. Fragments smaller than ~1500bp were not well resolved on the gel, but were visible when the gain was turned up; this prevented them from being displayed alongside better resolved bands (Appendix II). Additional bands above the predicted pattern are representative of undigested hRyR2.

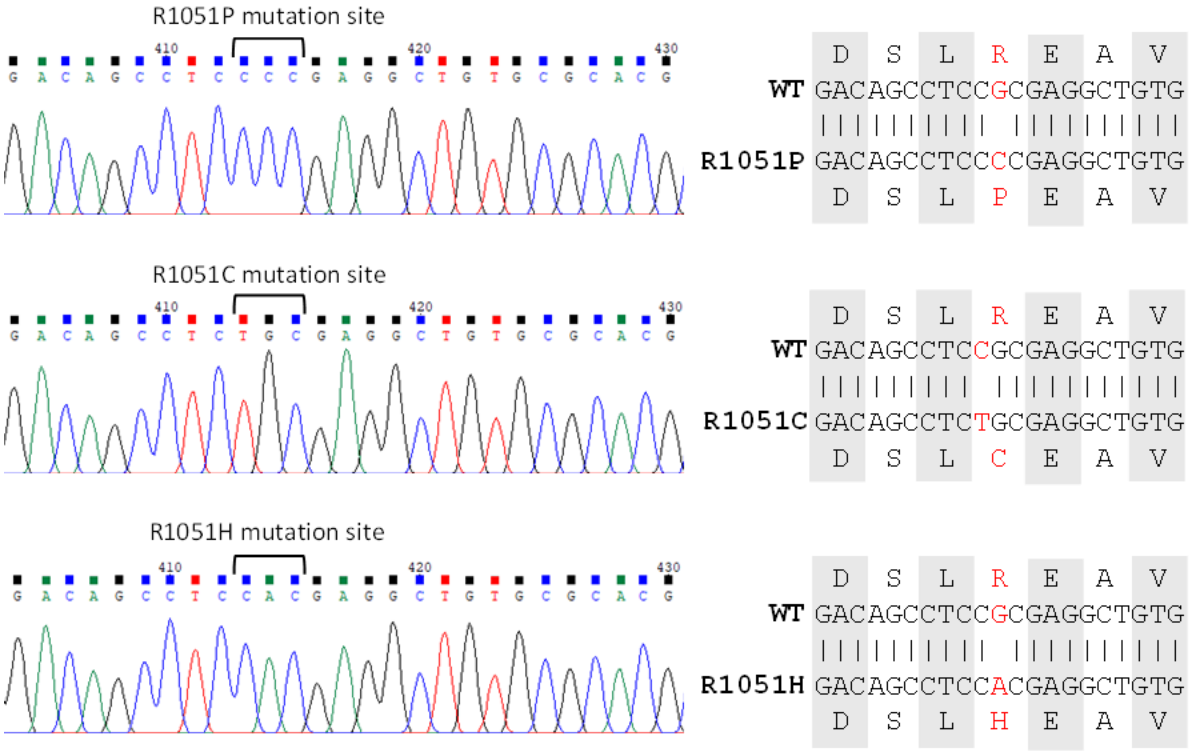

Figure 3.2. Chromatograms show successful introduction of R1051-mutations into the pcDNA3-eGFP-hRyR2 plasmid. The chromatograms indicate the required base changes to introduce the R1051-mutants into hRyR2 were successfully introduced by SDM, with the altered codon indicated by brackets and the change from the WT sequence shown on the right. Sequencing was performed by Eurofins.

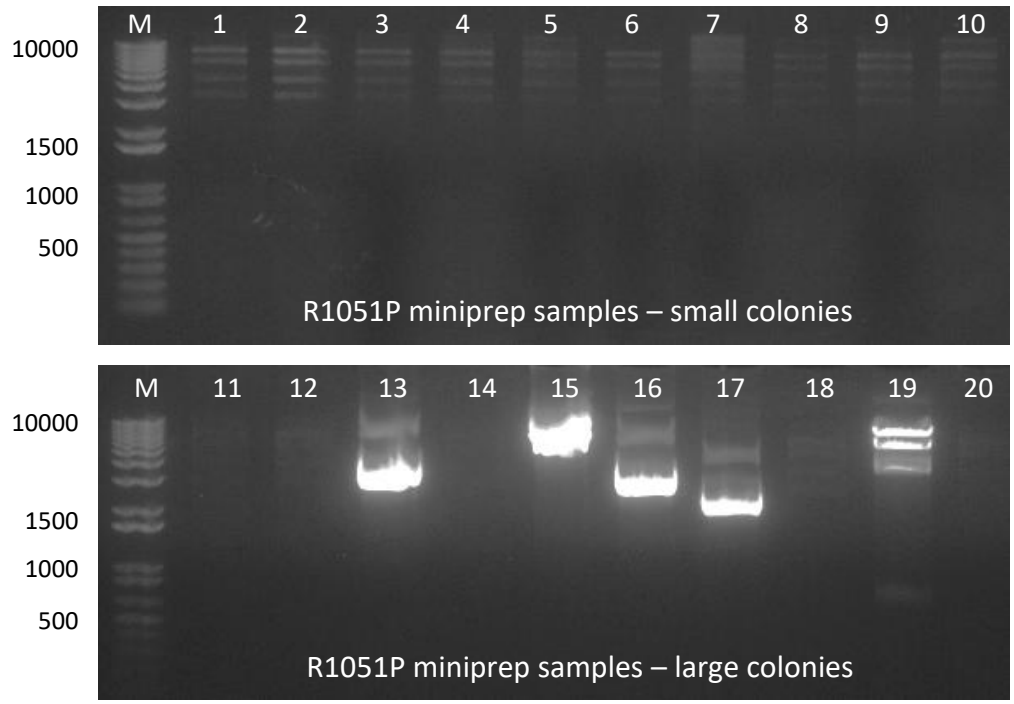

Figure 3.3. Restriction digest of miniprep following ligation of R1051P-hRyR2 plasmid shows recombination of DNA in some large colonies. Colony size of XL10-Gold E. coli was heterogeneous following ligation of the double digested pcDNA3-eGFP-hRyR2 plasmid and mutated *SpeI/SanDI* cassette, therefore colonies of all sizes were picked and miniprepped to increase the likelihood of selecting a positive clone that had not undergone recombination. Restriction digest of miniprepped samples with *EcoRI* indicated that recombination had occurred in 4/10 large colonies (lanes 13, 15, 16 and 17), whereas no small colonies showed recombination. Small colonies were therefore selected for large scale bacterial culture for R1051P and other hRyR2 variants. 'M' indicates the 1kb ladder marker; small colonies are numbered 1-10, and larger colonies 11-20.

3.3.2 The transfection efficiency of R1051-mutant hRyR2 was comparable to the WT

Two different transfection methods were used dependent on the application; Effectene® Transfection Reagent for IF and live cell Ca^{2+} imaging, and $CaPO_4$ transfection for making cell homogenate for Western blotting or solubilisation and purification. Transfection efficiency was calculated by capturing the same field of view (FOV) as a bright field image and a fluorescent image and expressing the number of cells showing eGFP fluorescence as a percentage of the total number of cells in the FOV.

There was no significant difference in the Effectene-mediated transfection efficiency of all R1051-mutant hRyR2 constructs compared to the WT (**Figure 3.4A**). The variability was high as indicated by the standard deviation, however this is likely due to the uneven distribution of transfected cells as they form localised clusters (**Figure 3.4B**). These transection efficiencies (~40%) are standard for hRyR2 (Viero et al. 2012).

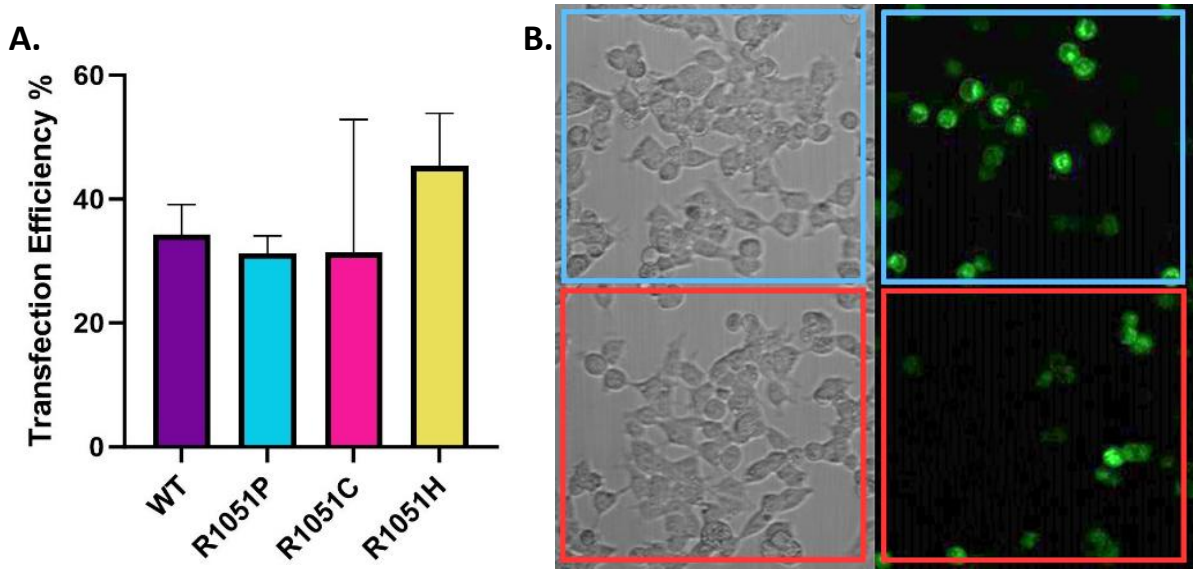

Figure 3.4. Transfection efficiency of R1051-mutant hRyR2 in HEK293 cells transfected by Effectene is comparable to WT-hRyR2. A. There was no significant difference in the transfection efficiency of cells transfected with R1051P, R1051C, R1051H or WT-hRyR2 using Effectene. Statistical analyses performed in GraphPad Prism 10.1.2 (GraphPad Software, 2023) by One-Way ANOVA with Tukey's post-hoc test. WT n = 5 FOV, R1051P n = 4, R0151C n = 5, R1051H n = 4. Transfection efficiencies were calculated from one plasmid preparation over multiple transfections. **B.** Example demonstrating variable transfection efficiency across a single FOV; the transfection efficiency of the blue rectangle is 31% compared to 20% in the red rectangle.

The transfection efficiency of cells after $CaPO_4$ transfection was estimated by eye after each transfection to ensure it exceeded 30%, as required for successful solubilisation and purification. The transfection efficiency of cells used to produce cell homogenate for Western blotting was; WT-hRyR2 = 34.6%, R1051P = 45.1%, R1051C = 45.3% and R1051H = 50.5% (calculated from one transfection each).

3.3.3 Immunofluorescence analysis indicated R1051P and R1051C-hRyR2 were not correctly trafficked within the cell.

IF was used to determine the localisation of hRyR2 within the cell and whether any of the three R1051-mutations alter the trafficking of hRyR2. Physiologically, hRyR2 is expressed primarily in the SR of cardiomyocytes, and is expected to be expressed in the ER of HEK293 cells as the equivalent organelle of non-contractile cells. Calreticulin is an ER-resident protein that was intended to be used as a marker of the ER in the cell and to indicate trafficking of hRyR2.

Across all hRyR2 variants and untransfected control cells there were issues with imaging the anti-calreticulin antibody as, while a reticular pattern was visible in some cells, there appeared to be general staining of the whole cell and patches of intense fluorescence in addition to typical ER staining (**Figure 3.5**). This makes comparisons by Manders overlap coefficient difficult as red fluorescence was present more widely throughout the cell (including the nucleus, although to a lesser extent than the cytosol), and therefore the values obtained do not accurately depict the co-occurrence of eGFP fluorescence with the ER only. However, the pattern of eGFP fluorescence in cells expressing WT and R1051H-hRyR2 shows a distinctly reticular pattern with typical net-like morphology, similar to that obtained by others for RyR2 (Kaya et al., 2013; Thomas et al., 2004). Due to this, more weight was placed on the appearance of eGFP fluorescence, rather than relying on the overlap coefficient.

Results of IF analysis in HEK293 cells expressing WT and R1051-mutant hRyR2 are shown in **Figure 3.5**. Cells expressing WT-hRyR2 showed a reticular pattern of eGFP fluorescence indicating trafficking to the ER; this matched the fluorescence of the anti-calreticulin ER marker antibody in the cytosol and produced a Manders overlap coefficient for green-to-red (G-R) of 0.62 ±0.13 (n = 22 cells). Cells expressing R1051H also tended to show a reticular pattern of eGFP fluorescence with a similar distribution to the WT and coefficients for G-R of

0.59 ±0.08 (n = 14 cells). R1051P and R1051C were more varied, and while some cells appeared to show trafficking of hRyR2 to the ER, there was a higher incidence of eGFP fluorescence appearing in a granular distribution throughout the cell with areas of concentrated fluorescence. This was found in 90% of cells expressing R1051P-hRyR2 (18 out of 20 cells analysed) and 69% of cells expressing R1051C-hRyR2 (11/16), compared to 14% of R1051H cells (2/14) and 4.5% of WT cells (1/22). The higher proportion of aggregation also corresponds with a lower overlap coefficient, with coefficients for R1051P of 0.40 ±0.12 G-R (n = 20 cells) and for R1051C of 0.51 ±0.16 G-R (n = 16 cells). The correlation co-efficient for R1051P was significantly lower than both WT and R1051H (**Figure 3.6**). No other comparisons were significantly different. Overall, this indicates that R1051-mutant expression does affect trafficking of hRyR2 to the ER, with R1051H behaving most similarly to the WT and both R1051P and R1051C showing atypical localisation of hRyR2.

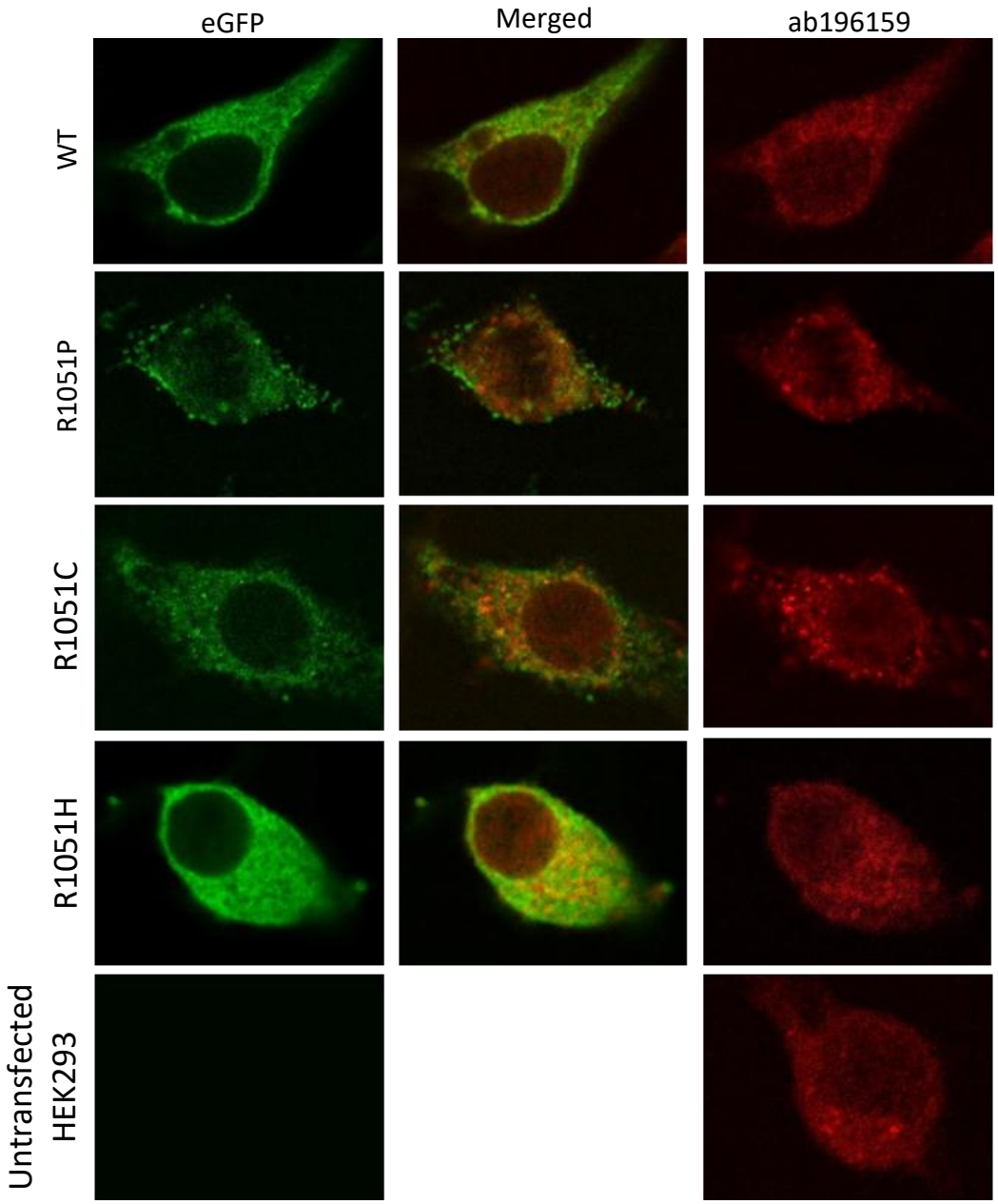

Figure 3.5. Immunofluorescence analysis of HEK293 cells expressing WT or R1051-mutant hRyR2 indicates abnormal trafficking of R1051P and R1051C-hRyR2. HEK293 cells transfected with WT or mutant hRyR2 were compared to determine any difference in hRyR2 trafficking within the cell. The Alexa Fluor® 647 anti-calreticulin antibody ab196159 (Abcam) did not show a typical reticular pattern in all cells and was not a good indicator of the ER; eGFP fluorescence was therefore considered more substantially. HEK293 cells expressing WT-hRyR2 showed a typical reticular pattern of eGFP staining, as did most cells expressing R1051H-hRyR2. R1051P and R1051C-hRyR2 expression resulted in areas of intense eGFP fluorescence that is not indicative of hRyR2 trafficking to the ER; this was observed in R1051H and WT but to a lesser extent.

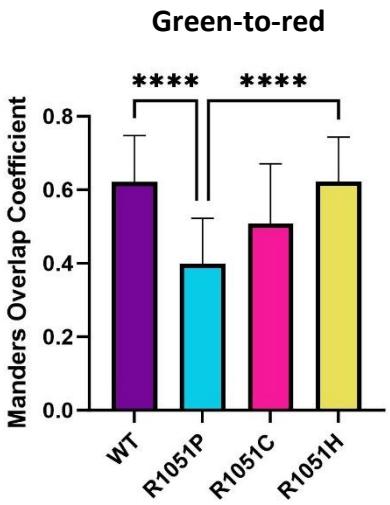

Figure 3.6. Co-occurrence of eGFP fluorescence with the ER marker calreticulin is significantly reduced in cells expressing R1051P-hRyR2. Comparison of Manders Overlap Coefficients for green to red pixels demonstrates that the co-occurrence of eGFP fluorescence (green) with the Alexa Fluor® 647 anti-calreticulin antibody ab196159 (Abcam) (red) was significantly lower in R1051P compared to both the WT and R1051H-hRyR2. This suggests that significantly more R1051P-hRyR2 was incorrectly trafficked within the cell than WT or R1051H-hRyR2. Statistical analysis performed in GraphPad Prism 10.1.2 by One-Way ANOVA with Tukey's post hoc tests; **** = p-value < 0.0001; WT n = 22 cells, R1051P n = 20, R1051C n = 16, R1051H n = 14.

3.3.4 R1051-mutants did not significantly differ in their expression level compared to WT-hRyR2 but do indicate reduced expression

Expression levels of the recombinantly expressed hRyR2 variants were assessed using an anti-eGFP antibody. Full-length hRyR2 was identified as a band at 565kDa (**Figure 3.7A**) on Western blots and normalised to the signal of the loading control (α-tubulin). Blotting for eGFP-hRyR2 often produces a slightly lower molecular weight band at approximately 400kDa (**Figure 3.7A**) representing a C-terminal proteolytic fragment due to cleavage at an N-terminal site by calpain (Zissimopoulos et al. 2013), a calcium-activated protease found in the cytosol (Goll et al. 2003).

Densitometric analysis revealed no significant difference in expression between the WT and R1051P, R1051C or R1051H for total hRyR2 levels (565kDa and 400kDa bands combined), full-length hRyR2 (565kDa) or calpain-cleaved (400kDa) hRyR2 (**Figure 3.7B**). Visual comparison of the results however does suggest lower expression of all R1051-mutants, but due to the large variation in results (**Figure 3.7B** and **Appendix III**) this does not reflect in the significance of comparisons.

3.3.5 Phosphorylation at S2808 is not significantly different in R1051-mutant hRyR2.

Phosphorylation at S2808 was detected using an antibody raised to the phosphoserine S2808 epitope to determine any effect on phosphorylation levels at this site due to mutation. Detection of phosphorylation is dependent on hRyR2 expression as well as phosphorylation level, so phosphorylation levels are expressed as a proportion of hRyR2 expression. This was carried out by first detecting hRyR2 expression using an anti-eGFP antibody, followed by stripping of the blot and re-probing with the S2808 antibody (**Figure 3.8A**). No significant difference in phosphorylation at S2808 was detected between WT, R1051P, R1051C and R1051H-hRyR2 when densitometry was performed on the combined 565kDa and 400kDa bands (**Figure 3.8B**). Variability was observed in the relative density of the 565kDa band and the 400kDa band that was not consistent between the eGFP antibody and phosphoserine S2808 antibody, so the total phosphorylation was considered a more reliable measure (**Appendix IV**). This variability was not attributable to stripping as complete stripping was confirmed by imaging of the stripped blot (**Appendix V**).

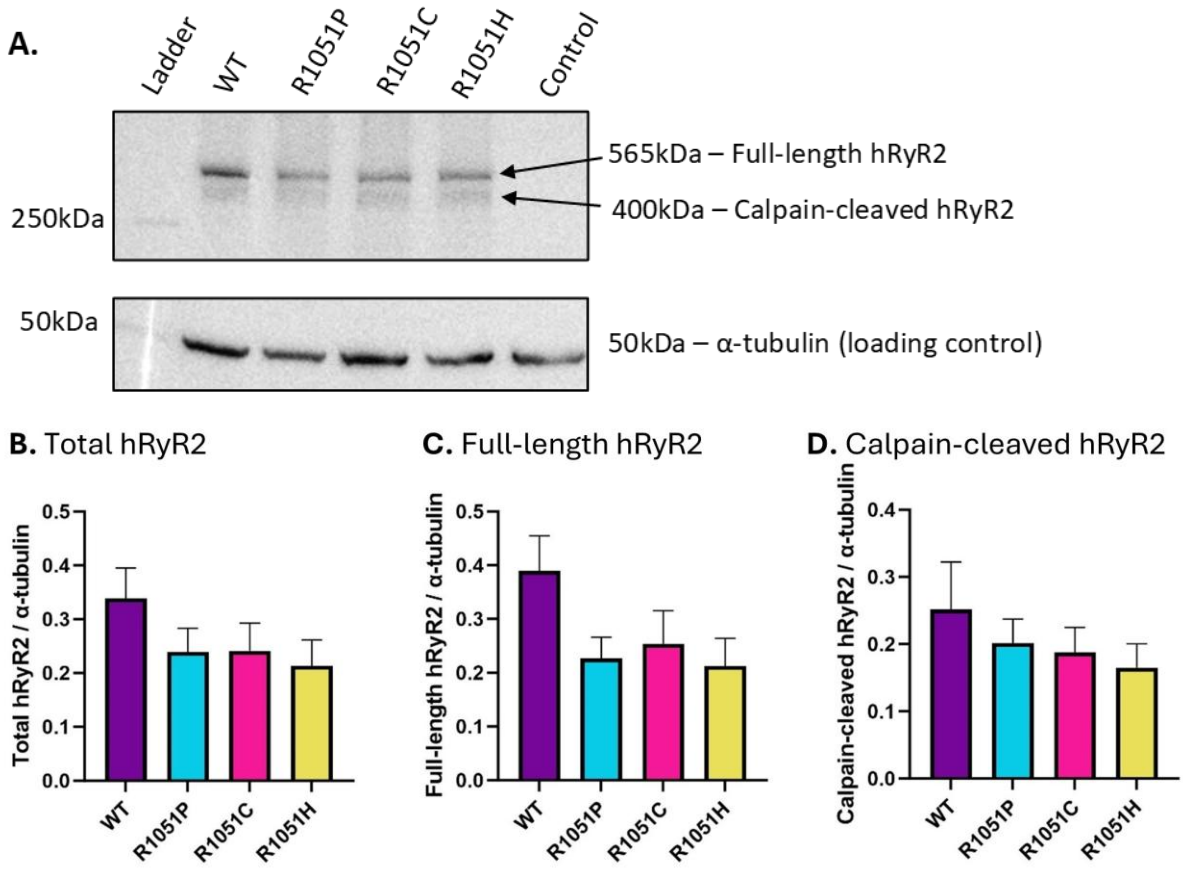

Figure 3.7. Densitometry analysis of Western blots shows no significant difference in expression of R1051-mutant hRyR2 in HEK293 cells compared to WT-hRyR2. A. Representative example of a Western blot of HEK293 cell homogenate expressing hRyR2. For total hRyR2 calculations, both the 565kDa and 400kDa band were grouped together. The control (untransfected HEK293) confirmed hRyR2 was only present after transfection and did not affect the expression of the loading control. **B**. Densitometry revealed no significant difference in the total expression of R1051-mutant hRyR2 compared to the WT, although for all mutants the total amount of hRyR2 was non-significantly lower than the WT. The relative proportions of full-length hRyR2 (**C**) and calpain-cleaved hRyR2 (**D**) were not significantly different in the mutants compared to the WT. Data are shown as mean ± SEM; significance was determined by One-Way ANOVA with Tukey post-hoc tests in GraphPad Prism 10.1.2 and non-significance assigned to p-values >0.05, n = 7 Western blots.

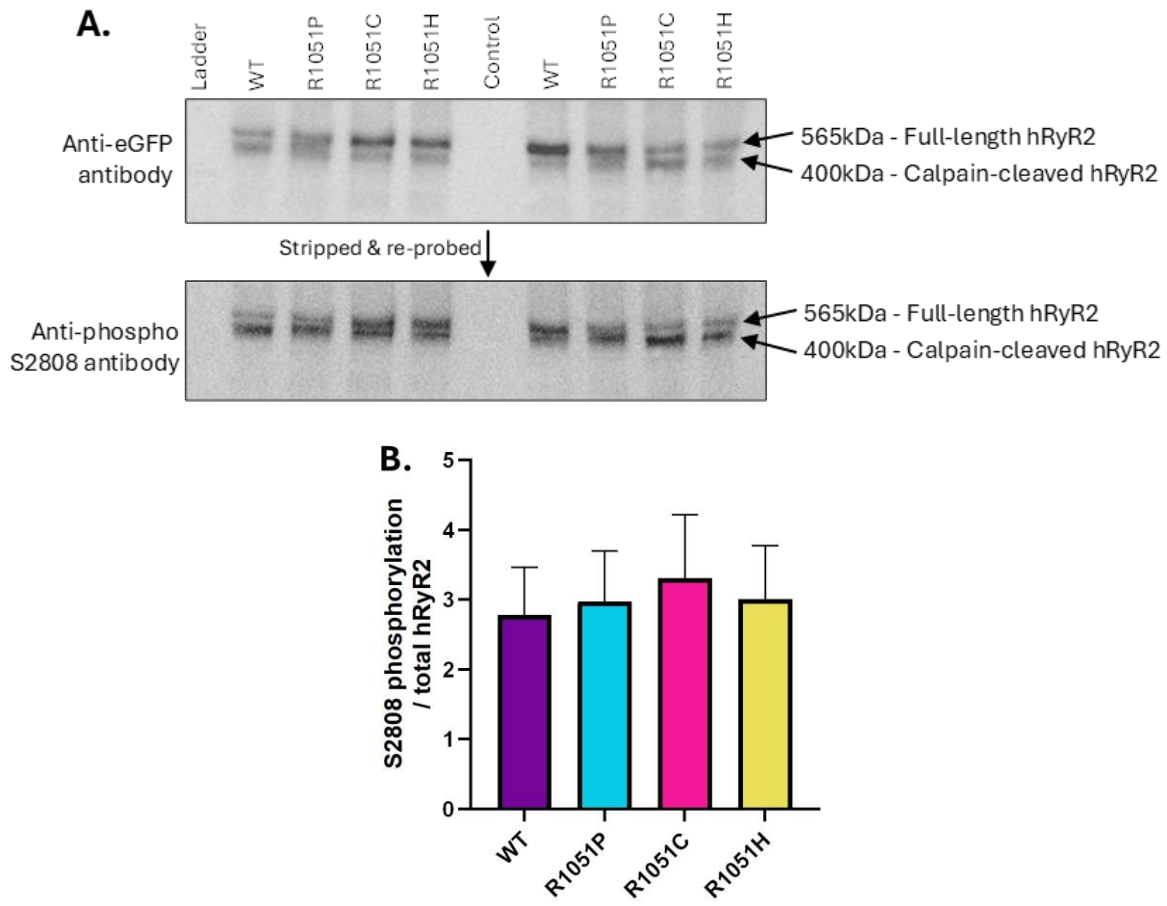

Figure 3.8. Densitometry analysis of phosphorylation at S2808 revealed no significant difference in phosphorylation of R1051-mutant hRyR2 compared to the WT. A. Blots were assessed for hRyR2 expression using an anti-eGFP antibody before stripping and re-probing with an S2808 phospho-specific antibody (**Section 3.2.6**). **B.** Phosphorylation levels were normalised to hRyR2 expression and densitometry showed no significant difference in phosphorylation at S2808. Data shows mean ±SEM; significance was determined by One-Way ANOVA with Tukey's post-hoc test in GraphPad Prism 10.1.2 and non-significance assigned to p-values >0.05, n = 7 Western blots.

3.4 Discussion

3.4.1 All R1051-mutant hRyR2 constructs were successfully engineered and expressed in HEK293 cells

Before functional characterisation of the R1051-mutant hRyR2 could begin, it was first necessary to engineer the mutant constructs and assess whether they could be expressed in the desired cell system. Following the heavily optimised protocol for mutagenesis of pcDNA3-eGFP-hRyR2 plasmid and then propagation of this in supercompetent *E. coli*, the three mutants, R1051, R1051C and R1051H-hRyR2 were all verified by Sanger sequencing (**Figure 3.2**). They were then successfully transfected into HEK293 cells by both Effectene-mediated and $CaPO_4$ transfection, as confirmed by successful IF-imaging of the eGFP-tag (**Figure 3.5**) and successful detection of eGFP-hRyR2 at the expected molecular weight in Western blotting (**Figure 3.7A**). While this demonstrates that all three R1051-mutants are successfully expressed to produce full-length hRyR2 (represented by the band at 565kDa in **Figure 3.7A**), this does not guarantee functional Ca^{2+} release which must be confirmed by live cell Ca^{2+} imaging (**Chapter 4**).

3.4.2 Immunofluorescence and expression analysis suggests varying levels of degradation of the different R1051-mutants

IF was used to assess the localisation of R1051-mutant hRyR2 and determine whether the mutant proteins were correctly trafficked to the ER, while expression levels were assessed to determine if changes in expression might contribute to any functional changes. IF results indicate that trafficking of R1051P and R1051C are significantly impacted, while expression is modestly impacted with no significant difference found.

Cells expressing R1051P-hRyR2 and R1051C-hRyR2 both showed a highly abnormal pattern of eGFP fluorescence in the cytosol characterised by a granular distribution of eGFP fluorescence in addition to a more typical reticular pattern (**Figure 3.5**). This suggests incorrect trafficking of a proportion of channels, possibly as a result of aggregation and degradation (discussed below). However, this was complicated by apparent technical issues with the ER marker antibody which showed staining of other cellular compartments in addition to the ER (**Figure 3.5**). The reason for this issue is unclear, however it may in part be explained by the function of calreticulin in the cell as well as the effect of mutation. Calreticulin is a chaperone protein predominantly expressed in the ER with important roles

in Ca^{2+} homeostasis, protein folding and apoptotic signalling (Michalak et al. 1999; Gelebart et al. 2005; Michalak 2024), however it is also found outside of the ER including within the nucleus and at the cell surface (Yoon et al. 2000; Gold et al. 2010; Bansal et al. 2023). Some staining with the anti-calreticulin antibody outside of the ER is therefore to be expected, however the extent seen within this study was unexpected and detrimental to the results. This might argue against the validity of the Manders Overlap Coefficienct analysis, and the incidence of colocalization is generally lower than might be expected for two ER-resident proteins, however there was still a significant decrease in coefficient for R1051P with calreticulin compared to WT-hRyR2, indicative of altered trafficking for this mutant (**Figure 3.6**).

Staining resembling protein aggregates were also observed with the anti-calreticulin antibody, though these did not exactly match the areas of eGFP-hRyR2 aggregation, suggesting there may be an effect of hRyR2 mutation on the distribution of calreticulin within the cell (**Figure 3.5**). This was particularly notable in cells expressing R1051P and R1051C-hRyR2 which, as discussed above, showed increased aggregation and signs of protein degradation. The presence of misfolded proteins in the cell, if not correctly degraded, leads to ER stress which in turn triggers the unfolded protein response (UPR) (Schröder and Kaufman 2005; Hetz et al. 2011; Woehlbier and Hetz 2011) and results in upregulation of calreticulin along with other chaperones (Zhao and Ackerman 2006; Zhang et al. 2014; Stoner et al. 2020) and reticulophagy (the degradation of the ER via lysosomes) (Song et al. 2018; Reggiori and Molinari 2022). This has been shown for RyR2 previously, with dysfunction and instability of RyR2 resulting in ER stress and activation of the UPR (Guo et al. 2023; Uchinoumi et al. 2025), and ER stress has also been shown to directly contribute to arrhythmogenesis in CPVT (Veress et al. 2024). It is therefore highly possible that these mutations do affect ER function and that this may exacerbate the phenotypes they produce.

Considering the pattern of eGFP fluorescence in isolation first, cells expressing WT or R1051H-hRyR2 largely produced the expected reticular pattern of fluorescence (Thomas et al. 2004; Kaya et al. 2013). This was a stark contrast to cells expressing R1051P or R1051C-hRyR2, the majority of which showed a granular pattern of fluorescence with concentrated areas that are indicative of aggregation within the cytosol, and is not representative of the net-like pattern of the ER in HEK293 cells. This was not entirely unexpected as these

mutations were hypothesised to disrupt hRyR2 function by causing conformational changes in the P1 domain (Bauerová-Hlinková et al. 2020), which could trigger regulated breakdown of dysfunctional or misfolded protein, although this has not been identified in other mutations in this region. This is particularly true for R1051P, where proline substitution would likely disrupt the domain structure and could result in severe conformational changes (Bauerová-Hlinková et al. 2020). Protein aggregation occurs when unfolded or misfolded proteins are not degraded by the relevant cellular pathways and instead accumulate together due to hydrophobic amino acids becoming exposed and interacting with hydrophobic residues on adjacent proteins, resulting in the formation of aggregates (Ellis and Minton 2006; Díaz-Villanueva et al. 2015; Majid and Khan 2023). In the case of RyR2, degradation initially occurs via calpains, Ca^{2+}-dependent cysteine proteases which cleave RyR2 at an N-terminal site and leave a large ~400kDa fragment that is then further degraded primarily via the ubiquitin-proteasome pathway (UPP) (Pedrozo et al. 2010) or via chaperone-mediated-autophagy and the lysosome (Pedrozo et al. 2013). This suggests that R1051P and R1051C may undergo increased degradation, however this is only weakly supported by results from Western blotting, which show a small but insignificant decrease in the expression of hRyR2 (**Figure 3.6**).

Decreased expression of RyR2 has been reported in disease-associated mutants, including the GoF CPVT mutation G357S, which increased the propensity for SOICR but decreased expression (Liu et al. 2017), however reduced expression is not usually associated with CPVT and is more commonly seen in cardiomyopathies (Alvarado et al. 2019). This includes the HCM-associated mutation P1124L-RyR2 which decreased expression of the channel and is implicated in both arrhythmia and HCM, although no localisation was performed for this mutant (Alvarado et al. 2019). Decreased expression of RyR2 has also been observed in other models of cardiomyopathy that do not arise from RyR2 mutation (Ding et al. 2004; Meurs et al. 2006a) and downregulation of RyR2 resulted in structural changes indicative of cardiomyopathy in a mouse model (Bround et al. 2012a). Since R1051C and R1051H have been linked to HCM and DCM, respectively, this indicates reduced expression may have a functional consequence in the R1051-mutants that contributes to cardiomyopathy, even if this change was not found to be statistically significant.

Collectively, while the apparent reduced expression of R1051-mutants was not statistically significant (**Figure 3.7**), the combination of this with the altered trafficking and aggregation of R1051P and R1051C-hRyR2 (**Figure 3.5**) does suggest that all three R1051 mutants undergo increased degradation or decreased expression, or a combination of the two. With this in mind, it would be beneficial to compare the localisation of eGFP fluorescence to markers of ubiquitination, the proteasome, or the lysosome to help confirm whether the changes are due to increased degradation, and if so, what pathway may be involved. In the absence of this data however, the reticular pattern of WT and R1051H-hRyR2 (Thomas et al. 2004; Kaya et al. 2013) compared to aggregation of eGFP fluorescence in cells expressing R1051P and R1051C-hRyR2 is distinct enough to demonstrate some dysfunction of these mutants that could be due to protein misfolding or instability. This is supported by the Manders overlap coefficients which show a significant decrease in R1051P-hRyR2 co-localisation with the ER marker compared to R1051H or WT-hRyR2. Overall, while additional IF experiments could be beneficial in understanding what is causing aggregation in R1051P and R1051C, the data presented here suggests a change in the localisation of some R1051-mutants that could impact their function in the cell.

3.4.3 Phosphorylation at S2808 is unaffected by mutations at R1051

Phosphorylation was assessed as it is often attributed as a causative mechanism in increased RyR2 activity and Ca^{2+} leak (**Section 1.4.1**) and several CPVT-linked mutations have been shown to alter the sensitivity of the channel to phosphorylation (Uchinoumi et al. 2010b) or require phosphorylation to reveal their dysfunction (Wehrens et al. 2003; Lehnart et al. 2004a; Meli et al. 2011). There have also been several studies demonstrating a notable difference in basal phosphorylation levels of RyR2 mutants (Loaiza et al. 2013; Hamilton 2017), although the general consensus is that most CPVT-linked RyR2 mutations don't impact basal phosphorylation levels (Chelu et al. 2009; Sedej et al. 2010; Meli et al. 2011; Dobrev and Wehrens 2014). Despite this, it was decided to assess phosphorylation levels for two main reasons; the location of the phosphorylation sites relative to R1051 and the potential effect of phosphorylation on FKBP12.6 binding. R1051 in the P1 domain is located relatively close to the two main phosphorylation sites, which sit on a flexible loop at the top of the P2 domain approximately 60-70Å away from R1051 (calculated using PDB accessions 7U9Q and 7U9R; **Figure 3.9**) (Miotto et al. 2022). S2808 was chosen specifically as

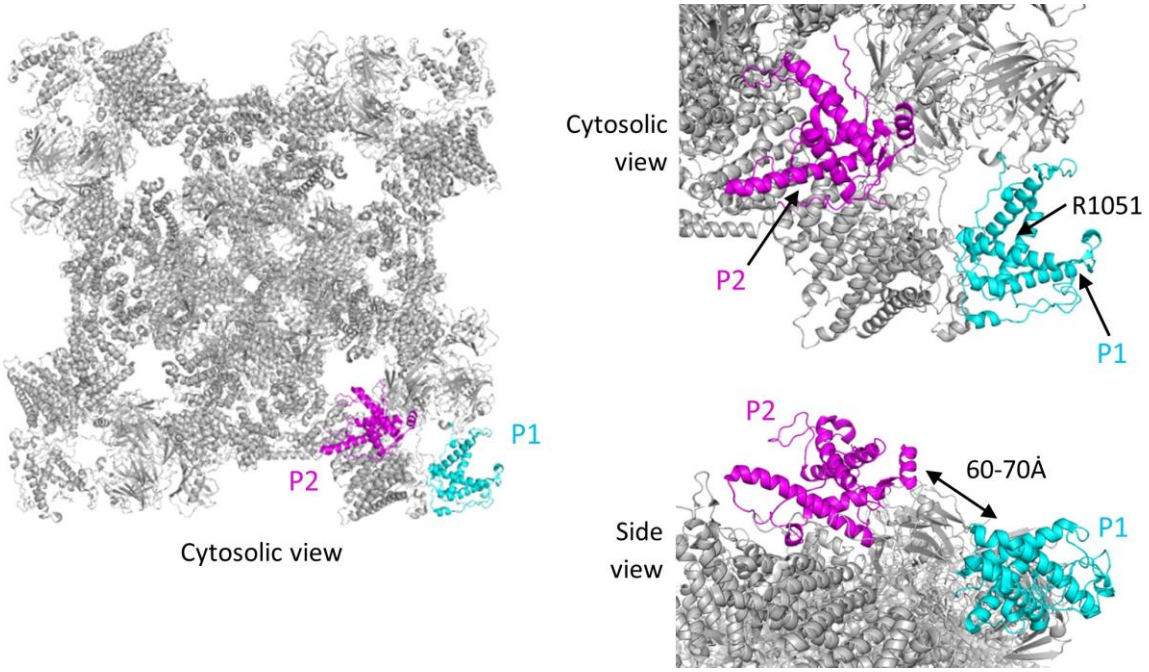

Figure 3.9. Proximity of P1 and P2 of the closest adjacent monomer in RyR1. R1051 on the P1 domain is approximately 60-70Å from the unresolved flexible loop of the phosphorylation domain in P2 in RyR1; RyR2 is predicted to have a similar structure. Models produced in PyMol using PDB accession code 7U9Q for RyR1 in the closed state.

hyperphosphorylation at this PKA-specific site has been proposed to increase RyR2 Ca^{2+} release and contribute to HF by causing dissociation of the stabilising accessory protein FKBP12.6 (Marx et al. 2000; Wehrens et al. 2006; Walweel et al. 2023b), although others have found no evidence for an effect of S2808 phosphorylation on FKBP12.6 association (Jiang et al. 2002a; Stange et al. 2003; Guo et al. 2006; Xiao et al. 2006; Guo et al. 2010). No significant difference in phosphorylation levels at S2808 were found between any of the R1051 mutants and WT-hRyR2 (**Figure 3.7B**) which suggests that phosphorylation at this site is unlikely to be altered as a result of mutation and is therefore not expected to contribute to their phenotype. This does not preclude basal phosphorylation levels at S2814 or S2030 being impacted by R1051 mutation, nor does it indicate whether phosphorylation is required for these mutations to exhibit dysfunction. Despite S2808 phosphorylation levels being comparable to that of the WT, investigation of the impact of mutation at R1051 on FKBP12.6 binding still represents an appropriate line of research, in particular due to the role of both P1 and FKBP12.6 in RyR2 channel clustering.

3.4.4 Conclusions

This chapter has demonstrated that recombinant R1051P, R1051C and R1051H-hRyR2 can all be successfully generated and expressed in HEK293 cells via both Effectene and $CaPO_4$-mediated transfection. While expression levels of all mutants were not significantly different to the WT, this may be due to the large degree of variation in Western blots as they did appear to show reduced expression. The localisation of R1051P-hRyR2 and R1051C-hRyR2 was also highly atypical and indicative of increased degradation which could impact future work as it might affect their ability to form functional channels. These findings warrant further functional characterisation of the R1051-mutants, beginning with assessing Ca^{2+} release at the whole cell level.

Chapter 4

Assessing the effect of R1051-mutation in hRyR2 on whole cell Ca^{2+} release via live cell Ca^{2+} imaging in HEK293 cells

4.1 Introduction

4.1.1 Functional characterisation of hRyR2 mutations

RyR2 mutations are diverse in their phenotypic presentation and their mechanism of dysfunction, and many techniques can be used to probe different aspects of mutation. This ranges from looking at their single channel function in a minimal environment (**Chapter 6**), to looking at how mutations affect spark propagation across the cell and global Ca^{2+} release into the cytosol, all the way to ECGs in animal models. While a combination of techniques is required to build a full picture of RyR2 function, initial studies benefit from high throughput techniques that can identify clear signs of RyR2 dysfunction before applying other techniques that are capable of characterising more detailed information about the mechanism of channel dysfunction. One such high throughput technique is live cell Ca^{2+} imaging in mammalian cells expressing recombinant hRyR2. This provides insight into how mutations affect global Ca^{2+} release from the SR in a system that mimics the physiological environment. While this technique does not reveal the precise mechanism of dysfunction, it is a useful tool to look at the cellular-level effects of mutation and can indicate both downstream effects of mutation and potential underlying causes. Given no functional data has been published for the R1051-mutants of interest in this study, live cell Ca^{2+} imaging was selected as an appropriate method to begin characterising these mutants before trying to narrow down their mechanism of dysfunction.

4.1.2 Ca^{2+} imaging for assessing whole cell calcium release

Live cell Ca^{2+} imaging has been extensively used to investigate arrhythmia-linked hRyR2 mutations and hRyR2 function as it gives an overall indication of channel function in a cellular environment. Ca^{2+} imaging uses high-powered laser scanning confocal microscopy (**Figure 4.1**) and Ca^{2+} sensitive dyes to visualise Ca^{2+} release from intracellular stores, with the fluctuation in fluorescence corresponding to the amount of Ca^{2+} released. While whole cell Ca^{2+} release cannot discern the underlying mechanism of dysfunction, it is an important step in functional characterisation of hRyR2 mutants as it is directly related to hRyR2 function and is often used as an initial, higher throughput experiment for characterisation compared to single channel analysis.

The dyes used in live cell Ca^{2+} imaging are acetoxymethyl (AM)-conjugated Ca^{2+}-sensitive dyes. In their conjugated form, AM dyes can pass through the cell wall in a non-fluorescent

and non-activable form, which becomes activated upon hydrolysis by endogenous esterases in the cytosol. Hydrolysis allows the dye to bind Ca^{2+}, as well as making the dye hydrophobic and no longer able to pass through the cell wall, thus containing it within the cytosol. Here the dye can bind to free Ca^{2+} in the cytosol which results in an increase in fluorescence when Ca^{2+} is released from intracellular stores via opening of RyR2 or other ion channels. Fluorescence subsequently decreases upon reuptake of Ca^{2+} to the intracellular store, resulting in oscillations in fluorescence that match that of Ca^{2+} with high temporal resolution (Lock et al. 2015).

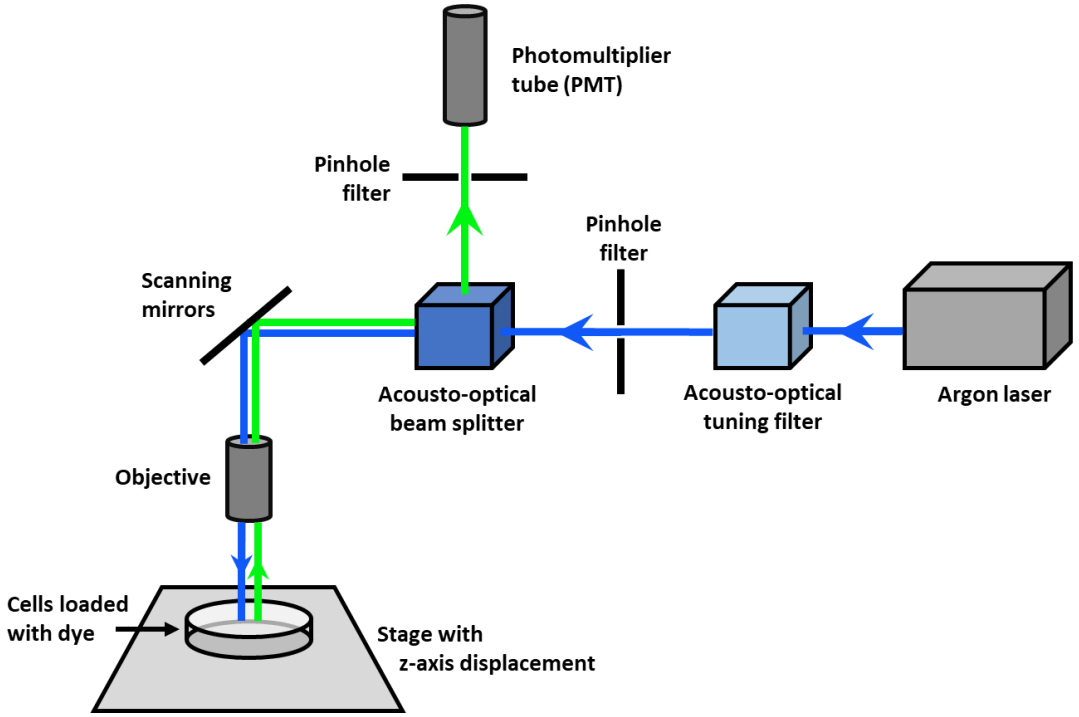

Figure 4.1. Diagram of confocal microscope setup for live cell Ca^{2+} imaging. An argon laser of an appropriate wavelength for excitation passes through a tuning filter and pinhole filter before passing through an acousto-optical beamsplitter and hitting the scanning mirrors. The laser is redirected by the mirrors to the sample where it excites fluorescence molecules (this could include fluorescent tags such as eGFP, or fluorescent dyes). The laser scans back and forth across the sample to illuminate each point individually, rather than illuminating the entire sample at once. Emitted light from the sample passes through the objective back to the scanning mirrors and back to the beamsplitter where the emitted light is tuned to separate the emitted light from the excitation light. The emitted light is then filtered again by a pinhole filter and then detected by the photomultiplier tube where the signal is amplified and converted to an electrical signal that captures the fluorescence of the sample. Diagram modified from documentation by Leica Microsystems CMS GmbH.

4.1.3 Measuring spontaneous Ca^{2+} release in a recombinant cell system

As discussed in **Section 3.1.2**, HEK293 cells present an effective system for the expression of recombinant RyR2 for both purification and for functional studies. This is possible as HEK293 cells expressing RyR2 still exhibit SOICR, which can be assessed to gain an understanding of mutant RyR2 function (Jiang et al. 2004; Thomas et al. 2004; Kong et al. 2008). In cardiomyocytes, SOICR occurs when the Ca^{2+} content of the SR reaches a critical threshold, termed the activation threshold for Ca^{2+} release (Jiang et al. 2005). This same process applies in non-contractile cells such as HEK293 cells when the Ca^{2+} content of the ER reaches the activation threshold, triggering SOICR events that are comparable to those observed in cardiomyocytes (Jiang et al. 2005). This spontaneous Ca^{2+} release is terminated when the Ca^{2+} content drops to the termination threshold, after which the cycle continues to produce spontaneous Ca^{2+} transients that can be analysed to determine the effects of mutation (Jiang et al. 2004; Jiang et al. 2005; Tang et al. 2012). This often includes analysis of the frequency of Ca^{2+} transients as an indicator of channel sensitivity to luminal or cytosolic Ca^{2+}, as increased channel sensitivity is strongly implicated in CPVT (**Section 1.6.2.1**). Other aspects of Ca^{2+} release can also be assessed such as the kinetics of Ca^{2+} release, which reflect how quickly RyR2 channels open and close during SOICR, or the amplitude of transients as an indicator of the total amount of Ca^{2+} release per event.

Many CPVT and disease linked mutations have been investigated in this way, including several pivotal studies that have shaped the way RyR2 mutations are viewed. The first study using SOICR in HEK293 cells showed that the CPVT-associated mutations R4496C, N4104K and N4895D increased the sensitivity of the channel to luminal Ca^{2+} and reduced the threshold for Ca^{2+} release leading to increased arrhythmogenic activity (Jiang et al. 2004). Live cell Ca^{2+} imaging in HEK293s also identified LoF behaviour in SCD-linked RyR2 mutation L433P that reduced the sensitivity of the channel to activation, highlighting the functional heterogeneity RyR2 mutations (Thomas et al. 2004). More recently, HEK293 cells have been used to investigate the impact of cardiomyopathy associated mutations on RyR2 function. This includes the DCM-associated mutation E3DS which was revealed to increase the propensity for SOICR and result in larger Ca^{2+} transients (Tang et al. 2012), and two HCM mutations – T1107M (Tang et al. 2012) and P1124L (Alvarado et al. 2019). The mouse equivalent of T1107M (A1107M) was shown to increase the threshold for Ca^{2+} release and

decrease the propensity for SOICR (Tang et al. 2012), whereas P1124L increased the propensity for SOICR but also decreased channel sensitivity to cytosolic Ca^{2+} (Alvarado et al. 2019). Many of these studies employ the genetically encoded Ca^{2+} sensitive fluorescence resonance transfer energy (FRET) dye D1ER in HEK293 cells to determine the ER load at which SOICR initiation and termination occurs. In these experiments, tetracaine (an inhibitor of RyR2) is used to inhibit SOICR, which results in an increase in ER [Ca^{2+}] until it reaches a steady state; this is the 'maximum' store load. Caffeine is then added to cells to trigger opening of RyR2, depleting the store until it reaches its steady 'minimum' level. This can be used to indirectly measure Ca^{2+} leak, which is calculated as the difference between the steady state of the ER following RyR2 inhibition and the level at which SOICR initiates (Shannon et al. 2002). However, the results are not always straightforward to interpret and there is little consensus on what the functional consequence of altered termination or initiation of SOICR is for CPVT or cardiomyopathies. Genetically encoded Ca^{2+} indicators also have a lower sensitivity and temporal resolution, limiting their ability to detect small or rapid Ca^{2+} release events compared to cytosolic AM dyes (Lock et al. 2015).

4.1.4 Chapter Aims

This chapter aims to characterise R1051P, R1051C and R1051H mutants of hRyR2 at the whole cell level via live cell Ca^{2+} imaging as a first indication of how they differ in function from WT-hRyR2. As these mutants have all been linked to CPVT it is hypothesised that they will result in Ca^{2+} leak from hRyR2. However, as R1051C and R1051H are also associated with HCM and DCM, it is possible that they will present with a more complex phenotype as is often observed in these cardiomyopathies (**Section 1.6.6** and **Section 1.6.7**); this could include some LoF characteristics which might arise from increased degradation or decreased expression (**Section 3.4.2**). This will be assessed by the following steps:

- Investigate whole cell Ca^{2+} release from HEK293 cells transfected with R1051-mutant hRyR2 constructs by live cell Ca^{2+} imaging to determine whether spontaneous Ca^{2+} release events are altered compared to WT-hRyR2 and to quantify these differences where possible.
- Assess the response of cells expressing R1051-mutant hRyR2 to caffeine as an indication of ER store load compared to WT-hRyR2.

4.2 Materials & Methods

4.2.1 Materials

- CalbryteTM 520 AM (AAT Bioquest) – prepared on the day as 10 µM stocks with DMSO with 20% w/v Pluronic F-127.
- Leica SP5 Laser Scanning Confocal Microscope – used with a Leica 20x dry objective (Leica Microsystems CMS GmbH)
- Krebs Ringer HEPES buffer (KRH) - 9 g/L glucose, 7 g/L NaCl, 6 g/L HEPES, 0.35 g/L KCl, 0.16 g/L KH_2PO_4, 0.29 g/L $MgSO_4$, 1.3 mM $CaCl_2$, pH adjusted to 7.4, filter sterilized

4.2.2 Live cell Ca^{2+} imaging in HEK293 cells

For live cell Ca^{2+} imaging, HEK293 cells were seeded at a density of $1x10^5$ in a 200 µL meniscus on poly-lysine coated 35mm glass bottom dished (Mattek) and incubated at 37°C, 5% CO_2. Cells were then transfected with eGFP-hRyR2 constructs via the Effectene® transfection method (**Section 2.1.10**). Live cell Ca^{2+} imaging was achieved using the cell-permeable Ca^{2+} indicator CalbryteTM 520 AM (AAT Bioquest) and high-powered laser confocal microscopy. CalbryteTM 520 AM has an emission wavelength of 515nm and is detected in the same range as eGFP (509nm), however the aim of imaging is to determine the relative change in fluorescence of cells in response to Ca^{2+} and it has been established by previous studies that background fluorescence from eGFP does not affect this as its fluorescence intensity is far lower in comparison (Thomas et al. 2004; Thomas et al. 2005).

CalbryteTM 520 AM working stocks (10 µM) were prepared by resuspending the lyophilised indicator in 15.3 µL DMSO with 20% w/v Pluronic F-127 and diluting (1:300) in mDMEM. Cells were incubated with dye at 37°C, 5% CO_2 for 1 hour before de-esterification for 10 minutes by flooding with mDMEM. Imaging was carried out in a 200 µL meniscus of KRH buffer. Live cell Ca^{2+} imaging was performed using a Leica SP5 laser scanning confocal microscope with a 20x objective and argon laser at 488nm with photomultiplier tube detection in the range of 500 to 570nm. Data were acquired using Leica LAS-AF software with a resolution of 512x512 pixels and captured at a rate of 5 frames per second for 6 minutes.

4.2.3 Data processing and analysis

Following acquisition, FIJI image processing software was used to select regions of interest (ROIs) containing individual cells that showed activity over the course of the recording. Analyses were carried out in MatLab (The MathWorks Inc, 2020) using a custom applet designed to automatically detect different parameters (**Figure 4.2**) of Ca^{2+} transients and produce traces from each ROI. All traces were then manually sorted to exclude those in which the software did not correctly identify Ca^{2+} release events (e.g. peak assigned incorrectly, registering transients where none were present, or where there were too few transients (<3) to accurately calculate frequency), those where no distinct transients were visible, or where abnormalities were observed that needed additional classification. The parameters assessed by the applet are outline below:

- *Frequency* – The frequency was calculated by the number of periods per minute, where a period includes the duration of Ca^{2+} oscillation event and the inter-transient interval. This is dependent on the ER Ca^{2+} store load, the sensitivity of the channel to $[Ca^{2+}]_{cyt}$, and the refractory period (i.e. the time after channel closure in which it is non-responsive to reactivation).
- *Duration* – The duration was calculated as the time from the start of a Ca^{2+} oscillation until the signal returns to the baseline, measured in seconds. This indicates the time taken from the start of Ca^{2+} release until Ca^{2+} has been removed from the cytosol.
- *Inter-transient-interval (ITI)* – The ITI measures the time between the end of one event and the start of the next, measured in seconds.
- *Amplitude* – The amplitude of Ca^{2+} release was calculated by subtracting the basal signal intensity (F0) from the peak signal intensity (F), as a proportion of the baseline intensity ((F-F0)/F0 or ΔF/F0). This is a reflection of how much Ca^{2+} is released during one event, in combination with duration.
- *Rise Rate* – The rise rate (sometimes called 'time to peak') is the rate of increase of signal intensity to the peak from the baseline, expressed as (ΔF/F0)/second. This reflects the rate of activation of channels.

- *Fall Rate* – The fall rate (sometimes called 'decay rate') is the rate of decrease of signal intensity from the peak, expressed as (ΔF/F0)/second. This is a reflection of the rate of termination of Ca^{2+} release.

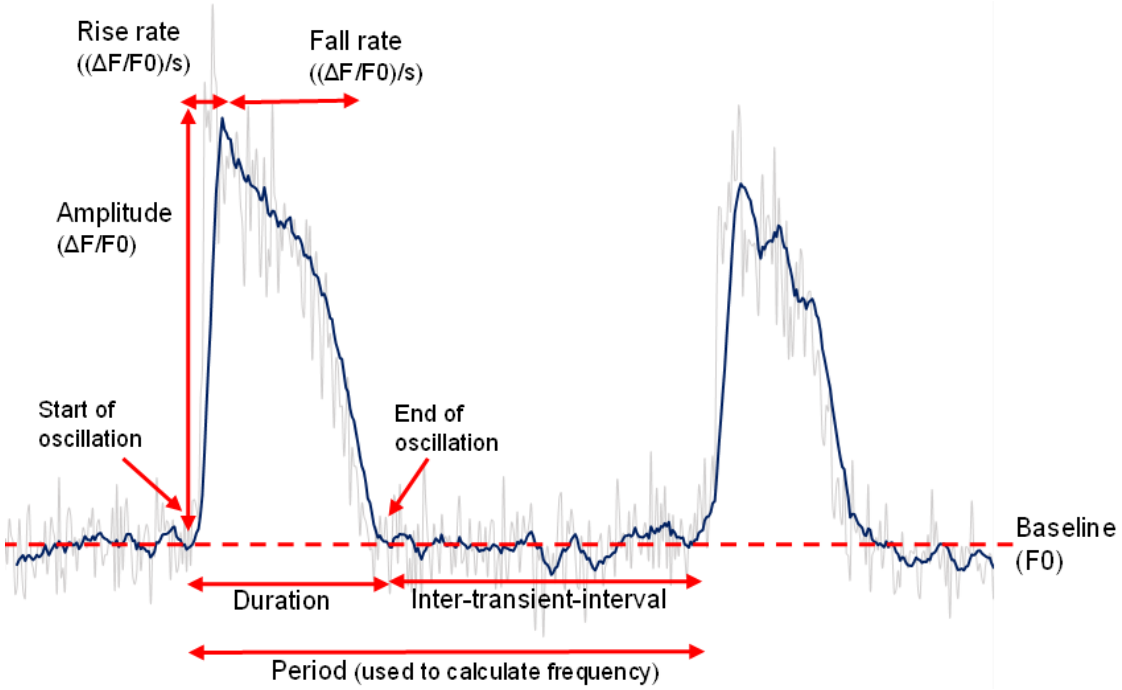

Figure 4.2. Parameters measured from Ca^{2+} imaging data. The software used for analysis measures the following parameters that can be used for characterising Ca^{2+} release; Period – the time between the start of one event and the start of the next. Frequency – number of events per minute, defined by the number of periods in a set time. Duration – time from start of oscillation until signal returns to the baseline. Inter-transient-interval – time between the end of one event and the start of the next. Amplitude – calculated by subtracting F0 from F, as a proportion of the baseline intensity ((F-F0)/F0 or ΔF/F0). Rise Rate – rate of increase of signal intensity to the peak, expressed as (ΔF/F0)/second. Fall Rate - rate of decrease of signal intensity from the peak, expressed as (ΔF/F0)/second.

4.2.4 Caffeine experiments

Experiments were set up as in **Section 4.2.2** and cells recorded for 5 minutes prior to caffeine addition. Caffeine was added directly to the cell medium during recording by gentle pipetting in order to not disturb the meniscus for a final caffeine concentration of 10 mM and recorded for a further 1 minute. After caffeine addition no further recordings were taken as spontaneous Ca^{2+} release was impaired due to depletion of stores.

4.3 Results

4.3.1 R1051 mutation desynchronises spontaneous hRyR2-mediated Ca^{2+} release from HEK293 cells.

HEK293 cells display spontaneous Ca^{2+} release events when expressing hRyR2 and provided with supplemental external Ca^{2+} (in the form of KRH buffer) that they do not otherwise exhibit when not expressing hRyR2 (Jiang et al. 2004). This makes them a good system to assess the function of RyR2 on the whole cell level and characterise the effect of mutations on Ca^{2+} release from the main intracellular Ca^{2+} store.

Analysis of traces revealed that the morphology of spontaneous Ca^{2+} transients from each mutant was markedly different than the WT. Ca^{2+} transients produced by cells transfected with WT-hRyR2 tended to display a sharp rise to the peak and a sharp gradient back to the baseline (**Figure 4.3**). All three mutants gave transients with a slower rise to the peak; in R1051P this is a steady gradient leading to a bell-curve shaped transient, whereas in R1051C and R1051H there tends to be a very gentle slope before a sharp rise (**Figure 4.3**). In-depth analysis of the characteristics of transients produced by each construct is shown in **Figure 4.4**. Data were non-normally distributed and normality was not achieved by transformation (Logarithmic transformation (log(y)), square root transformation (√2), reciprocal transformation (1/y)) (**Appendix VI**). Statistical analyses were performed by Kruskall-Wallis test with Dunn's post-hoc analysis in GraphPad Prism 10.1.2 and are shown in **Table 4.1**.

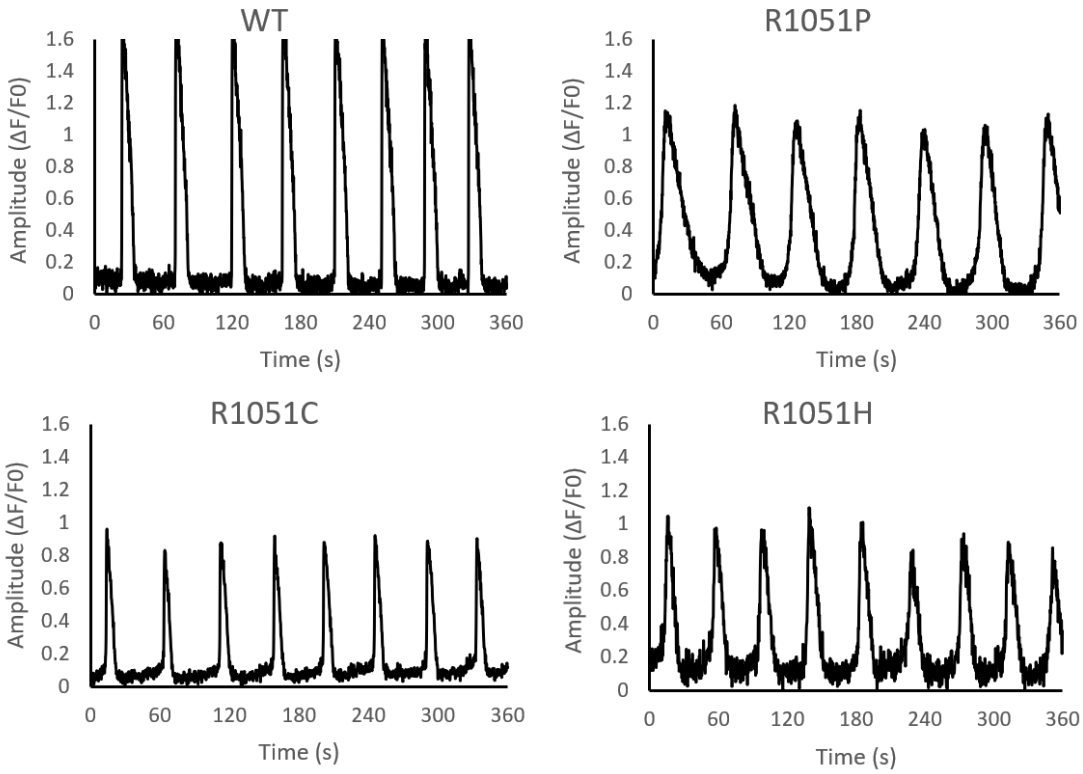

Figure 4.3. Representative traces of spontaneous Ca^{2+} release events in HEK293 cells transfected with WT or R1051-mutant hRyR2 show different morphologies. Examples of common features seen in Ca^{2+} transients for each construct when expressed in HEK293 cells and given supplemental extracellular Ca^{2+}; traces are representative and not averaged. A small degree of Ca^{2+} alternans is observed in the R1051H representative trace, with transients of varying amplitude.

Table 4.1. Median values for all Ca^{2+} imaging parameters in HEK293 cells show significant differences between WT-hRyR2 and R1051-mutant hRyR2. Parameters are calculated as stated in **Section 4.2.3**. Values represent the median (interquartile range (IQR)). Values in blue show a statistically significant decrease compared to the WT; pink indicates a significant increase. Calculated by Kruskall-Wallis statistical tests and Dunn's post-hoc analysis. P ≤ 0.05 = *, p ≤ 0.01 = **, p ≤ 0.001 = ***, p ≤ 0.0001 = ****. WT n = 644, R1051P n = 204, R1051C n = 357, R1051H n = 444.

	WT	R1051P	R1051C	R1051H
Frequency	1.40 (0.86)	1.22 (0.75)****	1.30 (0.79)**	1.36 (0.99)
Amplitude	1.09 (0.67)	0.82 (0.68)****	0.69 (0.57)****	0.64 (0.52)****
Duration	17.25 (6.09)	20.13 (9.63)****	20.32 (7.86)****	19.50 (7.87)****
ITI	18.23 (15.34)	18.11 (15.42)	16.32 (12.78)	16.62 (14.44)
Rise Rate	0.182 (0.15)	0.077 (0.067)****	0.055 (0.059)****	0.062 (0.050)****
Fall Rate	0.069 (0.035)	0.053 (0.054)****	0.043 (0.039)****	0.042 (0.031)****

Compared to WT RyR2, all three R1051-mutants caused significant changes to the amplitude, duration, rise rate and fall rate of Ca^{2+} release events (**Table 4.1**; **Figure 4.4**). Cells expressing R1051-mutant hRyR2 resulted in a lower amplitude, longer duration, and slower rise and fall rate compared to WT-hRyR2. R1051P and R1051C also had a significantly lower frequency of transients than WT (**Figure 4.4**). R1051C and R1051H were not significantly different from each other for any parameter measured, however R1051P was significantly different compared to R1051C and R1051H for some parameters (**Figure 4.4**). The other parameter considered was ITI; ITI was not significantly different under any comparison.

From these results (**Figure 4.4**) it is clear that, due to the large sample size, even very small changes are considered significant by statistical analysis, however these very small but significant changes may not represent functional significance. For example, while the frequency of Ca^{2+} transients was significantly lower in R1051C compared to the WT (p-value <0.05), this only represents a 7.1% decrease in the median. This is a smaller percentage decrease than some of the non-significant comparisons made, such as the ITI of R1051H compared to the WT which produced an 8.8% decrease in the median. Conversely, some comparisons saw a very large percentage change from the WT, such as a 65.9% decrease in rise rate for R1051C compared to the WT. For this reason, 95% confidence intervals (CIs) were calculated to give an indication of the precision and magnitude of differences between mutants and the WT (**Table 4.2**), and to assess the functional relevance of statistically significant findings. Overlapping CIs were interpreted as indicating potentially limited practical effect even where results were statistically significant, whereas non-overlapping CIs were taken to suggest a meaningful difference between groups. The 95% CIs of R1051P, R1051C and R1051H all overlapped the WT for the frequency of events and the ITI indicating that, despite R1051P and R1051C having a significantly reduced frequency compared to the WT, this might represent a relatively small change in practical terms. The CIs of all three mutants for duration, amplitude, rise rate and fall rate of transients did not overlap the WT (**Table 4.2**) and suggest that the changes observed represent a practical effect, which was accompanied by statistical significance in all cases (**Figure 4.4**).

Variation between Ca^{2+} release events on a cell-to-cell basis is to be expected, however some cells exhibited behaviours that did not fit a normal Ca^{2+} release profile of equally

spaced and equal amplitude transients. All hRyR2 variants, including the WT, produced some abnormal traces with these characteristics, all of which were excluded from the analysis on the basis that they could not be accurately quantified by the software. Abnormal transients were analysed further in **Section 4.3.2**.

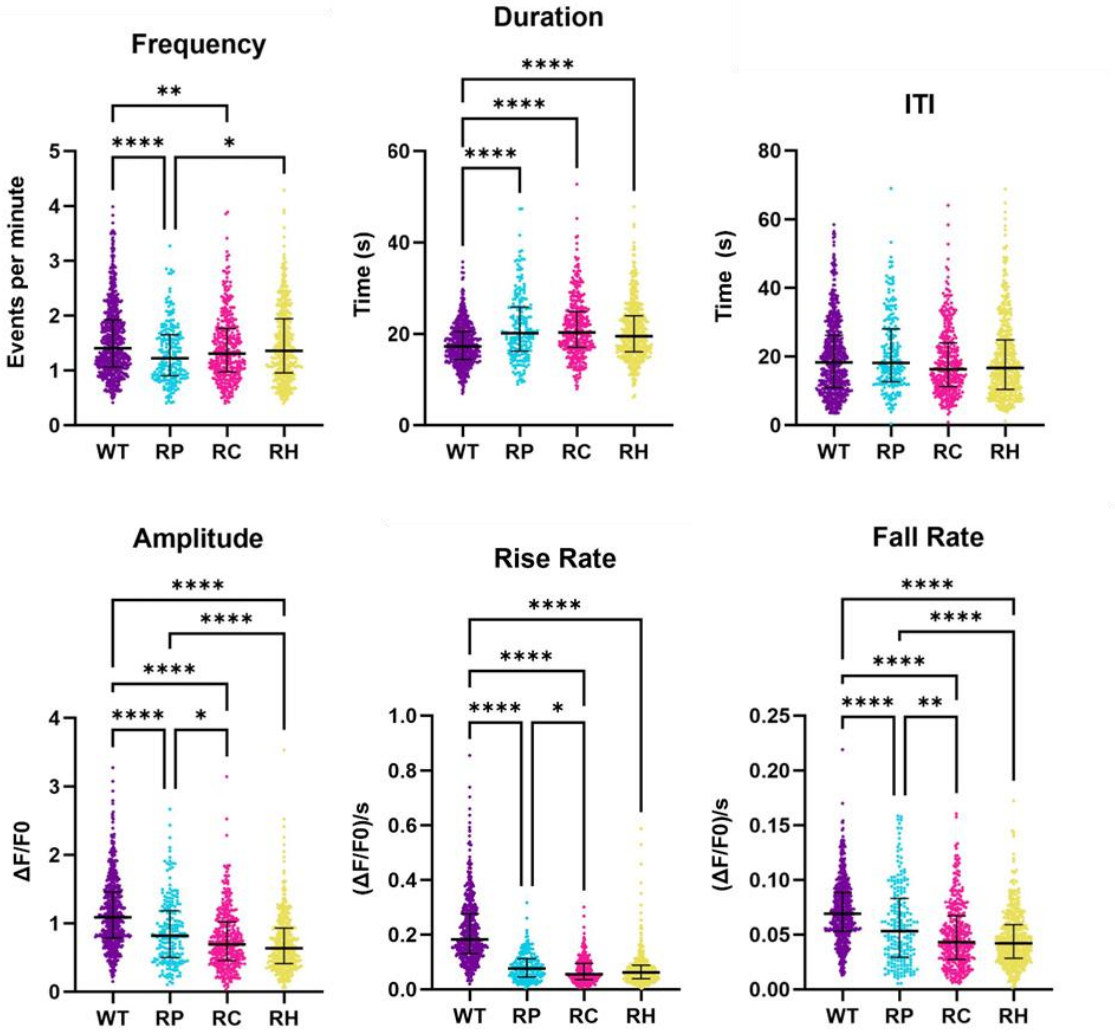

Figure 4.4. Quantification of Ca^{2+} transients produced by HEK293 cells transfected with WT or R1051-mutant hRyR2 show significant differences between all mutants and the WT. Parameters are calculated as stated in **Section 4.2.3**. Results indicate that all R1051 mutants are significantly different from the WT in their duration, amplitude, rise rate and fall rate, and both R1051P and R1051C are significantly different in the frequency of transients. Data were non-normally distributed and statistical significance was calculated by Kruskall-Wallis and Dunn's post-hoc analysis in GraphPad Prism 10.1.2; $p \leq 0.05$ = *, $p \leq 0.01$ = **, $p \leq 0.001$ = ***, $p \leq 0.0001$ = ****. Error bars indicate the median ± IQR. WT n = 644, R1051P n = 204, R1051C n = 357, R1051H n = 444.

Table 4.2. Confidence intervals indicate that altered Ca^{2+} transient characteristics due to mutation at R1051 likely represent practical changes in hRyR2 function. The upper and lower 95% CI represent the range between which the true population parameter (i.e. median) is expected to fall with 95% confidence based on the sample. Median values indicated in bold are significantly different from the WT based on the Kruskall-Wallis test with Dunn's post hoc (p-value < 0.05). Blue cell shading indicates upper and lower CIs that do not overlap with the WT CIs, indicating a practical difference in results. Based on this, the altered duration, amplitude, rise rate and fall rate of Ca^{2+} transients in R1051P, R1051C and R1051H are likely a relevant practical effect of mutation. CIs calculated in GraphPad Prism 10.1.2.

		WT	R1051P	R1051C	R1051H
Frequency	**Median**	1.404	**1.223**	**1.304**	1.356
	Lower CI	1.327	1.101	1.197	1.269
	Upper CI	1.504	1.361	1.389	1.438
Duration	**Median**	17.25	**20.13**	**20.32**	**19.5**
	Lower CI	16.89	19.12	19.58	18.75
	Upper CI	17.68	20.7	21.45	20.26
ITI	**Median**	18.23	18.11	16.32	16.62
	Lower CI	16.38	16.52	15	14.9
	Upper CI	19.35	20.06	17.75	17.59
Amplitude	**Median**	1.089	**0.8173**	**0.6935**	**0.6361**
	Lower CI	1.034	0.7476	0.6362	0.5821
	Upper CI	1.124	0.881	0.7406	0.6746
Rise Rate	**Median**	0.1823	**0.0765**	**0.0552**	**0.0620**
	Lower CI	0.1733	0.0659	0.0521	0.0566
	Upper CI	0.1942	0.0838	0.0619	0.0670
Fall Rate	**Median**	0.0690	**0.0532**	**0.0431**	**0.0421**
	Lower CI	0.0662	0.0455	0.0403	0.0391
	Upper CI	0.0714	0.0600	0.0477	0.0450

4.3.2 Aberrant Ca^{2+} release is increased in R1051-mutant hRyR2

Ca^{2+} transient abnormalities are associated with dysregulated Ca^{2+} release and can be causative of arrhythmia (Lehnart et al. 2006; Wehrens 2007; Landstrom et al. 2017b). All hRyR2 variants showed some abnormal transient behaviours that did not fit a regular pattern of Ca^{2+} transient oscillation such as is shown in **Figure 4.3** and were excluded from the main analysis (see below for in depth description of different abnormalities). All three mutants had a significantly higher proportion of abnormal Ca^{2+} transient traces than the WT traces (**Table 4.3**) indicative of severe dysfunction.

Table 4.3. HEK293 cells transfected with R1051-mutant hRyR2 show an increased number of Ca^{2+} transient abnormalities compared to WT-hRyR2. Cells were considered 'Normal' if they displayed a regular Ca^{2+} transient morphology even if they could not be correctly analysed; this includes cells where too few transients were present to calculate parameters, cells with missing calculations, and cells that were incorrectly analysed by the MatLab applet. Abnormal cells were any cells that showed transients with irregular morphologies. Logistic regression was used to analyse the relationship between hRyR2 variant and transient abnormality, and all R1051-mutants were found to have a higher likelihood of producing abnormal transients (WT – R1051P odds ratio (OR) = 0.186, $p < 0.0001$, WT – R1051C OR = 0.216, $p < 0.0001$, WT – R1051H OR = 0.335, $p < 0.0001$). Statistical analysis was performed in RStudio (RStudio Team, 2019).

	Normal	Abnormal	Total	% Total
WT	1025	152	1177	**12.9%**
R1051P	446	356	802	**44.4%**
R1051C	951	653	1604	**40.7%**
R1051H	1232	545	1777	**30.7%**

Abnormal traces from live cell Ca^{2+} imaging were excluded from the main dataset if they presented with one or more of the abnormalities listed below (Penttinen et al. 2015; Pölönen et al. 2018).

- *Amplitude variation* (**Figure 4.5A**) – Characterised by consecutive transients varying in amplitude by greater than ~25% of the mean for that particular trace; includes both increasing or decreasing amplitude over time, and variability transient-to-transient.
- *Repeated amplitude variation* (**Figure 4.5B**) – Characterised by repeated and regular variation in amplitude, e.g. 3 low amplitude transients followed by 1 high amplitude

transient followed by 3 low amplitude transients, repeated. This includes traces where at least one full cycle of this behaviour was observed.

- *Shoulder variation* (**Figure 4.5C**) – Characterised by lower amplitude transients that adjoin directly to a larger transient; in some cases, the shoulder forms a more defined peak but still appears adjoined to the main larger transient.
- *Irregular* (**Figure 4.5D**) – Characterised by variation in ITI such that the transients appear out of phase.
- *Extended* or *Plateau* (**Figure 4.5E**) - Characterised by very long duration transients, often with other shorter duration transients present or adjoined, or by transients that appear to plateau before returning to the baseline. Often observed with other abnormalities.
- *Double Peak* (**Figure 4.5F**) – Characterised by a secondary peak of same or similar amplitude to main transients. Often observed with other abnormalities.
- *Multiple* (**Figure 4.5F**) – Where multiple abnormalities are present or where trace did not fit any of the above categories, e.g. Irregular transient intervals were often accompanied by variation in amplitude.

Traces were categorised based on the main abnormalities observed (**Figure 4.5**). The distribution of abnormalities varied significantly between all four hRyR2 variants (Chi-squared test for homogeneity, $X^2 = 176.03$, degrees of freedom (df) = 18, n = 1034, $p<0.0001$). All three R1051-mutants had a significantly different distribution to the WT (Chi-squared test with pairwise comparisons and Bonferroni correction; WT – R1051P $X^2 = 56.703$, df = 6, $p < 0.0001$; WT – R1051C $X^2 = 90.113$, df = 6, $p < 0.0001$; WT – R1051H $X^2 = 75.281$, df = 6, $p < 0.0001$), and R1051P also had a significantly different distribution to R1051C and R1051H (R1051P – R1051C $X^2 = 71.275$, df = 6, $p < 0.0001$; R1051P – R1051H $X^2 = 63.887$, df = 6, $p < 0.0001$;) (**Table 4.4**) .All mutants showed an increased number of amplitude abnormalities as a proportion of the various abnormality subtypes, and R1051P showed an increase in the number of traces with multiple abnormalities. Cells expressing WT-hRyR2 showed a higher proportion of repeated, shoulder, and irregular abnormalities, however as a proportion of the total number of traces analysed (both abnormal and normal) these were found at a comparable rate in the mutants.

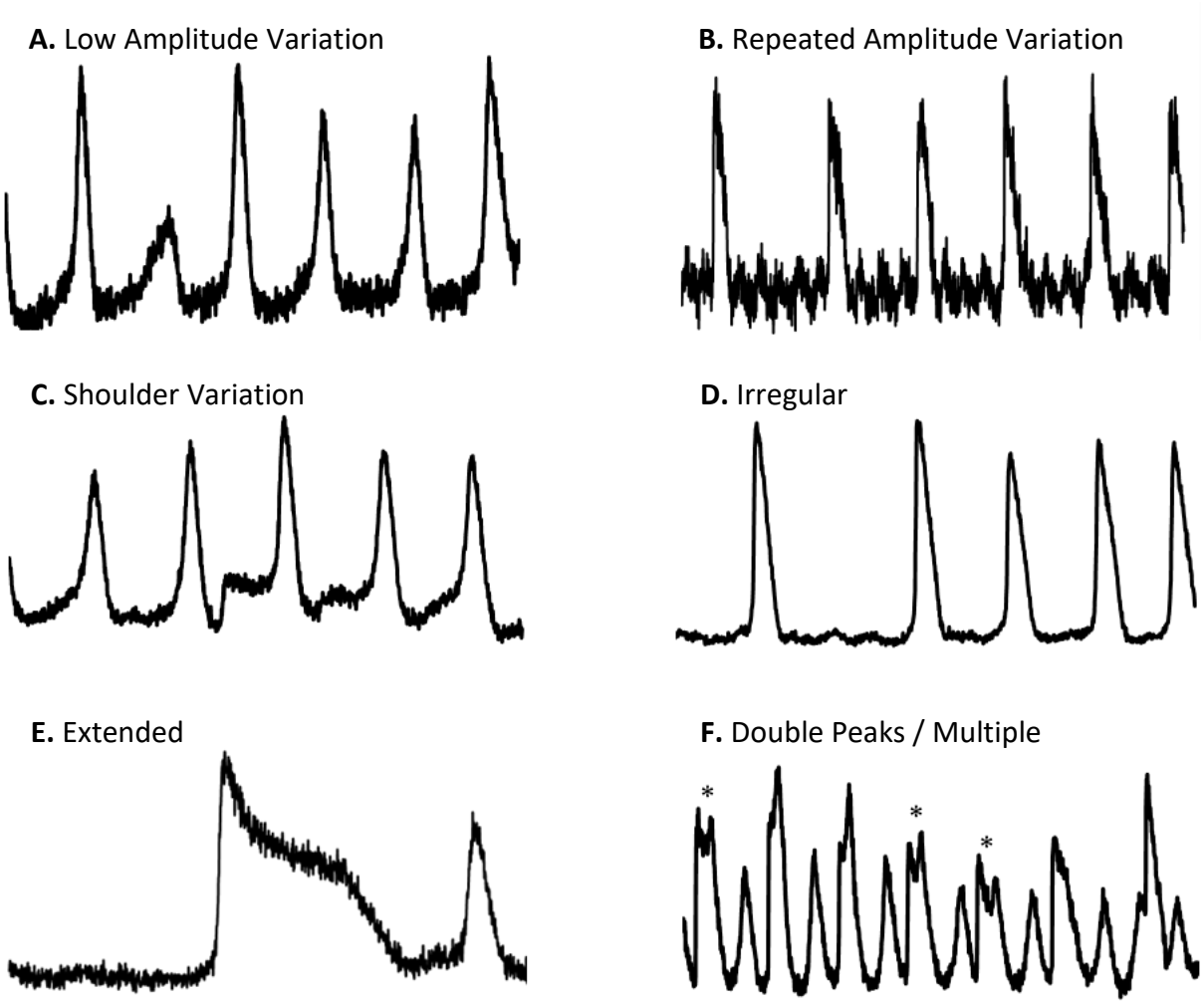

Figure 4.5. Examples of aberrant Ca^{2+} release traces from HEK293 cells expressing WT or R1051-mutant hRyR2. A-E. Examples of individual abnormalities seen in HEK293 cells expressing recombinant hRyR2. **F**. An example of double peaks (indicated by *) in addition to multiple other abnormalities (low amplitude peaks; shoulders); traces such as this were classified as having multiple abnormalities.

Table 4.4. The distribution of Ca^{2+} transient abnormalities is different in HEK293 cells transfected with R1051-mutant hRyR2 compared to WT-hRyR2. Counts relate to the total number of traces classified as the given abnormality type for each variant; the % values in black are relative to the total number of abnormal traces for that variant; the % value in red is relative to the total number of traces overall (normal + abnormal; WT n = 1177 traces, R1051P n = 802, R1051C = 1604, R1051H n = 1777). There was a significant difference in the distribution of abnormalities between hRyR2 variants (Chi-squared test for homogeneity, $X^2 = 116.01$, degrees of freedom (df) = 18, n = 1034, $p<0.0001$), and when pairwise comparisons were made, all comparisons were found to have a significantly different distribution except R1051C – R1051H (WT – R1051P $X^2 = 35.129$, df = 6, $p < 0.0001$; WT – R1051C $X^2 = 57.817$, df = 6, $p < 0.0001$; WT – R1051H $X^2 = 48.598$, df = 6, $p < 0.0001$, R1051P – R1051C $X^2 = 54.483$, df = 6, $p < 0.0001$; R1051P – R1051H $X^2 = 38.967$, df = 6, $p < 0.0001$, R1051C – R1051H $X^2 = 4.953$, df = 6, $p = 0.5499$). WT n = 152, R1051P n = 365, R1051C n = 653, R1051H n = 545. Statistical analysis was performed in RStudio.

		WT	R1051P	R1051C	R1051H
Abnormality	Amplitude	37 (24.3% / 3.1%)	119 (33.4% / 14.8%)	332 (50.8% / 20.7%)	296 (54.3% / 16.7%)
	Repeated	11 (7.2% / 0.9%)	3 (0.8% / 0.4%)	36 (5.5% / 2.2%)	22 (4.0% / 1.2%)
	Shoulder	32 (21.1% / 2.7%)	24 (6.7% / 3.0%)	56 (8.6% / 3.5%)	49 (9.0% / 2.8%)
	Irregular	30 (19.7% / 2.6%)	45 (12.6% / 5.6%)	24 (3.7% / 1.5%)	32 (5.9% / 1.8%)
	Extended	5 (3.3% / 0.4%)	33 (9.3% / 4.1%)	36 (5.5% / 2.2%)	35 (6.4% / 2.0%)
	Double	4 (2.6% / 0.3%)	3 (0.8% / 0.4%)	5 (0.8% / 0.3%)	3 (0.6% / 0.2%)
	Multiple	33 (21.7% / 2.8%)	129 (36.2% / 16.1%)	164 (25.1% / 10.2%)	108 (19.8% / 6.1%)
	Totals	152 (100% / 12.9%)	356 (100% / 44.4%)	653 (100% / 40.7%)	545 (100% / 30.7%)

4.3.3 Caffeine response of R1051-mutant hRyR2 is impaired and SR Ca^{2+} load is reduced

HEK293 cells expressing functional hRyR2 channels release Ca^{2+} from intracellular stores in response to the addition of caffeine (10 mM), an RyR2 agonist that sensitises the channel to Ca^{2+} activation and therefore increases channel P_O and Ca^{2+} release (Sitsapesan and Williams 1990; Kong et al. 2008) which manifests as a caffeine-induced Ca^{2+} transient (**Figure 4.6**). Caffeine-induced Ca^{2+}-release is used as a measure of ER Ca^{2+} load, as it triggers emptying of the intracellular store and therefore the increase in fluorescent signal from Ca^{2+} binding to the Ca^{2+}-sensitive dye is proportional to the store load.

The caffeine response of cells expressing R1051-mutant hRyR2 was significantly altered compared to WT-hRyR2 (**Figure 4.7**). When comparing all cells subjected to caffeine addition, HEK293 cells expressing R1051P, R1051C or R1051H-hRyR2 produced a peak of significantly smaller amplitude than those expressing WT-hRyR2 (**Figure 4.7A**), showing that all R1051-mutants have a significantly decreased ER Ca^{2+} store load compared to the WT.

Cells were subdivided into cells that oscillated prior to caffeine addition and those that did not. The proportion of oscillating cells relative to the total number of caffeine-responding cells was 51.4% for the WT, 47.8% for R1051P, 55.6% for R1051C and 54.9% for R1051H. For cells that oscillated prior to caffeine addition, both R1051P and R1051H produced caffeine-induced transients that were significantly smaller than both the WT and R1051C (**Figure 4.7B**). For cells expressing R1051P and R1051H the caffeine-induced transient was often indistinguishable from normal Ca^{2+} transients appearing comparable to the preceding transients in amplitude followed by a steady return to the baseline. In non-oscillating cells, R1051P and R1051H produced caffeine-induced transients of a significantly smaller amplitude than the WT, and caffeine-induced transients from R1051H were also significantly lower amplitude than those of R1051C (**Figure 4.7C**). The mean amplitude of caffeine-induced transients was significantly lower in oscillating cells than non-oscillating cells for all hRyR2 variants (**Figure 4.7D**).

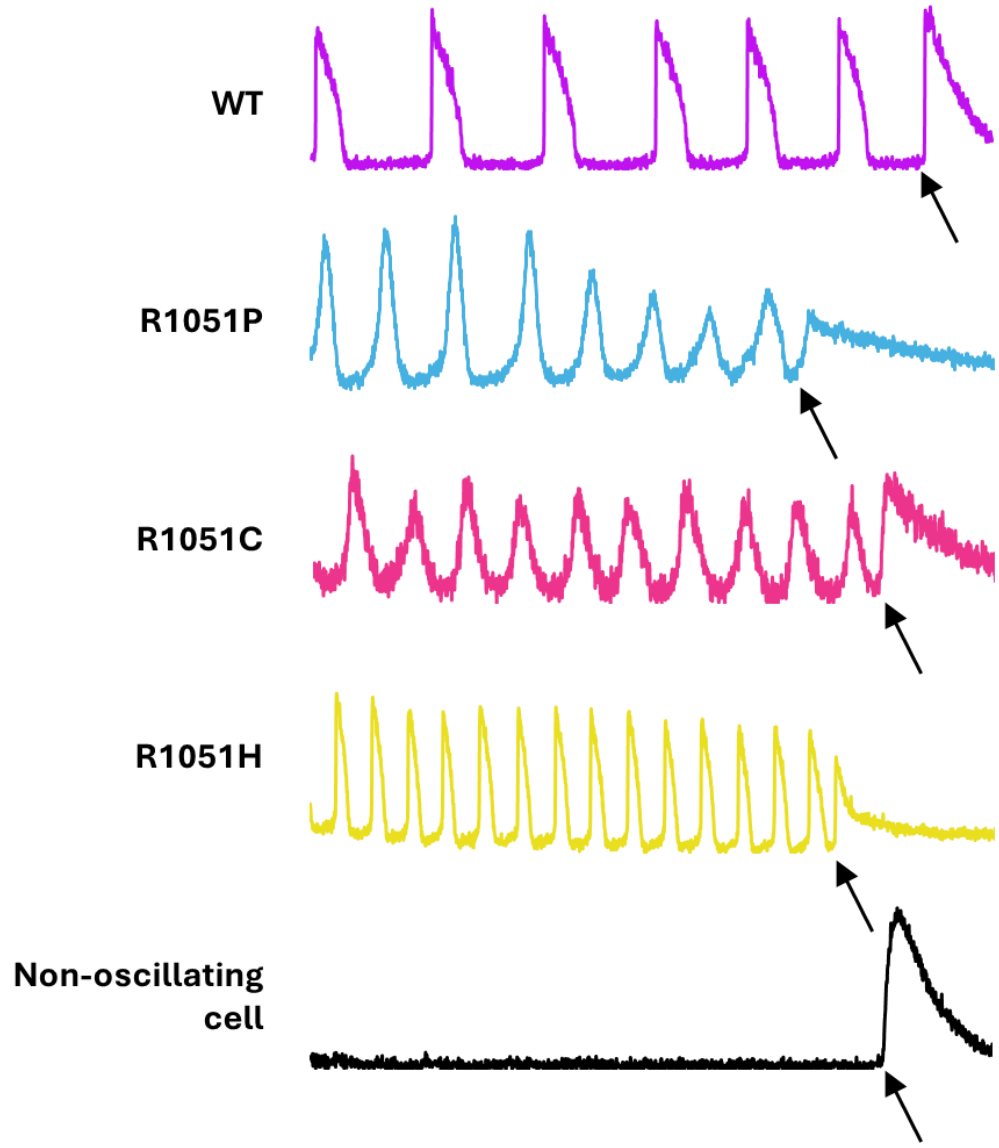

Figure 4.6. Representative example of caffeine-induced Ca^{2+} release in HEK293 cells expressing R1051-mutant hRyR2 or WT-hRyR2. Representative examples of the caffeine-induced transient in oscillating cells demonstrate impaired caffeine response of mutants, particularly R1051P and R1051H. The morphology of caffeine-induced transients in non-oscillating cells was comparable between all RyR2 variants. Black arrows indicate the point of caffeine addition.

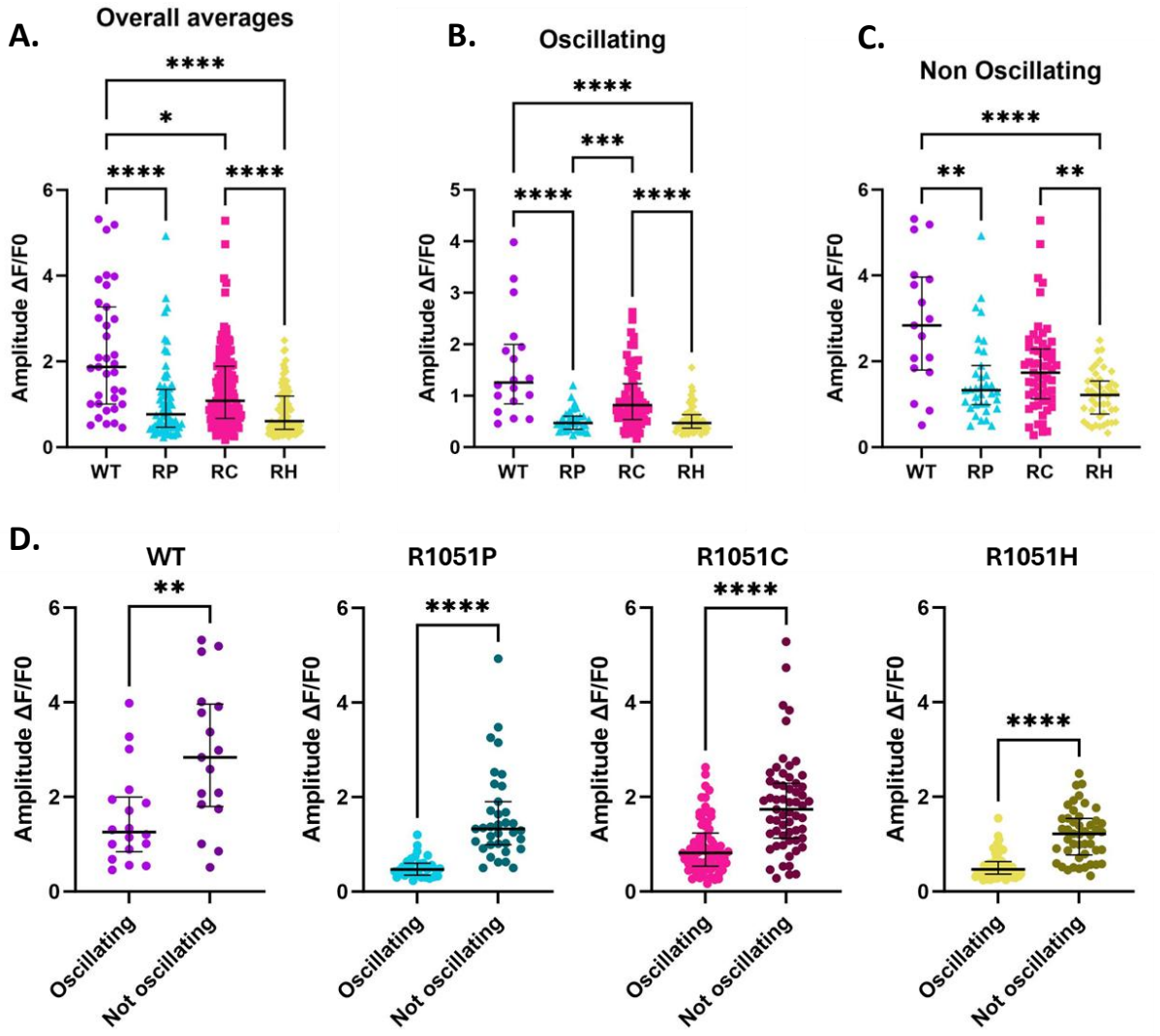

Figure 4.7. HEK293 cells expressing R1051P and R1051H-hRyR2 have an impaired response to caffeine activation and a lower ER Ca^{2+} load. A. Comparison of caffeine-induced transients across all cells shows that R1051P, R1051C and R1051H all produce significantly smaller transients than WT-hRyR2. **B.** Comparison of non-oscillating cells only. **C.** Comparison of oscillating cells only. **D.** Comparison for each variant of oscillating vs non-oscillating cells. Statistical analysis was performed in GraphPad Prism 10.1.2; test applied for A-C was Kruskall-Wallis test with Dunn's post hoc, and D used Mann-Whitney test; $p \leq 0.05$ = *, $p \leq 0.01$ = **, $p \leq 0.001$ = ***, $p \leq 0.0001$ = ****. WT oscillating/non-oscillating n = 18 / 17, R1051P n = 32 / 35, R1051C n = 74 / 59, R1051H n = 56 / 46. Error bars show median ± IQR.

4.4 Discussion

4.4.1 R1051 mutations result in slower Ca^{2+} release kinetics that may indicate Ca^{2+} leak

Live cell Ca^{2+} imaging has revealed that all three R1051 mutants of RyR2 display highly abnormal spontaneous Ca^{2+} release, with significantly increased duration and decreased amplitude, rise and fall rate of transients, R1051P and R1051C also resulted in a significantly reduced frequency of transients (**Figure 4.4**; **Table 4.1**), as well as altered caffeine-induced Ca^{2+} release that indicates a decreased ER Ca^{2+} store load (**Figure 4.7**). These changes to the Ca^{2+} transients indicate an overall slowing of the kinetics of Ca^{2} release and decreased store load that points to potentially severely impaired Ca^{2+} release function, as slowed Ca^{2+} release kinetics have been reported extensively in association with both HF and arrhythmia (Hasenfuss et al. 1994; Hasenfuss and Pieske 2002; Wehrens et al. 2005; Wehrens 2007; Kolstad et al. 2018). Regarding HF, multiple studies have reported a decreased amplitude of Ca^{2+} transients associated with this condition (Yao et al. 1998; Marx et al. 2000; Jiang et al. 2002b; Lehnart et al. 2004b; Kubalova et al. 2005) and increased duration of release (Kubalova et al. 2005). Several have cited impaired reuptake of Ca^{2+} into the SR as a primary cause (Gómez et al. 2001; Jiang et al. 2002b; Kubalova et al. 2005), with some demonstrating that inhibition of SERCa by PLB or downregulation of SERCa lowers Ca^{2+} transient amplitude by reducing the amount of Ca^{2+} available to RyR2 in the SR lumen (Gómez et al. 2001; Jiang et al. 2002b). Increased Ca^{2+} leak via RyR2 (potentially as a product of PKA hyperphosphorylation (**Section 1.4.1**)) also leads to the slowing of transient kinetics, as the Ca^{2+} load of the SR is reduced leading to slower Ca^{2+} spark kinetics and de-synchronization of global release dynamics (Marx et al. 2000; Wehrens et al. 2006; Wehrens 2007; Kolstad et al. 2018). Ca^{2+} leak is heavily implicated in the generation of arrhythmia (**Section 1.6.2.1**) (Venetucci et al. 2007; Wehrens 2007; Bers 2014; Landstrom et al. 2017b) and is also more tentatively linked to cardiomyopathies like DCM and HCM, with growing evidence that the functional changes associated with RyR2 GoF can result in structural remodelling (Fauconnier et al. 2011; Lan et al. 2013; Coppini et al. 2018; Souidi et al. 2024). This reflects in the altered morphology of Ca^{2+} transients produced by the R1051-mutants, all of which show a distinctly more drawn out Ca^{2+} release process than the WT (**Figure 4.3** and **4.4**).

Ca^{2+} leak is described as any Ca^{2+} release via RyR2 during diastole (Venetucci et al. 2007b; Bers 2014) and was initially attributed to hyperphosphorylation causing disassociation of FKBP12.6 resulting in destabilisation of the channel (**Section 1.4.1**) (Marx et al. 2000; Marx et al. 2001; Reiken et al. 2003) although the importance of FKBP12.6 binding on RyR2 function is highly debated (**Section 1.5.1**). Regardless of the exact mechanism, Ca^{2+} leak is identified as a leading cause of dysfunction in RyR2 GoF mutations and can occur on multiple levels; a smaller scale 'silent' or 'quarky' Ca^{2+} leak (Lipp and Niggli 1996; Brochet et al. 2011), and a larger scale leak from spontaneous Ca^{2+} sparks. In both of these cases, intracellular stores are constantly depleted by persistent Ca^{2+} leak, resulting in slower Ca^{2+} spark kinetics and decreased SR Ca^{2+} load. Slower kinetics of Ca^{2+} release have also been implicated in DCM (via E3DS) and HCM (A1107M and P1124L) (Tang et al. 2012; Alvarado et al. 2019). Interestingly, these mutations are associated with LoF (A1107M) or a dual LoF / GoF phenotype (E3DS and P1124L), with slower kinetics tied to an increased threshold for activation (slower rise rate) and abnormal termination (slower fall rate) (Tang et al. 2012; Alvarado et al. 2019). However, LoF mutations typically increase the store load as SOICR is not so easily triggered (which also decreases Ca^{2+} leak) and therefore, in light of the significantly decreased store load observed here (**Figure 4.7**), LoF leading to slower kinetics is not a likely mechanism in R1051-mutants. Overall, this strongly indicates that Ca^{2+} leak may be responsible for the dysfunction of spontaneous Ca^{2+} release in R1051-mutant hRyR2.

An alternative cause of slowed transient kinetics is reuptake of Ca^{2+} into the SR by SERCa2a, which pumps Ca^{2+} from the cytosol into the SR. SERCa is inhibited by PLB, and PLB is in turn regulated by PKA and CaMKII phosphorylation which results in decreased inhibition of SERCa. SERCa1a is the skeletal isoform of SERCa and is expressed in HEK293 cells (Tong et al. 1999a; Tong et al. 1999b), however PLB is not expressed in HEK293 cells (Toyofuku et al. 1994; Kimura et al. 1996; Asahi et al. 2003). SERCa1a expression was not assessed in this study, so the possibility that this is altered due to transient expression of R1051-mutant-hRyR2 cannot be confirmed. Few studies have sought to assess this when characterising RyR2 mutations, potentially due to the relatively limited amount of time for cellular remodelling to occur when performing a transient expression of RyR2 (in this case in HEK293). Using this method, cells are imaged at approximately 36 to 48 hours after

transfection (**Section 4.2.2**), which is slightly longer than the average doubling time of HEK293 cells (33 hours (Abaandou et al. 2021)), therefore imaging occurs in a time frame that could facilitate some degree of cellular remodelling. The most comprehensive study that has assessed SERCa expression in response to several ARVD2-linked RyR2 mutations mutation found no significant difference in its expression; however it should be noted that ER Ca^{2+} load was also unaffected in these mutants (Thomas et al. 2005). Given the R1051-mutants do affect ER Ca^{2+} load based on their caffeine-induced Ca^{2+}-release (**Figure 4.7**), it would be beneficial to assess SERCa expression to determine whether this may be impacting store load and therefore Ca^{2+} release from RyR2.

Working on the assumption that SERCa expression and function are not affected by transient expression of R1051-mutant hRyR2, this would point to Ca^{2+} leak as the likely leading cause of the altered global Ca^{2+} release observed in this study (**Figure 4.4**). When considering how this might arise, it is important to consider that FKBP12.6 is not expressed in HEK293 cells and therefore changes in its interaction with RyR2 cannot be the cause for the difference in Ca^{2+} release between the WT and R1051-mutant as suggested in one hypothesis of Ca^{2+} leak (Marx et al. 2000; Wehrens et al. 2004a). FKBP12 is expressed HEK293 cells, although its affinity for RyR2 is much lower and the contribution of both proteins to RyR2 function remains highly debated (**Section 1.5.1**) (Marx et al. 2000; Galfré et al. 2012a; Gonano and Jones 2017). Equally, hyperphosphorylation by PKA at S2808 does not appear to be a factor as phosphorylation at this site was not significantly altered in R1051-mutants (**Section 3.3.5**). It is possible that phosphorylation at other sites could contribute to Ca^{2+} leak in the R1051 mutants, namely S2814 and S2030, however this was beyond the scope of the current project and represents an avenue for future research. Among other causes, altered CaM binding (Guo et al. 2006), oxidation by ROS (Cooper et al. 2013; Hamilton et al. 2020) and domain unzipping (Oda et al. 2005; Uchinoumi et al. 2010a) have all been implicated in Ca^{2+} leak from RyR2 in CPVT and / or HF. This demonstrates that there may not be one unifying mechanism through which Ca^{2+} leak occurs and that many of these interconnected processes likely contribute.

One way in which RyR2 protects against Ca^{2+} leak is via clustering, which results in spatial separation of Ca^{2+} release to control propagation of CICR and potentially allows for coupled gating between channels (Stern 1992; Marx et al. 2001; Sobie et al. 2006) (**Section 1.2.4**).

For this reason, it was hypothesized that mutation of R1051, which is located in the P1 domain of RyR2 and is proposed to be involved in the clustering interaction (Cabra et al. 2016), could cause a conformational change that may impair the inter-tetramer interaction and affect both cooperativity of channels and cluster size. This is pertinent to Ca^{2+} leak as multiple studies have found a relationship between cluster size or density and diastolic Ca^{2+} release (Sobie et al. 2006; Asghari et al. 2014; Walker et al. 2014; Kolstad et al. 2018; Asghari et al. 2020). Several studies have demonstrated increased Ca^{2+} leak from smaller clusters (Sobie et al. 2006; Kolstad et al. 2018), whereas others have shown a tendency for 'silent' leak in small clusters compared to spark-based leak in larger clusters (Walker et al. 2014). This is thought to happen due to smaller clusters being less able to initiate a Ca^{2+} spark, leading to invisible Ca^{2+} leak (Kolstad et al. 2018). Cluster density is also an important factor in regulating Ca^{2+} release from RyR2, with several studies indicating a lower channel density (implying fewer inter-tetramer interactions) increases Ca^{2+} leak (Marx et al. 2000; Wehrens et al. 2006; Asghari et al. 2014; Asghari et al. 2020). In the case of the R1051-mutants, impaired inter-tetramer interactions that alter any allosteric interactions between channels or cause changes to cluster size or arrangement could result in pathological Ca^{2+} leak, that would lead to the slower kinetics of Ca^{2+} release observed here (**Figure 4.4**). This is discussed in more detail in **Chapter 5**.

Interestingly, in addition to showing significantly different kinetics of spontaneous Ca^{2+} release to the WT, there were also significant differences between the mutants. Notably, R1051P was significantly different from R1051C in the amplitude, rise rate and fall rate of transients, and was also significantly different from R1051H in the frequency, amplitude and fall rate of transients (**Figure 4.4**). R1051C and R1051H were not significantly different from each other in any of the spontaneous Ca^{2+} transient parameters. Regarding the difference in rise rate, there was notable difference in Ca^{2+} transient morphology that is visible by eye (**Figure 4.4**) that wasn't possible to pick up in data analysis (**Figure 4.4**; **Table 4.1**). R1051P generally showed a more consistent gradient up to the peak (rise rate), whereas R1051C and R1051H are more unevenly distributed, showing a slow start to Ca^{2+} release followed by a more rapid rise (**Figure 4.3**). It is possible that this is an indicator of the degree of dysfunction; cells expressing R1051C/H may struggle to initiate global Ca^{2+} release events but once initiated Ca^{2+} release may resume at a more typical pace to a (albeit lower

amplitude) peak. In R1051P however, the kinetics remain slow throughout, possibly indicating that even after many clusters have been activated and global Ca^{2+} concentrations have increased that there is still a lack of synchronisation between clusters. This does not appear to be a direct reflection of the ER Ca^{2+} store load as while R1051C and R1051H appear relatively similar in their transient morphology (**Figure 4.3**), the store load is more comparable between R1051H and R1051P (**Figure 4.7**), suggesting that this is not the only factor affecting their different morphologies. These results could be supplemented by further research using leak-load type experiments (Shannon et al. 2002) to determine whether a specific difference in ER Ca^{2+} leak is contributing to these variable results between mutants.

Despite the clear differences in Ca^{2+} transients observed during live cell imaging, one aspect that has not yet been considered is whether the total Ca^{2+} released during an individual event is lower in the mutants, and this could be assessed by looking at the area under the transient as opposed to amplitude and duration individually. While all R1051-mutants result in spontaneous Ca^{2+} release events of lower amplitude than WT, this occurs over a longer duration (**Table 4.1**) so it is possible that the total volume of Ca^{2+} released is more comparable between WT and R1051-mutant hRyR2 than the amplitude alone might suggest. This may reflect a reduced store load as the whole Ca^{2+} release and reuptake cycle becomes desynchronised by reduced availability of Ca^{2+} in the store, which as mentioned previously is an indicator of Ca^{2+} leak. It could also reflect a change in the gating mechanism of channels that results in longer open times and shorter closed times possibly as a result of increased sensitivity to Ca^{2+}, however this would require further research to confirm. In practice, calculating the area under the curve of a Ca^{2+} transient is mathematically complicated and is not a feature built into the Matlab applet used (**Section 4.2.3**), although several groups have more recently developed software that performs this analysis on Ca^{2+} transients (Hawey et al. 2023; Mozneb et al. 2024). Future analyses would benefit from calculating this parameter to better understand the full effect of the R1051 mutations on whole cell Ca^{2+} release.

4.4.2 Ca^{2+} transient abnormalities may indicate the mechanism of dysfunction in R1051-mutant hRyR2

In addition to displaying slower Ca^{2+} release kinetics than cells expressing WT-hRyR2, expression of each of the three R1051-mutants resulted in an increased number of cells

producing abnormal spontaneous Ca^{2+} release (**Figure 4.5**). Such abnormalities are widely reported to be a direct effect of Ca^{2+} leak and are strongly associated with arrhythmias (Lehnart et al. 2006; Wehrens 2007; Landstrom et al. 2017b), particularly the generation of DADs, EADs, and Ca^{2+} alternans (Lehnart et al. 2006; Xie and Weiss 2009). DADs are membrane depolarisations that occur during phase 4 of the cardiac AP cycle (diastole; **Section 1.1.2**) due to increased intracellular Ca^{2+} activating NCX and leading to an influx of Na^{+} (Priori and Corr 1990) that can trigger VT if the amplitude of the DAD is large enough (Priori et al. 2002). This arises due to SR Ca^{2+} overload (Rubenstein et al. 1993; Miura et al. 1999; Katra and Laurita 2005) resulting in spontaneous Ca^{2+} release from the SR (Marban et al. 1986; Boyden et al. 2000). EADs on the other hand are depolarisations that occur during phase 2 or 3 of the AP cycle (repolarisation; **Section 1.1.2**) (Marban et al. 1986; Priori and Corr 1990; Katra and Laurita 2005; Xie and Weiss 2009), and can also be triggered by spontaneous Ca^{2+} waves during Ca^{2+} overload of the SR (Xie and Weiss 2009; Zhao et al. 2012) as well as reactivation of LTCCs (Priori and Corr 1990; January and Moscucci 1992; Zhao et al. 2012). Finally, Ca^{2+} alternans is described as a beat-to-beat alteration in Ca^{2+} transient amplitude (Lehnart et al. 2006) that results in altered strength of cardiac contractions and is linked to VT (Lehnart et al. 2006; Weiss et al. 2006), atrial fibrillation (AF) (Hiromoto et al. 2005; Narayan et al. 2011), and SCD (Walker 2003).

DADs, EADs and alternans have all been linked to specific Ca^{2+} transient abnormalities which were observed in all hRyR2 variants analysed but were more common in the R1051-mutants compared to the WT (**Table 4.3**). Ca^{2+} alternans usually refers to regular beat-to-beat variation in Ca^{2+} transient amplitude but it is also applied more widely to other variations in transient amplitude (Lehnart et al. 2006). Overall, amplitude variations were the most frequent abnormality across all variants (**Table 4.4**), however there was much heterogeneity between traces of this classification. The most distinctive abnormality that is associated with Ca^{2+} alternans is the 'repeated amplitude' behaviour in which several small transients surround individual larger transients (Pölönen et al. 2018) (**Figure 4.5B**). This made up a higher proportion of abnormalities in cells expressing R1051C-hRyR2 (2.2% of all cells analysed) compared to WT (0.9%) and R1051H (1.2%) and was notably less prominent in R1051P (0.4%) (**Table 4.4**), although this represents a very small number of traces overall. Ca^{2+} transient alternans is associated with both LoF and GoF mutations in RyR2, however

the mechanism of generating alternans in each is different. For LoF mutations such as those that cause CRDS (**Section 1.6.4**), alternans arises due to low activity of RyR2 causing the store load to increase beyond its normal threshold (i.e. an increased threshold for Ca^{2+} activation) which results in a large Ca^{2+} transient (Sun et al. 2021). The store is then depleted for the next beat causing a smaller transient; this cycle repeats as the store refills and results in beat-to-beat alternans (Sun et al. 2021). In GoF mutations, alternans is associated with abnormal Ca^{2+} handling that desynchronises Ca^{2+} release, decreases channel refractoriness, depletes the store and reduces the amount of Ca^{2+} available to be released by a less regular mechanism (Xie et al. 2008; Xiao et al. 2016; Pölönen et al. 2020). This highlights an interesting paradox that Ca^{2+} alternans can present in both LoF and GoF mutations and does not indicate a defined way in which this could occur in R1051-mutants. It is also intriguing that this behaviour, while still a very small proportion of traces overall, is more frequently observed in cells expressing WT, R1051C and R1051H than R1051P. This could be a product of the higher rate of multiple abnormalities observed in R1051P (**Table 4.4**) but could also reflect a difference in function as R1051C and R1051H are associated with HCM and DCM in addition to CPVT, whereas R1051P has only been linked to CPVT; this is discussed further in **Section 4.4.3**.

DADs are also associated with lower amplitude Ca^{2+} transients (Kopljar et al. 2018; Pölönen et al. 2018), however there are subtle differences in the way these present. Ca^{2+} transients indicating DADs are thought to include less regular low amplitude transients (**Figure 4.5A**), shoulders on peaks (**Figure 4.5C**) or irregular phasing of transients (**Figure 4.5C**) (De Ferrari et al. 1995; Xie and Weiss 2009; Shinnawi et al. 2015; Pölönen et al. 2018), with these small out of phase increases in fluorescence representing diastolic Ca^{2+} release from the SR. Shoulder variation peaks made up a comparable proportion of the total number of traces for WT and all three mutants (2.7-3.5%), however as a proportion of all abnormality subtypes this was notably more common in the WT (21.1%) than all three mutants (6.7%-9%) (**Table 4.4**). Irregularly phased peaks were also a more common subtype in the WT at 19.7% compared to 12.6% for R1051P, and less than 6% for both R1051C and R1051H, but again when considered as a percentage of all traces analysed this is still a very small proportion (**Table 4.4**). Where the mutants stand apart from the WT is in the proportion of low amplitude transients, which accounted for between 14.8% and 20.7% of all transients

for the mutants compared to just 3.1% for WT (**Table 4.4**), and for R1051C and R1051H this subtype made up more than 50% of all abnormalities classified. As mentioned, this behaviour is linked to both DADs and Ca^{2+} alternans and the higher proportion observed in the mutants suggests it may be an important contributor to their resulting phenotypes.

EADs are best represented by extended transients and double peaks (**Figure 4.5E** and **4.5F**) (Xie and Weiss 2009; Kopljar et al. 2018; Pölönen et al. 2018; Prajapati et al. 2018). Double peaks were the least common abnormality across both WT and mutants, and extended transients, while still uncommon, were notably more frequent in cells expressing R1051P (**Table 4.4**). EADs are related to an extended duration of the AP and are heavily linked to long QT syndrome (LQTs) (Shimizu et al. 1991; El-Sherif and Turitto 1999; Lankipalli et al. 2005), which is characterised by a prolonged QT interval and can be caused by RyR2 mutation (Cai et al. 2022; Lv et al. 2025). However, there have been reports of patients being misdiagnosed with LQTs where subsequent genetic testing revealed CPVT as a more appropriate diagnosis (Priori et al. 2002; Tester et al. 2005; Medeiros-Domingo et al. 2009; Letsas et al. 2020) and several studies have identified EADs in CPVT cardiomyocytes (Kujala et al. 2012; Bezzerides et al. 2019; Pölönen et al. 2020). This is most notably associated with atypical CPVT due to LoF mutations (Zhao et al. 2015; Hirose et al. 2022) although others have indicated that diastolic Ca^{2+} release (i.e. GoF leak) can trigger EADs which may explain their occurrence in CPVT (Priori and Corr 1990; Xie and Weiss 2009). CRDS has also been shown to contribute to EADS and is exclusively associated with LoF (Sun et al. 2021; Hirose et al. 2022). Overall, this behaviour generally points towards RyR2 LoF which is a less common result of RyR2 mutation, however this accounts for only a small number of cells in this study and therefore may not represent a significant functional consequence of mutation.

There were also a large number of cells in which multiple Ca^{2+} transient abnormalities were detected, which makes pinning down precise mechanisms such as Ca^{2+} alternans or DADs / EADs difficult, but highlights the high degree of dysfunction in the R1051-mutants. These traces almost always included amplitude variations in addition to other abnormalities. This is most notable in R1051P in which more than 16% of all traces analysed demonstrated multiple abnormalities, which agrees with the hypothesis that the proline mutation is likely to be the most damaging to RyR2 function, likely due to its effect on protein secondary

structure. While this cannot be confirmed by live cell imaging, these results serve as a good starting point for probing the function of R1051-mutant hRyR2.

4.4.3 Altered Ca^{2+} release can contribute to the generation of cardiomyopathy

While these results demonstrate a similar effect on Ca^{2+} release from RyR2 due to the mutation of R1051 to either proline, cysteine, or histidine (**Figure 4.4**), the clinical data that identified these mutants, although inconclusive, suggests they have different phenotypes (**Section 1.7.1**). There are also subtle differences in their spontaneous Ca^{2+} release (**Figure 4.4**). All three mutants have been associated with CPVT via genetic testing to some degree (Marjamaa et al. 2009) and the alterations to whole cell Ca^{2+} release align well with the normal changes seen in arrhythmia-linked mutants (Venetucci et al. 2007; Wehrens 2007; Bers 2014; Landstrom et al. 2017b; Kolstad et al. 2018). However, R1051C has additionally been linked to HCM (Lopes et al. 2015) and R1051H to DCM (Pugh et al. 2014), indicating a broader role for R1051 mutation in cardiomyopathies.

While both HCM and DCM can arise from dysregulated Ca^{2+} handling due to changes in RyR2 function their effects are due to mostly opposing mechanisms (**Section 1.6.6** and **Section 1.6.7**). In general, in HCM dysfunction is characterised by impaired diastolic function leading to elevated cytosolic Ca^{2+} which triggers chronic activation of hypertrophic remodelling pathways like the calcineurin / NFAT pathways (Fatkin and Graham 2002; Robinson et al. 2007; Lan et al. 2013; Coppini et al. 2018). DCM on the other hand is characterised by impaired systolic function and reduced Ca^{2+} transients that result in hypocontractility of the myocyte (Robinson et al. 2007; Schultheiss et al. 2019; Souidi et al. 2024). Crucially, both of these effects can be caused by Ca^{2+} leak despite their different outcomes due to differences in the specifics of Ca^{2+} release such as the timing and magnitude of Ca^{2+} release events. This indicates a potential way by which R1051-mutants could cause these diseases, but it is unclear how the largely comparable spontaneous Ca^{2+} release profiles of the mutants would lead to such different phenotypes.

The most notable difference between R1051C and R1051H identified during live cell Ca^{2+} imaging was their caffeine-induced Ca^{2+} release, in which R1051H exhibits a more severely reduced store load compared to the WT than R1051C (**Figure 4.7**). As discussed, a reduced store load is an indicator of Ca^{2+} leak and is frequently associated in the literature with DCM both in RyR2 and in other proteins associated with DCM (Sun et al. 2012; Tang et al. 2012;

Liu et al. 2015; Dridi et al. 2021). However, the reduced store load of R1051H does not appear to manifest in the characteristics of spontaneous Ca^{2+} transients, as R1051H and R1051C were not significantly different from each other for any parameters (**Figure 4.4**). R1051H was also observed to produce fewer abnormalities than R1051C (**Table 4.3**), although the distribution of each abnormality type was very similar (**Table 4.4**). This raises the question of what the practical effect of a more depleted store in R1051H means. It could be that R1051H reduces the threshold for both the activation and termination of Ca^{2+} release from the ER to a greater extent than R1051C, resulting in an equivalent transient despite an overall lower store load. This combines some of the characteristics of DCM-associated E3DS, which reduced both the threshold for activation and termination of Ca^{2+} release but did not impact store load relative to the WT (Tang et al. 2012), and other DCM mutations in proteins such as PLB, troponin T, and LMNA which decreased the store load and increased Ca^{2+} leak (Sun et al. 2012; Liu et al. 2015; Dridi et al. 2021).

There are also other factors within the cell that might have an impact on the triggering of remodelling pathways but were not within the scope of this study. Increased CaMKII activity is heavily implicated in hypertrophic remodelling and driving HCM (Zhang and Brown 2004; Coppini et al. 2018; Lehman et al. 2019) and its activity might be affected differently in the R1051-mutants. This was the case in the HCM-associated P1124L-RyR2 mutation in which increased CaM expression was thought to play an important role in hypertrophy of this mutant in addition to direct effects of mutation on Ca^{2+} release from RyR2 (Alvarado et al. 2019). Alternatively, excess Ca^{2+} leak from R1051H that depletes the store could be compensated for by altered reuptake via SERCa, which might balance spontaneous Ca^{2+} release at the expense of a lower store load, although it is unclear why a similar mechanism might not rescue the aberrant behaviour of any mutation at R1051. There is also the possibility that other mutations were present in these patients that contribute to their resulting phenotypes; this is particularly pertinent for R1051H where multiple mutations in genes associated with DCM were identified (Pugh et al. 2014). This reinforces the complex nature of Ca^{2+} handling in cardiomyopathies and how conflicting mechanisms can lead to similar phenotypes, and vice versa.

4.4.4 Conclusions

Live cell Ca^{2+} imaging in HEK293 cells has revealed a significant dysfunction of R1051-mutant hRyR2 that leads to desynchronised and slower Ca^{2+} release with increased abnormalities compared to the WT, which could be due to increased Ca^{2+} leak. The hypothesis that this is due to Ca^{2+} leak is also supported by the decreased ER Ca^{2+} load of HEK293 cells expressing R1051-mutant hRyR2 and the increased number of Ca^{2+} transient abnormalities observed in these cells. This could arise from several mechanisms, including single channel dysfunction that increases the activity and open time of channels, or could be due to mutation altering communication between channels in a cluster which might impact the cooperativity of channels, but this is unclear from live cell Ca^{2+} imaging alone. Regardless, this serves as the first functional characterisation of Ca^{2+} release from these mutants and supports the hypothesis they have a damaging effect on cardiac function, although further investigation is needed to determine the mechanism behind their altered Ca^{2+} release.

Chapter 5

Investigating Ca^{2+} release from populations of R1051-mutant hRyR2 using droplet interface bilayers

5.1 Introduction

5.1.1 Analysing population function in droplet interface bilayers with total internal reflection fluorescence microscopy

Characterisation of RyR2 function at the single channel level is well established (**Chapter 6**) and likewise there are many ways RyR2 function can be probed on a larger scale, including measuring global Ca^{2+} release in whole cells (**Chapter 4**), assessing propagation of Ca^{2+} sparks, or using animal models. However, one of the biggest questions in RyR2 research is the question of coupled gating within clusters of RyR2. Coupled gating is proposed as a mechanism to control Ca^{2+} release via allosteric communication, and while it has been demonstrated in planar lipid bilayers (Marx et al. 2001; Ondrias and Mojzisová 2001; Gaburjakova and Gaburjakova 2008; Gaburjakova and Gaburjakova 2010; Porta et al. 2012), these experiments provide no spatial information and therefore no confirmation that this process is a product of clustering. Our understanding of the organisation of clusters has improved massively in recent years using super-resolution microscopy techniques in fixed cells (Baddeley et al. 2009; Shen et al. 2019), and recently live-cell super-resolution imaging using photo-activated localization microscopy (PALM) has been used to analyse Ca^{2+} spark propagation between clusters (Hou et al. 2023), however these techniques do not provide the simultaneous functional and spatial data needed prove coupled gating, or to bridge the gap between single channel Ca^{2+} release and spark generation. An emerging technique that may be able to answer this question is Droplet Interface Bilayers (DIB), which can be combined with Total Internal Reflection Fluorescence Microscopy (TIRF) to gather electrophysiological and optical data simultaneously (Leptihn et al. 2013).

The DIB system uses the ability of monolayers to spontaneously form bilayers on contacting another monolayer; this can be applied to two droplets contacting each other, or between a droplet and a planar hydrogel (Castell et al. 2012; Leptihn et al. 2013). The latter of these two techniques also allows the system to be mounted onto a TIRF microscope for detailed optical interrogation (Castell et al. 2012). This allows for the bilayer to be visualised and can facilitate single-molecule imaging of proteins embedded in the bilayer, which for RyR2 allows for measurement of Ca^{2+} flux using Ca^{2+} sensitive dyes (Castell et al. 2012). At the same time, electrophysiological recordings can be taken by inserting an electrode into the droplet, meaning single channel gating can be measured, albeit with a lower temporal

resolution and lower signal-to-noise ratio than single channel recording (Castell et al. 2012; Leptihn et al. 2013). This setup allows individual channels and populations of channels to be monitored optically for Ca^{2+} flux using TIRF, while electrical recordings taken at the same time can be used to measure activity.

DIBs are a minimal system in which the precise environment can be controlled and modified as needed and has the potential to add modulators to assess their effect on channel function. Both bilayer formation and channel incorporation (using solubilised and purified RyR2) are relatively straightforward compared to single channel recordings (**Chapter 6**), however the data obtained requires significant processing to extract meaningful insights about Ca^{2+} release behaviour from 2D fluorescent imaging. This is additionally complicated by the difficulty in aligning optical data with electrophysiological recordings, as imaging normally captures a small portion of the bilayer whereas electrophysiology captures the entire droplet.

Previous work by the group (Cumbes et al. *unpublished*) has spent considerable time optimising the system for monitoring Ca^{2+} flux optically from RyR2 and has laid the groundwork for assessing clustering and Ca^{2+} release from RyR2 populations by this method. DIB / TIRF allows for quantification of cluster size either via visualisation of eGFP on the hRyR2 construct (**Appendix VII**), or an estimate of the minimum number of active channels to be made based on a combination of electrophysiological readings and optical data. These foundations form the building blocks for assessing the relationship between the ability of RyR2 to form clusters and Ca^{2+} flux behaviour. In the context of this research, it will allow comparison of Ca^{2+} release behaviour from populations of WT and R1051-mutant hRyR2 and will indicate whether dysfunction of these mutants may be in part due to their effects on clustering dynamics.

5.1.2 Aims

The P1 domain of RyR2 is located on the corner of the RyR2 tetramer and is proposed to be involved in the clustering interaction (Cabra et al. 2016), which is a key regulator of RyR2 function. R1051 is located within the P1 domain and therefore may alter the ability of channels to form clusters or affect Ca^{2+} release from clusters. This research aims to assess WT and R1051-mutant hRyR2 (with a focus on R1051P-hRyR2) in the DIB / TIRF system to determine whether mutation affects the number of channels per cluster or their ability to

form, and to assess whether Ca^{2+} release from R1051-mutants differs at the population level. The primary aims of this chapter are to:

- Investigate the size of clusters formed spontaneously by hRyR2 in the DIB and TIRF system and determine whether R1051 mutants have altered cluster size compared to WT-RyR2.
- Assess function of populations of WT and R1051-mutant hRyR2 channels in the DIB system using Ca^{2+} flux behaviour measured optically using Ca^{2+}-reactive dyes and TIRF microscopy. Changes in Ca^{2+} release over time will be used to categorise different Ca^{2+} release behaviour patterns, and this will be correlated to cluster size. This will help indicate whether channels in a cluster behave cooperatively together, or whether their Ca^{2+} release behaviour is independent of other channels in the cluster.

5.2 Materials and Methods

5.2.1 Materials

- 7.5 mg/mL agarose – made up in Chelex-treated dH_2O. Chelex 100 resin chelates metal ions and was used to remove contaminant metal ions in buffers.
- 35 mg/mL agarose - made in buffer containing 0.33 M $CaCl_2$, 10 mM HEPES, pH 7.35, heated to 80°C; used in rehydrating agarose.
- 1,2-Diphytanoyl-sn-glycero-3-phosphocholine (DPhPC) (Avanti) – lipid used for droplet formation.
- Cal-590 sodium salt (AAT Bioquest) – stock of 50 mg/mL made up in Chelex-dH_2O.
- Nikon Eclipse TI microscope (Nikon Instruments) – used with a 60x TIRF objective

5.2.2 Droplet interface bilayers and total internal reflection fluorescence microscopy

A glass coverslip was cleaned in an oxygen environment in a plasma reactor to remove any contamination prior to mounting onto a vacuum spin coater. The coverslip was coated in 120 µL of 7.5 mg/mL agarose (made-up in Chelex-treated dH_2O) heated to 80°C and spun for 30 seconds, then placed on the bottom of a milled acrylic device so that the agarose contacts the device (substrate agarose in **Figure 5.1A**). The device itself consists of a block of acrylic, micro-milled to form wells that allow droplets placed into them to contact agarose on the bottom coverslip, and ports in which electrodes can contact the agarose (**Figure 5.1A**). The device was then placed on a heat block at 30°C and filled carefully with 170 µL 35 mg/mL agarose containing Ca^{2+} heated to 80°C (**Section 5.2.1**; rehydrating agarose in **Figure 5.1A**). A visual check under a light microscope was carried out to verify that the agarose had filled the device evenly. It was then secured over a hole in the bottom of a faraday cage that was placed on the microscope stage of the Nikon Eclipse TI microscope (Nikon Instruments). The device wells were filled with 8 mg/mL DPhPC in a mix of 60% hexadecane / 40% silicone oil, and a 1mm silver electrode connected to an Axopatch Amplifier was placed in one of the ports to contact the agarose; this electrode was held at ground (**Figure 5.1B**).

Droplet mixtures were made containing 10 µL KCl/HEPES buffer (1.5 M KCl, 10 mM HEPES, pH 7.35), 0.6 µL 50 mg/mL Cal-590, 0.6 µL 10 mM EDTA, 0.6 µL purified RyR2 protein (**Section 2.2.14**) (diluted 1:10 (WT, R1051P, R1051H) or 1:5 (R1051C) and 3.2 µL Chelex-treated dH_2O.

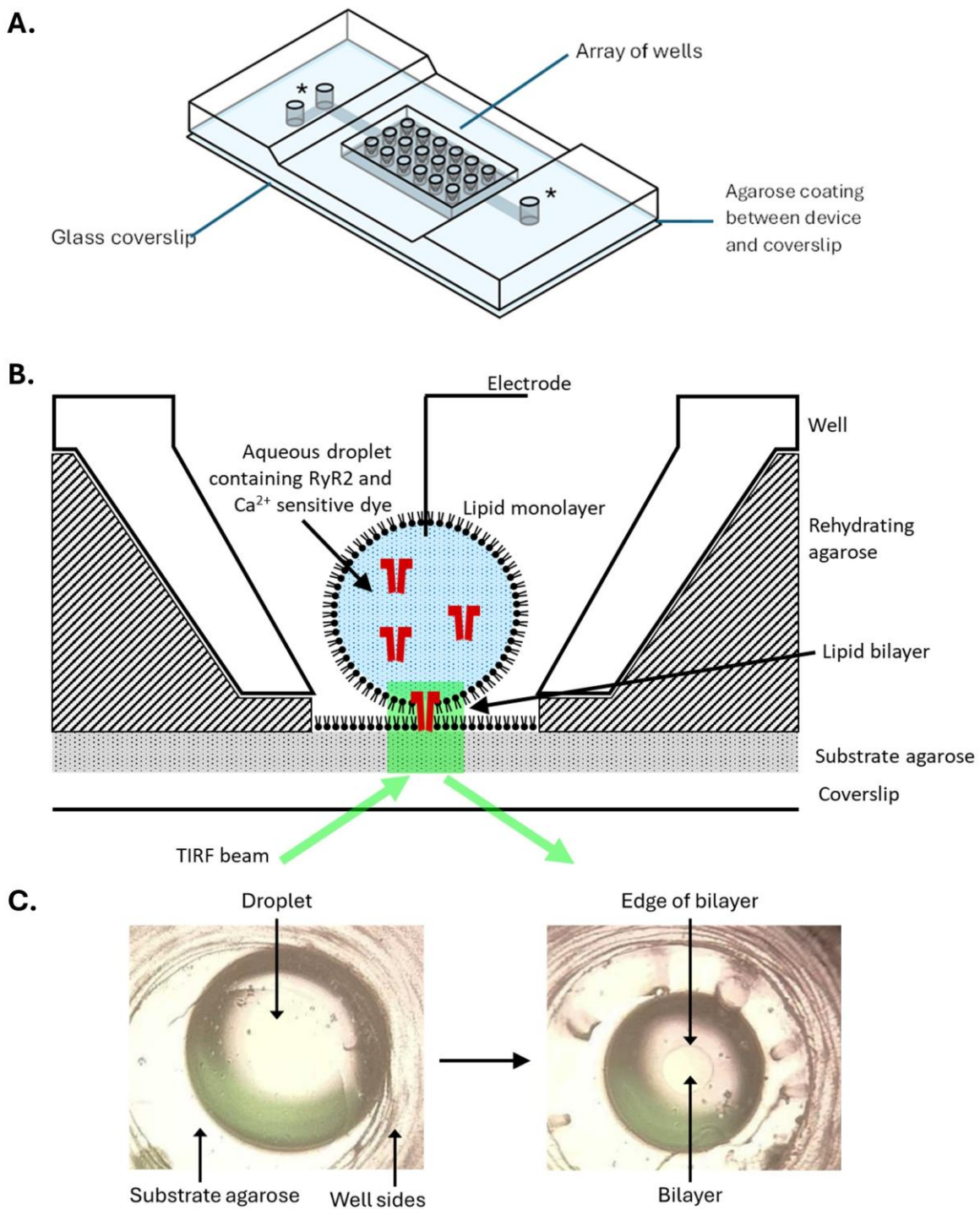

Figure 5.1. Schematic of droplet interface bilayer device and setup on a TIRF microscope. A. Diagram showing the acrylic device used to house droplets. The ground electrode can be inserted into any one of the three larger ports (denoted *); these ports are also used to fill the device with a rehydrating agarose (35 mg/mL). **B**. Cross-section shows a single well in the device, containing a droplet that has spontaneously formed a bilayer on contacting the lipid/oil mixture in the well. The orientation of channels in the droplet is representative of the orientation in which they incorporate into the bilayer. **C**. Bilayer formation is spontaneous and monitored optically. On bilayer formation, a small circle can be seen in the bottom of the droplet showing the bilayer area.

Droplets were formed by pipetting up to 50 nL of droplet mixture into a trough containing 8 mg/mL DPhPC in 60% hexadecane / 40% silicone oil, then incubated at RT in the dark for at least 30 minutes. After incubation, individual droplets were pipetted into wells on the device and monitored visually for bilayer formation (**Figure 5.1C**). Once a bilayer had formed, a 0.1mm silver electrode was dipped in 80°C 7.5 mg/mL agarose and lowered towards the droplet via a micro-manipulator until the droplet was pierced. The 60x TIRF objective (Nikon Instruments) was then prepared by adding a drop of low-fluorescence immersion oil to the lens, bringing the objective up to the device until the oil contacted the coverslip and focused. The shutter was opened and the blue laser (473nm Ventus laser; Laser Quantum) and green laser (532nm Ventus laser; Laser Quantum) were switched on (the full laser path and filter setup is included in **Appendix VIII**). The two lasers were aligned and their power checked (this was to ensure uniformity across different experiments), then the TIRF angle and TIRF focus were adjusted to correct the depth of field and bring the bilayer into focus. Optical information was detected via an Andor iXon Ulta EMCCD camera (Oxford Instruments) and visualised using Andor Solis I software (Oxford Instruments); electrophysiological data were recorded via an Axopatch 200B Amplifier (Molecular Devices) and WinEDR.

Andor Solis camera acquisition and analysis software was used to scan the bilayer for oscillating patches of fluorescence which indicate Ca^{2+} plumes from hRyR2, as indicated by Cal-590 (excited by the green 532nm laser and detected in the range 573nm to 613nm). The 473nm laser was used to excite the eGFP-tag on the N-terminus of the hRyR2 recombinant protein (detected in the range 500nm to 550nm). Once a plume was located, 1000 frames were recorded at 33Hz at constant voltage to capture both fluorescence and electrophysiological data (10,000kHz). The voltage was varied across different recordings due to difficulty in observing any channel activity at lower voltages in some cases and ranged from 0mV to -90mV relative to the ground (luminal) electrode.

The 0.1mm electrode was used to manipulate the size of the bilayer by pulling up on the electrode, which decreases the area of droplet in contact with the substrate agarose. If the area of the bilayer is reduced such that the whole bilayer is visible via the recording software, any channel activity as visualised by TIRF should align with the electrophysiological data as both recordings capture the entirety of the bilayer. This is not

the case if the bilayer extends outside of the FOV, as there may be other channels contributing to the electrophysiological data that cannot be imaged.

All DIB / TIRF experiments were performed with guidance and assistance from Hannah Baird.

5.2.3 Processing of droplet interface bilayer and total internal reflection microscopy data

Optical data from the DIB and TIRF experiments were saved as .tiff files and then processed using a combination of FIJI image processing software (Schindelin et al. 2012) and a custom MatLab App designed by Dr Oliver Castell for analysing this data; this is referred to as the Gaussian Fitting Suite (GFS). The aim of the GFS is to fit a 3D Gaussian to the optical data generated from these experiments to attempt to accurately quantify Ca^{2+} release; this captures the volume under the Ca^{2+} plume and represents the total amount of Ca^{2+} released from that site per frame. An overview of the process is described below and illustrated in **Figure 5.2**.

Optical data stored in a .tiff file from one recording was loaded into FIJI, where files were cropped to show only the illuminated area and to remove the first frame (underexposed due to shutter opening). The Z-project function in FIJI was used to generate an average (mean) image and coordinates of Ca^{2+} flux spots in the recording were collected; both of these items were saved. The GFS was opened in MatLab and the Z-projected image and coordinates used to create a 'spotless' image. This 'spotless' image and the original .tiff stack were concatenated in FIJI before running a macro to perform laser fluctuation correction, illumination flattening and background subtraction; this results in a .tiff file containing only the corrected spots. The image processing macro also produces a value called 'Standard Measure of Difference' (SMOD) that provides quantitative information about the background correction, cropping and illumination; the SMOD can be used to normalise data between different recordings at a later stage. The .tiff file containing corrected spots was reloaded into the GFS and processed again to fit the Gaussian, which was then saved into the MatLab workspace. Here another round of processing was conducted, including applying a Chung-Kennedy filter and step detection to the trace; data were also normalised by the SMOD value at this stage. The output from this process includes Gaussian volume over time, dwell times and levels, mean and median fluorescence, and various other parameters that can be used for plotting the data.

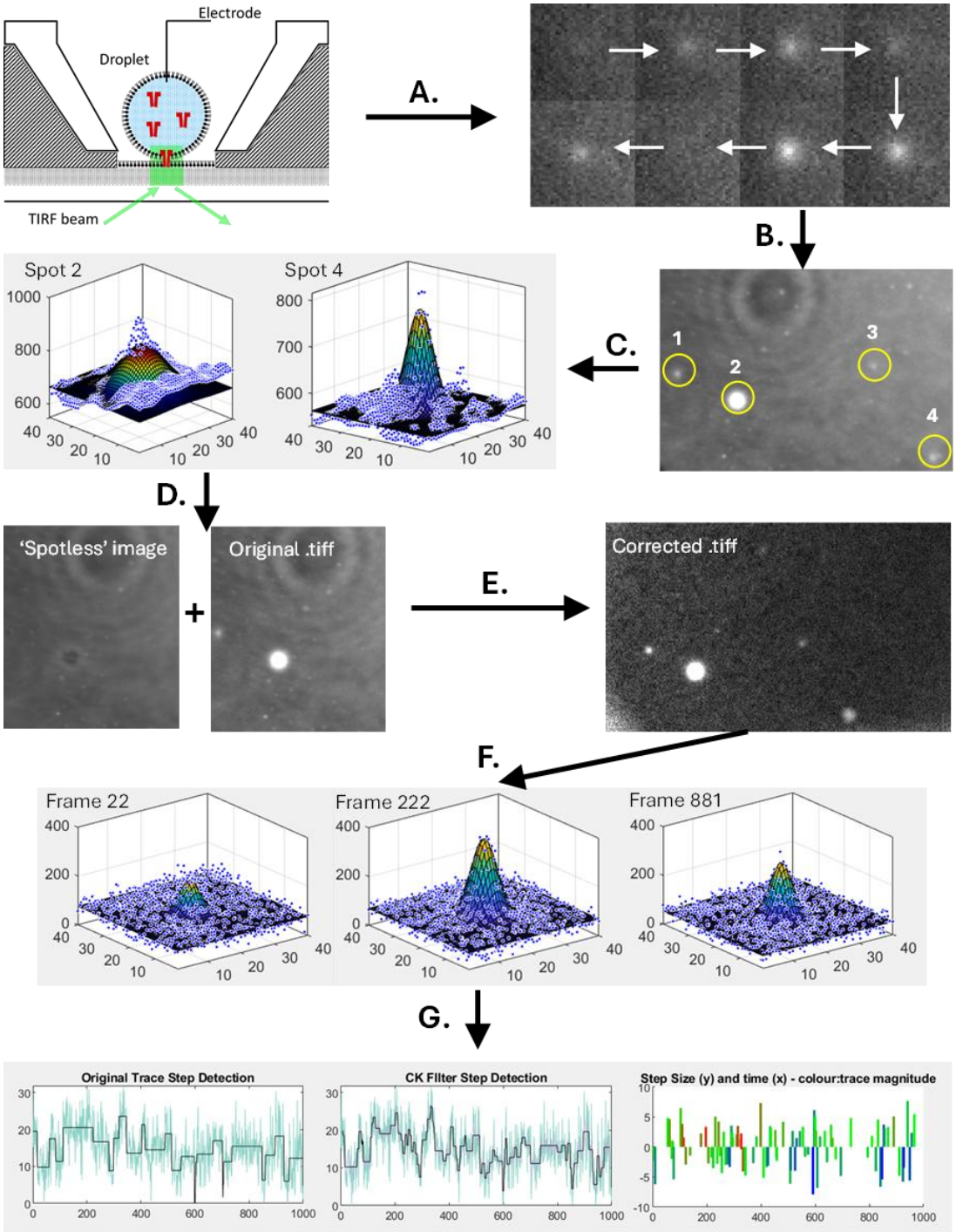

Figure 5.2. Schematic of main steps of Gaussian Fitting Suite to analyse DIB data. A. Optical data from TIRF saved as image stack and used to identify areas of fluctuating fluorescence (Ca^{2+} flux spots). **B.** All frames are averaged (mean) and spot locations plotted. **C**. Averaged image and spot coordinates are input into GFS to 3D reconstruct spot averages. **D**. Spot averages are subtracted from background to create a 'spotless' image; this is added to the start of the original image stack. **E**. Correction algorithm is applied to remove background ('spotless' image) and correct for laser fluctuation and image flattening. **F**. Corrected stack is processed through GFS again; fits 3D Gaussian to all spots for all frames. **G**. Post-processing applies CK-filter (to filter out background signal) and step detection to create an idealised trace that describes the raw data.

5.2.4 Classifying Ca^{2+} flux behaviours from hRyR2 populations and quantifying cluster size from Gaussian Fitting Suite data

After processing through the GFS, each individual Ca^{2+} flux spot (a site consisting of one or more RyR2 channels) was plotted as fluorescence (using the Gaussian volume normalised by SMOD) against time to create a corrected trace of activity over the recording period. Six broad categories of behaviour were identified by eye and mathematical criteria assigned to quantify these behaviours by their activity level and defining features via a series of 'IF' functions in Microsoft Excel (see **Appendix X**). This grouped traces into one of the six behaviour categories, and then traces were checked by eye to confirm no obvious errors in categorisation.

Cluster size was estimated based on previous data generated by the group (**Figure 5.3**) that used comparison between Gaussian-fitted TIRF data and electrophysiological recordings taken from the same droplet to calculate the normalised fluorescence of a single channel. This was obtained by diluting the purified hRyR2 preparation to minimise the likelihood of multiple channels being present and reducing the bilayer size so that only one Ca^{2+} flux spot was visible; the optical and electrophysiological recordings were then overlayed, and this showed a correlation between fluorescence amplitude and current (**Figure 5.3**). The maximum current was measured as ~4pA with Ca^{2+} as the permeant ion, which agrees with other studies that have measured the maximum current of a single RyR2 channel (Lehnart et al. 2008; Porta et al. 2011; Gillespie and Fill 2013); this corresponded to ~40AU as recorded by TIRF in DIBs (**Figure 5.3**). The 3 highest Gaussian volume datapoints for each Ca^{2+} flux spot (normalised by SMOD; referred to as Maximum Fluorescence Intensity) were averaged and divided by 40 to give an estimate of the minimum number of active channels per cluster.

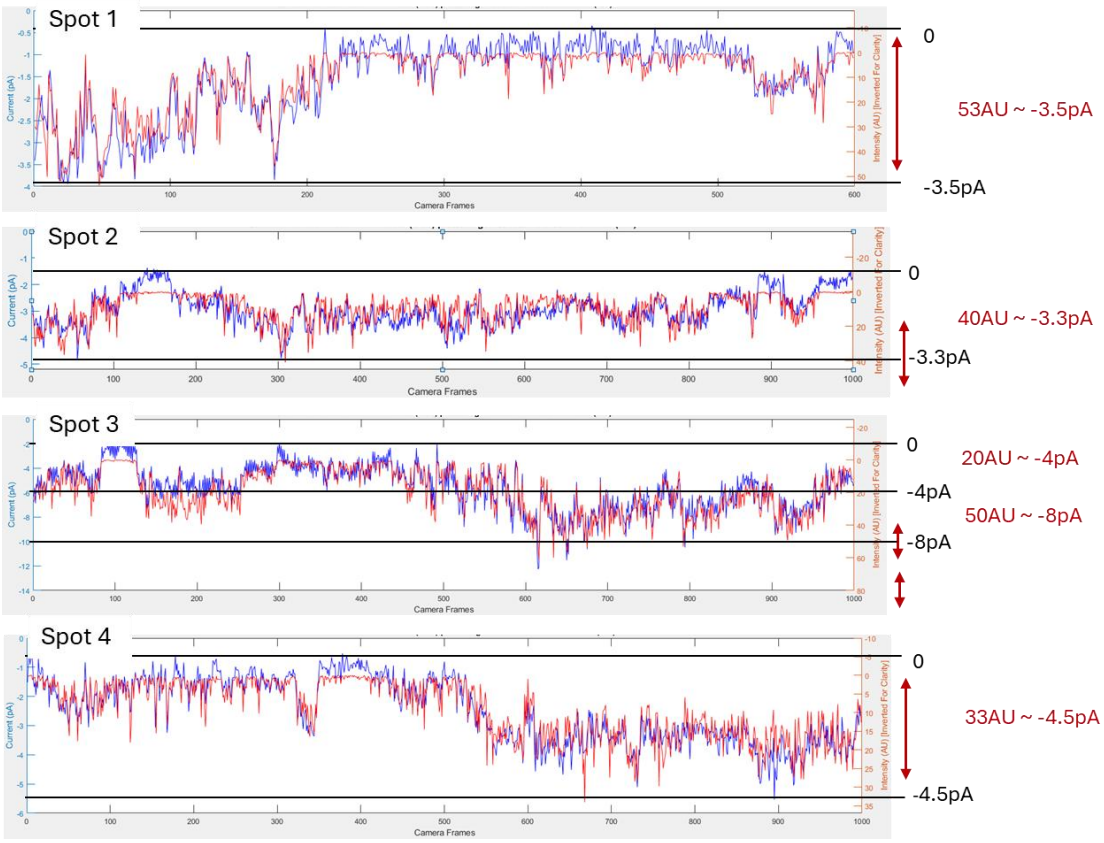

Figure 5.3. Alignment of electrophysiological and optical traces to estimate fluorescence equivalent to 1 channel. Electrophysiological data acquired from DIBs and optical data from TIRF were overlayed to determine the approximate fluorescence (AU) for 1 WT-hRyR2 channel at max conductance. From 4 Ca^{2+} flux spots (containing 5 total channels), a fluorescence of ~40AU was equated to ~4pA. Note that the fluorescence data does not match the lowest level of conductance, therefore at lower fluorescence the change in pA is smaller than at higher fluorescence. Data obtained from Dr Bevan Cumbes via personal correspondence.

5.3 Results

5.3.1 R1051P-hRyR2 populations display a different Ca^{2+} release profile in droplet interface bilayers than WT-hRyR2

Traces of Gaussian volume over time for individual Ca^{2+} flux spots (each spot could contain 1 channel or a cluster of channels) from DIBs containing R1051P and WT-hRYR2 displayed distinctly different behaviours, allowing them to be categorised. The main characteristics used to classify traces were amplitude, fluctuation and time spent at baseline (~0 fluorescence – channels closed). This resulted in a total of 6 behaviour categories, however only 4 of these behaviours were observed with WT-hRyR2; the other 2 behaviours were exclusive to R1051-mutant hRyR2 (**Figure 5.4**; the main analysis compares WT and R1051P-hRyR2 only). The basic characteristics of each behaviour, the criteria by which they were sorted and the implications for Ca^{2+} release are as follows;

- *Infrequent Events* – long periods at very low/no fluorescence (baseline; indicates channels mainly in the closed state) interspersed with events; >25% of values in the bottom 5% of the range, <50% of values in the top 50% of the range, >25% of values in bottom 5% are continuous. Suggests generally low or no Ca^{2+} release activity, followed by defined periods of Ca^{2+} release activity from the Ca^{2+} flux spot.

- *Frequent Events* - frequent peaks in fluorescence with high fluctuation, interspersed with multiple short returns to the baseline; >25% of values in the bottom 20% of the range, <50% of values in the top 50% of the range, <25% but >5% of values in bottom 5% are continuous. Suggests relatively high Ca^{2+} release activity but still interspersed with shutdown periods.

- *Fluctuating* - frequent fluctuations in fluorescence with few plateaus or returns to the baseline; baseline visits are very short and immediately followed by return to higher activity levels; >50% of values in the bottom 40% of the range, at least 1 visit to baseline (fluorescence value 0-1), <55% of values in bottom 5% are continuous. Suggests high activity and minimal shutdown of Ca^{2+} release.

- *Always On* – a consistently high level of fluorescence with some fluctuation but no returns to the baseline; no values in the bottom 1% of the range from 0 fluorescence to maximum fluorescence. Suggests near constant Ca^{2+} release activity.

- *Inverted* – majority of time spent at stable high fluorescence with only occasional short returns to baseline or other stable level and little other fluctuation; >80% of values in the top 50%, at least 2 visits to the bottom 5%. Suggests consistent Ca^{2+} release that reactivates immediately after brief shutdown.
- *Stepped* – defined steps in fluorescence intensity between relatively stable fluorescence levels with sharp transitions, interspersed with peaks/fluctuation; >5% of values in top and bottom 5% are continuous. Suggests cooperative opening and closing of channels to produce defined 'on' and 'off' periods.

These behaviours do exist on a spectrum, for example 'Infrequent' and 'Frequent', or 'Frequent' and 'Fluctuating', where a very small change in the time spent at the baseline might affect the categorisation. While the criteria were applied initially, a secondary visual check was performed to check the correct classification of traces; this was particularly important for the 'Inverted' and 'Stepped' behaviours, as while they are both defined by very rapid transitions between high and low Ca^{2+} flux states, there were multiple overlapping criteria with other categories (for example, some 'Stepped' and 'Inverted' traces did not ever visit the baseline, but still presented clear changes in Ca^{2+} flux state, unlike the 'Always On' behaviour). Overall, less than 5% of traces were misclassified across all hRyR2 variants. It is also likely that populations of hRyR2 switch behaviour over time, as is observed in single channels (discussed in **Chapter 6**), therefore where any change in behaviour was noted the trace was classified based on the majority behaviour over the recording period.

Post CK-filtering in the GFS, traces from each category in both WT and R1051P were compared using step size (between different levels of fluorescence) against time as another means to compare and classify Ca^{2+} flux behaviours. Traces classified as the same behaviour by visual comparison of traces were backed up by similar step size profiles, providing a tertiary means of organising populations of hRyR2 where the criteria did not fit and visual comparison was not sufficient (**Appendix IX**).

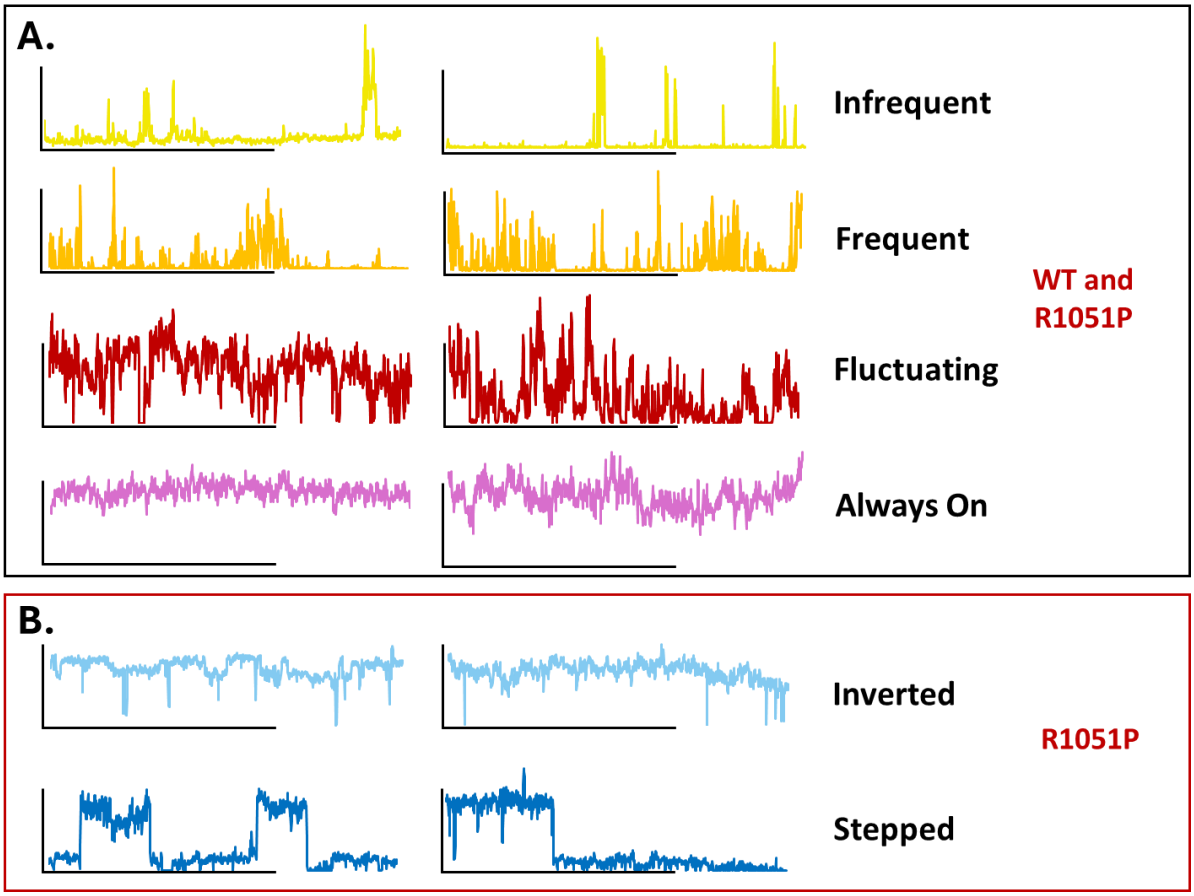

Figure 5.4. R1051P-hRyR2 populations exhibit novel Ca^{2+} flux behaviours not seen in WT-hRyR2 in DIB / TIRF. Traces are representative and were chosen to best depict the characteristics of each Ca^{2+} release behaviour. Amplitudes are not to scale; this is due to a high degree of amplitude variation in traces of the same behaviour. **A.** The 4 behaviours – 'Infrequent', 'Frequent', 'Fluctuating' and 'Always On' – were observed in both WT and R1051P-hRYR2 populations (and to some extent in R1051C and R1051H populations). **B.** The 'Inverted' and 'Stepped' behaviours were only observed in mutant populations (R0151P predominantly; the 'Stepped' behaviour was also observed in R1051C populations).

5.3.2 Distribution of common behaviours is relatively comparable between different hRyR2 variants

All four behaviours that were observed in WT-hRyR2 were also observed in R1051-mutant hRyR2; these were 'Infrequent', 'Frequent', 'Fluctuating', and 'Always On'. The two other behaviours observed – 'Stepped' and 'Inverted' – appeared to be exclusive to R1051-mutant hRyR2; both behaviours were observed in R1051P populations, and the 'Stepped' behaviour was observed once in R1051C (**Table 5.1**). For R1051P, 13.2% of spots analysed exhibited either the 'Inverted' or 'Stepped' behaviour. The 'Always On' behaviour was also more frequently observed in R1051P at 10.3% of spots (7 of 68 spots), compared to 2.3% (1 of 44 spots) for WT-hRyR2. The most common behaviour in both WT and R1051P was 'Fluctuating', at 45.5% and 29.4%, respectively (**Table 5.1**).

Fewer experiments were conducted using R1051C and R1051H-hRyR2 than WT (n = 44 Ca^{2+} flux spots) and R1051P (n = 68), with 10 and 12 Ca^{2+} flux spots recorded, respectively. This was an intentional experimental choice to prioritise WT and R1051P due to the predicted impact of the R1051P mutation (**Section 1.7.3**). When the same behaviour groups were applied to these two mutants, neither were found to exhibit the 'Always On' or 'Inverted' behaviours, and only one Ca^{2+} flux spot was classified as 'Stepped' (R1051C). All other Ca^{2+} flux spots were classified as 'Infrequent', 'Frequent', or 'Fluctuating', which reflects the most frequently observed behaviours in WT and R1051P and may be a product of the smaller sample size (**Table 5.1**). No other novel behaviours were noted in either R1051C or R1051H.

Table 5.1. The distribution of Ca^{2+} release behaviours is different in R1051-mutant hRyR2 Ca^{2+} flux spots compared to WT-hRyR2 spots. The main observed differences in behaviour frequency are the notable lack of 'Inverted' and 'Stepped' behaviours in both WT and R1051H populations, and the absence of the 'Always On' behaviour in R1051C and R1051H populations. The sample size for R1051C and R1051H (R1051C n = 10 Ca^{2+} flux spots, R1051H n = 12) was much lower than either the WT or R1051P (WT n = 44, R1051P n = 68). Generally, WT, R1051P and R1051C showed similar distributions of the 'Infrequent', 'Frequent' and 'Fluctuating' behaviours.

	Infrequent	Frequent	Fluctuating	Always On	Inverted	Stepped
WT	29.5% (13)	22.7% (10)	45.5% (20)	2.3% (1)		
R1051P	19.1% (13)	27.9% (19)	29.4% (20)	10.3% (7)	7.4% (5)	5.9% (4)
R1051C	20% (2)	30% (3)	40% (4)			10% (1)
R1051H	8.3% (1)	58.3% (7)	33.3% (4)			

5.3.3 R1051C-hRyR2 and R1051H-hRyR2 appear to form larger clusters than WT-hRyR2

Initial attempts to estimate cluster size based on photobleaching of eGFP on the N-terminus of the recombinant hRyR2 protein used in this study were unsuccessful due to the rate of photobleaching of eGFP. This was due to the strength of the lasers used to acquire optical data on Ca^{2+} release, resulting in almost immediate photobleaching of eGFP during recording. Efforts to align electrophysiology recordings (which captures the activity of all channels in the bilayer) with Cal590 fluorescence (ie. Ca^{2+} release from hRyR2) to estimate population size based on current were also unsuccessful, due to difficulty in reducing the bilayer size to fit entirely within the TIRF FOV. An alternative method to estimate the minimum number of active channels per cluster was employed using data obtained from earlier research that revealed one channel at maximum conductance equals approximately 40AU after processing in the GFS (Cumbes et al., *unpublished*; **Figure 5.3**). It is important to note that this method is likely to underestimate the number of channels present in a cluster as not all channels may be active at a time, and even when multiple channels are active their collective fluorescence may not reach the threshold to be classified as more than one channel; this is discussed in more detail in **Section 5.1**.

Of all Ca^{2+} flux spots analysed (both WT and mutant), 68.7% were classified as minimum 1 channel (≥1 channel), 23.9% were classed as minimum 2 channels (≥2 channels), and 7.5% were classed as 3 or more channels (designated 'cluster') (**Table 5.2**). Only for R1051H were there more Ca^{2+} flux spots categorised as ≥2 channels than ≥1 channel. Statistical analysis on this discrete data indicated that there was no significant association between hRyR2 variant and cluster size (**Table 5.2**; Chi-squared test for Independence, $X^2 = 12.32$, df = 6, p-value = 0.055, n = 134). However, when analysed using continuous data (using Maximum Fluorescence Intensity, which gives a better indication of relative cluster sizes than discrete categories), R1051C and R1051H populations were shown to be significantly larger than WT-hRyR2 populations (**Figure 5.5**) despite a much smaller sample size.

Table 5.2. Distribution of estimated minimum cluster size for all hRyR2 is comparable. The minimum number of active channels per cluster was calculated from the Maximum Fluorescence Intensity divided by 40AU, which has been calculated to represent one channel open at maximum conductance. This reveals a relatively similar distribution of population sizes across all hRyR2 variants tested (Chi-Squared test for Independence, $X^2 = 12.33$, df = 6, p-value = 0.055), although there is a slight deviation from the trend in R1051H, which is the only variant to have more clusters of minimum 2 or more active channels than single channels.

	>1 Channel	>2 Channels	Cluster
WT	33	9	2
R1051P	50	12	6
R1051C	5	4	1
R1051H	4	7	1
Total spots	92	32	10

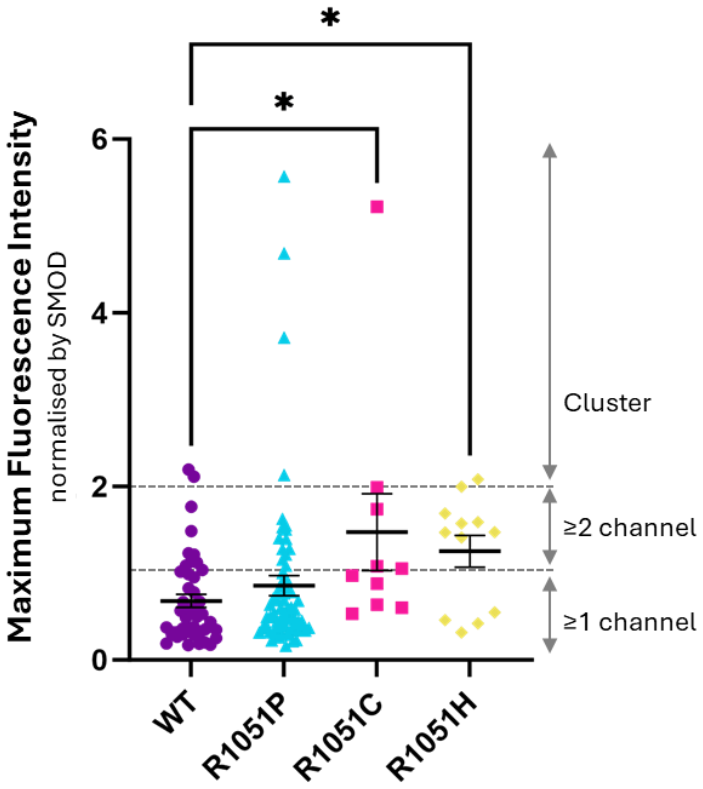

Figure 5.5. R1051P-hRyR2 populations contain a comparable number of channels to WT-hRyR2 populations, but R1051C-hRyR2 and R1051H-hRyR2 populations are significantly larger. When compared on a continuous scale, the mean cluster size of R1051C and R1051H-hRyR2 populations were significantly larger than WT-hRyR2 (p-value = <0.05 (*)); no other significant comparisons were found. Outliers from R1051P (Maximum Fluorescence Intensity = >10, n = 2) have been removed, but statistical analysis showed that their inclusion did not change the significance of any results (**Appendix XI**). Statistical analysis was performed in GraphPad Prism 10.1.2 using Kruskall-Wallis non-parametric test with Dunn's post-hoc test.

5.3.4 The distribution of Ca^{2+} flux behaviours changes as the estimated number of channels increases

Overall, across all 4 hRyR2 variants there was a significant change in distribution of behaviours as predicted cluster size increased (**Table 5.3**; Chi-squared Test for Independence; Chi-squared statistic (X^2) = 36.45, degrees of freedom = 10, p-value = 7.04^{-5}, n = 134). In Ca^{2+} flux spots classified as '≥1 channel', the predominant behaviours were 'Infrequent', 'Frequent' and 'Fluctuating', which made up 94.6% of the behaviours observed at this cluster size (**Figure 5.6**). At the '≥2 channel' and 'cluster' levels, the 'Always On', 'Inverted' and 'Stepped' behaviours represented a larger proportion of Ca^{2+} flux spots analysed at 18.8% and 70% respectively (**Figure 5.6**), despite a much smaller sample size of '≥2 channel' and 'cluster' populations.

Table 5.3. There is a significant association between Ca^{2+} release behaviour from hRyR2 and cluster size. Chi-squared test for independence indicated that there was a significant association between Ca^{2+} flux behaviour and cluster size (X^2 = 36.45, df = 10, p-value = 7.04^{-5}, n = 134, n = 134) across all four variants of hRyR2 analysed, including the WT. Values in bold indicate individual cells that contributed most to the overall Chi-squared statistic based on adjusted residuals, and * indicates a cell that differs significantly from the predicted distribution (p-value <0.05). The number of Ca^{2+} flux spots classified as 'Frequent' in the Cluster category was significantly lower than predicted, and the number of spots classified as 'Always On' in the Cluster category was significantly higher than predicted. The Chi-squared test was performed with Bonferroni-correction and using marginal totals in RStudio.

	1 Channel	2 Channels	Cluster
Infrequent	16	3	0
Frequent	45	14	**1***
Fluctuating	26	9	3
Always On	**1**	2	**4***
Inverted	2	2	1
Steplike	2	2	1

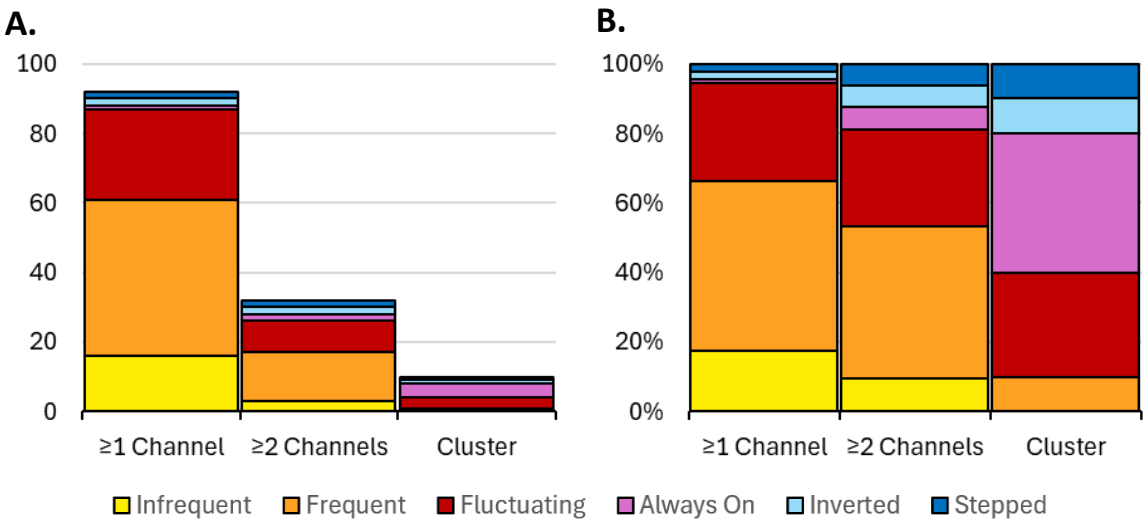

Figure 5.6. The distribution of Ca^{2+} release behaviours changes as estimated cluster size increases. A. Graph showing absolute counts (Y-axis) of behaviour type for each size category, demonstrating the smaller number of populations classified as '≥2 channels' or 'cluster'. **B.** Graph showing proportional distribution of behaviours. The distribution of Ca^{2+} flux behaviours changes as cluster size increases, with the 'Infrequent', 'Frequent' and 'Fluctuating' behaviours becoming less common as cluster size increases, and the 'Stepped', 'Inverted' and 'Always On' behaviours representing a much larger proportion of 'clusters'.

There was a significant difference in the distribution of behaviours as cluster size changed when R1051P was compared to the WT dataset (**Table 5.4**; Chi-squared Test for Homogeneity; $X^2 = 24.58$, df = 10, p-value = 0.0062, n = 112), however no individual counts were found to be significantly different. Analysis of this data was complicated by the presence of zeros in the dataset, namely in the 'Always On', 'Inverted' and 'Stepped' categories of the WT data. Zeros can invalidate many statistical tests, including the Chi-squared test; in an attempt to negate this, a small value (0.5) was added to all values, however this did not drastically alter the result (Chi-squared Test for Homogeneity; $X^2 = 20.76$, df = 10, p-value = 0.0228, n = 112). Regardless of this result, the presence of these behaviours at all in R1051P and the higher proportion of them in larger clusters suggests (**Figure 5.7**) there is an important relationship between predicted cluster size and the 'Inverted', 'Stepped', and 'Always On' Ca^{2+} flux behaviours, even if this cannot be shown statistically.

Due to the small sample size obtained for R1051C (n = 10 Ca^{2+} flux spots; **Figure 5.7C**) and R1051H (n = 12, **Figure 5.7D**), the statistical power to detect a meaningful difference was reduced; therefore, statistical analyses were not performed for these mutants.

Table 5.4. The distribution of Ca^{2+} release behaviours as cluster size increases in R1051P-hRyR2 populations is different than in WT-hRyR2 populations. Statistical analysis showed that that there was a significant difference in the distribution of Ca^{2+} flux behaviours as cluster size increased in R1051P-hRyR2 populations compared to WT-hRyR2 populations (Chi-squared Test for Homogeneity; X^2 = 24.58, df = 10, p-value = 0.0062, n = 112). Three comparisons had standardised residuals greater than 1 (bold underlined numbers) indicating that they contributed more to the overall statistic, however no significant difference in any one variable was detected (p-value >0.05). Several categories could not be compared due to the presence of zeros in the dataset; this includes any category where the WT (i.e. expected count) equalled zero.

	1 channel		2 channel		Cluster	
	WT	**RP**	**WT**	**RP**	**WT**	**RP**
Infrequent	6	9	**2**	**1**	0	0
Frequent	16	23	4	4	0	0
Fluctuating	11	13	**3**	**2**	1	0
Always On	0	1	0	2	**1**	**3**
Inverted	0	2	0	2	0	1
Stepped	0	2	0	1	0	1

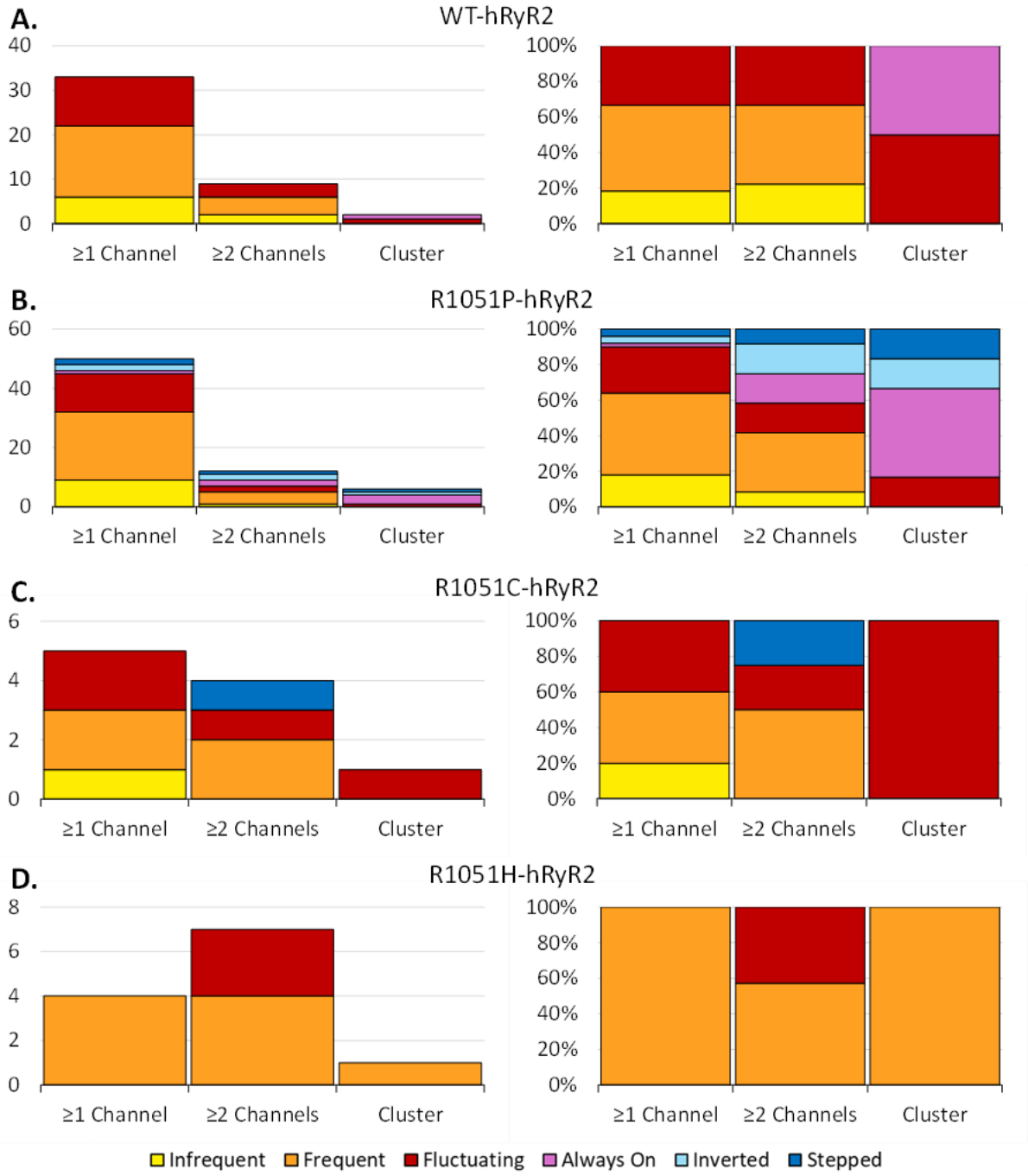

Figure 5.7. The distribution of Ca^{2+} release behaviours from populations of WT and R1051-mutant-hRyR2 changes with cluster size. Graphs on the left show absolute counts of behaviours at each size category; graphs on the right show behaviours as a proportion of the whole for each size category. **A**. WT-hRyR2 populations show a comparable distribution of behaviours at the '≥1 channel' and '≥2 channels' level, but this changes in clusters as the 'Always On' behaviour manifests. **B.** R1051P populations show an increased proportion of the 'Stepped', 'Inverted' and 'Always On' behaviours as cluster size increases. R1051C (**C**) and R1051H (**D**) show a less defined trend in behaviour relative to cluster size; this may be due to their small sample size. WT n = 44 Ca^{2+} flux spots; R1051P n = 68; R1051C n = 10; R1051H n = 12.

5.3.5 Novel behaviours observed in R1051P-hRyR2 have a higher activity regardless of cluster size

The activity and relative fluctuation in signal intensity from Ca^{2+} flux spots were used as measures to compare Ca^{2+} release from WT and R1051P, and also to compare different behaviour classifications. Activity was calculated as the median Ca^{2+} signal amplitude as a proportion of the maximum signal, with values closer to 1 indicating higher activity. Fluctuation was calculated from the step frequency and size (from idealised traces) as a proportion of the maximum fluorescence. Cluster size was plotted on a continuous scale using the Maximum Fluorescence Intensity of each Ca^{2+} flux spot as a better way of visualising estimated cluster size.

Populations categorised as 'Infrequent', 'Frequent' and 'Fluctuating' had comparable activity between the WT and R1051P datasets (**Figure 5.8**), tending towards lower activity with the exception of 'Fluctuating' which shows a broader range up to approximately 0.5 median:max ratio. Populations classified as 'Always On', 'Stepped' and 'Inverted' tended to have higher and more variable activity than other behaviours regardless of cluster size (**Figure 5.8**). In WT populations there appeared to be an upper limit of activity relative to cluster size, particularly in the 'Fluctuating' category, illustrated by the wedge-shaped distribution of data (**Figure 5.8A**). This relationship between cluster size and activity was less defined in R1051P-hRyR2 (**Figure 5.8B**).

Relative fluctuation of each behaviour was largely comparable between WT (**Figure 5.8C**) and R1051P (**Figure 5.8D**), however in R1051P populations there appears to be an upper threshold of fluctuation for a given cluster size, although nonlinear regression revealed no relationship (Semilogarithmic regression, df = 64, R^2 (values close to 1 indicate good fit of model) = 0.004, 95% CI for slope = -0.085, 0.051). WT values were more evenly distributed, and cluster size did not appear to affect relative fluctuation.

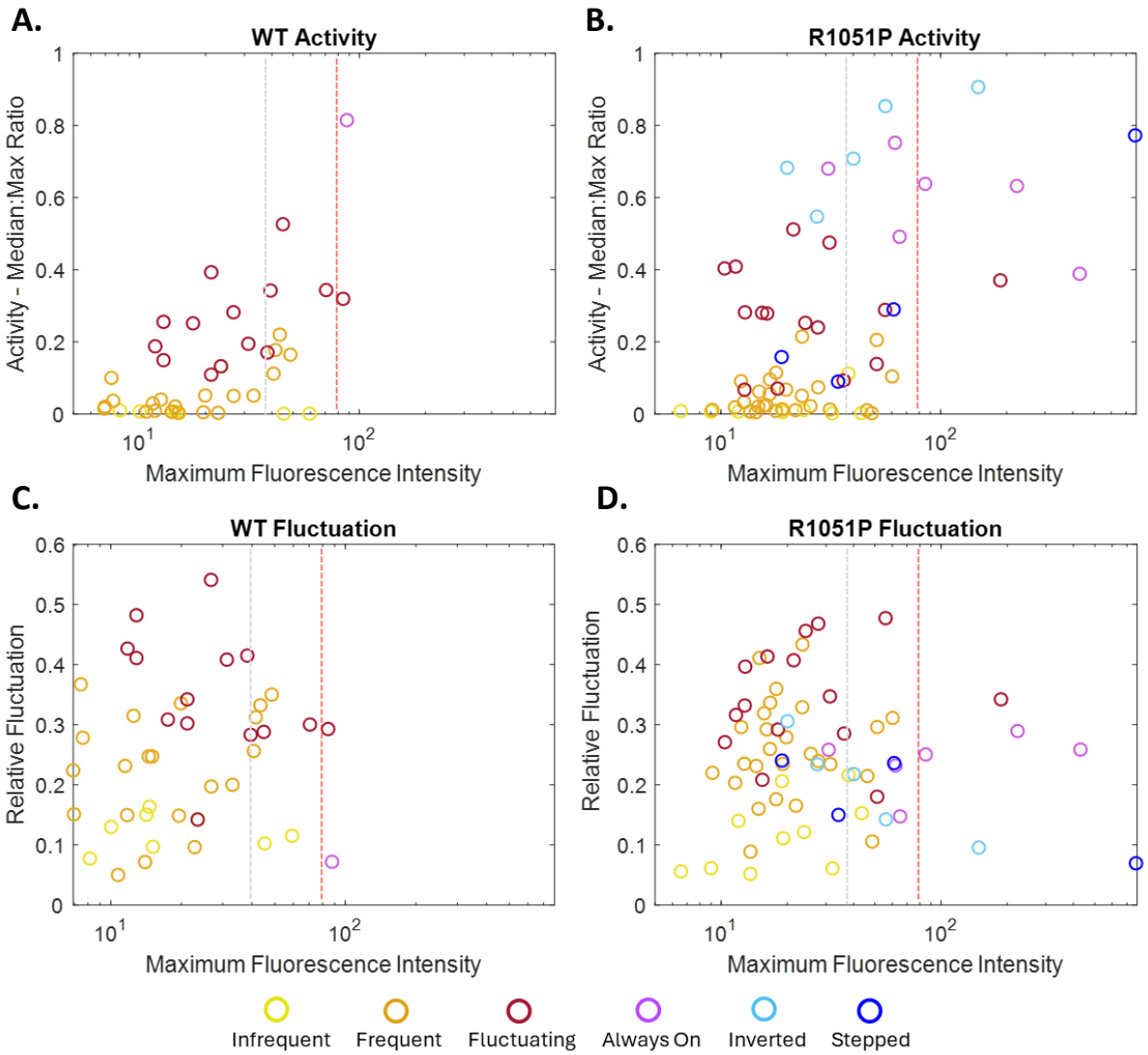

Figure 5.8. Relationship between estimated cluster size and channel activity or fluctuation of activity in WT and R1051P-hRyR2 populations recorded in DIBs. Maximum Fluorescence Intensity was used as a gauge of cluster size; the grey dotted line indicates the upper threshold of populations classed as '≥1 channel', the red dotted line is the upper threshold for '≥2 channels'; to the right of the red line indicates populations classified as 'clusters'. **A.** Activity of WT-hRyR2 populations. **B.** Activity of R1051P-hRyR2 populations. In WT-hRyR2 populations (**A**), activity appears to be limited by cluster size, with smaller populations unable to achieve higher levels of activation; in R1051P (**B**) this relationship is less defined indicating higher activity of smaller clusters. The novel behaviours 'Inverted' and 'Stepped', as well as the 'Always On' behaviour all tend towards higher activity than the other behaviour classifications. **C.** Relative fluctuation in WT-hRyR2 populations. **D**. Relative fluctuation in R1051P-hRyR2 populations. In both WT (**C**) and R1051P-hRyR2 (**D**) populations, relative fluctuation of the 'Infrequent', 'Frequent' and 'Fluctuating' behaviours is comparable, although there appears to be a loose relationship between larger cluster size and higher fluctuation in R1051P-hRyR2 populations. The remaining behaviours display overall very variable fluctuation.

5.4 Discussion

5.4.1 R1051C-hRyR2 and R1051H-hRyR2 mutants may have the capacity to form larger clusters than WT-hRyR2

The initial hypothesis behind this study was that mutation of R1051 may affect the ability of hRyR2 channels to form functional clusters, of which one consideration is cluster size. Results shown here (**Figure 5.5**; **Table 5.2**) indicate that there is no significant difference in the minimum number of active channels per cluster between WT-hRyR2 and R1051P-hRyR2, however R1051C and R1051H populations were estimated to be significantly larger than WT-hRyR2 populations.

If R1051C and R1051H mutants have an increased propensity to form larger clusters than WT-hRyR2 (**Figure 5.5**), it is necessary to examine how or why this might occur. R1051 is located in the P1 domain which is believed to be involved in the inter-tetramer interaction and may need to undergo domain rearrangement to facilitate tight clustering (Cabra et al. 2016). Mutation at R1051 could disrupt or alter this remodelling, but is it possible that this results in a strengthened interaction that facilitates the formation of larger clusters? P1 is proposed to interact with FKBP12.6 on adjacent tetramers (Cabra et al. 2016), and while FKBP12.6 is lacking in these experiments, its binding is associated with decreased cluster size containing fewer hRyR2s (Asghari et al. 2020) and so this should not interfere with large clusters forming in either WT or R1051-mutants. Detailed modelling of the P1 domain during clustering has not been performed to date, but this would help determine whether rearrangement is needed for a tight clustering interaction, and whether R1051-mutation might interfere with this. However, this brings its own complications as modelling in detail such a large protein as hRyR2 is computationally complex and as with all *in silico* methods, does not provide a definitive result. X-ray crystallography would provide a more definitive answer, however to truly understand the impact of these mutations on the clustering interaction would require crystallisation of two hRyR2s in a cluster; given the difficulty of crystallising RyR2 alone, maintaining clustering interactions during crystallisation would be a significant challenge. A more achievable approach could be to look at the P1 domain in isolation and examine the structural impact of R1051 mutation. As of yet, the P1 domain of RyR2 has not been crystalised, although the equivalent domain of RyR1 is resolved to 1.5 Å

(Yuchi et al. 2015), however crucially R1051 and the surrounding residues are not conserved in RyR1 (**Section 1.7.2**).

It is important when considering these results to take into account both the method of calculating cluster size and the smaller sample size for R1051C and R1051H. In this study, cluster size is calculated based on the Maximum Fluorescence Intensity, not via an objective count of the number of channels present (discussed in more detail in **Section 5.4.2**). Therefore, it is possible that R1051-mutant hRyR2 is simply more active (**Figure 5.8**), releasing more Ca^{2+} than the WT, which with this measure of cluster size would reflect as larger clusters (**Section 5.3.3**). This is discussed further in **Section 5.4.2**.

It is also worth noting that, while no significant difference in cluster size was found between R1051P and WT (**Figure 5.5**), several large, bright Ca^{2+} flux spots (10-19 active channels) presumed to come from very large clusters were observed for R1051P which far exceed the size of any populations observed in WT, R1051C or R1051H. Earlier research by Cumbes et al., (*unpublished)* did identify Ca^{2+} flux spots from WT-hRyR2 populations with these characteristics, so while they may not be exclusive to the R1051P mutant, it is possible that they occur more frequently. These large spots could represent RyR2 'superclusters'; groups of several clusters within 100nm of each other thought to act as one functional CRU (Baddeley et al. 2009). The number of channels required to form a supercluster is not certain, with different studies obtaining averages of 21.6 (Baddeley et al. 2009) to 103 channels (Hou et al. 2015), but there is agreement that these frequently consist of multiple distinct smaller clusters of RyR2 (Baddeley et al. 2009; Hou et al. 2015; Hou et al. 2023). Logically, superclusters of many RyR2s acting in concert could facilitate greater Ca^{2+} release to contribute to spark generation (Hou et al. 2023), and if they form more readily with R1051P-hRyR2 this would have implications for Ca^{2+} release.

5.4.2 Limitations in calculating cluster size

As mentioned above, it is important to note that the method used to calculate cluster size (**Section 5.2.3**) is an estimate, which considers only active channels and therefore is inherently likely to underestimate the total number of channels in a population. It is probable that a single Ca^{2+} flux spot recorded at a different time would be calculated to contain a different number of channels as its activity (and therefore fluorescence) changes stochastically, despite being in buffered conditions. It is also clear that, while 40AU was used

as an estimate of 1 channel at maximum conductance based on earlier research (**Figure 5.3**), many populations exhibit a maximum fluorescence much lower than this. This is due to fluorescence not being a direct measurement of channel open time; a shorter open time of an individual channel would result in lower fluorescence intensity than a channel with a longer open time due to time averaging, as the total amount of Ca^{2+} released would be lower. This means that the cumulative fluorescence produced by multiple short openings of multiple channels may still not reach the 40AU threshold to count as more than 1 channel. The P_O of channels in a cluster is also predicted to be relatively low with many channels remaining inactive (Hou et al. 2023), so with the combination of inactive channels and low P_O, the minimum number of active channels is likely to represent a very conservative count of the total number of channels present.

Initially it was intended to measure the photobleaching of the eGFP-tag on the recombinant hRyR2 protein to more accurately calculate the number of channels present. This was unsuccessful due to complications in the acquisition of this data (**Section 5.3.3**), despite eGFP photobleaching having been measured previously in this system (Cumbes et al., *unpublished*) (**Appendix VI**). Other studies that have aimed to quantify the number of RyR2 channels in a cluster have largely relied on super-resolution imaging of fixed samples via techniques such as direct stochastic optical reconstruction microscopy (dSTORM) or electron microscopy (Baddeley et al. 2009; Asghari et al. 2012; Asghari et al. 2014), however this isn't compatible with the DIB system due to the need for fixed samples. An alternative that has been used to quantify RyR2 clusters previously (Jayasinghe et al. 2018) and could be applied in this system is DNA-paint. In DNA-paint, a target-specific antibody is linked to a short DNA strand, and a complementary DNA strand is covalently linked to a fluorophore. When the DNA strands hybridize, the fluorescent signal increases, resulting in fluorophore 'blinking' as the DNA transiently binds and un-binds; this temporal separation allows precise mapping of single molecules beyond the diffraction limit. In combination with TIRF, this would allow the location of each tetramer of RyR2 to be mapped based on the position of individual monomers, which would indicate both the number of channels in a cluster well as their organisation (Jungmann et al. 2014; Schnitzbauer et al. 2017; Stehr et al. 2019). The spatial resolution of DNA-paint reaches around 10-20nm compared to dSTORM and PALM which achieve resolutions of around 20nm, and it is not so heavily impacted by

photobleaching as dSTORM and PALM as the fluorophores can replenish (Jungmann et al. 2010; Jungmann et al. 2014). Future work will aim to optimise DNA-paint for DIBs to allow for quantification of cluster size and organisation (**Section 5.4.1**), as these are important factors in understanding Ca^{2+} release and dysfunction in R1051 mutants.

Finally, when considering cluster size, it is also important to consider the density of RyR2 in the droplet mixture, as this could artificially affect the propensity for RyR2 to form clusters by forced proximity of channels. Measuring the concentration of hRyR2 in these preparations is not straightforward; while total protein concentration can be determined by absorbance at 280nm or through use of assays (such as a BCA Assay), this does not give an actual hRyR2 concentration. This is due to the sucrose density centrifugation method (**Section 2.2.14**) used to purify hRyR2 in this study; this preserves channel function, however as it relies on density alone to isolate hRyR2 it does not produce 'clean' protein. This is a compromise with alternative methods that can be used for purification of hRyR2 such as ion-exchange chromatography or affinity chromatography that are more specific and would allow for exact concentrations of hRyR2 to be calculated but produce a lower yield of protein (Hu et al. 2021). In practice, visual comparison of concentration of Ca^{2+} flux spots in DIBs was used, and the dilution of protein added to the droplet mix was adjusted to give an approximate similar concentration. However, the actual number of populations is likely higher as not all channels are active at any given time. A potential solution would be to assess eGFP fluorescence; this could be used as preliminary step before recording (to overcome issues with photobleaching as discussed above) to determine the correct dilution of hRyR2 in the droplet mixture to ensure more comparable hRyR2 concentrations between different protein preparations. It was attempted to artificially increase the concentration of channels by corralling the proteins by manipulation of the bilayer (Gross et al. 2011). In practice, this requires the electrode in the droplet to be gently lifted up, which lifts the droplet with it and reduces the area of the droplet in contact with the substrate agarose, therefore reducing bilayer size. With other proteins and peptides this has successfully corralled them into a smaller area (Gross et al. 2011), however hRyR2 does not appear to behave in the same way, likely due to its large size preventing it from moving so freely through the bilayer. This prevented corralling of hRyR2 and as such the density could not be adjusted during experiments.

5.4.3 Novel Ca^{2+} release behaviours in R1051P-hRyR2 populations indicate dysfunction that could cause Ca^{2+} leak

A total of six behaviour groups were identified across WT and R1051-mutant hRyR2 Ca^{2+} flux spots, four of which were observed in both WT and mutant populations, and two which were only observed in the mutant (predominantly R1051P, and to a lesser extent R1051C; **Figure 5.7**). The four conserved behaviours, labelled 'Infrequent', 'Frequent', 'Fluctuating' and 'Always On', are characterised by increasing activity, from sporadic Ca^{2+} release between periods of inactivity, to steady Ca^{2+} release with no shutdown periods (**Figure 5.4**). The emergence of two seemingly novel behaviours in the mutants is a significant event and suggests mutation at this location does impact RyR2 function at the population level. This dysfunction becomes more apparent as the estimated number of active channels increases with an increased proportion of these behaviours in larger clusters (**Figure 5.7**), despite no significant difference in estimated cluster size (**Figure 5.5**).

The 'Stepped' and 'Inverted' behaviours observed exclusively in mutant-hRyR2 are both characterised by rapid step-wise transitions between relatively stable high or low Ca^{2+} flux states, suggestive of increased cooperativity between active channels in the cluster (**Figure 5.4**) and a tendency for higher activity (**Figure 5.8B**). Concerted opening and closing of channels in a cluster has been demonstrated previously (Marx et al. 2001), and this behaviour appears to be an amplification of that with defined 'on' and 'off' levels, as if most (if not all) active channels are acting in unison. The main distinction between the 'Stepped' and 'Inverted' behaviours are the dwell times; 'Stepped' traces had longer dwell times at their low activity level (usually equivalent to no Ca^{2+} release activity) than 'Inverted', which tended to return to high activity quickly (~1 second) after low activity periods.

While not exclusive to the mutant, the prevalence of the 'Always On' behaviour is also more than three-times greater in R1051P populations than the WT (8.8% of R1051P spots compared to 2.3% of WT). This behaviour is characterised by high activity with consistent Ca^{2+} release and no 'off' time, although some fluctuation is observed (**Figure 5.8**). This tendency for consistent and high levels of Ca^{2+} release does point to a degree of cooperativity, however this is less defined than in the 'Stepped' and 'Inverted' behaviours. Perhaps more importantly however is the lack of termination of Ca^{2+} release observed in the 'Always On' category. The activation and termination of Ca^{2+} release, both at the single

channel level and population level, is an important regulatory factor in CICR and Ca^{2+} spark propagation which is essential for normal heart function. The absence of this, as is apparent in 'Always On' populations and to some extent in the 'Inverted' population, may therefore be an important factor in impaired Ca^{2+} release from R1051P-hRyR2.

It is important to note that this aberrant behaviour occurs in the absence of a depleting Ca^{2+} store (i.e. the SR load), as there is excess Ca^{2+} in the rehydrating agarose (0.33 M; simulates luminal Ca^{2+}). This highlights that dysfunction of these mutants is a function of hRyR2 itself and not a product of depleting store influencing Ca^{2+} release. These conditions are representative of conditions similar to diastole, with high luminal [Ca^{2+}] but low cytosolic [Ca^{2+}]. This means that Ca^{2+} release from populations in DIBs essentially mimic SOICR and indicates that this is severely dysregulated in large populations of R1051P channels. This dysregulated Ca^{2+} is likely to contribute to diastolic Ca^{2+} leak which is a causative factor in arrhythmias (Wehrens 2007; Kolstad et al. 2018; Dridi et al. 2020).

One experimental factor that might potentially have impacted channel activity is the voltage. The voltage applied to the bilayer across different recordings was not consistent, as in some droplets no activity was observed at -30mV (the planned experimental voltage) relative to the luminal electrode. The voltage was therefore adjusted to a more negative potential (up to -90mV) to prompt channel activation. This was most notable in droplets containing WT-hRyR2 in which very little activity was observed at -30mV (1 droplet (3 Ca^{2+} flux spots) of a total 20 droplets (41 Ca^{2+} flux spots)). This contrasts with all 3 R1051- mutants, which displayed activity in the range of 0mV to -60mV. Activity, behaviour and estimated cluster size were retrospectively assessed in association with voltage and revealed no significant association (**Figure 5.9**). As RyR2 is not a voltage-gated channel this was not unexpected, however increasing the voltage increases the driving force for ion migration so this could be expected to increase Ca^{2+} release. While this doesn't appear to be the case, it does seem that increasing the voltage may initiate channel activity in the WT, and that the mutant is more active even with a lower drive. Any future works should bear this in mind and strive to use comparable voltages, or further research should be conducted on the relationship between voltage and hRyR2 population activity and Ca^{2+} release behaviour.

A.

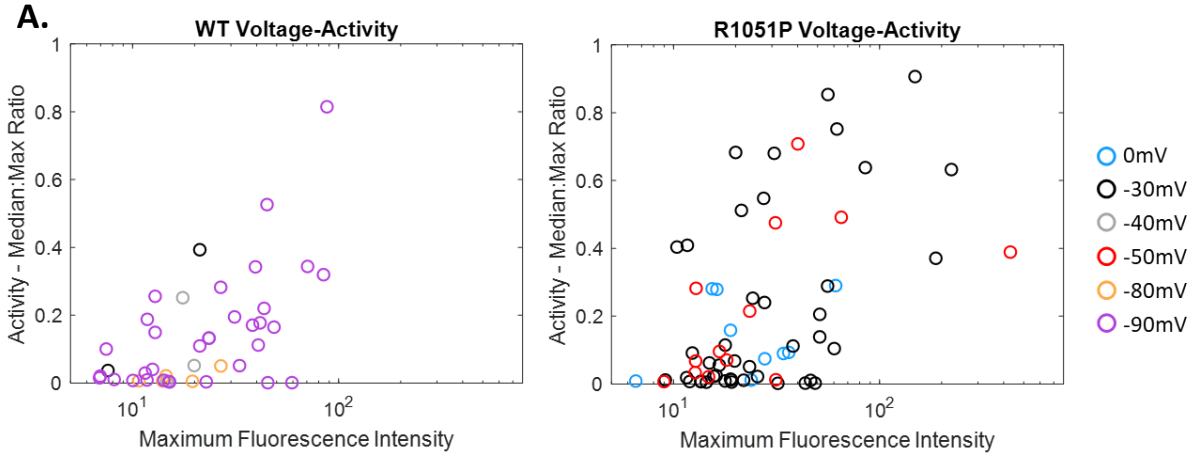

B.

WT	-30mV	-40mV	-80mV	-90mV
≥1 channel	2	3	5	23
≥2 channels	0	0	2	7
Cluster	0	0	1	1

R1051P	0mV	-30mV	-50mV
≥1 channel	10	30	11
≥2 channels	1	9	1
Cluster	0	5	1

C.

WT	-30mV	-40mV	-80mV	-90mV
Infrequent	0	1	2	10
Frequent	1	0	3	6
Fluctuating	1	2	2	16
Always On	0	0	1	0
Inverted	0	0	0	0
Stepped	0	0	0	0

R1051P	0mV	-30mV	-50mV
Infrequent	2	10	1
Frequent	1	15	3
Fluctuating	4	10	6
Always On	0	5	2
Inverted	0	4	1
Stepped	3	1	0

Figure 5.9. Relationship between applied voltage and estimated cluster size, channel activity,and behaviour in WT and R1051P-hRyR2 populations recorded in DIBs. A. Scatterplot showing the relationship between Maximum Fluorescence Intensity and activity for WT (left) and R1051P (right), with different voltages indicated by different colour markers. No significant association between voltage and activity was found (Kruskall-Wallis with Dunn's post hoc test, WT p-value = 0.100, R1051P p-value = 0.836). **B**. Table showing the number of Ca^{2+} flux spots classified as each cluster sizes for all recording voltages for WT (left) and R1051P (right). No significant association was found between voltage and cluster size (Fishers Exact Test with Monte-Carlo simulation, WT p-value = 0.740, R1051P p-value = 0.663). **C.** Table showing the number of Ca^{2+} flux spots classified as each Ca^{2+} release behaviour for all recording voltages for WT (left) and R1051P (right). No significant association was found between voltage and behaviour (Fishers Exact Test with Monte-Carlo simulation, WT p-value = 0.299, R1051P p-value = 0.207).

Taking all of this into account, it appears that R1051P-hRyR2 populations result in distinct dysfunctional Ca^{2+} release behaviours that are characterised by increased cooperativity and impaired termination at high luminal [Ca^{2+}]. While this behaviour is somewhat reminiscent of the proposed effect of coupled gating, which is hypothesised to keep channels closed during diastole to prevent Ca^{2+} leak but promote concerted opening during systole to facilitate Ca^{2+} spark generation (Marx et al. 2001), this does not appear to be the case with R1051P populations. Instead, under the diastole-like conditions of DIBs, R1051P seems to increase Ca^{2+} release via hRyR2 which would contribute to Ca^{2+} leak. It is unclear how this might manifest under systolic conditions; it is possible that the increased cooperativity of channels could assist in termination of Ca^{2+} release if one channel spontaneously closes and the other 'cooperate', however it is also possible that the opposite is true and systolic Ca^{2+} release may be sustained in R1051P clusters. This latter seems more likely given the increased prevalence of the 'Always On' behaviour in R1051P that appears to show impaired termination of Ca^{2+} release; this could be an indication that activity of a single channel could lead to activity of others in the cluster. Either way, results thus far demonstrate significant dysfunction of R1051P-hRyR2 at the population level.

5.4.4 Possible mechanisms of R1051-mutant hRyR2 dysfunction

As discussed above, the increased cooperativity of the 'Inverted', 'Stepped', and to a degree the 'Always On' behaviours points to enhanced coupled gating and an overall higher activity level at high luminal [Ca^{2+}] that could cause Ca^{2+} leak. This appears to be associated with increased cluster size, as these behaviours represent a higher proportion of the behaviours observed in larger clusters (**Figure 5.7**), despite no significant difference in cluster size of WT and R1051P-hRyR2 (**Figure 5.5**). What is unclear is how this dysfunction arises, but there are several possibilities that seem plausible from the data.

One possible mechanism is altered allosteric communication between channels, which is predicted to contribute to coupled gating within clusters, although this has yet to be proven (Stern et al. 1999; Marx et al. 2001). R1051 is located in P1, and it was hypothesised that mutation might affect the ability of P1 to interact in the inter-tetramer interaction during clustering. As discussed, this does not appear to have a direct effect on cluster size for R1051P, but it is possible that mutation impacts the inter-tetramer interaction in more subtle ways that have knock on effects on Ca^{2+} release. In this scenario, mutation appears to

result in enhanced cooperativity of channels (i.e. the 'Stepped' and 'Inverted' behaviours), which would be exacerbated in larger clusters due to an increased number of these altered interactions; this could be a logical explanation for why such behaviours become more apparent as cluster size increases. This is significant as research has shown silent Ca^{2+} leak is a result of reduced cluster size and loss of stabilising interactions, and that larger clusters protect against this (Sobie et al. 2006; Kolstad et al. 2018). One study did suggest larger clusters have an increased likelihood of Ca^{2+} leak, although this was in the context of Ca^{2+} sparks and involved far larger clusters of RyR2 (10-50 channels being considered moderate size, and >70 being considered large) and this was attributed to the increased likelihood of a small number of channels being open resulting in silent Ca^{2+} leak (Galice et al. 2018). This suggests that an important regulatory mechanism in hRyR2 might be heavily impaired by R1051P mutation, and might reveal a novel mechanism of dysfunction that can contribute to arrhythmias and cardiomyopathies.

It is also possible that the density and spatial organisation of clusters may be affected in R1051 mutants, which further complicates the RyR2 cluster size-function relationship. Of the two main organised RyR2 cluster configurations, the checker-board (corner-to-corner) arrangement of tetramers is associated with lower channel density, which is promoted by phosphorylation which in turn is associated with increased cluster size, dissociation of FKBP12.6 (Asghari et al. 2014; Asghari et al. 2020) and increased Ca^{2+} leak (Marx et al. 2000; Wehrens et al. 2006). Conversely, denser packing of RyR2 via a side-by-side arrangement is associated with decreased cluster size, increased FKBP12.6 binding, improved channel stability and reduced Ca^{2+} leak (Wehrens et al. 2004a; Asghari et al. 2020). Further to this, RyR2 configurations are not limited to these two arrangements; less regular and more dispersed organisation of RyR2 has also been demonstrated with super-resolution microscopy, highlighting the complexity of cluster formation (Asghari et al. 2014; Asghari et al. 2020). In disease, remodelling of clusters has been observed to cause 'fragmentation' of CRUs into more numerous, smaller (but still functionally associated) clusters during HF, which promotes Ca^{2+} leak (Kolstad et al. 2018).

Finally, it is possible that the dysfunction observed in DIBs is an exaggeration of dysfunction at the single channel level. The results from small clusters (≥1 channel) in DIBs suggest that Ca^{2+} release from R1051P and the WT are comparable at this level (**Figure 5.7**), so this

appears unlikely, however in the absence of true single channel data this cannot be ruled out; this is discussed in **Chapter 6**. With such a complex size-arrangement-function relationship, it is clear that a much more detailed assessment of R1051P cluster organisation is needed to understand the mechanism of dysfunction. DNA-paint would be a suitable method to investigate the spatial arrangement of RyR2 in DIBs and could be used in concert with optical and electrophysiological data to better understand the circumstances under which aberrant Ca^{2+} release behaviours occur and elucidate the mechanism of dysfunction.

5.4.5 Conclusions

These results show a clear difference in Ca^{2+} release behaviour of some R1051-mutant hRyR2 populations compared to the WT. Of the three mutants of interest, R1051P appeared to form clusters of a similar size to WT-hRyR2, however it exhibited two aberrant Ca^{2+} release behaviours not seen in the WT that were characterised by increased cooperativity. These behaviours, along with the 'Always On' behaviour that was observed more frequently in R1051P populations, were found to be more prevalent in larger clusters and had generally high Ca^{2+} release activity that is indicative of diastolic Ca^{2+} leak. On the other hand, R1051C and R1051H were shown to form larger clusters than WT-hRyR2 but exhibit behaviours largely similar to the WT, although R1051C also exhibited the aberrant 'Stepped' behaviour seen in R1051P. This interpretation is however limited due to their small sample size.

Given the role of the P1 domain in the inter-tetramer interaction that facilitates cluster formation, it is proposed that the differences observed in R1051-mutants are a product of changes to this interaction. This may be due to altered allosteric communication between channels that increases cooperativity, although this is hard to prove without understanding the mechanism of allosteric communication. This could in part be clarified by an improved understanding of cluster size and organisation, which could be accomplished using DNA-paint technology; preliminary experiments are ongoing and as such no data is yet available, however this has demonstrated that DNA-paint can be accomplished in the DIB system. The possibility of dysfunction at the single channel level also remains (**Chapter 6**), however the results so far show that WT and R1051P exhibit largely similar behaviours at the 'single channel' (≥1 channel) level (**Figure 5.7**). In conclusion, Ca^{2+} release behaviour exhibited by R1051P-hRyR2 is novel in its characteristics and demonstrates a clear difference in function between R1051P and WT-hRyR2 at the population level.

Chapter 6

Analysis of single channel gating of R1051P-hRyR2 and WT-hRyR2

6.1 Introduction

6.1.1 Analysing single channel function in artificial lipid bilayers

The effects of RyR2 mutation are wide reaching and there are many techniques that can be used to determine how they contribute to disorders such as CPVT or cardiomyopathy. However, elucidating the exact mechanism of dysfunction is complicated by the array of other processes involved in controlling cardiac and cardiomyocyte function, in particular, the interplay between the SR load and RyR2 Ca^{2+} sensitivity can make the exact role of RyR2 difficult to determine in experiments which assay Ca^{2+} release alone. It is therefore necessary to isolate RyR2 function at its most basal level to begin to understand the effect of mutation, which can be done via single channel analysis. Due to its intracellular location on the SR membrane, traditional patch clamp techniques cannot be used to assess single channel function of RyR2 (Laver 2001). Instead, RyR2 can be incorporated into planar lipid bilayers, acting as artificial membranes, and the current flowing through the channel measured in real time (Favre et al. 1999). This allows for detailed analysis of channel gating that can be used to determine channel function in the absence of regulators or other channels (i.e. in the absence of clustering, see **Chapter 5**), with the added benefit of being able to add modulators to observe their effects on channel function in isolation (Laver 2001; Williams et al. 2001).

Single channel experiments can be carried out using either solubilised purified proteins or native membrane vesicles containing bound accessory proteins and other ion channels. While native membrane vesicles may provide a more physiological environment for RyR2 by maintaining regulatory accessory protein interactions, the introduction of other ion channels (namely K^+ channels) can distort current recordings and therefore interfere with results. This can be circumvented by using divalent permeant ions, including RyR2's endogenous activator Ca^{2+}, however monovalent permeant ions increase the signal-to-noise ratio and improve the amplitude resolution of gating events (Williams et al. 2001). Alternatively, solubilised and purified protein can be used in single channel experiments to look at channel function in isolation. The process of solubilisation and purification is not straightforward, requiring a highly optimised process to successfully isolate channels at a suitable yield for experiments. There are of course inherent issues with removing RyR2 from its native environment due to the use of detergents, however the experimental procedure

used in this study has been optimised to use the lowest possible detergent concentration (**Section 2.2.14**), maintaining channel function and Ca^{2+} sensitivity (Laver et al. 1995; Mukherjee 2014). Solubilisation of RyR2 also removes accessory proteins that regulate its function, and while this might not reflect the environment of the channel *in vivo* compared to native vesicles, it allows functional defects inherent to the channel itself to be characterised and allows for more precise control over the regulators present, as well as providing an improved signal-to-noise ratio. Taking this into consideration, purified RyR2 incorporated into an artificial planar lipid bilayer system serves as a useful method in determining single channel function of RyR2 and, in combination with other techniques that study function at different organisational levels, can contribute to an overall understanding of RyR2 channel function and the impact of mutations.

6.1.2 Idealisation of RyR2 single channel currents

Single channel recordings in planar lipid bilayers monitor electrical current through RyR2 in a similar way to standard electrophysiological techniques like patch clamp, and the resulting traces show gating of the channel as transitions between the open and closed state. During analysis, the amplitude and duration of each state transition is used to characterise channel activity. One of the primary parameters of interest from single channel recording is the P_O which describes how likely a channel is to be open at any given time, where a P_O of 1 is a channel that is always open and a P_O of 0 represents a channel that is always closed. This however is a simplistic view of channel gating, as a comparable P_O can be used to describe channels with drastically different gating (**Figure 6.1**). To better understand the precise gating of channels, modelling can be used to build gating schemes that mathematically describe RyR2 function at the single channel level. This gives a much more in-depth look at the specifics of gating and reveals nuanced differences in channel function that are not described by P_O and can help determine the impact of hRyR2 mutations.

One of the first steps in determining P_O and building models is idealisation, where the raw data is processed to characterise all opening and closing events. There are multiple methods that can be employed for this; Hidden Markov Models (HMMs) are one of the most frequently applied analysis techniques and were used to analyse the data in this study in QuB analysis software (Milescu et al. 2000). HMMs are employed to model systems with a 'hidden' state (i.e. whether the channel is open or closed) that generates observable data

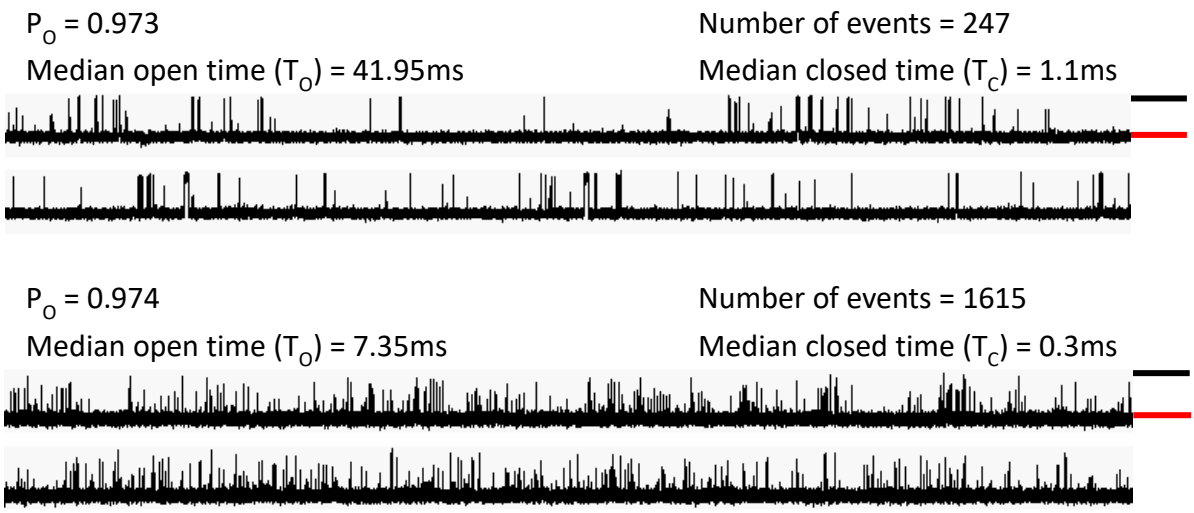

Figure 6.1. Example of different channels gating at the same P_O but with notable visible differences in behaviour. Two traces were selected with a similar P_O (0.973 vs. 0.974) that demonstrate visible differences in the frequency and dwell time of events. The closed state is indicated by the black bar; the open state is indicated by the red bar. In the top trace (P_O = 0.973) there are fewer events, but the dwell time of both the open and closed states are longer. In the bottom trace (P_O = 0.974) there are many more events, but both open and closed events have a shorter duration. This shows that, while the frequency, duration and distribution of events is different in each trace, the P_O calculation simplifies this into a measure of the channel's activity but doesn't capture the nuances of RyR2 gating.

(i.e. the current through the channel) that is accompanied by extraneous noise. This is a memoryless system and uses the current state to predict a future state based on probabilities. For analysis of RyR2, this can first be used for idealisation of raw data assuming a simple open to closed model. Additional open and closed states can then be added, and the model fitted to the new scheme to determine the likely gating kinetics and identify states with different dwell times (i.e. how long a state is) and frequencies (i.e. how often the state is visited).

The gating kinetics of WT-hRyR2 have been studied extensively before and a comprehensive minimal model of its gating at sub-activating, activating and saturating Ca^{2+} conditions was constructed by Mukherjee et al., (2012) (**Figure 6.2**). Each model contains at least three open states and three closed states, however the organisation of these differs depending on the channel P_O, which corresponds to $[Ca^{2+}]$cyt. All possible channel states in the Mukherjee et al., (2012) models are listed below;

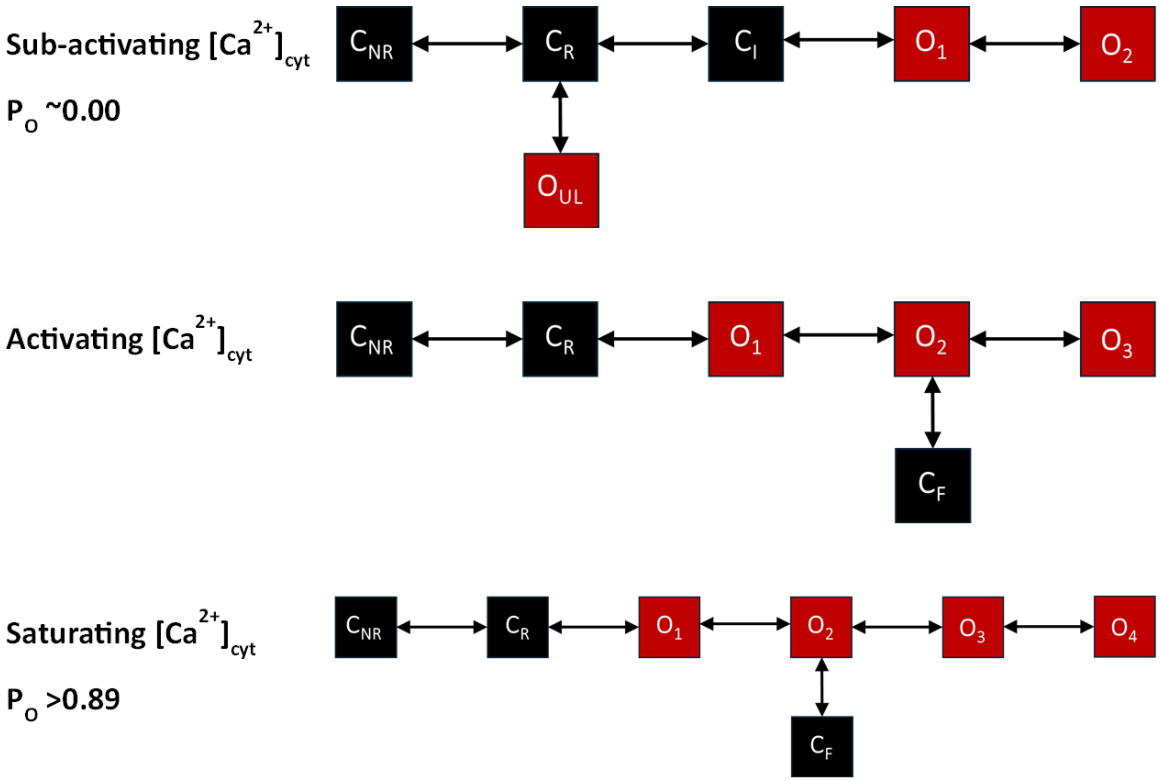

Figure 6.2. Gating models of WT-hRyR2 at sub-activating, activating and saturating $[Ca^{2+}]_{cyt}$ from single channel recording. The gating models demonstrate the changing kinetics of WT-hRyR2 gating in response to increasing $[Ca^{2+}]_{cyt}$. The sub-activating level contains two unique states; 'ligand bound' (C_I) and 'unliganded-open' (O_{UL}), that only manifest at low P_O. The activating model introduces a 'flicker' state (C_F), a short ligand-bound closed state likely resulting from ion pore collapse. This state persists in the saturating model, but this model is defined by an additional open state (O_4) that represents a stable open state. Modified from Mukherjee et al., (2012).

- 'Non-responsive' (C_{NR}) – a terminal closed state that does not directly transition to any open states.
- 'Responsive' (C_R) – a closed state able to transition to ligand-bound open states, responsive to ligand binding.
- 'Flicker' (C_F) – a short-lived closed state emerging from ligand-bound open states, likely as the result of Ca^{2+}-independent collapse of the ion pore.
- 'Ligand-bound' (C_I) – this closed state is only resolved at the sub-activating level and is an intermediate between C_R and the open states.
- 'Unliganded-open' (O_{UL}) – this open state is only resolved at the sub-activating level and likely occurs due to thermodynamic fluctuation.

- Ca^{2+} bound open states (O_1, O_2, O_3, O_4) – these states represent Ca^{2+} bound open states where O_1 has the lowest amount of Ca^{2+} bound and O_4 the greatest.

These models serve as a starting point to investigate the effect of regulatory accessory proteins or pharmaceuticals on RyR2 gating (Mukherjee et al. 2012), and they also provide a means to compare the gating of hRyR2 mutants at the single channel level. In the context of this research, modelling will be used to determine whether the R1051-mutants demonstrate different gating from the WT at the single channel level under saturating conditions, and whether changes to their gating could contribute to their overall dysfunction. This will be done in sub-activating (nominally 0 nM $[Ca^{2+}]_{cyt}$) and saturating (100 µM $[Ca^{2+}]_{cyt}$) conditions.

6.1.3 Potential impact of R1051-mutation on single channel function

As discussed previously (**Section 1.7.2**), R1051 is located in one of four α-helices in the 'C'-shaped P1 domain of RyR2 (also known as the clamp or RY1&2), on the corner of the tetramer. Its position is far removed from the C-terminal domain where the ion pore is located, neither is it in close proximity to the known Ca^{2+} binding sites in the central domain (Murayama et al. 2016; Xu et al. 2018) or at the interface of other domains; it is proposed to interact with FKBP12.6 or P1 on adjacent tetramers during clustering (Cabra et al. 2016). It was therefore hypothesized that mutation of R1051 would not significantly affect hRyR2 function at the single channel level.

6.1.4 Aims

Earlier chapters have probed the effect of mutation at R1051 (with a focus on R1051P) on hRyR2 at the population (**Chapter 5**) and whole cell level (**Chapter 4**), and this chapter aims to assess the impact of R1051P mutation at the single channel level. This will demonstrate whether dysfunction of this mutant is likely to arise due to alterations to single channel function, or whether higher level organisation such as clustering or interactions with accessory proteins is more likely to be responsible. The main aims of this chapter are as follows;

- Incorporate solubilised and purified WT and R1051P hRyR2 into planar lipid bilayers and record gating in saturated Ca^{2+} conditions (100 µM $[Ca^{2+}]_{cyt}$) to investigate function under systolic conditions. The ability of the channel to shut down in the

absence of Ca^{2+} (~0 nM $[Ca^{2+}]_{cyt}$) will also be assessed by chelating Ca^{2+} to determine any dysfunction in conditions that partially mimic diastole. The main mutant of interest is R1051P, with a secondary focus on R1051C and R1051H.

- Build gating models for WT and R1051P-hRyR2 to compare their gating kinetics and determine any difference in function at the single channel level under saturating Ca^{2+} conditions.

6.2 Materials and Methods

6.2.1 Materials

- Styrene copolymer cup – *cis* chamber.
- Perspex block – *trans* chamber.
- Bovine heart phosphatidylethanolamine (PE) (Avanti) – made as 50 mg/mL stock in chloroform and stored at -20°C. Made into working stocks of 35 mg/mL in n-decane on the day of experiments.
- Recording solution – 210 mM KCl, 20 mM HEPES, pH 7.4.
- LiCl – 3 M for electrode wells.
- Agar salt bridge - 2% w/v agar in 3 M LiCl in a curved glass capillary.
- KCl – 3 M stock to create osmotic gradients.
- EGTA – 5 mM stock for buffering *trans* chamber; 90 mM stock for buffering.
- Nitrilotriacetic acid (NTA) – 90 mM stock for buffering.
- EMD-41000 – caffeine analogue.

6.2.2 Single channel recording in artificial lipid bilayers

Bilayers are established in a cup and block system representing the cytosolic (*cis*) and luminal (*trans*) chambers (**Figure 6.3**). The cup (**Figure 6.3A**) is made of a styrene copolymer with a concave cavity on the outside that forms into a thin septum with a 200µm hole drilled in the centre, across which the artificial bilayer is created. The block (**Figure 6.3B**) contains a rectangular cavity (*trans* chamber) and an adjoining circular cavity in which the cup can be placed, with the 200µm hole facing the *trans* chamber. The cup and block system and electrical components are set up within a faraday cage on a vibration isolation table to reduce mechanical noise and electrical interference. A magnetic stirrer under the cup and block allows for mixing of solutions in the *cis* chamber with minimal interference to the bilayer setup. The electronic system is connected to the cup and block via two silver wire electrodes coated in silver chloride that are placed in wells within the block containing 3M LiCl (**Figure 6.3C**). The wells are connected to the recording solution via agar salt bridges.

Bilayers were formed using PE (Avanti) stored at -20 °C as 50 mg/mL stocks in chloroform. For each experiment, an aliquot was taken out and dried in a stream of N_2, then resuspended in n-decane to a final concentration of 35 mg/mL. Before assembling the cup and block, lipid was painted across the inside of the 200µm hole of the cup using the back of

modified Pasteur pipette (termed 'painting stick') and allowed to dry; this is called priming and helps to disperse the lipid across the hole. The cup was then placed into the block and recording solution added to the *cis* (500 µL) and *trans* (1000 µL) chambers. The painting stick was recoated in a small amount of lipid and dragged upwards across the hole on the *cis* side to disperse lipid across the hole to form a bilayer, which should occur spontaneously due to the natural properties of the lipid (White 1986; Laver 2001). The *trans* chamber was held at virtual ground while the *cis* chamber was clamped at different voltages relative to the ground, so that the lipid bilayer can act as a capacitor that charges up and discharges with changes in membrane potential. As capacitance of the lipid film is inversely proportional to its thickness, formation of bilayers was monitored in real-time on Acquire v5.0.1 software (Bruxton) by application of a square wave pulse oscillating between ±4mV and visualising capacitance spikes in response to thinning of the membrane; capacitance spikes increase in size to ~200pA as the lipid approaches a planar bilayer (Laver 2001).

Channels were incorporated by addition of a small volume (1-5 µL dependent on preparation) of purified recombinant hRyR2 to the *cis* chamber. The exact concentration of purified protein in the preparation is unknown as it is so low that it is unquantifiable by most biochemical means. However, the aim is to incorporate a single RyR2 channel into the bilayer, something that can be quantified during single channel recording. Due to the structure of RyR2 and its large cytosolic domain, incorporation always occurs in the same orientation with the cytosolic domain facing the *cis* chamber and the luminal domain facing the *trans* chamber. To aid channel incorporation, an osmotic gradient from the *cis* to *trans* side was created by addition of 3 M KCl (2 x 100 µL) to the *cis* chamber and stirred using a magnetic stirrer, after which purified hRyR2 was added. During additions, the recording chambers were isolated from the electronic set up using a magnetised reed switch that prevents breaking of the bilayer during adjustment of the recording solutions. Channel incorporation was monitored using Acquire software. Once it was confirmed that a channel had incorporated, channel shutdown and activation experiments were performed.

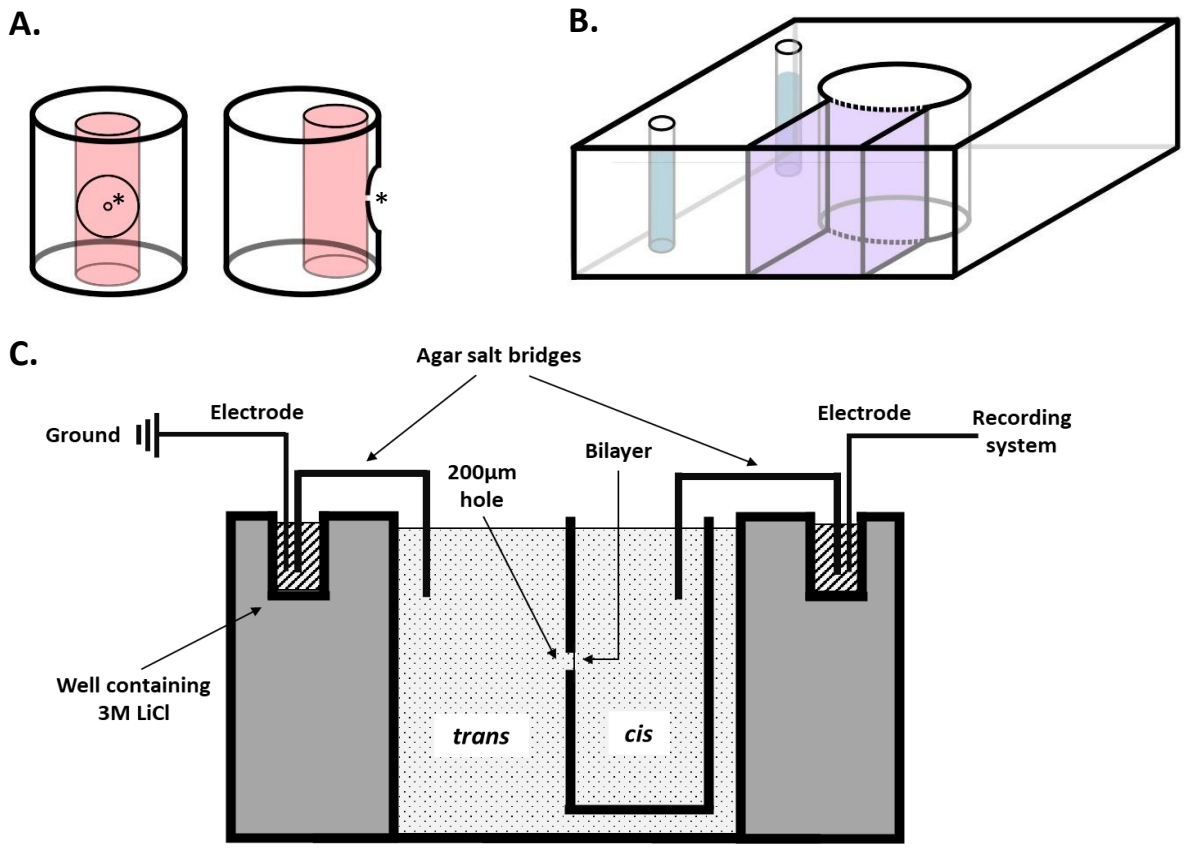

Figure 6.3. Schematic of cup and block system used in artificial lipid bilayer setup. A. Schematic of cup from front and side view. Red shading indicates the *cis* chamber that is filled with buffer during experiments; the 200µm hole is indicated by *. **B.** Schematic of the block. Small blue shaded wells indicate the LiCl solution; purple shaded area indicates the *trans* chamber. The cup is inserted into the circular chamber with the 200µm hole facing the *trans* chamber. **C.** Diagram shows a basic cross section of the main set up. Channels are added to the *cis* chamber and insert so that the cytosolic domain faces the *cis* chamber. Electrodes connect to an electronic recording system to measure channel gating.

6.2.3 hRyR2 channel shutdown and activation

After incorporation of a single channel, the voltage was turned to 0mV, the stirrer turned on, and the reed switch placed to isolate the chambers before the *cis* chamber was perfused with recording solution (2.5x *cis* chamber volume) using a peristaltic pump to restore symmetrical conditions. After perfusion the reed switch was removed, the stirrer and oscillator were turned off and the voltage adjusted to +30mV, which provided a sufficient signal-to-noise ratio for event detection. This meant that under symmetrical ionic conditions the flow of ions was in the *cis* to *trans* direction, thus limiting the effect of Ca^{2+} flow on the Ca^{2+} concentration in the cis chamber (equivalent to $[Ca^{2+}]_{cyt}$). The *trans* chamber was buffered with 25 µM EGTA (5 µL of 5 mM EGTA stock in 1000 µL *trans* chamber volume) to give a free $[Ca^{2+}]_{lum}$ of ~ 50 nM. The *cis* chamber was then buffered to ~0 nM free $[Ca^{2+}]_{cyt}$ (approximately 0.3 nM, calculated using the MaxChelator app (https://somapp.ucdmc.ucdavis.edu/pharmacology/bers/maxchelator)) using 1 mM EGTA and 1 mM NTA (5.5 µL from 90 mM stocks); both chelators were used to ensure good Ca^{2+} buffering in both the low nanomolar range (EGTA) and the high micromolar to millimolar range (NTA). These conditions should result in the channel being closed due to sub-activating levels of Ca^{2+} on both the cytosolic and luminal sides. Channels were recorded for ~1 minute before proceeding.

$CaCl_2$ was added to the *cis* chamber to reach 100 µM free $[Ca^{2+}]_{cyt}$ (15.1 µL of 50 mM $CaCl_2$ stock in 500 µL *cis* chamber) and the channel recorded for at least 1 minute. After sufficient data had been collected, up to 150 µM EMD-41000 (a caffeine analogue and RyR2 agonist (McGarry and Williams 1994)) was added to the *cis* chamber to attempt to maximally activate hRyR2 and reveal the total number of channels incorporated into the bilayer.

6.2.4 Maximal activation of hRyR2 channels present in the bilayer

In this scenario, a full channel shutdown to ~0 nM free $[Ca^{2+}]_{cyt}$ was not performed, and instead the *cis* chamber was perfused with recording buffer containing supplemental NTA (1 mM) and $CaCl_2$ (510 µM) to give a final free Ca^{2+} concentration of 100 µM. Channels were recorded at +30mV for at least 1 minute before addition of up to 150 µM EMD-41000 to confirm the number of channels present in the bilayer.

6.2.5 Analysis of channel gating

Single channel data recorded by Acquire were saved as .acquire files, which were opened in Review v5.0.1 (Bruxton) and saved as Axon Binary Format (.abf) files. These files were then loaded into Clampfit 8 software (Axon Instruments) where the 5kHz trace was isolated and sections of the data selected (to exclude times where the magnetic stirrer was turned on or where no channel was present) and saved again as .abf files that could be used for analysis in the QuB analysis suite v2.0.032 (Milescu et al. 2000). In QuB, data files were opened in the preprocessing window and visually inspected and cropped to remove any remaining periods of excessive noise, stirring, baseline drift and segments of channel activity that differed from the majority behaviour. This included atypical behaviours, for example long closed periods in an otherwise high activity channel (provided they represented <5% of the total recording time) which represent modal gating, a phenomenon that occurs intrinsically in RyR2 (Saftenku et al. 2001). This is to ensure homogeneity in the data to allow modelling to accurately capture the typical behaviour of the channel. The data files were re-extracted and then idealized using the *idl/base* function in QuB (**Figure 6.4**) with a dead time (T_d; represents the minimum length of an event to be detected) of 50µs (1x the sampling interval); this simplifies the data into discrete states. This produces several parameters describing the idealization of the trace including P_O, median open time (T_O) and median closed time (T_C).

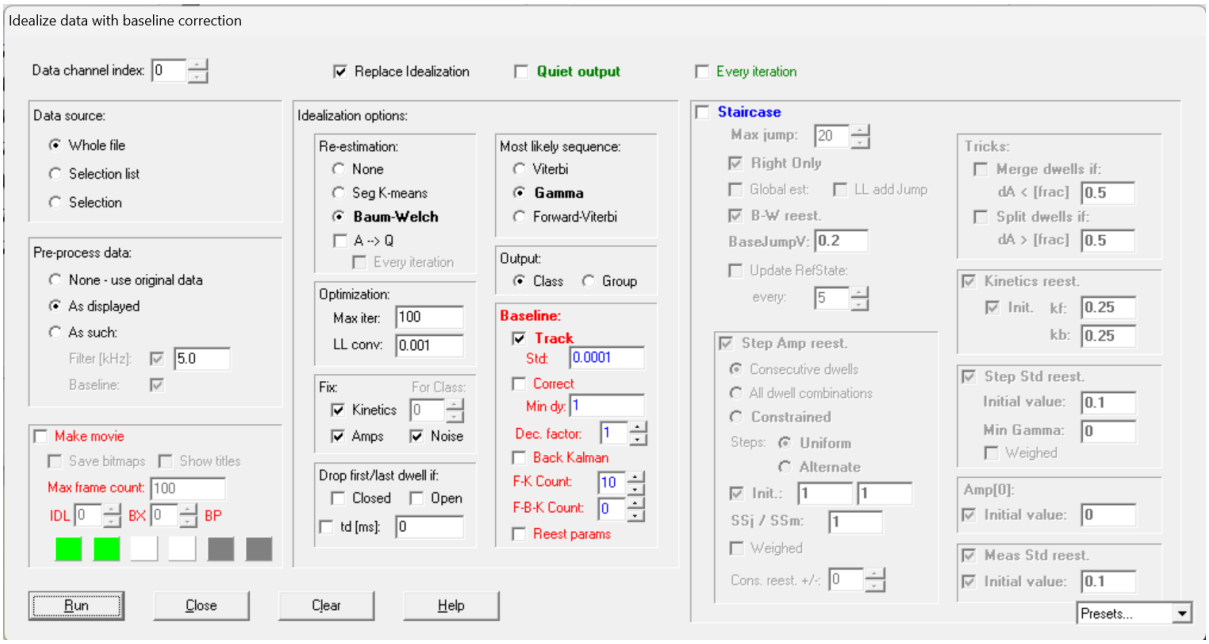

Figure 6.4. Settings applied in QuB using idl/base function. Settings were kept the same between all analyses and were based on QuB analysis of hRyR2 performed by Mukherjee et al, (2012).

6.2.6 Modelling of channel gating

QuB was used to model gating behaviour of channels after idealisation, using the MIL rates function on the idealised data. Initially, the MIL rates function (Qin et al. 1997) was applied to a simple closed-to-open model and a T_d of 120µs (2.4 x the sampling interval; Mukherjee 2014). The model was then refined by adding additional open and closed states to the model, ensuring that the fit (illustrated in QuB by successive histograms; **Figure 6.5**) improved with each change and that the maximum log likelihood value (LL) increased by at least 10 with each change (> 5 for 3rd additional state onwards) until adding more states did not improve the model or the LL (Mukherjee 2014). Multiple iterations of each model in which alternative states were added were tested for each trace to ensure that the final model was the best fit, based on the models described by Mukherjee et al., (2012).

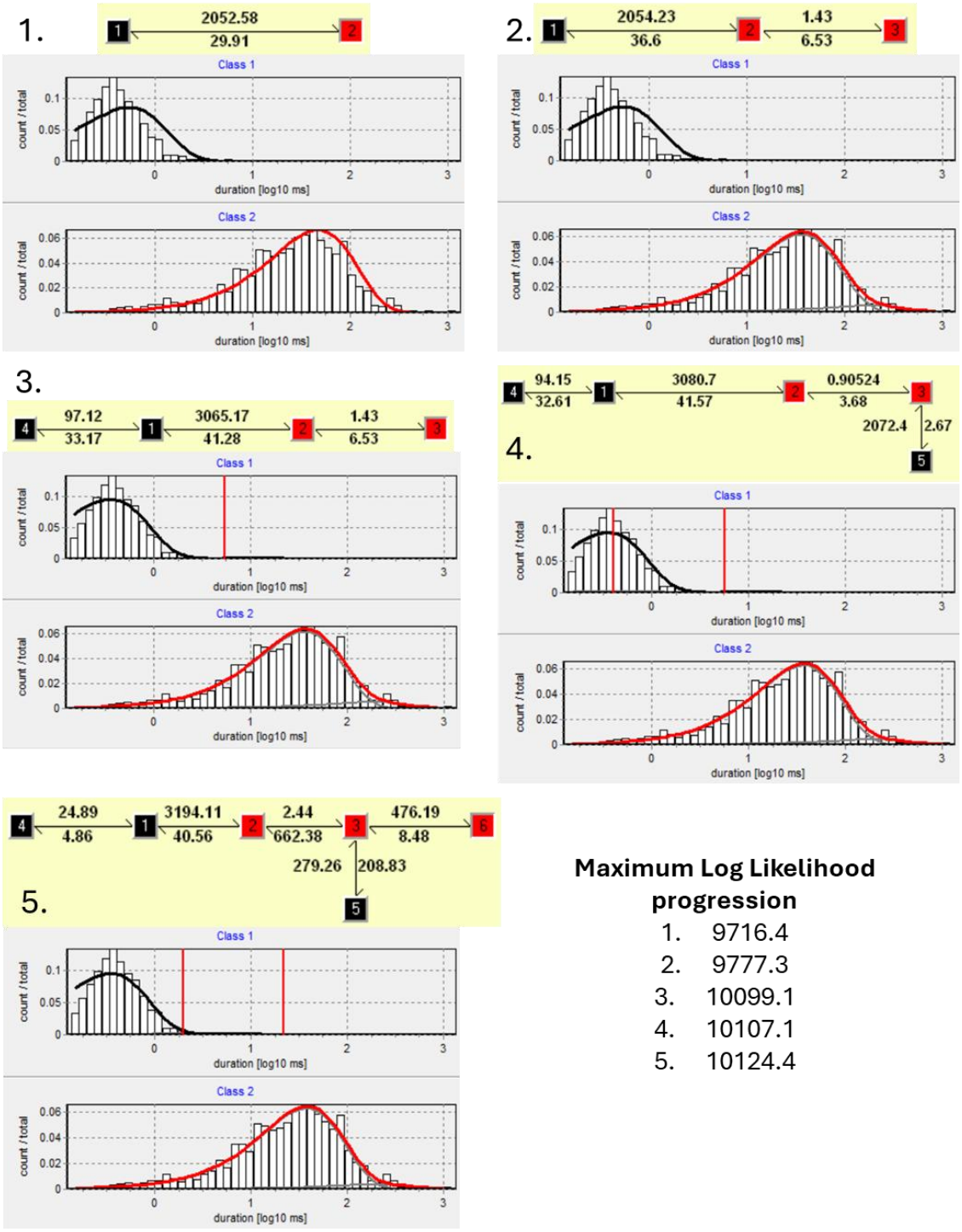

Figure 6.5. Progressive building of gating model in QuB based on histograms and Maximum Log Likelihood for WT-hRyR2. Histograms and models 1 through 5 show the addition of open (red) and closed (black) states to the starting 2-state model; open and closed states were added until the model better fit the data, as demonstrated by the histograms. Additional states also alter the LL, and an improvement to the model was considered only when the LL increased by >10 in the early stages (first 2 additional states) and then >5 in the later stages (3rd additional state onwards). Model taken from a recording of a WT-hRyR2 channel.

6.3 Results

6.3.1 Open probability and dwell times of R1051P-hRyR2 under saturating Ca^{2+} conditions are not significantly different from WT-hRyR2

P_O, T_O and T_C were compared for traces obtained from WT and R1051P-hRyR2 at saturating $[Ca^{2+}]_{cyt}$. Statistical analysis of WT and R1051P-hRyR2 gating revealed no significant difference in P_o, T_O or T_C at saturating $[Ca^{2+}]_{cyt}$ (**Figure 6.6**) (Mann-Whitney, $p < 0.05$). P_o distributions were generally split into two distinct groups; low (below 0.2) or high (above 0.9) P_o for both WT and R1051P-hRyR2 (**Figure 6.6A**). A P_O of at least 0.89 is expected for channels saturated with ligand (Mukherjee et al. 2012).

Comparing all 4 RyR2 variants statistically was not possible given R1051C and R1051H-hRyR2 were only analysed under unbuffered conditions in contaminant Ca^{2+} with an unknown Ca^{2+} concentration and only one data point is available for these mutants (**Figure 6.6D**).

Both WT and R1051P channels responded to 'shutdown' conditions (~0.3 nM free $[Ca^{2+}]_{cyt}$ due to chelation; this is below the threshold for RyR2 activation) in comparable ways resulting in few opening events (**Figure 6.7A**) and P_O measurements of between 0.00005 and 0.0008 (**Figure 6.7B**). It was noted that in some recordings activity appeared to cease completely after shutdown and no activity was observed after addition of Ca^{2+} or EMD, suggesting that the channel had potentially moved out of the bilayer. This prompted additional experiments to be conducted in which the system was perfused directly with buffer containing a saturating Ca^{2+} concentration (**Section 6.2.2**). Of five WT channels that were subjected to shutdown conditions, three showed no signs of activation and were presumed to have left the bilayer, one activated on addition of Ca^{2+} to a P_O of 0.995 and one activated to a P_O of 0.556. Of two R1051P channels that were subjected to shutdown conditions, one channel failed to reactivate on addition of Ca^{2+} but did reactivate after addition of EMD; the other channel reactivated after Ca^{2+} addition to a low P_O (**Figure 6.7B).**

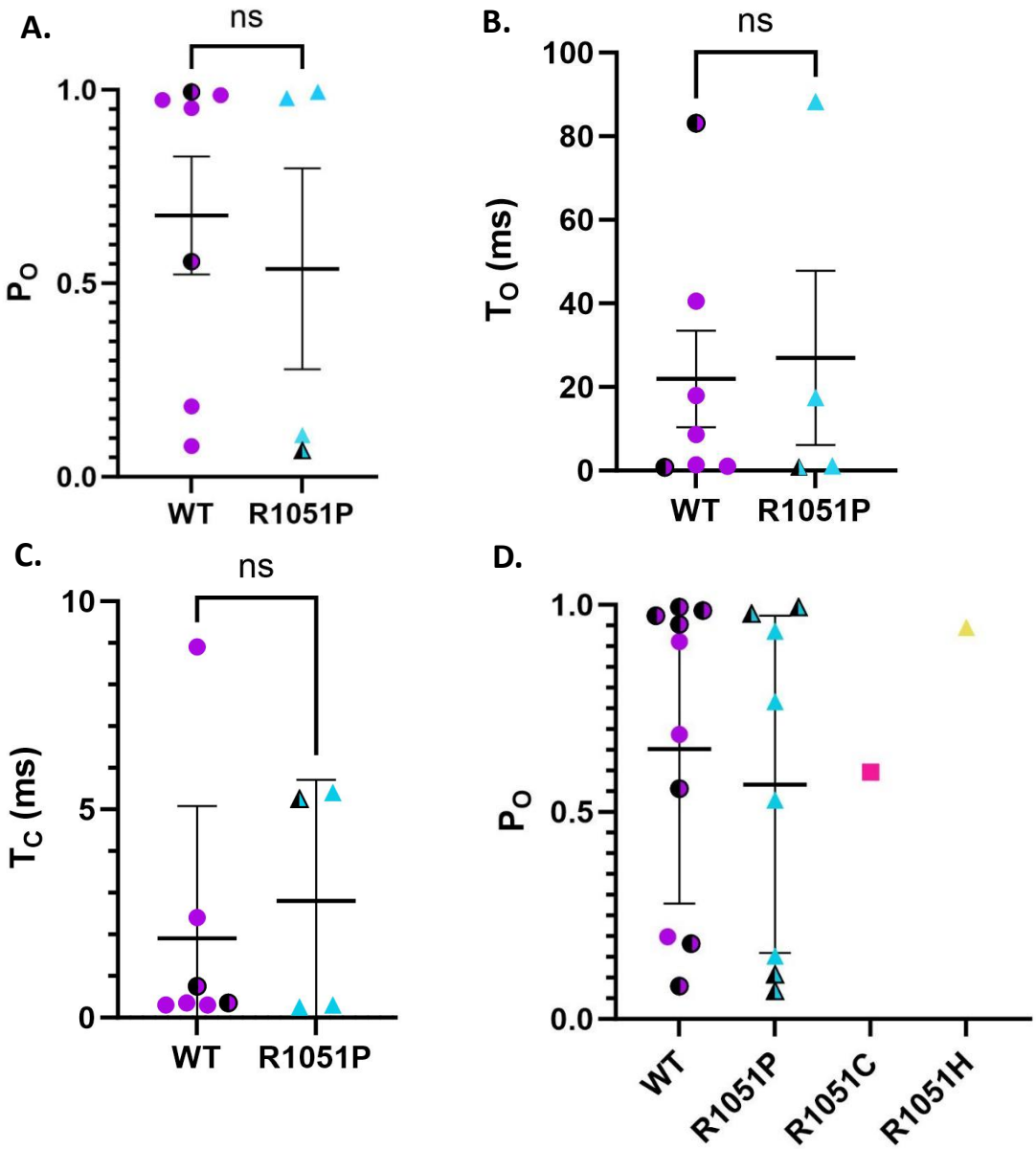

Figure 6.6. P_O, T_O and T_C of W-hRyR2 and R1051P-hRyR2 in 100 µM $[Ca^{2+}]_{cyt}$ were not significantly different. A. P_O of channels recorded in 100 µM $[Ca^{2+}]_{cyt}$ are comparable between WT and R1051P-hRyR2. Both hRyR2 variants demonstrate a mostly split distribution of values at the top and bottom of the range. Points partially filled with black indicate channels that were subjected to shutdown (~0 nM free $[Ca^{2+}]_{cyt}$) prior to activation with 100 µM $[Ca^{2+}]_{cyt}$. **B.** The T_O of WT and R1051P-hRyR2 channels recorded in 100 µM $[Ca^{2+}]_{cyt}$ was not significantly different. **C.** The T_C of WT and R1051P-hRyR2 channels recorded in 100 µM $[Ca^{2+}]_{cyt}$ was not significantly different. **D.** P_O of all channels recorded in both 100 µM $[Ca^{2+}]_{cyt}$ and unbuffered conditions; points partially filled with black indicate channels recorded in 100 µM $[Ca^{2+}]_{cyt}$. Statistical analyses in **A**-**C** were performed in GraphPad Prism 10.1.2 by Mann-Whitney tests; all results were non-significant with a p-value > 0.05. **A-C** WT n = 7 channels, R1051P n = 4, **D** WT n = 10, R1051P n = 8, R1051C n = 1, R1051H n = 1.

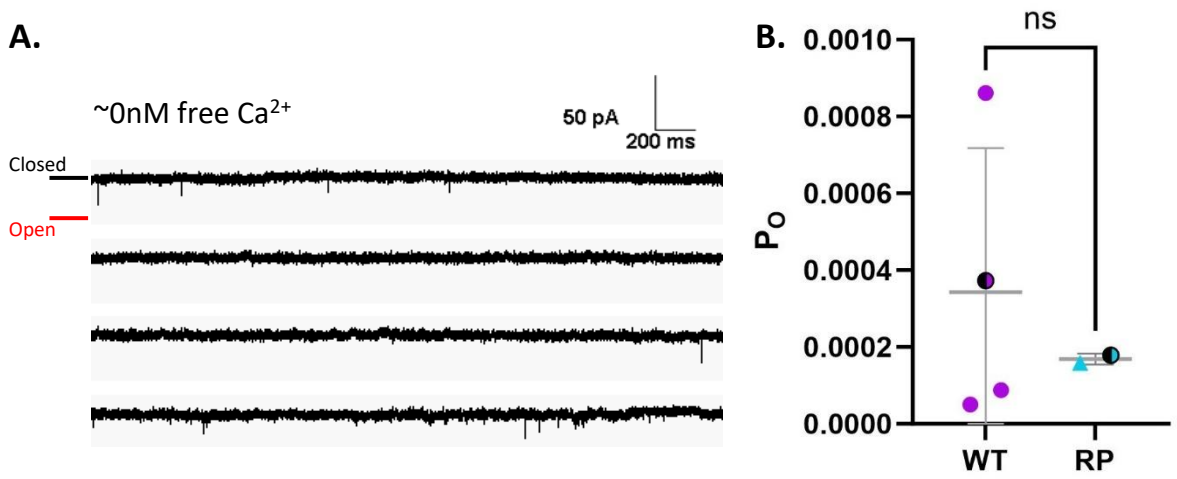

Figure 6.7. R1051P-hRyR2 and WT-hRyR2 show similar gating behaviours at sub-activating $[Ca^{2+}]_{cyt}$. A. Representative trace of channel activity after chelation, showing infrequent brief opening events. Recording taken from a WT-hRyR2 channel. **B.** Comparison of channel P_O for WT (n = 4 channels; one additional channel was subjected to shutdown conditions but not recorded; this channel reactivated on addition of 100 µM $[Ca^{2+}]_{cyt}$ to a P_O of 0.556) and R1051P (n=2). Points half filled with black indicate channels that reactivated on addition of Ca^{2+}; other data points indicate channels that either moved out of the bilayer or only reactivated on addition of EMD. Statistical analysis was performed in GraphPad Prism 10.1.2 by Mann-Whitney test; p-value = > 0.05; WT n = 4 channels, R1051P n = 2.

6.3.2 Modelling indicates no significant difference in the gating of R1051P-hRyR2 channels compared to WT-hRyR2

Detailed modelling of channel gating was performed to compare channels that had a high P_O following addition of 100 µM free $[Ca^{2+}]_{cyt}$ to determine whether more nuanced changes to gating contribute to overall dysfunction of the R1051P mutant. Modelling shows the different conformational states a channel visits, the dwell time of that conformational state, and how frequently they are visited. The first ~3000 events from six traces with high P_o (0.94 – 1) from WT (n=4) and R1051P (n=2) were modelled in QuB (**Figure 6.8**). An additional three channels (one each from WT, R1051P and R1051H) recorded in unbuffered experiments with unknown free Ca^{2+} but a high P_O indicative of saturation (P_O 0.91 – 0.95) were also modelled for additional comparisons (**Figure 6.9**).

All 6 channels recorded in 100 µM $[Ca^{2+}]_{cyt}$ fitted the 7-state model proposed by Mukherjee et al., (2012) for channels in saturating Ca^{2+} conditions (**Figure 6.8**). (Mukherjee et al. 2012).

Across all states, no significant difference in dwell time or frequency was detected between WT and R1051P channels when analysed by T-test (unpaired, two-tailed, p-value = >0.05) or Mann-Whitney test (for non-normally distributed data, p-value = >0.05) (**Appendix XII** and **Appendix XIII**). The variability of the data is relatively large, particularly in the dwell time and frequency of O_3 and O_4 (**Figure 6.8A**), but this likely reflects an overall difference in P_O (**Figure 6.6A**) and does not represent dysfunctional behaviour. It must be noted that due to the small sample size the statistical power to detect differences is limited. However, due to the inherent variability in gating kinetics between individual channels, statistical comparisons of modelled states are not frequently performed and therefore this was not considered a major limitation.

Of the three channels recorded in unbuffered Ca^{2+}, all three fitted the 6-state model proposed for activating concentrations of Ca^{2+}. The dwell time of C_R was increased and the dwell time of open states was decreased in all three channels (**Figure 6.9**) compared to those recorded in 100 µM free Ca^{2+} (**Figure 6.8**); C_{NR} was also increased in the unbuffered R1051P channel however this represents only a small percentage of the total closed time (**Figure 6.9B**). Overall, these differences can be attributed to the lower P_O of these channels than those recorded in 100 µM free Ca^{2+} and therefore do not reveal any notable differences between R1051P, R1051H and WT-hRyR2 channels.

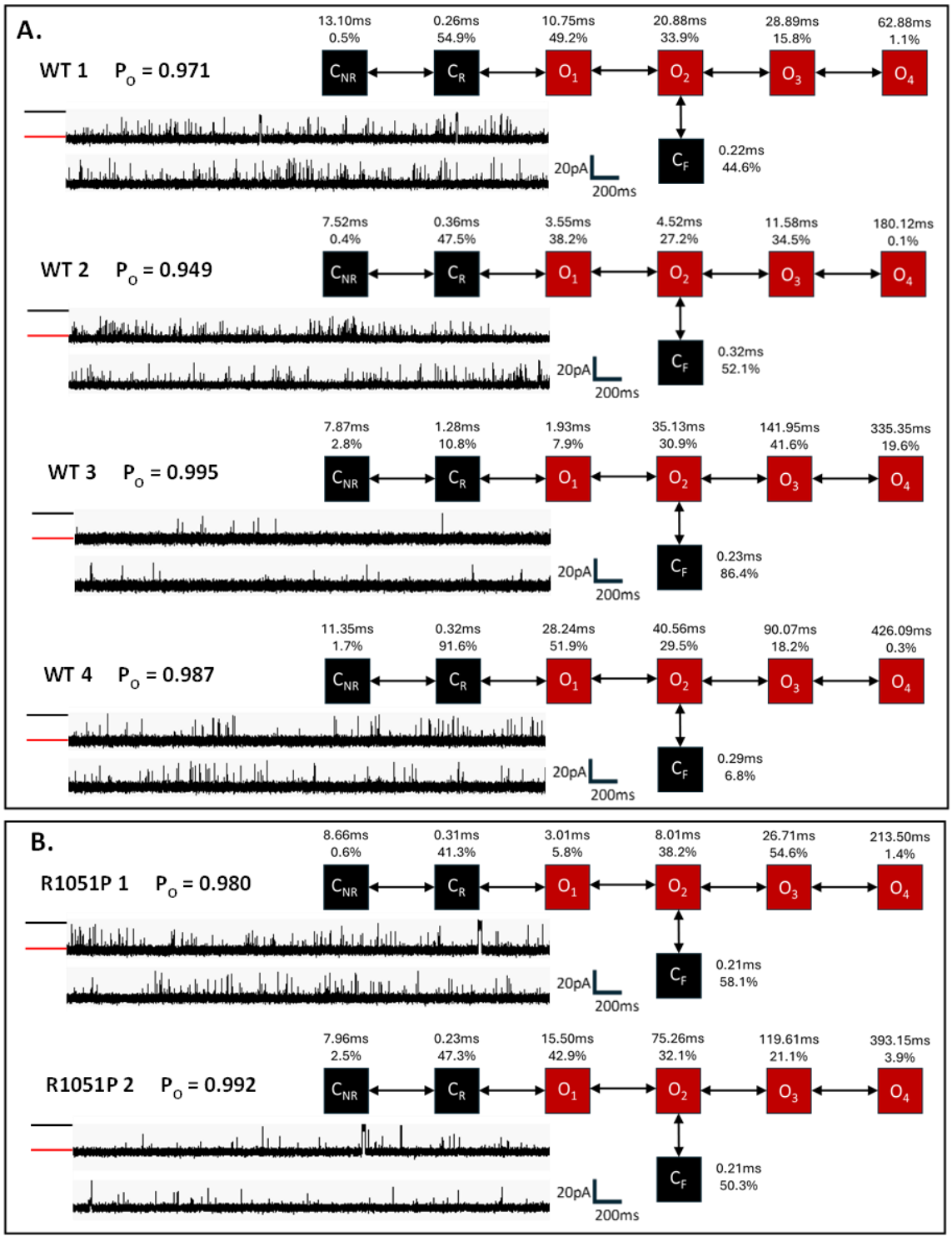

Figure 6.8. Gating models of WT-hRyR2 and R1051P-hRyR2 channels in saturating Ca^{2+} conditions are comparable. A. Gating kinetics of WT-hRyR2 channels in 100 µM $[Ca^{2+}]_{cyt}$. **B.** Gating kinetics of R1051P-hRyR2 channels in 100 µM $[Ca^{2+}]_{cyt}$. A snapshot of each recording and the corresponding gating model is shown for WT (**A**) and R1051P (**B**) channels. The black bar adjacent to traces indicates the closed level and the red bar the open level; the dwell time (ms) and frequency (%) are indicated above each state. All channels produced a 7-state model that matched the model produced by Mukherjee et al. (2012) for saturating $[Ca^{2+}]_{cyt}$ conditions and showed no notable differences between WT and R1051P-hRyR2.

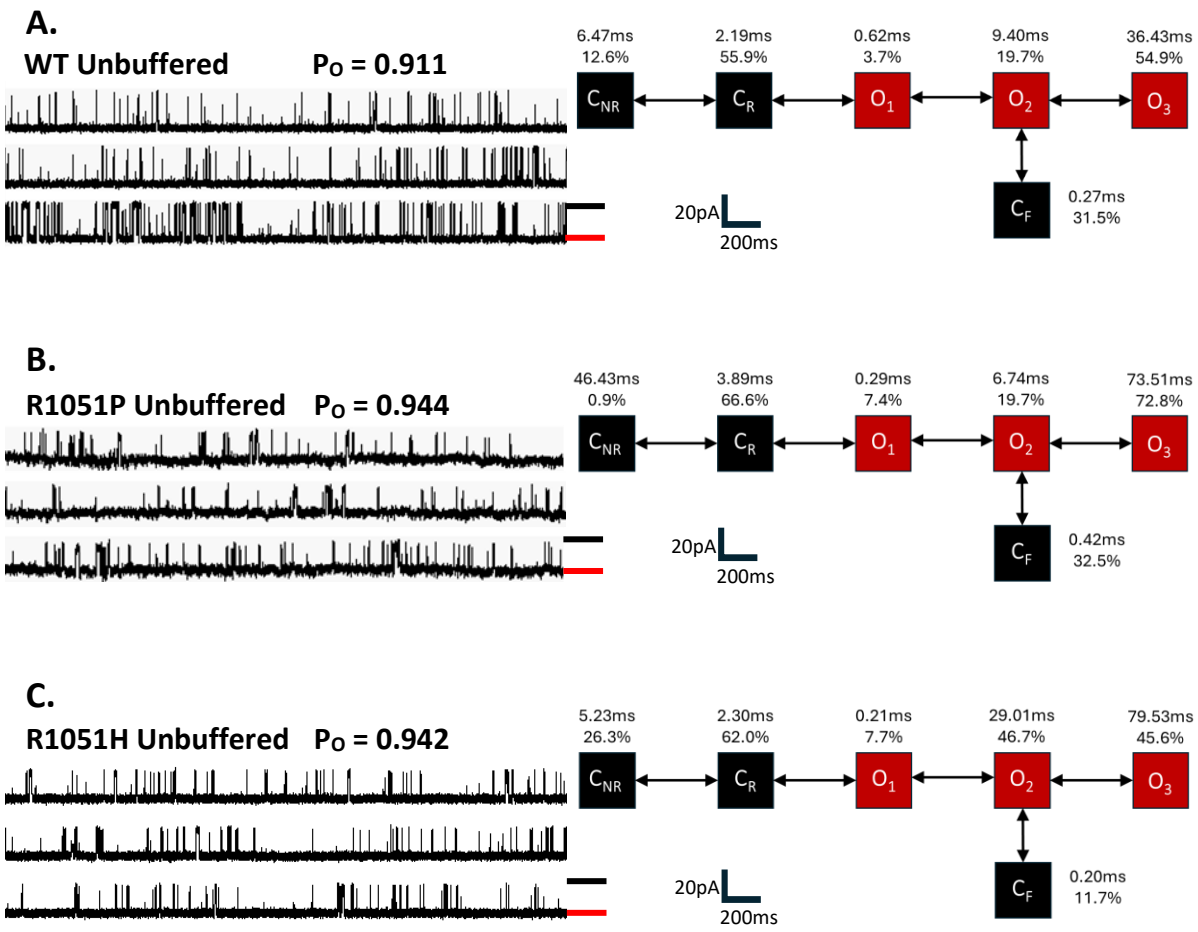

Figure 6.9. Gating models of WT, R1051P and R1051H-hRyR2 at high P_O in contaminant $[Ca^{2+}]_{cyt}$ are comparable. Panels show non-consecutive 10 second clips of recordings for WT (**A**), R1051P (**B**) and R1051H (**C**) hRyR2 channels that presented with a high P_O in unbuffered conditions with contaminant Ca^{2+}. The black bar indicates the closed level and the red bar the open level. The three models are comparable in most parameters and fit the standard six-state model for RyR2 gating at a high activating $[Ca^{2+}]_{cyt}$ (Mukherjee et al. 2012), however the exact Ca^{2+} concentration is unknown and is present only as contaminant.

6.3.3 WT and R1051P-hRyR2 both demonstrate modal gating

All channels demonstrated modal gating to some extent over the full recording period, showing atypical behaviour on both a short (~second) scale and a longer (minute-to-minute) scale that reflects in the P_O of channels (**Figure 6.10A**). These sections were removed from the main analysis of P_O and gating models but were analysed separately to compare modal gating between R1051P-hRyR2 and WT-hRyR2. No notable difference in modal gating was observed between WT and R1051P channels recorded in 100 µM $[Ca^{2+}]_{cyt}$ (**Figure 6.10B**).

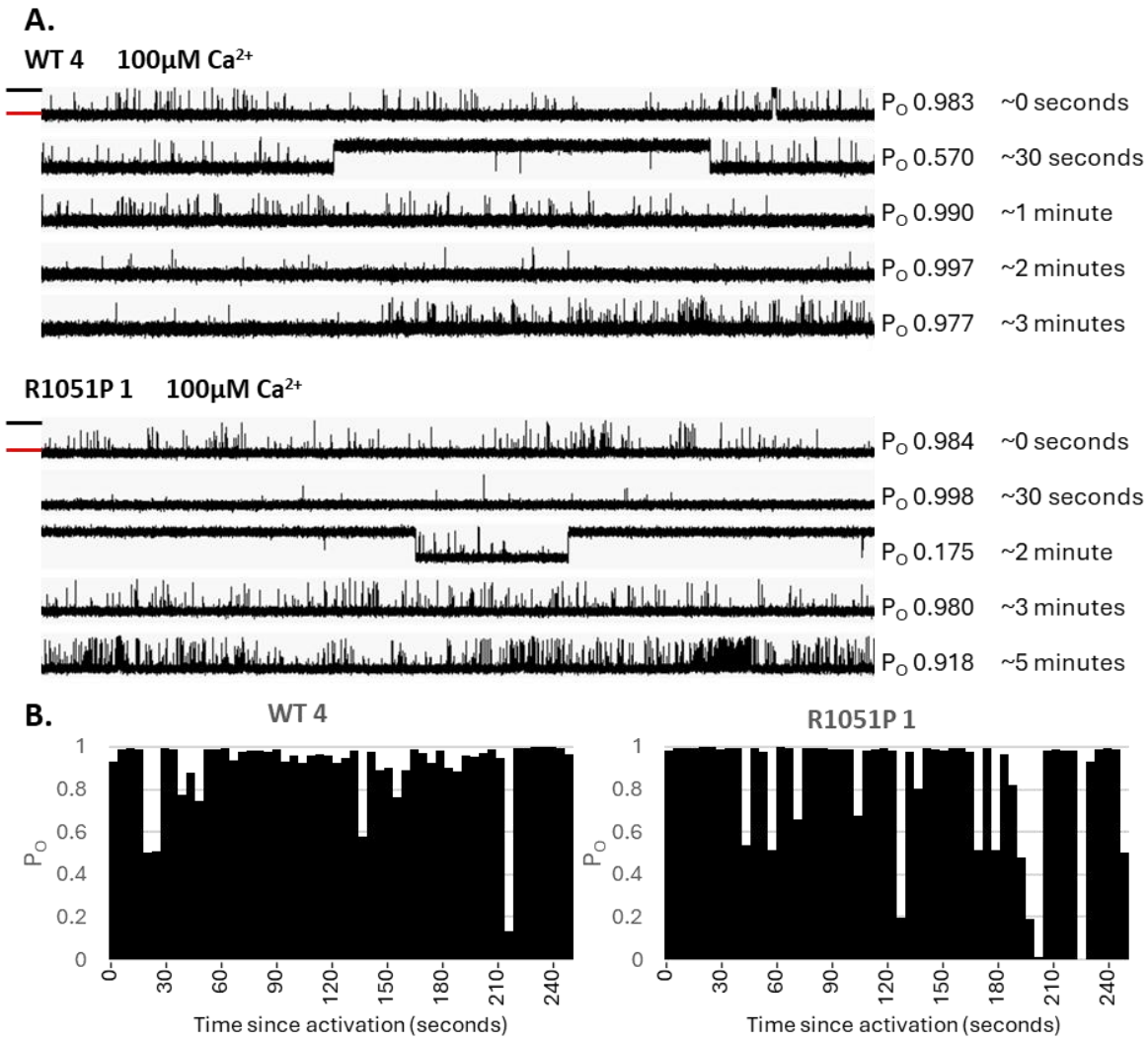

Figure 6.10. Modal gating results in changes to the P_O of WT and R1051P-hRyR2 channels over time. A. Non-consecutive 5-second sections of recording demonstrate modal gating at the minute-to-minute scale in both a WT (top) and R1051P (bottom) hRyR2 channel. The P_O is calculated for the displayed 5-second segment with an approximate time from the point of buffering to 100 µM $[Ca^{2+}]_{cyt}$. **B**. Corresponding graphs of P_O changes over time for WT (left) and R1051P (right) channels demonstrate that, while both channels spend the majority of the recorded period at P_O >0.9, there are multiple spontaneous drops to a lower P_O. P_O values for all 5-second segments of all WT channels recorded in 100 µM $[Ca^{2+}]_{cyt}$ were compared to R1051P and revealed no significant difference in P_O distribution (Mann-Whitney test, p-value = 0.5546, WT n = 133 P_O values, R1051P n = 77). Statistical analysis performed in GraphPad Prism 10.1.2.

6.4 Discussion

The aim of single channel recording was to determine the function of hRyR2 under complete shutdown (~0 nM $[Ca^{2+}]_{cyt}$) and saturating (~100 µM $[Ca^{2+}]_{cyt}$) conditions to identify any dysfunction at the single channel level of the R1051-mutants compared to WT-hRyR2. Based on the location of R1051 within the P1 domain of hRyR2, which is likely involved in clustering of channels but is distant from the central ion pore and the majority of known pathogenic RyR2 mutations, it was hypothesized that single channel function may not be impaired by these mutations. Given dysfunction of all three R1051 mutants has been shown at a global Ca^{2+} release level (**Chapter 4**) and to some degree the population level (**Chapter 5**), single channel recording is the necessary next step to pinpoint the organisational level at which dysfunction occurs in these mutants.

6.4.1 P_O and modelling reveal no conclusive evidence for a difference in function at the single channel level of R1051P and WT-hRyR2.

The results presented here demonstrate no conclusive difference in gating between WT and R1051P-hRyR2 channels in regard to P_O, T_O, T_C (**Figure 6.6**) or their gating models (**Figure 6.8**) at sub-activating or saturating cytosolic Ca^{2+} concentrations (**Figure 6.7**). This analysis is somewhat limited by the small sample size, with only 2 R1051P channels of high P_O taken forward for modelling compared to 4 channels for WT-hRyR2, which reduces the statistical power to detect any difference and therefore any conclusions drawn from this data must be made with this in mind. The additional channels of high P_O recorded in an unknown Ca^{2+} concentration also do not reveal any novel gating behaviours of either R1051P or R1051H, although no data was available for R1051C to make comparisons for this mutant. Overall, these results do not indicate a significant difference in gating behaviours between WT and R1051-mutant-hRyR2 at the single channel level in sub-activating or saturating conditions.

There were some differences observed between the model produced for WT-hRyR2 in this research compared to the work by Mukherjee et al., (2012), predominantly in the dwell time of O_4. In the initial model the dwell time of O_4 was calculated as 64.14ms (±33.92) with a frequency of 6.08% (±3.53) (Mukherjee et al. 2012) compared to 251.11ms (±161.44) and a frequency of 5.28% (±9.56) in this study, indicating a tendency for a much longer O_4 state in WT-hRyR2 in the present research. Examining the methods, both experiments were performed via near identical methods (**Section 6.2**) with a few exceptions; the original

experiments also used HEDTA as an additional chelator (buffers in the range 1.5 - 16µM $[Ca^{2+}]_{cyt}$) in addition to NTA and EDTA, and $[Ca^{2+}]_{cyt}$ was increased gradually from ~0nM to saturation (100-200µM), however these factors should not greatly impact the gating of hRyR2 and the reason for this difference remains unclear. Therefore, as the model still applied and the main focus of the research was the comparison between WT and R1051P, differences between the proposed model by Mukherjee et al., (2012) the models obtained here were not considered to be detrimental to the results.

These results must take into account that, while R1051P-hRyR2 may have no discernible effect on channel gating at sub-activating or saturating $[Ca^{2+}]_{cyt}$, other aspects of RyR2 activation may be impacted by this mutation. This could include, but is not limited to, altered luminal or cytosolic Ca^{2+} sensitivity or altered accessory protein interactions, none of which would be detected with the current experimental protocol. Altered channel sensitivity to Ca^{2+} is a recognised mechanism of dysfunction in CPVT (**Section 1.6.2.1**) (Li and Chen 2001; Jiang et al. 2004; Jiang et al. 2005; Jones et al. 2008; Fernández-Velasco et al. 2009; Liu et al. 2013; Xiao et al. 2016; Uehara et al. 2017). This includes well characterised pathogenic mutations such as R4496C, which leads to increased channel openings at low cytosolic $[Ca^{2+}]$ (Jiang et al. 2002a) and has been directly implicated in arrhythmogenesis of CPVT (Jiang et al. 2002a; Fernández-Velasco et al. 2009; Liu et al. 2009). To assess this in the R1051-mutants, additional single channel experiments should be performed to determine the effects of increasing both cytosolic and luminal $[Ca^{2+}]$ on channel gating. It was intended to perform these experiments during this study as it could reveal vital information about the sensitivity of the R1051-mutants to Ca^{2+} that might indicate their mechanism of dysfunction. However, due to the significant time needed to assess this and the variability of data obtained from individual hRyR2 channels it was not feasible within the limited time frame. As a result, only the initial experiments presented here at the extremes of $[Ca^{2+}]_{cyt}$ were performed.

There is also the possibility that R1051C and R1051H-hRyR2 display a more notable difference in single channel gating than R1051P, however due to the focus of this research being placed on R1051P this was not fully explored. The association of these mutants with cardiac phenotypes is less well defined than R1051P, and while both have been linked to cardiomyopathy (HCM and DCM) as well as CPVT, no substantial evidence is available to

directly link them to these conditions (**Section 1.7.4** and **Section 1.7.5**). The effect of cardiomyopathy-associated mutants on hRyR2 function as a whole at the single channel level is also less well documented than for CPVT. The HCM-linked mutation P1124L resulted in a lower P_O than WT-hRyR2 in single channel experiments, but overall results in both a GoF and LoF phenotypes (Alvarado et al. 2019). T1107M has also been linked to HCM (Fujino et al. 2006), and the mouse model (A1107M) was shown to reduce Ca^{2+} release (Tang et al. 2012), however no single channel data is available for this mutant (Fujino et al. 2006; Tang et al. 2012). This indicates that LoF at the single channel level is likely implicated in HCM; this is also discussed in **Chapter 4** in the context of whole cell Ca^{2+} release. Further work to assess the function R1051C and R1051H at the single channel level is therefore necessary to determine whether they have a marked effect on single channel function, whether this differs to R1051P, and if so, how this contributes to their overall dysfunction.

6.4.2 Channels in high activating Ca^{2+} conditions do not always achieve a high P_O

Buffering of the cis chamber to 100 µM free $[Ca^{2+}]_{cyt}$ (**Figure 6.6A**) produced variable results with not all channels exhibiting a high P_O, however the reason for this marked difference in activity of channels subjected to the same experimental procedure is unknown. While a degree of variability in P_O is to be expected, the group of lower P_O channels are closer in P_O to RyR2s recorded in much lower (<5 µM) $[Ca^{2+}]_{cyt}$ (Mukherjee et al. 2012) than the conditions present here (**Figure 6.6A**), and that this occurs with both WT and R1051P-hRyR2 suggests it is not a product of mutation. The heterogeneity of RyR activity at the single channel level has been reported on previously in multiple studies (Laver et al. 1995; Copello et al. 1997). Laver et al., (1995) identified a range of P_O measurements spanning the full range of ~0 to 1 for channels recorded in saturating 1 mM $[Ca^{2+}]_{cyt}$, although this concentration is approaching the point at which RyR2 becomes inhibited by Ca^{2+} inactivation of the channel. Copello et al., (1997) also recorded a range of P_O values for RyR2 at 1 mM $[Ca^{2+}]_{cyt}$, although the heterogeneity of RyR1 was much greater. Total inactivation of channels has also been observed, with up to 50% of RyRs becoming inactivated after an initial period of activity in response to changing $[Ca^{2+}]_{cyt}$ or voltage and subsequently failing to reopen despite the presence of activators (Sitsapesan et al. 1995; Laver and Lamb 1998).

This heterogeneity in activity is observed not only between channels but can be seen within one channel over time as it spontaneously switches from a high to low P_O and vice versa in a

process called modal gating (Zahradníková and Zahradník 1995; Armisen et al. 1996) (**Figure 6.10**). This occurs over small (~seconds) timescales to much longer (~minutes) timescales and was initially believed to be a Ca^{2+}-dependent process (Zahradníková and Zahradník 1995; Armisen et al. 1996), but it has since been observed at various steady Ca^{2+} concentrations (Saftenku et al. 2001; Mukherjee et al. 2012). It is now thought to be an innate property of RyR and other ion channels (Yakubovich et al. 2000; Luvisetto et al. 2004; Chakrapani et al. 2011; Ullah et al. 2012). Modal gating was observed in both WT and R1051P-hRyR2 channels in multiple recordings, with no notable differences in the mutant. However, this demonstrates that one channel can spontaneously shift between high and low activity states (at constant $[Ca^{2+}]_{cyt}$), therefore it is possible that the channels recorded as having a low P_O (**Figure 6.6**) would increase to a more typical high P_O at a later time. This was observed in several channels; however the periods of high P_O were insufficient for modelling (<3000 events) and therefore were excluded.

The mechanisms behind modal gating and the lower innate activity of some channels are not fully understood, however multiple studies have identified factors that impact the gating of single channels and alter their P_O. The phosphorylation status of RyR2 has long been implicated in its activity, but there is much disagreement about the exact contribution of PKA and CaMKII and the effect of phosphorylation at multiple sites (**Section 1.4.1**). Multiple studies have indicated that both PKA- and CaMKII-dependent phosphorylation increase the P_O of RyR2 (Marx et al. 2000; Wehrens et al. 2004b; Xiao et al. 2007a; van Oort et al. 2010), although several others have indicated the opposite (Terentyev et al. 2003; Carter et al. 2006b). One study that sought to clarify this determined that hyperphosphorylation by PKA increases the P_O of RyR2 but desensitises the channel to the influence of Ca^{2+} such that they no longer respond to changing $[Ca^{2+}]_{cyt}$ (Carter et al. 2011). While the phosphorylation status of solubilised and purified channels cannot be determined directly, phosphorylation at S2808 in cell homogenate was assessed and found to be comparable to the WT in all R1051-mutants (**Chapter 3**); phosphorylation at S2030 and S2814 was not assessed. This could be addressed in future research, however given the contribution of phosphorylation to RyR2 function is uncertain and considering modal gating was observed in both WT and R1051P-hRyR2 channels, this may offer limited additional insight in the context of modal gating. FKBP12.6 is also proposed as a regulator of single

channel function, with early research suggesting that its dissociation promotes dysfunctional gating (Marx et al. 2000; Marx et al. 2001) (**Section 1.5.1**), however more recent data suggests that this is not the case and that FKBP12.6 is not needed for functional RyR2 gating (Xiao et al. 2007b; Stewart et al. 2008; Galfré et al. 2012b). FKBP12.6 was not present in any single channel experiments as it is not expressed in HEK293 cells, and as such any effect of this accessory protein cannot explain the variable P_O observed. Ultimately, while the variability in P_O and the presence of modal gating is unexplained, this affected both WT and mutant channels similarly and is a well reported phenomena that doesn't impact the results.

6.4.3 Conclusions

In summary, single channel recording of WT and R1051P-hRyR2 revealed no evidence of major dysfunction at the single channel level of the R1051P-mutant at sub-activating or saturating cytosolic Ca^{2+} concentrations. R1051C and R1051H-hRyR2 must also be recorded in buffered Ca^{2+} conditions in future studies to assess their effect on single channel function, which may help differentiate these cardiomyopathy-associated mutations from CPVT-associated R1051P. Preliminary experiments with R1051C and R1051H however do not indicate obvious dysfunction of these mutants at the single channel level. Many of the caveats and difficulties encountered during this study are a product of the technicalities of the single channel recording method, but it remains the most established and reliable way to assess single channel gating in such detail. Alternative methods, such as the Orbit Mini (Nanion Technologies; a miniaturised, four-channel recorder) are emerging, however as yet they remain relatively untested in the RyR field (Woll et al. 2021; Joseph et al. 2024) and present their own difficulties in determining bilayer formation and control of conditions. Ultimately, these results do not support a pathological effect of the R1051P mutation at the single channel level at sub-activating or saturating $[Ca^{2+}]_{cyt}$ which is expected to reveal inherent dysfunction of single channels. It is possible that mutation at R1051 alters the sensitivity of channels to Ca^{2+} however this was not assessed within this study. This suggests that dysfunction of R1051P-hRyR2 arises at a higher organisational level and may not manifest in single channels.

Chapter 7

General discussion

7.1 General discussion and future work

The main aim of this study was to generate and characterise three disease-linked mutations found at R1051 in hRyR2 to build a picture of their dysfunction. The main focus was placed on R1051P due to the greater evidence of dysfunction for this mutant in causing CPVT (Marjamaa et al. 2009); see **Section 1.7.3**. R1051C and R1051H were also examined due to their potentially different effect on RyR2 function, being linked instead to cardiomyopathy (Pugh et al. 2014; Lopes et al. 2015; Walsh et al. 2017). The investigation was split into four main parts, beginning with generation and expression of the mutants followed by a multi-level assessment of their function at the whole cell, population and single channel level. This specific approach was taken as it was hypothesized that the R1051 mutations may interfere with the clustering interaction of hRyR2 due to their location in the tetramer and may cause dysfunction due to alterations to this interaction.

7.1.1 Are R1051P, R1051C and R1051H-hRyR2 dysfunctional and at which organisational level is that dysfunction evident?

Dysfunction of R1051P, R1051C and R1051H-hRyR2 was first assessed at the whole cell level by live cell Ca^{2+} imaging in HEK293 cells to determine whether these mutations had an impact on the kinetics of spontaneous Ca^{2+} release via hRyR2. The spontaneous Ca^{2+} release profile of all R1051-mutants was significantly different to the WT, revealing slower Ca^{2+} release kinetics and aberrant Ca^{2+} release behaviour indicative of arrhythmogenesis (**Figure 4.4** and **Figure 4.5**). Two mutants (R1051P and R1051C) also showed altered localisation within the cell that was indicative of degradation (**Section 3.4.2**). Collectively, this confirms dysfunction at the whole cell level (**Chapter 4**).

The next objective was to determine at which organisational level dysfunction originates. Considering the distance of R1051 to the ion pore, the known Ca^{2+} binding sites, and the domains involved in unzipping, it was proposed that mutation may not have an effect at the single channel level, but that dysfunction might occur at a higher organisational level. To assess dysfunction at the population level, TIRF imaging of RyR2s incorporated into DIBs was used to measure Ca^{2+} release from groups of RyR2 ranging in size from a single channel to >15 channels. RyR2 Ca^{2+} release has never before been characterised in this experimental system and it has undergone substantial optimisation by the group to achieve this (Cumbes et al, *unpublished*). While unable to pinpoint the exact positions of individual channels

within clusters as yet, this technology enabled estimation of the numbers of channels within clusters while simultaneously monitoring their Ca^{2+} release behaviour, allowing correlation between cluster size and Ca^{2+} release behaviour for both WT and mutant channel populations. Data obtained from DIBs demonstrated novel Ca^{2+} release behaviours in populations of R1051P-hRyR2 that were not observed in the WT (**Figure 5.4**) which were indicative of cooperative Ca^{2+} release and increased activity from the mutant (**Figure 5.8**) particularly in larger groups of channels (**Section 5.3.5**). R1051C and R1051H were analysed less extensively and did not produce such pronounced differences, however results indicate that they may enable RyR2 to form larger cluster (**Section 5.3.3**). This confirms dysfunction of R1051P, and likely R1051C and R1051H, at the population level, although the way these manifest may be different.

By contrast, dysfunction was not observed at the single channel level. Single channel recording has been extensively used to assess the function of CPVT-mutant hRyR2 (Jiang et al. 2004; Jiang et al. 2005; Tester et al. 2007; Fernández-Velasco et al. 2009; Liu et al. 2013; Loaiza et al. 2013; Uehara et al. 2017) and improve the understanding of RyR2 regulation by endogenous modulators and drugs (Chen et al. 1997; Laver 2001; Stewart et al. 2008; Oo et al. 2015; Bannister et al. 2016). Analysis of WT and R1051P single channel gating under sub-nanomolar and saturating cytosolic Ca^{2+} conditions revealed no significant differences in the range of P_Os achieved or the gating schemes modelled (**Section 6.3.1** and **Section 6.3.2**). This suggests that R1051P-hRyR2 gating doesn't differ from that of the WT under saturating and sub-activating Ca^{2+} levels. This is supported by data from DIBs which showed comparable behaviour of R1051P and WT-hRyR2 in Ca^{2+} flux spots thought to comprise a single channel (**Section 5.3.4**). As discussed in **Section 6.4.1**, there is the possibility that R1051C and R1051H affect single channel gating, however insufficient data were obtained to draw any conclusions. It is also possible that single channel function is impaired but does not present at the cytosolic Ca^{2+} concentrations examined. For example, it is possible that channel activity is affected at the lower range of activating $[Ca^{2+}]_{cyt}$ (1-10 µM) or that the threshold for activation or sensitivity to cytosolic or luminal Ca^{2+} activation may be altered in these mutants. However, the comparable gating of WT and mutant channels at saturating and sub-activating Ca^{2+} suggests dysfunction at the single channel level for R1051P makes a minimal contribution to the overall Ca^{2+} release phenotype.

Taken together, these results suggest that dysfunction of the R1051-mutants, specifically R1051P, manifests at the population level and above, with the whole cell behaviour indicating arrhythmogenic behaviour that is frequently observed in disease.

7.1.2 What is the mechanism of dysfunction in R1051P-hRyR2?

As discussed in previous chapters, all R1051-mutants show characteristics that are associated with GoF and LoF mechanisms that could contribute to both CPVT and cardiomyopathies. At the whole cell level, R1051 mutant channel expression decreased ER Ca^{2+} store load and increased Ca^{2+} transient abnormalities, indicating Ca^{2+} leak; a phenomenon strongly associated with a GoF (**Chapter 4**) (Thomas et al. 2004; Jiang et al. 2007; Li et al. 2021; Sun et al. 2021; Zhong et al. 2021). DIB data from R1051P also supports a GoF for this mutant due to the increased Ca^{2+} flux activity of R1051P populations compared to the WT (**Chapter 5**), but this was not so evident for R1051C or R1051H. The apparent decreased expression of the mutants (not statistically significant) (**Section 3.3.4**) would however suggest a LoF. This was likely the product of increased degradation for R1051P and R1051C as indicated by their altered localisation (**Section 3.3.3**), reducing the number of functional channels that could lead to overall LoF; although in R1051H this appears to be independent of degradation or altered trafficking. Slower transient kinetics and Ca^{2+} alternans are also frequently associated with a LoF, but these may also occur as a function of Ca^{2+} leak. This indicates that some RyR2 mutations can result in nuanced Ca^{2+} release changes which don't easily fall into GoF or LoF definitions, as is the case for other mutations that have been characterised (Thomas et al. 2004; Loaiza et al. 2013; Zhao et al. 2015).

This also highlights that the main point of differentiation between CPVT-linked R1051P and cardiomyopathy-linked R1051C / R1051H appears to be their behaviour at the population level. The original hypothesis proposed here was that mutation at R1051, most notably R1051P, would impact the ability of channels to interact during clustering due to its position in the P1 domain (Cabra et al., 2016; Yin & Lai, 2000). This is largely supported by the results presented in this study, however how altered inter-tetramer interactions in R1051P might lead to the arrhythmogenic Ca^{2+} release dynamics seen in whole cells is unclear. To begin to understand this, it is important to correlate the effects observed at the population level with the effects on global Ca^{2+} release; this is discussed below for R1051P, and in **Section 7.1.4**

for R1051C / R1051H. There are a number of key factors to consider including cluster size, activity, and the cooperativity of Ca^{2+} release.

Beginning with cluster size, this has been reported in the literature to affect Ca^{2+} release, with larger clusters generally proposed to reduce Ca^{2+} leak (Sobie et al. 2006; Asghari et al. 2014; Kolstad et al. 2018; Asghari et al. 2020), and cluster fragmentation has been implicated in arrhythmia and HF (Macquaide et al. 2015; Galice et al. 2018; Munro et al. 2021). Both WT and R1051P-hRyR2 channels were equally able to form spontaneous clusters in DIBs with no significant difference in the number of channels per population, however the prevalence of the aberrant behaviours observed in R1051P channels was increased in larger clusters (**Figure 5.7**). In the absence of accessory proteins such as FKBP12.6 that might affect clustering (**Section 1.2.4**), there are limited explanations for this other than a direct effect of mutation on the clustering interaction. If R1051P alters the secondary structure of P1 then this would likely disrupt the inter-tetramer interaction and any allosteric communication that may occur between the interaction regions (Marx et al. 2001; Sobie et al. 2006), which could be exacerbated in larger clusters where more of these impaired interactions are present. This would also explain why single channel gating in planar lipid bilayers appears unaffected, as the mechanism of dysfunction would be entirely absent.

While some R1051P channel populations behaved comparably to the WT, two novel Ca^{2+} release behaviours ('Inverted' and 'Stepped') were observed, and one behaviour ('Always On') was observed more frequently in mutant channels. These behaviours were all characterised by higher activity (**Figure 5.8**) that was more cooperative in nature than the WT, showing step-wise changes between high and low Ca^{2+} flux states or consistent Ca^{2+} release with little fluctuation in signal, denoting concerted behaviour (**Figure 5.4**). There are two aspects to examine here: increased activity, and increased cooperativity.

Regarding higher activity, increased channel P_O has been associated with Ca^{2+} leak and the generation of DADs and triggered arrhythmias in many studies (Marx et al. 2000; Tester et al. 2007; Wehrens 2007; Bers 2014; Miotto et al. 2024), so this effect at the population level is easily reconciled with signs of Ca^{2+} leak at the whole cell level. However, the potential impact of the increased cooperativity of aberrant Ca^{2+} release in R1051P is more nuanced. To our knowledge, the only comparable reports of concerted opening and closing of

channels is from studies demonstrating coupled gating in planar lipid bilayers, where two or more channels were shown to gate in a concerted manner resulting in longer open and closed periods (Marx et al. 2001; Ondrias and Mojzisová 2001; Gaburjakova and Gaburjakova 2008; Gaburjakova and Gaburjakova 2010; Porta et al. 2012). As discussed in **Section 1.2.4** and **Section 5.4.4**, coupled gating has not been proven as no studies have shown concerted gating of channels that are functionally coupled together (i.e. in a cluster), and while DIBs provide a possible avenue to prove this, no data are yet available. It is therefore not possible to conclude that R1051P is demonstrating allosterically coupled gating, even if it appears to act in a concerted way. It is also important to consider that, should coupled gating be a real consequence of clustering, that WT-hRyR2 would be expected to demonstrate this in DIBs too as it has in planar lipid bilayers, however no such cooperative behaviour was observed in WT populations. It is clear that further assessment of Ca^{2+} release in DIBs, in combination with DNA-paint to obtain a more accurate count of the number of channels present and their organisation (**Section 5.4.2**), is necessary to better understand coupled gating, and how this might relate to the behaviour of R1051P.

Whether coupled gating is involved in regulation of clusters or not, the behaviour of R1051P is indicative of Ca^{2+} leak as it occurs under conditions that mimic diastole, which could translate to slower Ca^{2+} transient kinetics, reduced ER Ca^{2+} store load and increased transient abnormalities seen in live cell Ca^{2+} imaging. It also appears that R1051P populations may have a reduced ability to terminate Ca^{2+} release based on the increased prevalence of the 'Always On' behaviour compared to the WT, another indicator that this mutant might suffer from persistent Ca^{2+} leak; this is supported by results from Ca^{2+} imaging showing an increased decay time of Ca^{2+} transients which is an indicator of abnormal termination (Tang et al. 2012; Liu et al. 2013; Okudaira et al. 2014). In clusters, this could be due to R1051P enhancing allosteric interactions such that it promotes channels in a cluster to open even if only one RyR2 is open, giving the all-or-nothing type of response seen in the 'Always On', 'Inverted' and 'Stepped' behaviours. Conversely, the opposite also appears true in that some of these populations suddenly drop to a low Ca^{2+} flux state in a cooperative manner, suggesting that this cooperative gating aids channel closing as well as opening. While this appears at this stage to lead to preferential channel opening, it is possible that under different conditions this could cause concerted closing of channels (such as is seen in

the 'Stepped' behaviour) that serves to reduce Ca^{2+} release or assist in termination of CICR. Future analysis would benefit from DIBs experiments showing the effect of low luminal [Ca^{2+}] and high cytosolic [Ca^{2+}] on R1051P population function to determine whether R1051P is inherently high activity, or whether this is condition dependent.

7.1.3 How does the dysfunction of R1051-mutants fit with the mechanisms proposed for CPVT?

While the mechanism proposed in **Section 7.1.2** provides a plausible explanation for the aberrant Ca^{2+} release observed in R1051P, it is also important to consider whether the main mechanisms proposed for CPVT are involved in dysfunction. This is also relevant for R1051C and R1051H given their association (albeit tentative) with CPVT.

It seems unlikely that the Ca^{2+} release dysfunction seen with R1051-mutants was caused by altered FKBP12.6 binding (**Section 1.6.2.1**). FKBP12.6 was absent from all experiments as it is not expressed in HEK293 cells, therefore changes to this interaction that might cause channel destabilisation cannot explain the difference in function seen between R1051-mutants and the WT. It is possible that binding of FKBP12 (an activator of RyR2 which is expressed in HEK293 cells) is altered by R1051 mutation, however this protein is not commonly cited in RyR2 dysfunction (**Section 1.5.1**) and, due to channel purification, was also absent during DIB experiments, which still showed a difference in Ca^{2+} release behaviour between R1051P and the WT (**Section 5.4.3**). This mechanism of RyR2 dysfunction is also often linked to RyR2 hyperphosphorylation by PKA, specifically at S2808 (Marx et al. 2000; Wehrens et al. 2003; Wehrens et al. 2006), which was found to be unaffected in all R1051-mutants (**Figure 3.7**), further suggesting that this mechanism is not responsible for the altered Ca^{2+} release in R1051-mutants. The role of FKBP12.6 and FKBP12 is a highly controversial topic, as many groups disagree with the finding that FKBP12.6 stabilises RyR2 or affects Ca^{2+} activation (Timerman et al. 1996; Barg et al. 1997; Xiao et al. 2007b; Guo et al. 2010; Galfré et al. 2012) (**Section 1.5.1**). Regardless, it would be beneficial to assess binding of both FKBP12.6 and FKBP12 by immunoprecipitation and Western blotting in future work to determine if this is potentially an exacerbating factor in R1051-dysfunction, however it remains that altered Ca^{2+} release is present in the absence of FKBP12.6.

It also seems unlikely that altered inter-domain interactions in the form of domain unzipping (Ikemoto 2002; Oda et al. 2005; Uchinoumi et al. 2010a) are involved in R1051 mutant dysfunction. The P1 domain is located on the corner of the tetramer and R1051 does not appear to contact other domains within the channel tetramer, nor has unzipping been observed in this domain (Tateishi et al. 2008; Uchinoumi et al. 2010a; Seidel et al. 2015; Yin et al. 2021). This does not definitively rule out the possibility of mutation at R1051 (or the P1 domain as a whole) destabilising the channel in this way, however the evidence available at present suggests that this mechanism is unlikely to have any significant impact on the function of R1051-mutants.

While not directly investigated in this thesis, R1051 mutants may alter the sensitivity of channel activation by either cytosolic or luminal Ca^{2+}, leading to diastolic Ca^{2+} leak and reduced store load. This seems a plausible cause of R1051-mutant dysfunction at the whole cell level given their increased Ca^{2+} release abnormalities (**Table 4.4**), and reduced ER Ca^{2+} store load (**Section 4.3.3**), both of which can be caused by Ca^{2+} leak as a result of increased sensitivity to Ca^{2+}. This is also supported by DIB experiments, which showed increased Ca^{2+} release from R1051P-hRyR2 at high luminal [Ca^{2+}] and low cytosolic [Ca^{2+}] (**Figure 5.7** and **Figure 5.8**), potentially indicating increased sensitivity to luminal Ca^{2+}. However, one aspect of the data that points away from increased sensitivity of the channel is the frequency of Ca^{2+} transients, which was significantly reduced in both R1051P and R1051C (**Figure 4.4**). This is contrary to the effect of increased Ca^{2+} sensitivity which generally increases the frequency of spontaneous Ca^{2+} oscillations by increasing the propensity for SOICR (Jiang et al. 2004).

Collectively, while this suggests that altered cytosolic or luminal Ca^{2+} sensitivity is the most likely of the CPVT-related mechanisms of dysfunction to impact R1051-mutants, results thus far are inconsistent and do not provide a clear or unified picture of its role. Future studies should include more in-depth analysis in single channels to characterise the mutant's sensitivity to both cytosolic and luminal Ca^{2+} and produce full activation curves from sub-activating to saturating [Ca^{2+}]. Additional live cell Ca^{2+} imaging and DIB experiments to assess the response to changing cytosolic and / or luminal Ca^{2+} on a larger scale would also be beneficial. Nevertheless, while Ca^{2+} sensitivity may be somewhat altered in R1051-mutants, current evidence does not suggest that this is the sole mechanism of dysfunction.

7.1.4 Do R1051C and R1051H-hRyR2 cause dysfunction by a different mechanism to R1051P?

While R1051C and R1051H-hRyR2 share many of the same characteristics as R1051P-hRyR2, they both presented slightly differently to R1051P at the population and whole cell level, which could indicate either a different mechanism of dysfunction or a different degree of severity. This was not unexpected as each mutant has been predominantly linked to different conditions; R1051P to CPVT (Marjamaa et al. 2009), R1051C to HCM (Lopes et al. 2015), and R1051H to DCM (Walsh et al. 2017), although there is some evidence that the latter two may also contribute to CPVT (Landstrom et al. 2017a; Kapplinger et al. 2018) (**Section 1.7**).

As discussed in **Chapter 4**, R1051C and R1051H were significantly different from R1051P in several aspects of their spontaneous Ca^{2+} release, but this does not clearly distinguish their mechanism of dysfunction. All mutants showed significantly slowed Ca^{2+} transient kinetics, but the amplitude and fall rate of both R1051C and R1051H were also significantly decreased compared to R1051P (**Figure 4.4**). This is a subtle change and could reflect increased Ca^{2+} leak (leading to transient desynchronisation) or a loss of function leading to lower overall Ca^{2+} release. They also showed a different distribution of Ca^{2+} release abnormality subtypes to R1051P (**Table 4.4**), with a subtle shift to behaviours that may be associated with LoF mechanisms such as Ca^{2+} alternans (**Section 4.4.2**), but this is confounded by the increased number of abnormalities overall and the increased proportion of cells displaying multiple abnormalities in R1051P (**Table 4.4**). Likewise, the reduced store load of both R1051C and R1051H compared to the WT is in this case likely due to Ca^{2+} leak and is associated with both arrhythmias and cardiomyopathies (Marx et al. 2000; Wehrens 2007; Sun et al. 2012; Tang et al. 2012; Liu et al. 2015; Dridi et al. 2021), and was also observed in R1051P. It is possible that the more severe store depletion of R1051H is linked to DCM (Dridi et al., 2021; Liu et al., 2015; Sun et al., 2012; Tang et al., 2012), however it is unclear what mechanism would cause this in R1051H specifically, and how it would to contribute to DCM given all mutants showed a decreased store load and altered Ca^{2+} transients (**Section 4.4.1**). Ultimately, many of these differences are small shifts in Ca^{2+} release behaviour that are hard to delineate, let alone elucidate the precise mechanism of dysfunction at this level.

The results from assessing Ca^{2+} release at the population level are not much more revealing, largely because there is little to no understanding about how Ca^{2+} release from clusters differs in CPVT, HCM, or DCM. Results from the analysis of R1051C and R1051H thus far indicate that they may enable hRyR2 to form larger clusters (**Figure 5.5**), although it is possible that this was impacted by the density of protein in droplets; this was not stringently controlled for and could artificially increase cluster size if more channels are present (**Section 5.4.2**); this will be considered in future experiments. Their Ca^{2+} release behaviour was also not as drastically altered as R1051P, with only one trace classified as one of the novel behaviours between both R1051C and R1051H (R1051C n = 10, R1051H n = 12) (**Figure 5.7**). This is despite their apparent increased cluster size, which in R1051P was associated with increased aberrant Ca^{2+} release (**Section 7.1.2**). So, whether protein density affected their ability to form larger clusters or not, their behaviour still appears distinctly different from R1051P.

As discussed in **Section 5.4.4**, the effect of increased cluster size on RyR2 function is not fully understood, but it is generally agreed that large, densely packed clusters are more stable and reduce Ca^{2+} leak (Sobie et al. 2006; Kolstad et al. 2018; Asghari et al. 2020). If R1051C and R1051H do truly result in an increased cluster size, they might therefore be expected to be more stable and exhibit less Ca^{2+} release, however the dysfunction observed at the whole cell level does not support this conclusion, nor does the DIB data point to reduced Ca^{2+} release. This could be due to their organisation; while clusters may be larger, it is possible they have a looser arrangement which would increase the propensity for Ca^{2+} leak (Asghari et al. 2020). It is also possible that these mutants are dysfunctional at the single channel level, however further studies would be required to ascertain this. The indication from what are predicted to be single channels (≥1 channel) in DIBs show a similar distribution of behaviours to the WT for R1051C and a perhaps slightly different distribution for R1051H, but the sample size is so small that true comparisons are difficult to make (**Figure 5.7**).

Working on the hypothesis that altered inter-tetramer interactions are at least partly responsible for the dysfunction of R1051P-hRyR2 (**Section 7.1.2**), this raises the question of how R1051C and R1051H might differ if they do not induce the same cooperativity or increased Ca^{2+} release activity. Given their increased cluster size and in the absence of

altered FKBP12.6 binding (due to none being present in DIB / HEK293 cell experiments), it seems possible that they allow hRyR2 to form larger clusters by a direct effect on the inter-tetramer interaction, but perhaps not to such an extent or in such a way that it drastically alters allosteric communication. Taken with the evidence that R1051C and R1051H do still promote Ca^{2+} leak at the whole cell level, this might suggest that they promote the formation of larger clusters in a loose checker-board arrangement that does not control Ca^{2+} release as tightly as large, densely packed clusters might (Asghari et al. 2020). Intriguingly, larger corner-to-corner / checker-board arrays are the primary configuration of RyR1 clusters (Franzini-Armstrong et al. 1998; Franzini-Armstrong et al. 1999; Hernández-Ochoa et al. 2016; Ríos et al. 2019; Xu et al. 2024), and in RyR1 the equivalent reside to R1051 in P1 (also involved in the RyR1 clustering interaction (Samsó 2017)) is a cysteine residue (C1039-hRyR1), as in the R1051C mutation (**Figure 1.16**). While only tentative, this could suggest that mutation at this residue in P1 could play into the ultrastructural arrangement of channels and shift clusters from one conformation towards another. In depth structural analysis of cluster organisation via a technique such as DNA-paint would help determine whether mutation impacts the arrangement of RyR2s in such a way.

Overall, the mechanism of dysfunction in R1051C and R1051H-hRyR2 appears less clear than that of R1051P based on the current data. While the aberrant spontaneous Ca^{2+} release in whole cells confirms dysfunction of these mutants, DIB results at present do not suggest such a marked increase in activity or cooperativity as observed in R1051P, and they may in fact increase cluster size which is proposed to reduce Ca^{2+} leak in some cluster organisations. This does point to a different phenotype in R1051C and R1051H compared to R1051P, but further research is needed to clarify the details of any mechanistic difference. Additional DIB experiments to increase the sample size for R1051C and R1051H and DNA-paint to assess the organisation of channels in clusters would be beneficial, as well as single channel analysis to determine if dysfunction manifests in individual channels.

7.1.5 How would HCM and DCM arise from the altered Ca^{2+} release of R1051-mutants?

Taking into account all of the above, it seems plausible that different substitutions at the same residue in RyR2 could cause different Ca^{2+} release phenotypes and contribute to distinct conditions like CPVT, HCM and DCM. However, despite their subtle differences in

function, it is still unclear how such different phenotypes could arise from what are ostensibly very similar changes to Ca^{2+} release from hRyR2.

It is not unprecedented for different amino acid substitutions to have different effects on RyR2 function, but to our knowledge none that produce such distinct effects as CPVT, HCM and DCM have been characterised. For example, P4902L and P4902S have both been linked to CPVT (Laitinen et al. 2003; Postma 2005) and resulted in enhanced caffeine-induced Ca^{2+} release in HEK293 cells, however only P4902S significantly affected Ca^{2+}-dependent activation of the channel in [^{3}H] ryanodine binding assays (Guo et al. 2021). Likewise, R420Q and R420W have both identified in CPVT cases (Bauce et al., 2002; Domingo et al., 2015; Nishio et al., 2006) and cause structural changes to RyR2 that put the channel into a 'primed' position and cause diastolic Ca^{2+} leak and bradycardia (Okudaira et al. 2014; Domingo et al. 2015; Miotto et al. 2024). R420Q however produced more pronounced conformational changes that appeared to increase the severity of Ca^{2+} leak (Miotto et al. 2024) and was also less susceptible to treatment with flecainide (Beqaj et al. 2024). There is also precedent for one mutation to cause multiple phenotypes, such as P1124L which is linked to both bi-directional VT and HCM (Alvarado et al. 2019), T1107M to HCM and CPVT (Fujino et al. 2006; Medeiros-Domingo et al. 2009), and E3DS to DCM and a tachycardic-bradycardic arrhythmia phenotype (Bhuiyan et al. 2007; Ohno et al. 2014; Dharmawan et al. 2019).

The easiest condition to reconcile with the results observed for all R1051-mutants is CPVT, which is strongly associated with Ca^{2+} leak arising from channel GoF resulting in slower Ca^{2+} transient kinetics, Ca^{2+} transient abnormalities and decreased Ca^{2+} store load (Marx et al. 2000; Wehrens 2007; Landstrom et al. 2017b; Kolstad et al. 2018), all of which were observed in all mutants (discussed extensively in **Chapter 4)**. This is also the most commonly associated outcome of hRyR2 mutation, as approximately 70% of CPVT1 cases are due to mutation in hRyR2, where 170 CPVT mutations have been identified (Olubando et al. 2020; Priori et al. 2021). The Ca^{2+} release from R1051P does appear to better match this phenotype than R1051C and R1051H, which aligns with the initial study that identified this mutant in two related patients with symptoms of CPVT (Marjamaa et al. 2009). This primarily includes a higher proportion of Ca^{2+} transient abnormalities (**Table 4.3** and **Table**

4.4), the distribution of which might be slightly more indicative of DAD-causing behaviour (**Section 4.4.2**).

HCM and DCM are harder to reconcile, but there are still defined signatures seen in the R1051-mutants that could contribute to these conditions. One of the most compelling pieces of evidence for an involvement in cardiomyopathies is the potential for LoF. This could arise as a result of reduced expression or increased degradation (**Section 3.4.2**), both of which might cause an overall LoF due to fewer functional channels, even if individual channels show a GoF such as Ca^{2+} leak. For R1051P and R1051C, this could be a product of the apparent degradation observed during IF (**Figure 3.5**). However, for R1051H, which did not appear to show altered trafficking (**Figure 3.5**), reduced expression (albeit non-significant compared to the WT) may represent a true downregulation (**Figure 3.7**). Reduced RyR2 expression has been observed in several cardiomyopathy models; ~50% knockdown of RyR2 (specifically in cardiomyocytes) caused cardiomyopathy and arrhythmias in mouse models (Bround et al. 2012b); a canine model of ARVD2 showed reduced RyR2 expression (Meurs et al. 2006b); a mouse model with DCM caused by mutated tropomyosin showed significantly decreased RyR2 expression (Rajan et al. 2007); and HCM-linked P1124L-RyR2 had significantly reduced expression compared to the WT (Alvarado et al. 2019). This might therefore contribute to a mixed GoF / LoF phenotype (**Section 7.1.2**), which has been observed in both DCM (Tang et al. 2012) and HCM (Alvarado et al. 2019) RyR2 mutations. However, it remains that R1051P, which hasn't been associated with cardiomyopathies in the literature, exhibits many of the same characteristics as R1051C and R1051H regardless of several subtle differences.

Taking this into account, there is little evidence from this study to support a distinct role of R1051C in HCM or R1051H in DCM. At its core, HCM is characterised by diastolic dysfunction that leads to elevated $[Ca^{2+}]_{cyt}$ causing activation of hypertrophic signalling pathways and resulting in hypercontractility (Robinson et al. 2007; Smania 2025). Ca^{2+} leak constitutes diastolic dysfunction that elevates $[Ca^{2+}]_{cyt}$, however increased Ca^{2+} leak is also heavily associated with DCM (Liu et al. 2015; Dridi et al. 2021; Wang et al. 2025) which progresses via the same remodelling pathways (Robinson et al. 2007; Schultheiss et al. 2019; Souidi et al. 2024). This is confounded by the varied results of functional studies on HCM-linked RyR2 mutations, T1107M and P1124L, which caused LoF and dual LoF / GoF in functional studies,

respectively (Tang et al. 2012; Alvarado et al. 2019). In the P1124L study, increased sensitivity to luminal Ca^{2+} indicating a luminal GoF was linked to an arrhythmia phenotype that preceded hypertrophy, whereas hypertrophy itself was attributed to a cytosolic LoF and altered CaM expression (Alvarado et al. 2019). This could indicate that factors outside of those assessed in this study, such as CaM expression, could be the distinguishing factor between different phenotypes in R1051-mutants. This could be assessed via immunoprecipitation and Western blotting of associated proteins and is a reasonable next step in determining how these mutations contribute to Ca^{2+} handling in the cell.

It must also be considered that the association of these mutations with their respective conditions in the literature is tentative, and that the genetic testing by which these variants were identified could give an incomplete picture of their role in disease. R1051H was identified in one patient with DCM; the patient harboured 7 mutations in 6 different genes (2 mutations in *TTN* encoding titin) in a panel of 46 DCM-associated genes (Pugh et al. 2014). While this does not negate the fact that R1051H does appear to cause dysfunctional Ca^{2+} release from RyR2, it could mean that R1051H might not be the primary contributing mutation to DCM in this case, and as such on its own may not contribute to a DCM phenotype. No such information is available for R1051C, but it is possible the same is true and that other mutations present in the patient contributed to HCM (Lopes et al. 2015). This could be investigated using targeted knock-in animal models to determine whether cardiomyopathy is a real functional consequence of R1051C and R1051H mutation, although this would be a substantial undertaking. A more achievable alternative would be the use of iPSC-derived cardiomyocytes, which offer a more physiologically relevant context for studying altered Ca^{2+} release dynamics in R1051-mutants than HEK293 cells, but would provide less insight into the long-term or whole-organism effects of these mutations than animal models.

Ultimately, while the clinical and functional evidence does not strongly support a distinct role for R1051C in HCM and R1051H in DCM, there is considerable evidence that all of the R1051 mutations could contribute to both arrhythmia and cardiomyopathy.

7.1.6 What treatment options are likely to be most effective for mutations at R1051?

These results afford an improved understanding of the mechanism of dysfunction caused by mutation at R1051, which assists in determining what treatment options might be most

effective for patients. While standard treatment options such as the non-selective β-blockers propranolol or nadolol could be considered, more specific RyR2-targeted therapies would be preferable.

Carvedilol is another non-specific β-blocker that has shown efficacy in HF (Poole-Wilson et al. 2003; Remme 2010). Clinically it is used as a racemic mixture of the S-enantiomer (which acts as a β-blocker) and R-enantiomer (non-β-blocking), and the R-enantiomer specifically has been shown to be effective in inhibiting SOICR and DADs in CPVT models via a direct effect on RyR2 (Zhou et al. 2011; Pölönen et al. 2018), as well capable of suppressing hypercontractility in HCM (Seo et al. 2023). The racemic mixture also rescued aberrant Ca^{2+} release in an iPSC-cardiomyocyte model of E3DS (Pölönen et al. 2018); this indicates that carvedilol could be effective against both cardiomyopathies and arrhythmias, but also potentially in more complex GoF / LoF phenotypes such as E3DS. Given the somewhat mixed GoF / LoF characteristics of the R1051-mutants, this could be an interesting avenue to explore for these mutants.

Dantrolene is emerging as an effective therapeutic in CPVT and has been shown to abolish specific Ca^{2+} transient abnormalities in CPVT mutants (Penttinen et al. 2015), which were also observed in R1051 mutants. Its mechanism of action is believed to involve stabilisation of inter-domain interactions (Seidel et al. 2015; Kajii et al. 2020; Uchinoumi et al. 2025); this does not appear to be a primary mechanism in the R1051-mutants (**Section 7.1.3**) which might indicate that it would be ineffective in R1051-mutants. However, dantrolene also improves the association of CaM with RyR2, which could enhance the inhibitory effect of CaM binding and inhibit SOICR to limit Ca^{2+} leak (Oo et al. 2015; Walweel et al. 2017b).

A novel therapeutic that has been developed in recent years targeted to CPVT is therapeutic-CaM (TCaM) (Liu et al. 2018). TCaM works on the principle that WT-CaM inhibits RyR2 by stabilising its closed state, but that as Ca^{2+} dissociates from CaM its inhibition weakens; TCaM has an increased binding affinity for Ca^{2+}, which slows the dissociation of Ca^{2+} from CaM to prolong inhibition of RyR2 (Liu et al. 2018). Specifically, this would aim to increase the refractoriness of RyR2 (i.e. the channels ability to stay closed after activation) and reduce diastolic dysfunction by preventing Ca^{2+} leak, but without impacting systolic function (Liu et al. 2018). TCaM administered by gene transfer reduced the frequency of diastolic Ca^{2+} waves in a cardiomyocyte model of CPVT2 caused by R33Q mutation in CASQ2,

and reduced arrhythmogenesis in a mouse model with the same mutation (Liu et al. 2018). This is expected to have similar effects in CPVT1 and might constitute an effective treatment for the R1051-mutants, particularly given the high incidence of abnormal Ca^{2+} transients which are an indicator of Ca^{2+} leak and impaired refractoriness.

7.1.7 Future work

As discussed throughout this body of work, there are several key areas of further research that would supplement the results provided here and further clarify the mechanism of dysfunction of these mutations. The main priorities for future work are detailed below.

Single channel recording of R1051C and R1051H-hRyR2 in buffered Ca^{2+} conditions would help determine whether single channel dysfunction contributes to the impaired Ca^{2+} release of these mutants and may distinguish their mechanism of dysfunction from R1051P. In addition, experiments designed to assess both cytosolic and luminal Ca^{2+} activation of channels could identify more subtle changes to single channel gating or Ca^{2+} sensitivity that may contribute to altered Ca^{2+} release at higher organisational levels.

Further DIB experiments to increase the sample size for R1051C and R1051H would assist in determining if Ca^{2+} release from populations of these mutants is more comparable to the WT than R1051P as current data suggests; this would also help clarify whether they do form larger clusters. This would benefit from additional optimisation as discussed in **Section 5.4.2** to more accurately ensure the density of channels, as well as potentially using eGFP fluorescence as a measure of cluster size rather than the current method.

DNA-paint should be optimised for use in DIBs to determine the organisation of hRyR2 populations. This would identify whether mutation at R1051 induces changes to the ultrastructural arrangement of channels, which may shed light on the mechanism behind their altered Ca^{2+} release behaviour.

7.1.8 Concluding remarks

This research demonstrates a significant effect of the CPVT and cardiomyopathy-associated mutations R1051P, R1051C and R1051H on Ca^{2+} release from hRyR2. Results suggest that single channel function of R1051P is comparable to the WT at sub-activating and saturating cytosolic Ca^{2+} conditions, with dysfunction becoming evident at the population level, where R1051P results in cooperative gating of channels in a cluster and increased Ca^{2+} release from hRyR2. This may reveal a novel mechanism of dysfunction that arises from altered clustering, although further research is required to confirm this. At the whole cell level, all mutants exhibit significantly altered Ca^{2+} release with slower Ca^{2+} release kinetics, reduced ER Ca^{2+} store load and increased Ca^{2+} transient abnormalities that are indicative of a GoF leak. These behaviours are frequently observed in both arrhythmias and cardiomyopathies and indicate that mutation at R1051 is damaging to hRyR2 function. Future investigations will focus on clarifying the effects of mutation on single channel gating as well as more in-depth analysis of population dynamics to build a better picture of the mechanism of dysfunction.

Appendix

Appendix I. Primer sequences for Sanger sequencing of full-length hRyR2. Primers were used to verify restriction sites and successful site-directed mutagenesis. Sequencing was performed by Eurofins.

Name	Site	Sequence (5' – 3')	Length	GC %	Tm
SPFOR2832-2849	**Mutation site**	ATGGTCCGGTTAGAGATG	18	50%	53.7
V2-#1	***SpeI* restriction site**	CCACCTTGAGCAGTCTTC	18	55.6%	56.0
B23F2	***SanDI* restriction site**	GAACAAGTACATGCCTGG	18	50%	53.7

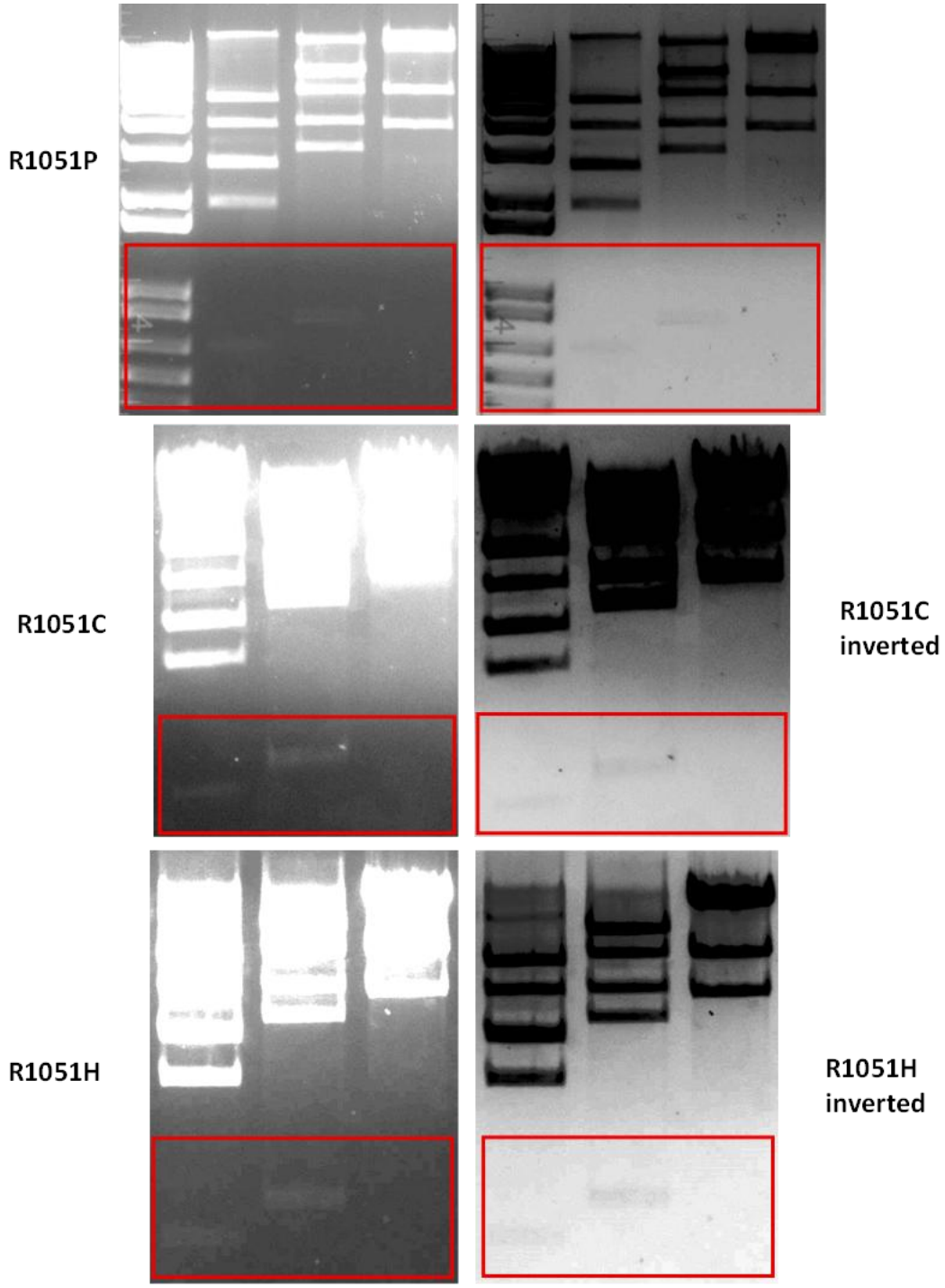

Appendix II. Enhanced agarose gels showing bands below 1500bp following maxiprep. Restriction enzymes *BglII* and *EcoRI* both produce a fragment of less than 1500bp when used to digest hRyR2. These fragments were not well resolved on gels and were not visible at the image contrast used to view bands of a higher molecular weight (**Figure 3.1**). Photo enhancement (gamma correction, contrast adjustment, inversion) reveals bands at the correct molecular weight and confirms the predicted fingerprint pattern of hRyR2 digestion in combination with **Figure 3.1** for R1051P, R1051C and R1051H-hRyR2, although resolution of bands, particularly *BglII*, was poor even after photo enhancement.

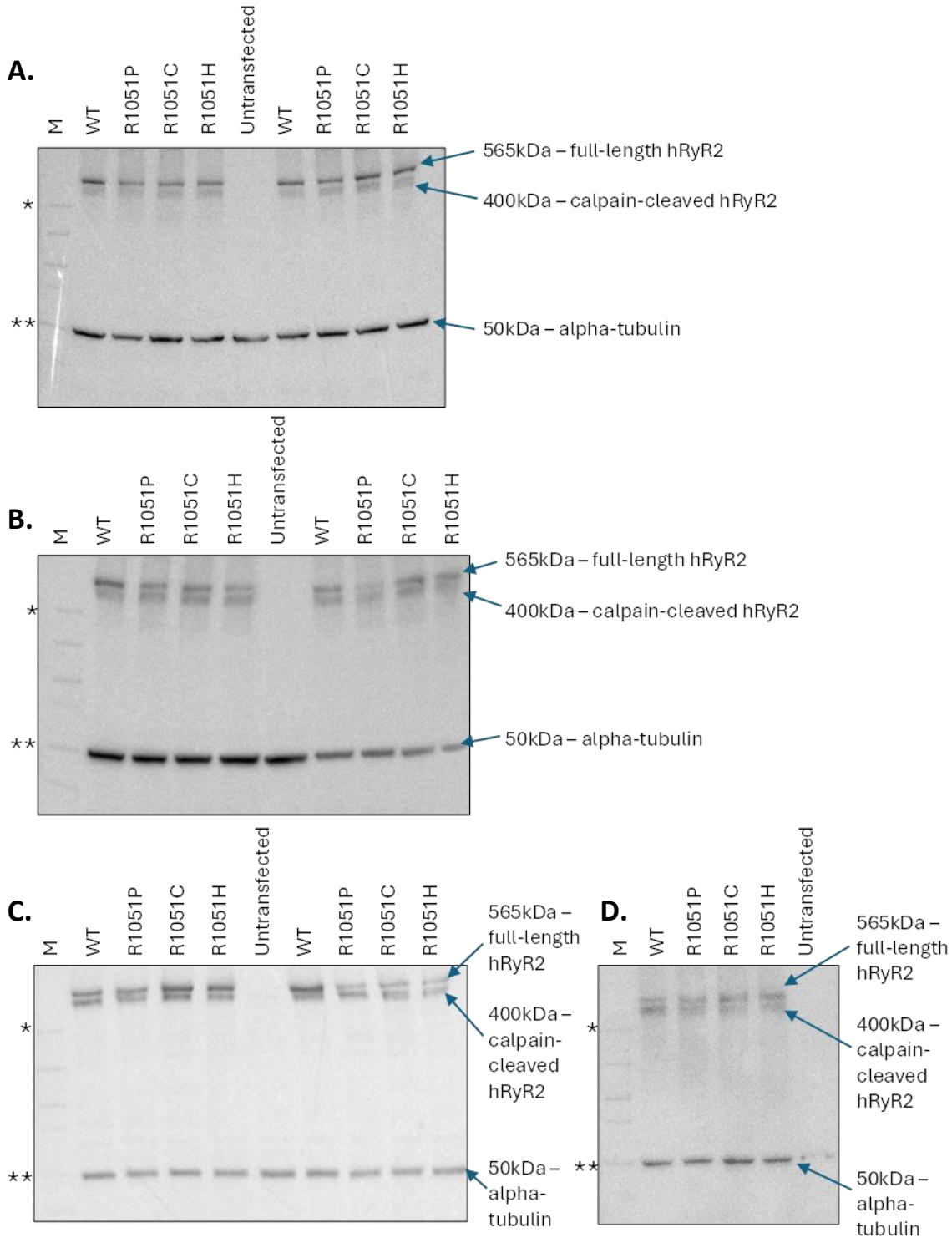

Appendix III. Western blotting of WT and R1051-mutant eGFP-hRyR2 expression in HEK293 cells. Western blotting for hRyR2 expression was performed following SDS-page of cell homogenate prepared from cells expressing WT or R1051-mutant eGFP-hRyR2 using an anti-eGFP antibody (**Section 3.2.4**); A-D represent repeats of the same cell homogenate samples. All sample lanes were loaded with the volume equivalent to 100µg total protein and normalised to the expression of the loading control, α-tubulin. A high degree of variability was observed in the results which likely contributed to the overall non-significant difference results (**Figure 3.7**), despite a seemingly lower expression of mutants compared to the WT on many blots shown here.

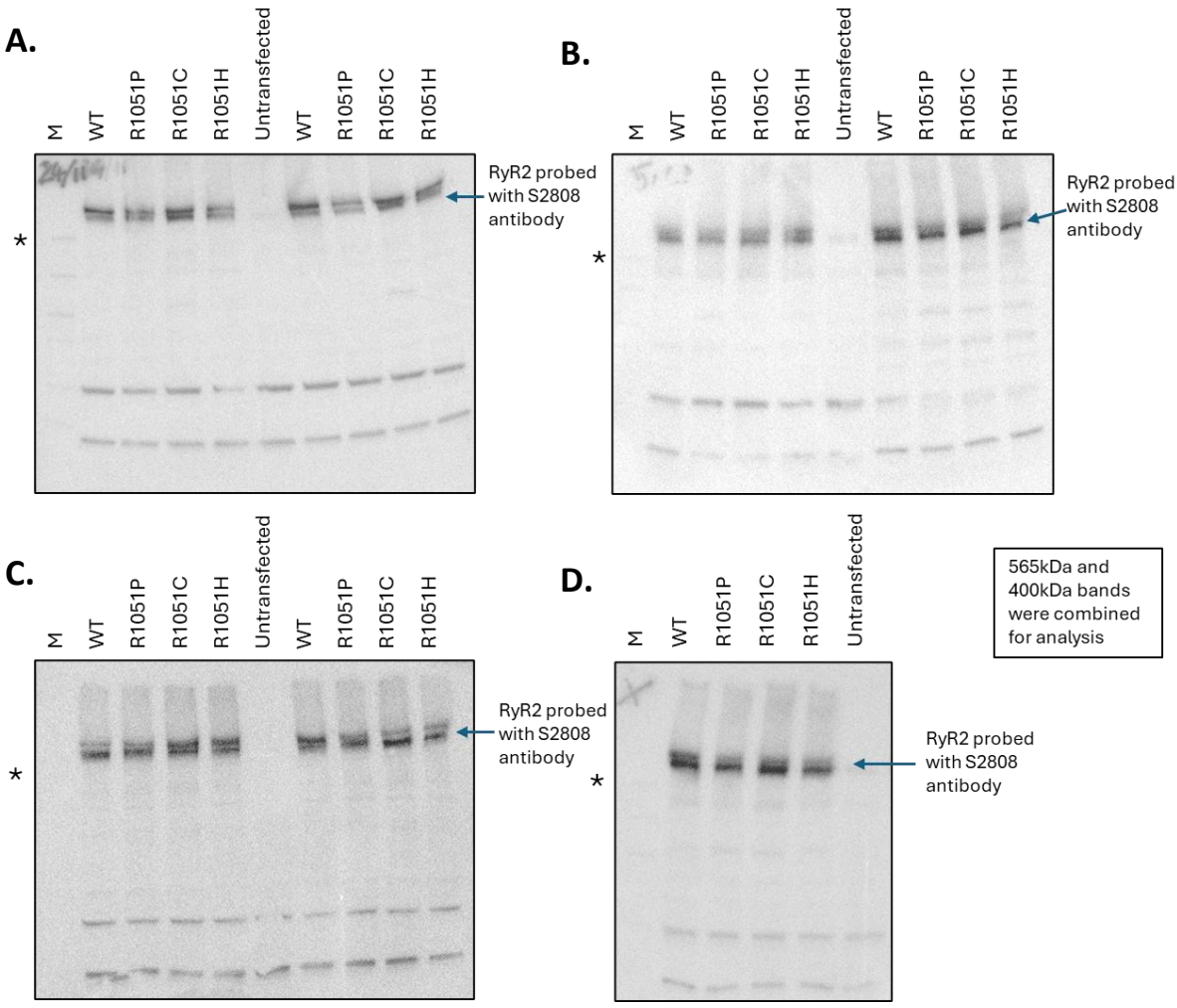

Appendix IV. Western blotting of phosphorylation at S2808 for WT and R1051-mutant hRyR2 expressed in HEK293 cells. Following stripping of blots, membranes were probed with an antibody raised to the phosphoserine S2808 epitope to detect phosphorylation levels at this residue. Both bands (565kDa and 400kDa) were combined due to variability in the signal from each band and due to difficulty separating bands visually. Asterisks (*) indicate the 250kDa marker band. Blot labels **A** – **D** correlate to the blot with the same label in **Appendix III**.

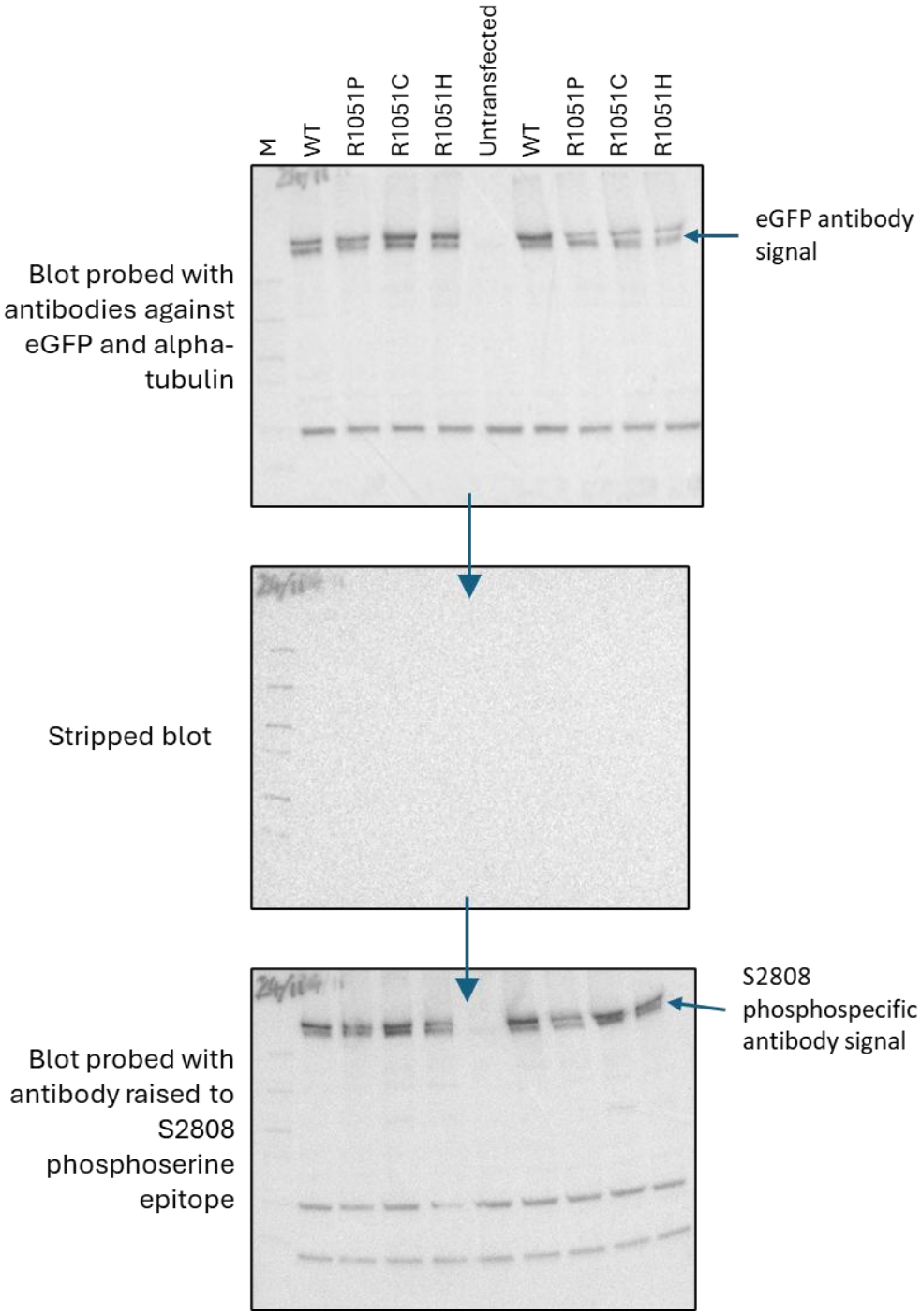

Appendix V. Example of stripped Western blot prior to assessing phosphorylation levels. After probing for hRyR2 expression, blots were stripped according to the protocol in **Section 3.2.5** and then ECL applied to image; this confirmed successful stripping of the blot. Blots were then re-probed to assess phosphorylation according to the protocol in **Section 3.2.5**.

Untransformed				
	WT	R1051P	R1051C	R1051H
Amplitude	<0.0001	<0.0001	<0.0001	<0.0001
Duration	<0.0001	<0.0001	<0.0001	<0.0001
ITI	<0.0001	<0.0001	<0.0001	<0.0001
Frequency	<0.0001	<0.0001	<0.0001	<0.0001
Rise Rate	<0.0001	<0.0001	<0.0001	<0.0001
Fall Rate	<0.0001	<0.0001	<0.0001	<0.0001
Logarithm (base 10)				
	WT	R1051P	R1051C	R1051H
Amplitude	<0.0001	0.0032	<0.0001	0.0002
Duration	0.0147	0.724	0.8342	0.1325
ITI	<0.0001	<0.0001	0.0001	0.0155
Frequency	0.0283	0.1338	0.5974	0.0032
Rise Rate	0.0005	0.0013	0.0045	0.0044
Fall Rate	<0.0001	0.0005	<0.0001	<0.0001
Inverse of natural logarithm				
	WT	R1051P	R1051C	R1051H
Amplitude	<0.0001	<0.0001	<0.0001	<0.0001
Duration	<0.0001	<0.0001	<0.0001	<0.0001
ITI	<0.0001	<0.0001	<0.0001	<0.0001
Frequency	<0.0001	<0.0001	<0.0001	<0.0001
Rise Rate	<0.0001	<0.0001	<0.0001	<0.0001
Fall Rate	<0.0001	<0.0001	<0.0001	<0.0001
Squareroot				
	WT	R1051P	R1051C	R1051H
Amplitude	<0.0001	<0.0001	<0.0001	<0.0001
Duration	<0.0001	0.0164	<0.0001	<0.0001
ITI	<0.0001	<0.0001	<0.0001	<0.0001
Frequency	<0.0001	0.0279	0.0023	0.0001
Rise Rate	<0.0001	<0.0001	<0.0001	<0.0001
Fall Rate	<0.0001	<0.0001	<0.0001	<0.0001

Appendix VI. Normality testing of Ca^{2+}transient data from HEK293 cells expressing WT or R1051-mutant hRyR2 reveals data were non-normally distributed. Shapiro-Wilks test for normality (Shapiro and Wilk 1965) revealed data were non-normally distributed for WT, R1051P, R1051C and R1051H. Three transformations – logarithmic (log(Y)), inverse of natural logarithm (1/Y), and square root √(Y) – were applied but did not sufficiently normalise data for use in parametric statistical analyses, and non-parametric measures were used instead. Transformation and normality testing was performed in GraphPad Prism 10.1.2. WT n = 644, R1051P n = 204, R1051C n = 357, R1051H n = 444.

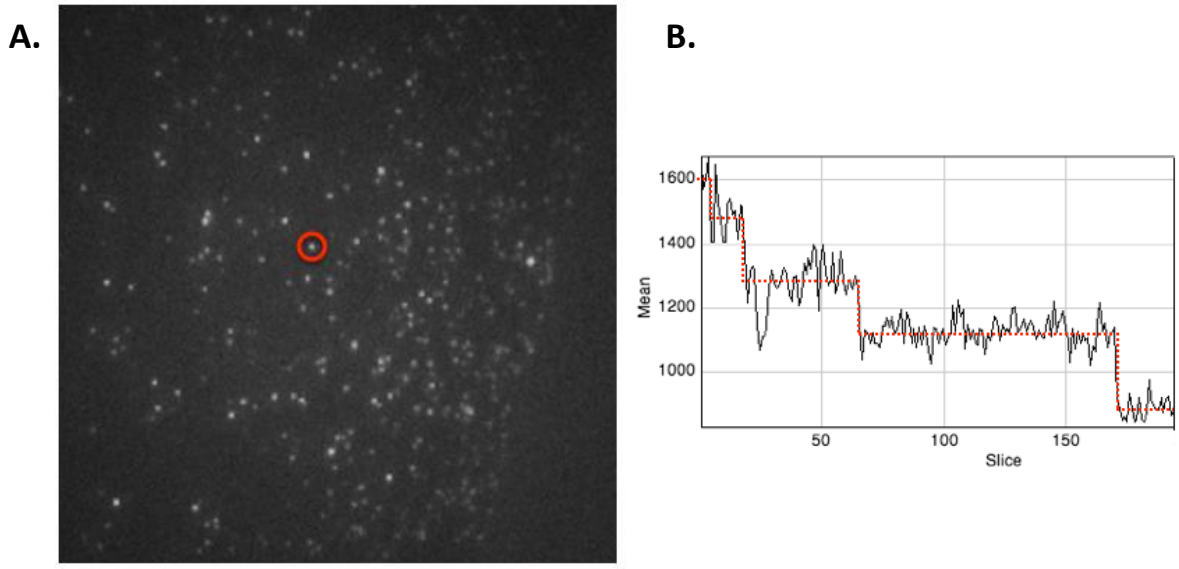

Appendix VII. Total internal reflection fluorescence microscopy allows eGFP fluorescence on individual hRyR2 channels to be visualised. A. Image from TIRF shows individual spots of fluorescence that indicate eGFP tagged onto hRyR2. **B.** Quantification of eGFP spot fluorescence (from red circle in A) allows subunits to be counted based on photobleaching step counting. Four steps indicates one hRyR2 tetramer, with one eGFP tag on each monomer. Data obtained from Dr Bevan Cumbes via personal correspondence.

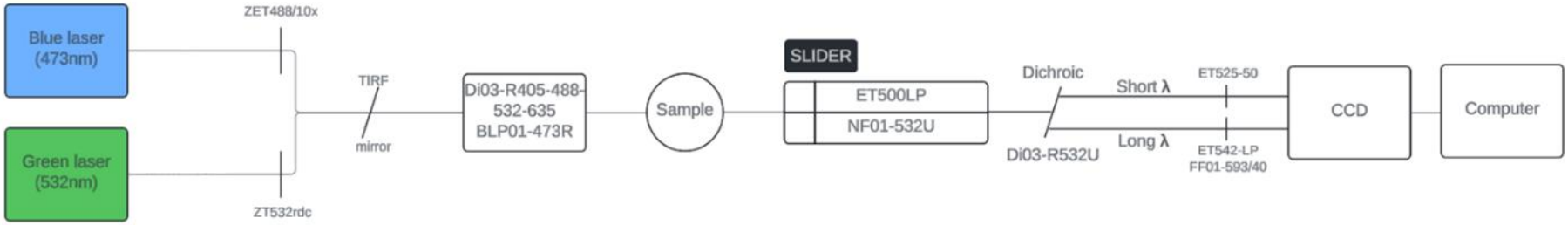

Appendix VIII. Laser path and filter setup used for TIRF microscopy in DIBs. The green 532nm laser was used to excite the Cal590 dye used to detect Ca^{2+} in the droplet; the blue 473nm laser was used to excite the eGFP tag on the recombinant hRyR2 construct. The 473nm laser first passed through the ZET488/10X bandpass filter before reaching the Nikon Eclipse Ti microscope, and the 532nm laser first passed through the ZT532rdc filter before reaching the microscope. The laser path then reached the quadband dichroic beamsplitter Di03-R405-488-532-635 placed in the filter cube and the BLP01-473R long-pass edge filter. The lasers then travelled through the 60x TIRF objective to illuminate the sample. Emitted light passed through the ET500LP and NF01-532U filters in the slider before reaching the single-edge dichroic beamsplitter Di03-R532U and splitting into the short wavelength, filtered by the ET525-50 bandpass filter, and long wavelength, filtered by the longpass ET542-LP filter. Light was captured by the Andor iXon Ultra EMCCD and processed using Andor Solis I software. Figure obtained from Hannah Baird.

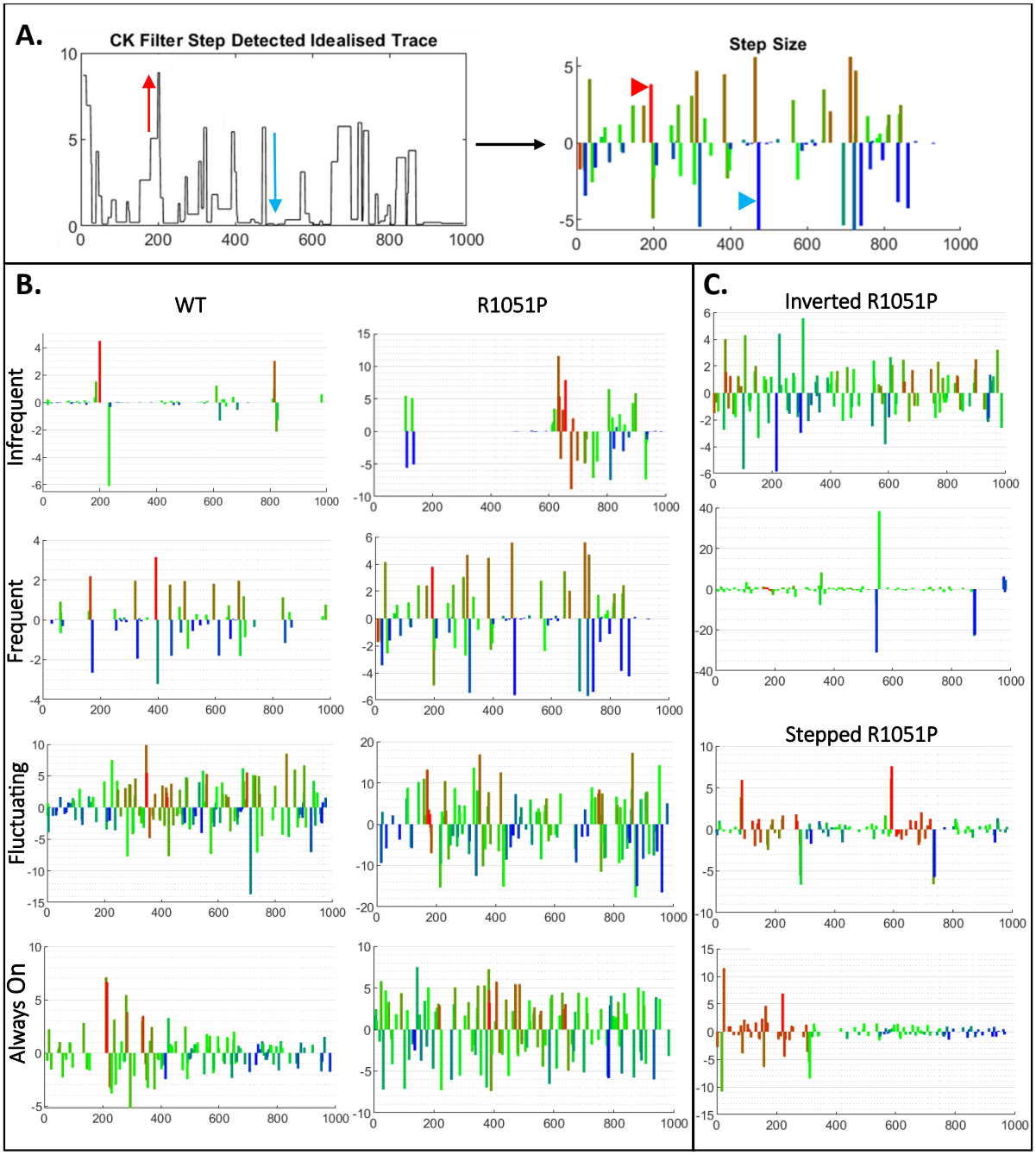

Appendix IX. Step size comparison can be used as a secondary classification for Ca^{2+} release behaviour from hRyR2 populations. A. Following trace idealisation, the direction and magnitude of steps can be plotted; green indicates the median fluorescence, red indicates a step up from the median (e.g. red arrow corresponding to red triangle); blue indicates a step down (eg. blue arrow corresponding to blue triangle). **B.** Comparison of step size changes between the four behaviours observed in both WT and R1051P; 'Infrequent', 'Frequent', 'Fluctuating' and 'Always On'. Step size changes are similar for both WT and R1051P. **C.** Step size graphs for the 'Inverted' and 'Stepped'. The 'Inverted' behaviour was less regular; this may be due to the frequency of fluorescence dropping to the baseline, however these traces were easily classified by visual comparison of raw fluorescence traces.

Infrequent	=IF(AND(COUNTIF(RANGE, "<=" & (MIN(RANGE) + (MAX(RANGE) - MIN(RANGE)) * 0.05)) >= COUNTA(RANGE) * 0.25, COUNTIF(RANGE, ">=" & (MAX(RANGE) - (MAX(RANGE) - MIN(RANGE)) * 0.5)) < COUNTA(RANGE) * 0.5, MAX(FREQUENCY(IF(RANGE <= (MIN(RANGE) + (MAX(RANGE) - MIN(RANGE)) * 0.05), ROW(RANGE)), IF(RANGE > (MIN(RANGE) + (MAX(RANGE) - MIN(RANGE)) * 0.05), ROW(RANGE)))) >= COUNTA(RANGE) * 0.25),"Yes","")
Frequent	=IF(AND(COUNTIF(RANGE, "<=" & (MIN(RANGE) + (MAX(RANGE) - MIN(RANGE)) * 0.2)) >= COUNTA(RANGE) * 0.25, COUNTIF(RANGE, ">=" & (MAX(RANGE) - (MAX(RANGE) - MIN(RANGE)) * 0.5)) < COUNTA(RANGE) * 0.5, MAX(FREQUENCY(IF(RANGE <= (MIN(RANGE) + (MAX(RANGE) - MIN(RANGE)) * 0.05), ROW(RANGE)), IF(RANGE > (MIN(RANGE) + (MAX(RANGE) - MIN(RANGE)) * 0.05), ROW(RANGE)))) <= COUNTA(RANGE) * 0.25, MAX(FREQUENCY(IF(RANGE <= (MIN(RANGE) + (MAX(RANGE) - MIN(RANGE)) * 0.05), ROW(RANGE)), IF(RANGE > (MIN(RANGE) + (MAX(RANGE) - MIN(RANGE)) * 0.05), ROW(RANGE)))) >= COUNTA(RANGE) * 0.05),"Yes","")
Fluctuating	=IF(AND(COUNTIF(RANGE, "<=" & (MIN(RANGE) + (MAX(RANGE) - MIN(RANGE)) * 0.5)) >= COUNTA(RANGE) * 0.4, COUNTIFS(RANGE, ">0", RANGE, "<1") / COUNTA(RANGE) >= 0.001, MAX(FREQUENCY(IF(RANGE <= (MIN(RANGE) + (MAX(RANGE) - MIN(RANGE)) * 0.05), ROW(RANGE)), IF(RANGE > (MIN(RANGE) + (MAX(RANGE) - MIN(RANGE)) * 0.05), ROW(RANGE)))) <= COUNTA(RANGE) * 0.05),"Yes","")
Always On	=IF(COUNTIFS(RANGE, ">0", RANGE, "<1") / COUNTA(RANGE) = 0,"Yes","")
Inverted	=IF(AND(COUNTIF(RANGE, ">=" & (MIN(RANGE) + (MAX(RANGE) - MIN(RANGE)) * 0.5)) > COUNTA(RANGE) * 0.8, COUNTIF(RANGE, "<=" & (MIN(RANGE) + (MAX(RANGE) - MIN(RANGE)) * 0.05)) >= 2),"Yes", "")

Stepped	=IF(
	AND(
	COUNTIF(RANGE, ">=" & (MAX(RANGE) - (MAX(RANGE) - MIN(RANGE)) * 0.5)) < COUNTA(RANGE) * 0.8,
	MAX(FREQUENCY(
	IF(RANGE <= (MIN(RANGE) + (MAX(RANGE) - MIN(RANGE)) * 0.5), ROW(RANGE)),
	IF(RANGE > (MIN(RANGE) + (MAX(RANGE) - MIN(RANGE)) * 0.5), ROW(RANGE))
	)) >= COUNTA(RANGE) * 0.05,
	MAX(FREQUENCY(
	IF(RANGE >= (MAX(RANGE) - (MAX(RANGE) - MIN(RANGE)) * 0.5), ROW(RANGE)),
	IF(RANGE < (MAX(RANGE) - (MAX(RANGE) - MIN(RANGE)) * 0.5), ROW(RANGE))
	)) >= COUNTA(RANGE) * 0.05),"Yes", "")

Appendix X. IF functions applied in Microsoft Excel to sort DIBs optical traces into categories. Criteria were applied to each raw trace (normalised by SMOD), where 'RANGE' includes every value for each trace (1000 per trace).

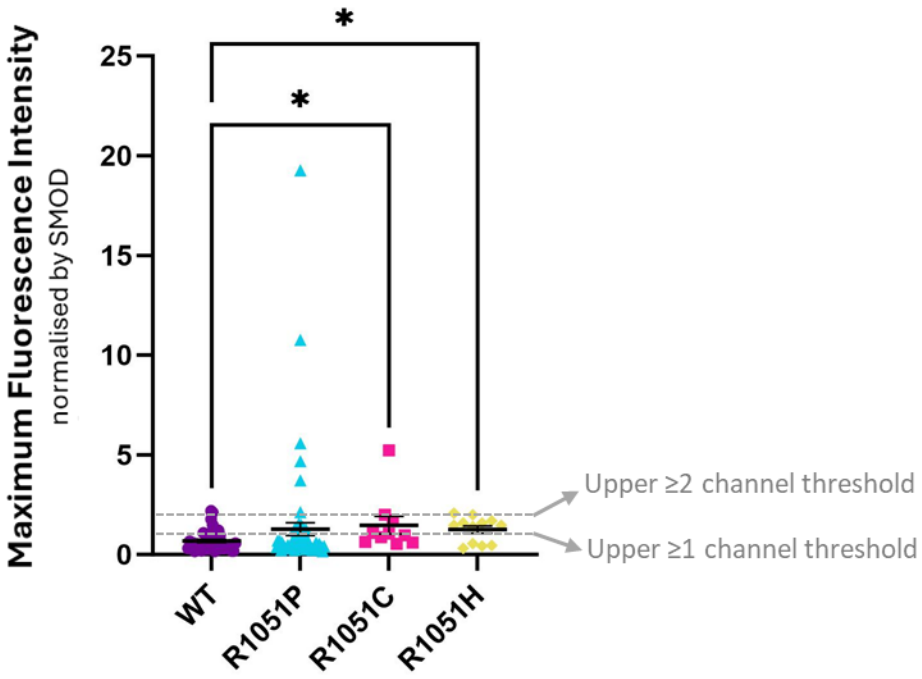

Appendix XI. R1051P-hRyR2 populations contain a comparable number of channels to WT-hRyR2 populations, despite the appearance of very large clusters. Inclusion of two very large clusters (estimated >10 channels based on Maximum Fluorescence Intensity) did not significantly alter the statistical comparison between hRyR2 clusters (**Figure 5.5**). P-value >0.05 = *, analysed using Kruskall-Wallis non-parametric test with Dunn's post-hoc test in GraphPad Prism 10.1.2.

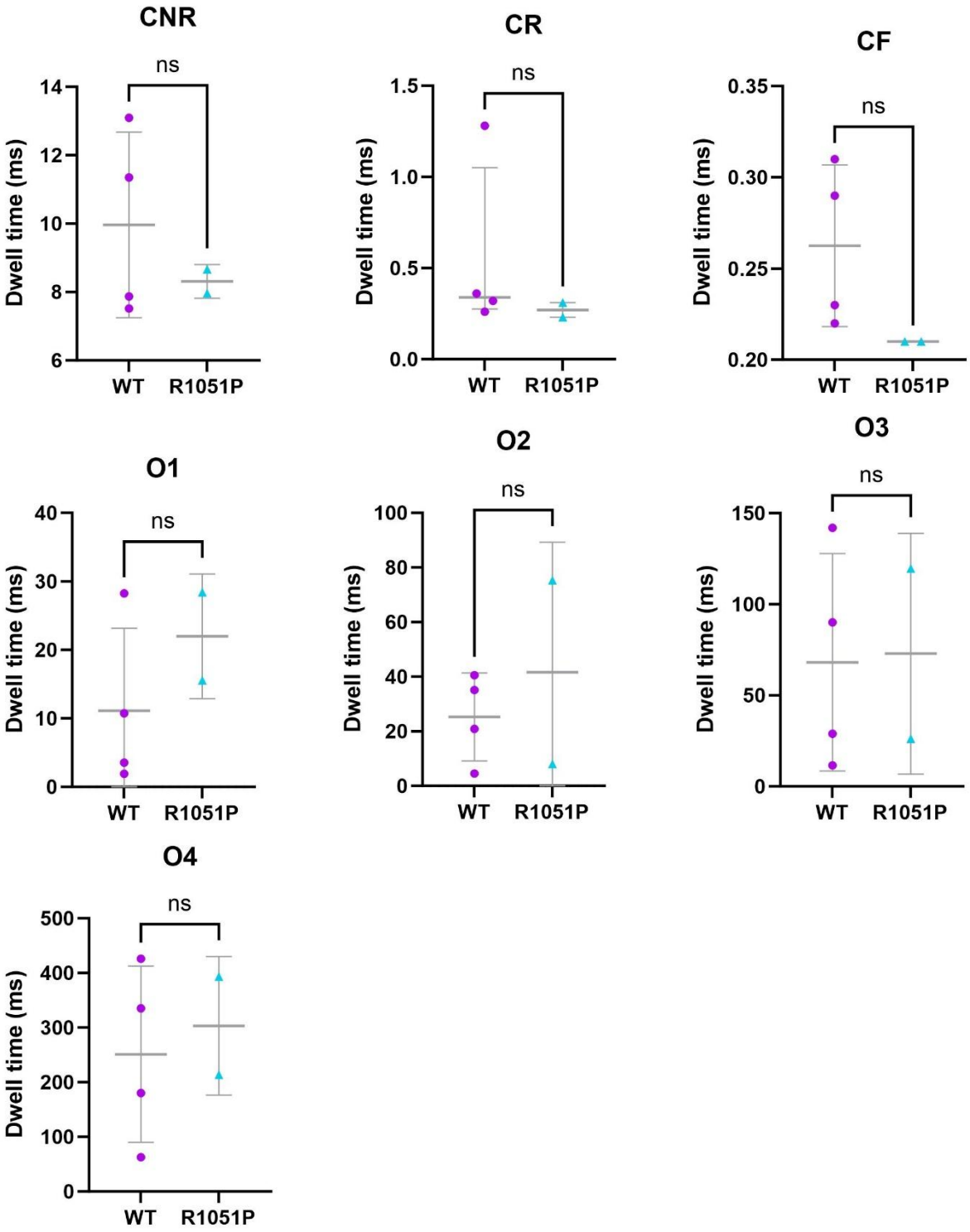

Appendix XII. Dwell times of each state in gating models of WT-hRyR2 and R1051P-hRyR2 channels were not significantly different. There was no significant difference between the dwell time of any state in R1051P-hRyR2 channels (n = 2) compared to WT-hRyR2 (n = 4). All graphs but 'CR' were analysed by T-test (for normally distributed data; unpaired, two-tailed, p-value > 0.05); 'CR' was analysed by Mann-Whitney U test (for non-normally distributed data; two-tailed, p-value > 0.05). Statistical analyses were performed in GraphPad Prism 10.1.2.

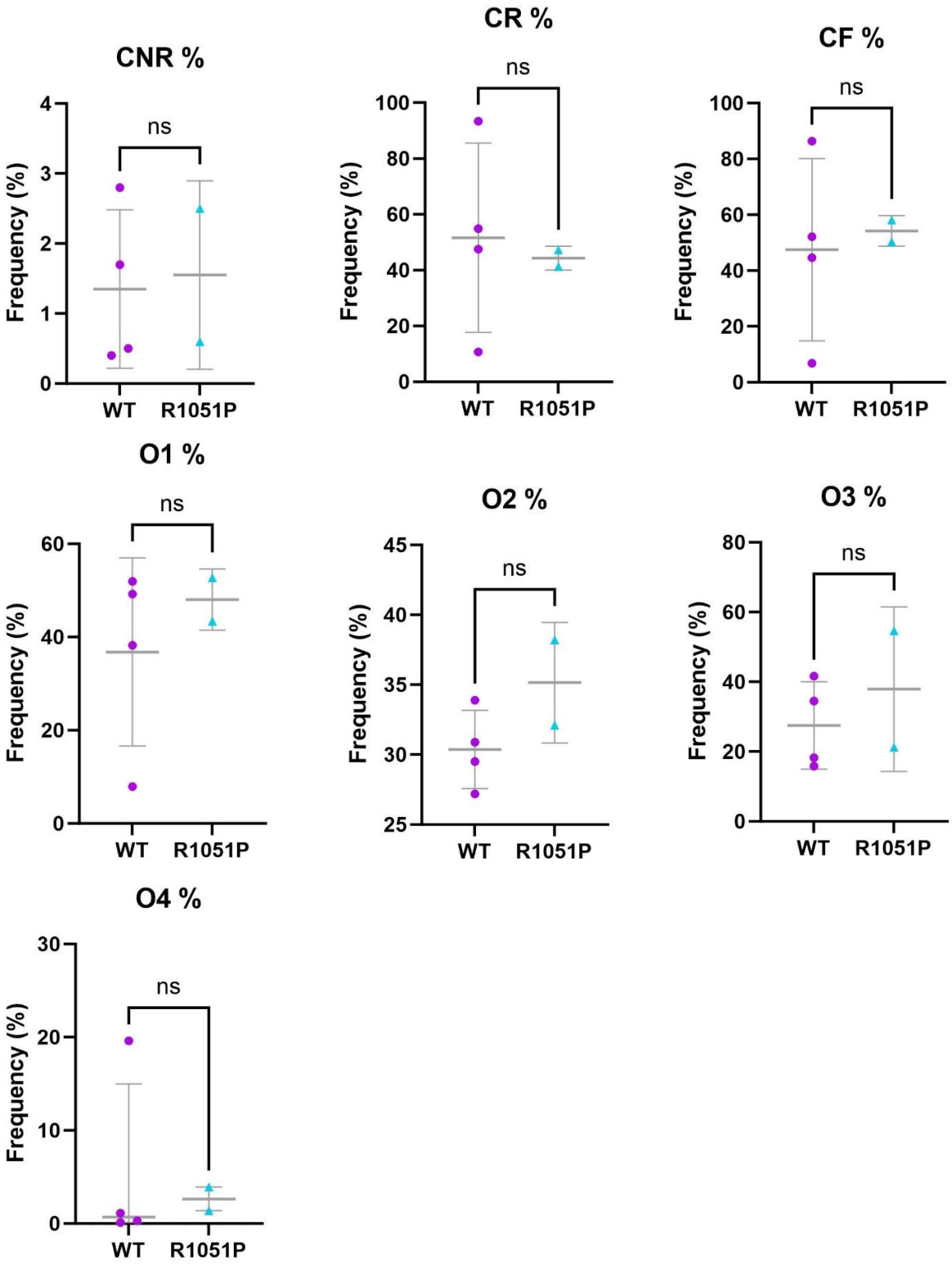

Appendix XIII. Frequency of each state in gating models of WT-hRyR2 and R1051P-hRyR2 channels were not significantly different. There was no significant difference between the dwell time of any state in R1051P-hRyR2 channels (n = 2) compared to WT-hRyR2 (n = 4). All graphs but 'O4%' were analysed by T-test (for normally distributed data; unpaired, two-tailed, p-value > 0.05); 'O4%' was analysed by Mann-Whitney U test (for non-normally distributed data; two-tailed, p-value > 0.05). Statistical analyses were performed in GraphPad Prism 10.1.2.

References

Abaandou, L., Quan, D. and Shiloach, J. 2021. Affecting HEK293 Cell Growth and Production Performance by Modifying the Expression of Specific Genes. *Cells* 10(7), p. 1667. doi: 10.3390/cells10071667.

Adzhubei, I.A. et al. 2010. A method and server for predicting damaging missense mutations. *Nature Methods* 7(4), pp. 248–249. doi: 10.1038/nmeth0410-248.

Altschafl, B.A., Arvanitis, D.A., Fuentes, O., Yuan, Q., Kranias, E.G. and Valdivia, H.H. 2011. Dual role of junctin in the regulation of ryanodine receptors and calcium release in cardiac ventricular myocytes. *The Journal of Physiology* 589(24), pp. 6063–6080. doi: 10.1113/jphysiol.2011.215988.

Alvarado, F.J. et al. 2019. Cardiac hypertrophy and arrhythmia in mice induced by a mutation in ryanodine receptor 2. *JCI Insight* 4(7). doi: 10.1172/jci.insight.126544.

Alvarado, F.J., Chen, X. and Valdivia, H.H. 2017. Ablation of the cardiac ryanodine receptor phospho-site Ser2808 does not alter the adrenergic response or the progression to heart failure in mice. Elimination of the genetic background as critical variable. *Journal of Molecular and Cellular Cardiology* 103, pp. 40–47. doi: 10.1016/j.yjmcc.2017.01.001.

Anderson, J.L. et al. 1989. Prevention of symptomatic recurrences of paroxysmal atrial fibrillation in patients initially tolerating antiarrhythmic therapy. A multicenter, double-blind, crossover study of flecainide and placebo with transtelephonic monitoring. Flecainide Supraventricular Tachycardia Study Group. *Circulation* 80(6), pp. 1557–1570. doi: 10.1161/01.CIR.80.6.1557.

Armisen, R., Sierralta, J., Velez, P., Naranjo, D. and Suarez-Isla, B.A. 1996. Modal gating in neuronal and skeletal muscle ryanodine-sensitive Ca2+ release channels. *American Journal of Physiology-Cell Physiology* 271(1), pp. C144–C153. doi: 10.1152/ajpcell.1996.271.1.C144.

Asahi, M., Sugita, Y., Kurzydlowski, K., De Leon, S., Tada, M., Toyoshima, C. and MacLennan, D.H. 2003. Sarcolipin regulates sarco(endo)plasmic reticulum Ca^{2+} -ATPase (SERCA) by binding to transmembrane helices alone or in association with phospholamban. *Proceedings of the National Academy of Sciences* 100(9), pp. 5040–5045. doi: 10.1073/pnas.0330962100.

Asghari, P., Scriven, D.R., Ng, M., Panwar, P., Chou, K.C., van Petegem, F. and Moore, E.D. 2020. Cardiac ryanodine receptor distribution is dynamic and changed by auxiliary proteins and post-translational modification. *eLife* 9. doi: 10.7554/eLife.51602.

Asghari, P., Scriven, D.R.L., Hoskins, J., Fameli, N., van Breemen, C. and Moore, E.D.W. 2012. The structure and functioning of the couplon in the mammalian cardiomyocyte. *Protoplasma* 249(S1), pp. 31–38. doi: 10.1007/s00709-011-0347-5.

Asghari, P., Scriven, D.R.L., Sanatani, S., Gandhi, S.K., Campbell, A.I.M. and Moore, E.D.W. 2014. Nonuniform and Variable Arrangements of Ryanodine Receptors Within Mammalian Ventricular Couplons. *Circulation Research* 115(2), pp. 252–262. doi: 10.1161/CIRCRESAHA.115.303897.

Ather, S., Respress, J.L., Li, N. and Wehrens, X.H.T. 2013. Alterations in ryanodine receptors and related proteins in heart failure. *Biochimica et Biophysica Acta (BBA) - Molecular Basis of Disease* 1832(12), pp. 2425–2431. doi: 10.1016/j.bbadis.2013.06.008.

Baddeley, D., Jayasinghe, I., Lam, L., Rossberger, S., Cannell, M.B. and Soeller, C. 2009. Optical single-channel resolution imaging of the ryanodine receptor distribution in rat cardiac myocytes. *Proceedings of the National Academy of Sciences* 106(52), pp. 22275–22280. doi: 10.1073/pnas.0908971106.

Baier, M.J., Noack, J., Seitz, M.T., Maier, L.S. and Neef, S. 2021. Phosphorylation of RyR2 Ser-2814 by CaMKII mediates β1-adrenergic stress induced Ca^{2+} -leak from the sarcoplasmic reticulum. *FEBS Open Bio* 11(10), pp. 2756–2762. doi: 10.1002/2211-5463.13274.

Balshaw, D.M., Xu, L., Yamaguchi, N., Pasek, D.A. and Meissner, G. 2001. Calmodulin Binding and Inhibition of Cardiac Muscle Calcium Release Channel (Ryanodine Receptor). *Journal of Biological Chemistry* 276(23), pp. 20144–20153. doi: 10.1074/jbc.M010771200.

Bannister, M.L. et al. 2015. The Mechanism of Flecainide Action in CPVT Does Not Involve a Direct Effect on RyR2. *Circulation Research* 116(8), pp. 1324–1335. doi: 10.1161/CIRCRESAHA.116.305347.

Bannister, M.L. et al. 2016. Effect of flecainide derivatives on sarcoplasmic reticulum calcium release suggests a lack of direct action on the cardiac ryanodine receptor. *British Journal of Pharmacology* 173(15), pp. 2446–2459. doi: 10.1111/bph.13521.

Bansal, S., Vachher, M. and Burman, A. 2023. Calreticulin: a quintessential multifaceted protein with therapeutic potential. *Journal of Proteins and Proteomics* 14(3), pp. 187–200. doi: 10.1007/s42485-023-00111-x.

Barg, S., Copello, J.A. and Fleischer, S. 1997. Different interactions of cardiac and skeletal muscle ryanodine receptors with FK-506 binding protein isoforms. *The American journal of physiology* 272(5 Pt 1), pp. C1726-33. doi: 10.1152/ajpcell.1997.272.5.C1726.

Basso, C., Thiene, G., Corrado, D., Angelini, A., Nava, A. and Valente, M. 1996. Arrhythmogenic Right Ventricular Cardiomyopathy. *Circulation* 94(5), pp. 983–991. doi: 10.1161/01.CIR.94.5.983.

Bauce, B. et al. 2002. Screening for ryanodine receptor type 2 mutations in families with effort-induced polymorphic ventricular arrhythmias and sudden death. *Journal of the American College of Cardiology* 40(2), pp. 341–349. doi: 10.1016/S0735-1097(02)01946-0.

Bauerová-Hlinková, V., Hajdúchová, D. and Bauer, J.A. 2020. Structure and Function of the Human Ryanodine Receptors and Their Association with Myopathies—Present State, Challenges, and Perspectives. *Molecules* 25(18). doi: 10.3390/molecules25184040.

Beard, N.A., Sakowska, M.M., Dulhunty, A.F. and Laver, D.R. 2002. Calsequestrin Is an Inhibitor of Skeletal Muscle Ryanodine Receptor Calcium Release Channels. *Biophysical Journal* 82(1), pp. 310–320. doi: 10.1016/S0006-3495(02)75396-4.

Beavers, D.L. et al. 2013. Mutation E169K in Junctophilin-2 Causes Atrial Fibrillation Due to Impaired RyR2 Stabilization. *Journal of the American College of Cardiology* 62(21), pp. 2010–2019. doi: 10.1016/j.jacc.2013.06.052.

Bellinger, A.M. et al. 2008. Remodeling of ryanodine receptor complex causes “leaky” channels: A molecular mechanism for decreased exercise capacity. *Proceedings of the National Academy of Sciences* 105(6), pp. 2198–2202. doi: 10.1073/pnas.0711074105.

Benitah, J.-P. and Gómez, A.M. 2021. Is the Debate on the Flecainide Action on the RYR2 in CPVT Closed? *Circulation Research* 128(3), pp. 332–334. doi: 10.1161/CIRCRESAHA.121.318706.

Benkusky, N.A. et al. 2007. Intact β-Adrenergic Response and Unmodified Progression Toward Heart Failure in Mice With Genetic Ablation of a Major Protein Kinase A Phosphorylation Site in the Cardiac Ryanodine Receptor. *Circulation Research* 101(8), pp. 819–829. doi: 10.1161/CIRCRESAHA.107.153007.

Beqaj, H. et al. 2024. Location of ryanodine receptor type 2 mutation predicts age of onset of sudden death in catecholaminergic polymorphic ventricular tachycardia – A systematic review and meta-analysis of case-based literature. doi: 10.1101/2024.03.15.24304349.

Berridge, M.J., Lipp, P. and Bootman, M.D. 2000. The versatility and universality of calcium signalling. *Nature Reviews Molecular Cell Biology* 1(1), pp. 11–21. doi: 10.1038/35036035.

BERS, D. 2004. Macromolecular complexes regulating cardiac ryanodine receptor function. *Journal of Molecular and Cellular Cardiology* 37(2), pp. 417–429. doi: 10.1016/j.yjmcc.2004.05.026.

Bers, D.M. 2002. Cardiac excitation–contraction coupling. *Nature* 415(6868), pp. 198–205. doi: 10.1038/415198a.

Bers, D.M. 2006. Cardiac ryanodine receptor phosphorylation: target sites and functional consequences. *Biochemical Journal* 396(1). doi: 10.1042/BJ20060377.

Bers, D.M. 2008. Calcium Cycling and Signaling in Cardiac Myocytes. *Annual Review of Physiology* 70(1), pp. 23–49. doi: 10.1146/annurev.physiol.70.113006.100455.

Bers, D.M. 2014. Cardiac Sarcoplasmic Reticulum Calcium Leak: Basis and Roles in Cardiac Dysfunction. *Annual Review of Physiology* 76(1), pp. 107–127. doi: 10.1146/annurev-physiol-020911-153308.

Bezzerides, V.J. et al. 2019. Gene Therapy for Catecholaminergic Polymorphic Ventricular Tachycardia by Inhibition of Ca^{2+} /Calmodulin-Dependent Kinase II. *Circulation* 140(5), pp. 405–419. doi: 10.1161/CIRCULATIONAHA.118.038514.

Bhuiyan, Z.A. et al. 2007. Expanding Spectrum of Human *RYR2* -Related Disease. *Circulation* 116(14), pp. 1569–1576. doi: 10.1161/CIRCULATIONAHA.107.711606.

Bovo, E., Lipsius, S.L. and Zima, A. V. 2012. Reactive oxygen species contribute to the development of arrhythmogenic Ca^{2+} waves during β-adrenergic receptor stimulation in

rabbit cardiomyocytes. *The Journal of Physiology* 590(14), pp. 3291–3304. doi: 10.1113/jphysiol.2012.230748.

Boyden, P.A., Pu, J., Pinto, J. and Keurs, H.E.D.J. ter. 2000. Ca $^{2+}$ Transients and Ca $^{2+}$ Waves in Purkinje Cells. *Circulation Research* 86(4), pp. 448–455. doi: 10.1161/01.RES.86.4.448.

Bozkurt, B. et al. 2016. Current Diagnostic and Treatment Strategies for Specific Dilated Cardiomyopathies: A Scientific Statement From the American Heart Association. *Circulation* 134(23). doi: 10.1161/CIR.0000000000000455.

Brillantes, A.-M.B. et al. 1994. Stabilization of calcium release channel (ryanodine receptor) function by FK506-binding protein. *Cell* 77(4), pp. 513–523. doi: 10.1016/0092-8674(94)90214-3.

Brochet, D.X.P., Xie, W., Yang, D., Cheng, H. and Lederer, W.J. 2011. Quarky Calcium Release in the Heart. *Circulation Research* 108(2), pp. 210–218. doi: 10.1161/CIRCRESAHA.110.231258.

Bround, M.J. et al. 2012a. Cardiac ryanodine receptors control heart rate and rhythmicity in adult mice. *Cardiovascular Research* 96(3), pp. 372–380. doi: 10.1093/cvr/cvs260.

Bround, M.J. et al. 2012b. Cardiac ryanodine receptors control heart rate and rhythmicity in adult mice. *Cardiovascular Research* 96(3), pp. 372–380. doi: 10.1093/cvr/cvs260.

Cabra, V., Murayama, T. and Samsó, M. 2016. Ultrastructural Analysis of Self-Associated RyR2s. *Biophysical Journal* 110(12), pp. 2651–2662. doi: 10.1016/j.bpj.2016.05.013.

Cai, W. et al. 2022. Abstract 11999: Molecular and Cellular Characterization of RyR2 Mutations Linked to Long-QT Syndrome. *Circulation* 146(Suppl_1). doi: 10.1161/circ.146.suppl_1.11999.

Campbell, M.J., Czosek, R.J., Hinton, R.B. and Miller, E.M. 2015. Exon 3 deletion of ryanodine receptor causes left ventricular noncompaction, worsening catecholaminergic polymorphic ventricular tachycardia, and sudden cardiac arrest. *American Journal of Medical Genetics Part A* 167(9), pp. 2197–2200. doi: 10.1002/ajmg.a.37140.

Cannell, M., Cheng, H. and Lederer, W. 1995. The control of calcium release in heart muscle. *Science* 268(5213), pp. 1045–1049. doi: 10.1126/science.7754384.

Cannell, M.B., Kong, C.H.T., Imtiaz, M.S. and Laver, D.R. 2013. Control of sarcoplasmic reticulum Ca2+ release by stochastic RyR gating within a 3D model of the cardiac dyad and importance of induction decay for CICR termination. *Biophysical journal* 104(10), pp. 2149–59. doi: 10.1016/j.bpj.2013.03.058.

Carter, S., Colyer, J. and Sitsapesan, R. 2006a. Maximum Phosphorylation of the Cardiac Ryanodine Receptor at Serine-2809 by Protein Kinase A Produces Unique Modifications to Channel Gating and Conductance Not Observed at Lower Levels of Phosphorylation. *Circulation Research* 98(12), pp. 1506–1513. doi: 10.1161/01.RES.0000227506.43292.df.

Carter, S., Colyer, J. and Sitsapesan, R. 2006b. Maximum Phosphorylation of the Cardiac Ryanodine Receptor at Serine-2809 by Protein Kinase A Produces Unique Modifications to Channel Gating and Conductance Not Observed at Lower Levels of Phosphorylation. *Circulation Research* 98(12), pp. 1506–1513. doi: 10.1161/01.RES.0000227506.43292.df.

Carter, S., Pitt, S.J., Colyer, J. and Sitsapesan, R. 2011. Ca2+-Dependent Phosphorylation of RyR2 Can Uncouple Channel Gating from Direct Cytosolic Ca2+ Regulation. *The Journal of Membrane Biology* 240(1), pp. 21–33. doi: 10.1007/s00232-011-9339-9.

Castell, O.K., Berridge, J. and Wallace, M.I. 2012. Quantification of Membrane Protein Inhibition by Optical Ion Flux in a Droplet Interface Bilayer Array. *Angewandte Chemie International Edition* 51(13), pp. 3134–3138. doi: 10.1002/anie.201107343.

Catterall, W.A. 2000. Structure and Regulation of Voltage-Gated Ca $^{2+}$ Channels. *Annual Review of Cell and Developmental Biology* 16(1), pp. 521–555. doi: 10.1146/annurev.cellbio.16.1.521.

Chakrapani, S., Cordero-Morales, J.F., Jogini, V., Pan, A.C., Cortes, D.M., Roux, B. and Perozo, E. 2011. On the structural basis of modal gating behavior in K+ channels. *Nature Structural & Molecular Biology* 18(1), pp. 67–74. doi: 10.1038/nsmb.1968.

Chazin, W.J. and Johnson, C.N. 2020. Calmodulin Mutations Associated with Heart Arrhythmia: A Status Report. *International Journal of Molecular Sciences* 21(4), p. 1418. doi: 10.3390/ijms21041418.

Chelu, M.G. et al. 2009. Calmodulin kinase II–mediated sarcoplasmic reticulum Ca2+ leak promotes atrial fibrillation in mice. *Journal of Clinical Investigation*. doi: 10.1172/JCI37059.

Chen, S.R., Leong, P., Imredy, J.P., Bartlett, C., Zhang, L. and MacLennan, D.H. 1997. Single-channel properties of the recombinant skeletal muscle Ca2+ release channel (ryanodine receptor). *Biophysical Journal* 73(4), pp. 1904–1912. doi: 10.1016/S0006-3495(97)78221-3.

Chen, W. et al. 2014. The ryanodine receptor store-sensing gate controls Ca2+ waves and Ca2+-triggered arrhythmias. *Nature Medicine* 20(2), pp. 184–192. doi: 10.1038/nm.3440.

Chen, W., Wasserstrom, J.A. and Shiferaw, Y. 2009. Role of coupled gating between cardiac ryanodine receptors in the genesis of triggered arrhythmias. *American Journal of Physiology-Heart and Circulatory Physiology* 297(1), pp. H171–H180. doi: 10.1152/ajpheart.00098.2009.

Chen, X., Piacentino, V., Furukawa, S., Goldman, B., Margulies, K.B. and Houser, S.R. 2002. L-Type Ca $^{2+}$ Channel Density and Regulation Are Altered in Failing Human Ventricular Myocytes and Recover After Support With Mechanical Assist Devices. *Circulation Research* 91(6), pp. 517–524. doi: 10.1161/01.RES.0000033988.13062.7C.

Chen, X., Weber, C., Farrell, E.T., Alvarado, F.J., Zhao, Y.-T., Gómez, A.M. and Valdivia, H.H. 2018. Sorcin ablation plus β-adrenergic stimulation generate an arrhythmogenic substrate in mouse ventricular myocytes. *Journal of Molecular and Cellular Cardiology* 114, pp. 199–210. doi: 10.1016/j.yjmcc.2017.11.017.

Cheng, H., Lederer, W.J. and Cannell, M.B. 1993. Calcium Sparks: Elementary Events Underlying Excitation-Contraction Coupling in Heart Muscle. *Science* 262(5134), pp. 740–744. doi: 10.1126/science.8235594.

Chen-Izu, Y. et al. 2006. Three-Dimensional Distribution of Ryanodine Receptor Clusters in Cardiac Myocytes. *Biophysical Journal* 91(1), pp. 1–13. doi: 10.1529/biophysj.105.077180.

Chen-Izu, Y. et al. 2007. Phosphorylation of RyR $_2$ and shortening of RyR $_2$ cluster spacing in spontaneously hypertensive rat with heart failure. *American Journal of Physiology-Heart and Circulatory Physiology* 293(4), pp. H2409–H2417. doi: 10.1152/ajpheart.00562.2007.

Chi, X. et al. 2019. Molecular basis for allosteric regulation of the type 2 ryanodine receptor channel gating by key modulators. *Proceedings of the National Academy of Sciences* 116(51), pp. 25575–25582. doi: 10.1073/pnas.1914451116.

Cooper, L.L., Li, W., Lu, Y., Centracchio, J., Terentyeva, R., Koren, G. and Terentyev, D. 2013. Redox modification of ryanodine receptors by mitochondria-derived reactive oxygen species contributes to aberrant Ca $^{2+}$ handling in ageing rabbit hearts. *The Journal of Physiology* 591(23), pp. 5895–5911. doi: 10.1113/jphysiol.2013.260521.

Copello, J.A., Barg, S., Onoue, H. and Fleischer, S. 1997. Heterogeneity of Ca2+ gating of skeletal muscle and cardiac ryanodine receptors. *Biophysical Journal* 73(1), pp. 141–156. doi: 10.1016/S0006-3495(97)78055-X.

Coppini, R., Ferrantini, C., Mugelli, A., Poggesi, C. and Cerbai, E. 2018. Altered Ca2+ and Na+ Homeostasis in Human Hypertrophic Cardiomyopathy: Implications for Arrhythmogenesis. *Frontiers in Physiology* 9. doi: 10.3389/fphys.2018.01391.

Curran, J., Hinton, M.J., Ríos, E., Bers, D.M. and Shannon, T.R. 2007a. β-Adrenergic Enhancement of Sarcoplasmic Reticulum Calcium Leak in Cardiac Myocytes Is Mediated by Calcium/Calmodulin-Dependent Protein Kinase. *Circulation Research* 100(3), pp. 391–398. doi: 10.1161/01.RES.0000258172.74570.e6.

Curran, J., Hinton, M.J., Ríos, E., Bers, D.M. and Shannon, T.R. 2007b. β-Adrenergic Enhancement of Sarcoplasmic Reticulum Calcium Leak in Cardiac Myocytes Is Mediated by Calcium/Calmodulin-Dependent Protein Kinase. *Circulation Research* 100(3), pp. 391–398. doi: 10.1161/01.RES.0000258172.74570.e6.

d'Amati, G. et al. 2005. Juvenile sudden death in a family with polymorphic ventricular arrhythmias caused by a novel RyR2 gene mutation: evidence of specific morphological substrates. *Human Pathology* 36(7), pp. 761–767. doi: 10.1016/j.humpath.2005.04.019.

Deivanayagam, C.C.S., Carson, M., Thotakura, A., Narayana, S.V.L. and Chodavarapu, R.S. 2000. Structure of FKBP12.6 in complex with rapamycin. *Acta Crystallographica Section D Biological Crystallography* 56(3), pp. 266–271. doi: 10.1107/S0907444999016571.

Dharmawan, T. et al. 2019. Identification of a novel exon3 deletion of RYR2 in a family with catecholaminergic polymorphic ventricular tachycardia. *Annals of noninvasive electrocardiology : the official journal of the International Society for Holter and Noninvasive Electrocardiology, Inc* 24(3), p. e12623. doi: 10.1111/anec.12623.

Díaz-Villanueva, J., Díaz-Molina, R. and García-González, V. 2015. Protein Folding and Mechanisms of Proteostasis. *International Journal of Molecular Sciences* 16(8), pp. 17193–17230. doi: 10.3390/ijms160817193.

Ding, J.-H. et al. 2004. Dilated cardiomyopathy caused by tissue-specific ablation of SC35 in the heart. *The EMBO Journal* 23(4), pp. 885–896. doi: 10.1038/sj.emboj.7600054.

Dobrev, D. and Wehrens, X.H.T. 2014. Role of RyR2 Phosphorylation in Heart Failure and Arrhythmias. *Circulation Research* 114(8), pp. 1311–1319. doi: 10.1161/CIRCRESAHA.114.300568.

Domingo, D. et al. 2015. Non-ventricular, Clinical, and Functional Features of the RyR2R420Q Mutation Causing Catecholaminergic Polymorphic Ventricular Tachycardia. *Revista Española de Cardiología (English Edition)* 68(5), pp. 398–407. doi: 10.1016/j.rec.2014.04.023.

Dridi, H. et al. 2021. Ryanodine receptor remodeling in cardiomyopathy and muscular dystrophy caused by lamin A/C gene mutation. *Human Molecular Genetics* 29(24), pp. 3919–3934. doi: 10.1093/hmg/ddaa278.

Dridi, H., Kushnir, A., Zalk, R., Yuan, Q., Melville, Z. and Marks, A.R. 2020. Intracellular calcium leak in heart failure and atrial fibrillation: a unifying mechanism and therapeutic target. *Nature Reviews Cardiology* 17(11), pp. 732–747. doi: 10.1038/s41569-020-0394-8.

Dries, E. et al. 2018. Hyperactive ryanodine receptors in human heart failure and ischaemic cardiomyopathy reside outside of couplons. *Cardiovascular Research* 114(11), pp. 1512–1524. doi: 10.1093/cvr/cvy088.

Del Duca, F. et al. 2024. Sudden Cardiac Death, Post-Mortem Investigation: A Proposing Panel of First Line and Second Line Genetic Tests. *Journal of Personalized Medicine* 14(5), p. 544. doi: 10.3390/jpm14050544.

Efremov, R.G., Leitner, A., Aebersold, R. and Raunser, S. 2015. Architecture and conformational switch mechanism of the ryanodine receptor. *Nature* 517(7532), pp. 39–43. doi: 10.1038/nature13916.

Eisner, D.A., Caldwell, J.L., Kistamás, K. and Trafford, A.W. 2017. Calcium and Excitation-Contraction Coupling in the Heart. *Circulation Research* 121(2), pp. 181–195. doi: 10.1161/CIRCRESAHA.117.310230.

El-Armouche, A. and Eschenhagen, T. 2009. β-Adrenergic stimulation and myocardial function in the failing heart. *Heart Failure Reviews* 14(4), pp. 225–241. doi: 10.1007/s10741-008-9132-8.

Eldar, M. 2003. A Missense Mutation in the CASQ2 Gene Is Associated with Autosomal-Recessive Catecholamine-Induced Polymorphic Ventricular Tachycardia. *Trends in Cardiovascular Medicine* 13(4), pp. 148–151. doi: 10.1016/S1050-1738(03)00025-2.

Ellis, R.J. and Minton, A.P. 2006. Protein aggregation in crowded environments. *Biological Chemistry* 387(5). doi: 10.1515/BC.2006.064.

El-Sherif, N. and Turitto, G. 1999. The Long QT Syndrome and Torsade De Pointes. *Pacing and Clinical Electrophysiology* 22(1), pp. 91–110. doi: 10.1111/j.1540-8159.1999.tb00305.x.

Fabiato, A. 1983. Calcium-induced release of calcium from the cardiac sarcoplasmic reticulum. *American Journal of Physiology-Cell Physiology* 245(1), pp. C1–C14. doi: 10.1152/ajpcell.1983.245.1.C1.

Fabiato, A. 1985a. Simulated calcium current can both cause calcium loading in and trigger calcium release from the sarcoplasmic reticulum of a skinned canine cardiac Purkinje cell. *The Journal of general physiology* 85(2), pp. 291–320. doi: 10.1085/jgp.85.2.291.

Fabiato, A. 1985b. Time and calcium dependence of activation and inactivation of calcium-induced release of calcium from the sarcoplasmic reticulum of a skinned canine cardiac Purkinje cell. *The Journal of general physiology* 85(2), pp. 247–289. doi: 10.1085/jgp.85.2.247.

Fan, G.-C., Yuan, Q. and Kranias, E.G. 2008. Regulatory Roles of Junctin in Sarcoplasmic Reticulum Calcium Cycling and Myocardial Function. *Trends in Cardiovascular Medicine* 18(1), pp. 1–5. doi: 10.1016/j.tcm.2007.10.002.

Farrell, E.F., Antaramian, A., Rueda, A., Gómez, A.M. and Valdivia, H.H. 2003. Sorcin Inhibits Calcium Release and Modulates Excitation-Contraction Coupling in the Heart. *Journal of Biological Chemistry* 278(36), pp. 34660–34666. doi: 10.1074/jbc.M305931200.

Fatkin, D. and Graham, R.M. 2002. Molecular Mechanisms of Inherited Cardiomyopathies. *Physiological Reviews* 82(4), pp. 945–980. doi: 10.1152/physrev.00012.2002.

Fauconnier, J. et al. 2011. Ryanodine receptor leak mediated by caspase-8 activation leads to left ventricular injury after myocardial ischemia-reperfusion. *Proceedings of the National Academy of Sciences* 108(32), pp. 13258–13263. doi: 10.1073/pnas.1100286108.

Favre, I., Sun, Y.-M. and Moczydlowski, E. 1999. Reconstitution of native and cloned channels into planar bilayers. pp. 287–304. doi: 10.1016/S0076-6879(99)94018-1.

Fernández-Velasco, M. et al. 2009. Increased Ca^{2+} Sensitivity of the Ryanodine Receptor Mutant RyR2 ^{R4496C} Underlies Catecholaminergic Polymorphic Ventricular Tachycardia. *Circulation Research* 104(2), pp. 201–209. doi: 10.1161/CIRCRESAHA.108.177493.

Fernández-Velasco, M. et al. 2009. Increased Ca2+ sensitivity of the ryanodine receptor mutant RyR2R4496C underlies catecholaminergic polymorphic ventricular tachycardia. *Circulation research* 104(2), pp. 201–9, 12p following 209. doi: 10.1161/CIRCRESAHA.108.177493.

De Ferrari, G.M., Viola, M., D'Amato, E., Antolini, R. and Forti, S. 1995. Distinct Patterns of Calcium Transients During Early and Delayed Afterdepolarizations Induced by Isoproterenol in Ventricular Myocytes. *Circulation* 91(10), pp. 2510–2515. doi: 10.1161/01.CIR.91.10.2510.

Fessenden, J.D., Chen, L., Wang, Y., Paolini, C., Franzini-Armstrong, C., Allen, P.D. and Pessah, I.N. 2001. Ryanodine receptor point mutant E4032A reveals an allosteric interaction with ryanodine. *Proceedings of the National Academy of Sciences* 98(5), pp. 2865–2870. doi: 10.1073/pnas.041608898.

Fischer, T.H. et al. 2014. Ca^{2+} /calmodulin-dependent protein kinase <scp>II</scp> equally induces sarcoplasmic reticulum Ca^{2+} leak in human ischaemic and dilated cardiomyopathy. *European Journal of Heart Failure* 16(12), pp. 1292–1300. doi: 10.1002/ejhf.163.

Fowler, E.D. and Zissimopoulos, S. 2022. Molecular, Subcellular, and Arrhythmogenic Mechanisms in Genetic RyR2 Disease. *Biomolecules* 12(8). doi: 10.3390/biom12081030.

Franzini-Armstrong, C., Protasi, F. and Ramesh, V. 1998. Comparative Ultrastructure of Ca^{2+} Release Units in Skeletal and Cardiac Muscle. *Annals of the New York Academy of Sciences* 853(1), pp. 20–30. doi: 10.1111/j.1749-6632.1998.tb08253.x.

Franzini-Armstrong, C., Protasi, F. and Ramesh, V. 1999. Shape, Size, and Distribution of Ca2+ Release Units and Couplons in Skeletal and Cardiac Muscles. *Biophysical Journal* 77(3), pp. 1528–1539. doi: 10.1016/S0006-3495(99)77000-1.

Fruen, B.R., Bardy, J.M., Byrem, T.M., Strasburg, G.M. and Louis, C.F. 2000. Differential Ca^{2+} sensitivity of skeletal and cardiac muscle ryanodine receptors in the presence of calmodulin. *American Journal of Physiology-Cell Physiology* 279(3), pp. C724–C733. doi: 10.1152/ajpcell.2000.279.3.C724.

Fujii, Y. et al. 2017. A type 2 ryanodine receptor variant associated with reduced Ca2+ release and short-coupled torsades de pointes ventricular arrhythmia. *Heart Rhythm* 14(1), pp. 98–107. doi: 10.1016/j.hrthm.2016.10.015.

Fujino, N. et al. 2006. Abstract 915: A Novel Missense Mutation in Cardiac Ryanodine Receptor Gene as a Possible Cause of Hypertrophic Cardiomyopathy: Evidence From Familial Analysis. *Circulation* 114, p. Number_suppl_18.

Gaburjakova, J. and Gaburjakova, M. 2008. Effect of luminal Ca^{2+} on the stability of coupled gating between ryanodine receptors from the rat heart. *Acta Physiologica* 193(3), pp. 219–227. doi: 10.1111/j.1748-1716.2008.01837.x.

Gaburjakova, J. and Gaburjakova, M. 2010. Identification of Changes in the Functional Profile of the Cardiac Ryanodine Receptor Caused by the Coupled Gating Phenomenon. *Journal of Membrane Biology* 234(3), pp. 159–169. doi: 10.1007/s00232-010-9243-8.

Galfré, E. et al. 2012a. FKBP12 Activates the Cardiac Ryanodine Receptor Ca2+-Release Channel and Is Antagonised by FKBP12.6. *PLoS ONE* 7(2), p. e31956. doi: 10.1371/journal.pone.0031956.

Galfré, E. et al. 2012b. FKBP12 Activates the Cardiac Ryanodine Receptor Ca2+-Release Channel and Is Antagonised by FKBP12.6. *PLoS ONE* 7(2), p. e31956. doi: 10.1371/journal.pone.0031956.

Galice, S., Xie, Y., Yang, Y., Sato, D. and Bers, D.M. 2018. Size Matters: Ryanodine Receptor Cluster Size Affects Arrhythmogenic Sarcoplasmic Reticulum Calcium Release. *Journal of the American Heart Association* 7(13). doi: 10.1161/JAHA.118.008724.

Garcia-Elias, A. and Benito, B. 2018. Ion Channel Disorders and Sudden Cardiac Death. *International Journal of Molecular Sciences* 19(3), p. 692. doi: 10.3390/ijms19030692.

Gelebart, P., Opas, M. and Michalak, M. 2005. Calreticulin, a Ca2+-binding chaperone of the endoplasmic reticulum. *The International Journal of Biochemistry & Cell Biology* 37(2), pp. 260–266. doi: 10.1016/j.biocel.2004.02.030.

George, C.H., Higgs, G. V. and Lai, F.A. 2003a. Ryanodine Receptor Mutations Associated With Stress-Induced Ventricular Tachycardia Mediate Increased Calcium Release in Stimulated Cardiomyocytes. *Circulation Research* 93(6), pp. 531–540. doi: 10.1161/01.RES.0000091335.07574.86.

George, C.H., Jundi, H., Thomas, N.L., Fry, D.L. and Lai, F.A. 2007. Ryanodine receptors and ventricular arrhythmias: Emerging trends in mutations, mechanisms and therapies. *Journal of Molecular and Cellular Cardiology* 42(1), pp. 34–50. doi: 10.1016/j.yjmcc.2006.08.115.

George, C.H., Sorathia, R., Bertrand, B.M.A. and Lai, F.A. 2003b. In situ modulation of the human cardiac ryanodine receptor (hRyR2) by FKBP12.6. *Biochemical Journal* 370(2), pp. 579–589. doi: 10.1042/bj20021433.

des Georges, A. et al. 2016a. Structural Basis for Gating and Activation of RyR1. *Cell* 167(1), pp. 145-157.e17. doi: 10.1016/j.cell.2016.08.075.

des Georges, A. et al. 2016b. Structural Basis for Gating and Activation of RyR1. *Cell* 167(1), pp. 145-157.e17. doi: 10.1016/j.cell.2016.08.075.

Gillespie, D. and Fill, M. 2013. Pernicious attrition and inter-RyR2 CICR current control in cardiac muscle. *Journal of Molecular and Cellular Cardiology* 58, pp. 53–58. doi: 10.1016/j.yjmcc.2013.01.011.

Gillespie, D., Xu, L., Wang, Y. and Meissner, G. 2005. (De)constructing the Ryanodine Receptor: Modeling Ion Permeation and Selectivity of the Calcium Release Channel. *The Journal of Physical Chemistry B* 109(32), pp. 15598–15610. doi: 10.1021/jp052471j.

Giudicessi, J.R. et al. 2019. Assessment and Validation of a Phenotype-Enhanced Variant Classification Framework to Promote or Demote *RYR2* Missense Variants of Uncertain Significance. *Circulation: Genomic and Precision Medicine* 12(5). doi: 10.1161/CIRCGEN.119.002510.

Godt, R.E. and Maughan, D.W. 1988. On the composition of the cytosol of relaxed skeletal muscle of the frog. *American Journal of Physiology-Cell Physiology* 254(5), pp. C591–C604. doi: 10.1152/ajpcell.1988.254.5.C591.

Gold, L.I. et al. 2010. Calreticulin: non-endoplasmic reticulum functions in physiology and disease. *The FASEB Journal* 24(3), pp. 665–683. doi: 10.1096/fj.09-145482.

Goll, D.E., Thompson, V.F., Li, H., Wei, W. and Cong, J. 2003. The Calpain System. *Physiological Reviews* 83(3), pp. 731–801. doi: 10.1152/physrev.00029.2002.

Golob, M., Moss, R.L. and Chesler, N.C. 2014. Cardiac Tissue Structure, Properties, and Performance: A Materials Science Perspective. *Annals of Biomedical Engineering* 42(10), pp. 2003–2013. doi: 10.1007/s10439-014-1071-z.

Gómez, A.M., Guatimosim, S., Dilly, K.W., Vassort, G. and Lederer, W.J. 2001. Heart Failure After Myocardial Infarction. *Circulation* 104(6), pp. 688–693. doi: 10.1161/hc3201.092285.

Gonano, L.A. and Jones, P.P. 2017. FK506-binding proteins 12 and 12.6 (FKBPs) as regulators of cardiac Ryanodine Receptors: Insights from new functional and structural knowledge. *Channels* 11(5), pp. 415–425. doi: 10.1080/19336950.2017.1344799.

Gong, D. et al. 2019. Modulation of cardiac ryanodine receptor 2 by calmodulin. *Nature* 572(7769), pp. 347–351. doi: 10.1038/s41586-019-1377-y.

Gonzalez, D.R., Treuer, A., Sun, Q.-A., Stamler, J.S. and Hare, J.M. 2009. S-Nitrosylation of Cardiac Ion Channels. *Journal of Cardiovascular Pharmacology* 54(3), pp. 188–195. doi: 10.1097/FJC.0b013e3181b72c9f.

Gonzalez, D.R., Treuer, A. V., Castellanos, J., Dulce, R.A. and Hare, J.M. 2010. Impaired S-Nitrosylation of the Ryanodine Receptor Caused by Xanthine Oxidase Activity Contributes to Calcium Leak in Heart Failure. *Journal of Biological Chemistry* 285(37), pp. 28938–28945. doi: 10.1074/jbc.M110.154948.

Gross, L.C.M., Castell, O.K. and Wallace, M.I. 2011. Dynamic and Reversible Control of 2D Membrane Protein Concentration in a Droplet Interface Bilayer. *Nano Letters* 11(8), pp. 3324–3328. doi: 10.1021/nl201689v.

Guo, A., Zhang, C., Wei, S., Chen, B. and Song, L.-S. 2013. Emerging mechanisms of T-tubule remodelling in heart failure. *Cardiovascular Research* 98(2), pp. 204–215. doi: 10.1093/cvr/cvt020.

Guo, T. et al. 2010. Kinetics of FKBP12.6 Binding to Ryanodine Receptors in Permeabilized Cardiac Myocytes and Effects on Ca Sparks. *Circulation Research* 106(11), pp. 1743–1752. doi: 10.1161/CIRCRESAHA.110.219816.

Guo, T., Zhang, T., Mestril, R. and Bers, D.M. 2006. Ca^{2+} /Calmodulin-Dependent Protein Kinase II Phosphorylation of Ryanodine Receptor Does Affect Calcium Sparks in Mouse Ventricular Myocytes. *Circulation Research* 99(4), pp. 398–406. doi: 10.1161/01.RES.0000236756.06252.13.

Guo, W. and Campbell, K.P. 1995. Association of Triadin with the Ryanodine Receptor and Calsequestrin in the Lumen of the Sarcoplasmic Reticulum. *Journal of Biological Chemistry* 270(16), pp. 9027–9030. doi: 10.1074/jbc.270.16.9027.

Guo, W., Wei, J., Estillore, J.P., Zhang, L., Wang, R., Sun, B. and Chen, S.R.W. 2021. RyR2 disease mutations at the C-terminal domain intersubunit interface alter closed-state stability and channel activation. *Journal of Biological Chemistry* 297(1), p. 100808. doi: 10.1016/j.jbc.2021.100808.

Guo, Y. et al. 2023. Ryanodine receptor 2 (RYR2) dysfunction activates the unfolded protein response and perturbs cardiomyocyte maturation. *Cardiovascular Research* 119(1), pp. 221–235. doi: 10.1093/cvr/cvac077.

Györke, I., Hester, N., Jones, L.R. and Györke, S. 2004. The Role of Calsequestrin, Triadin, and Junctin in Conferring Cardiac Ryanodine Receptor Responsiveness to Luminal Calcium. *Biophysical Journal* 86(4), pp. 2121–2128. doi: 10.1016/S0006-3495(04)74271-X.

Györke, S. 1999. Ca2+ Spark Termination. *The Journal of General Physiology* 114(1), pp. 163–166. doi: 10.1085/jgp.114.1.163.

Györke, S. and Fill, M. 1993. Ryanodine Receptor Adaptation: Control Mechanism of Ca^{2+}-Induced Ca^{2+} Release in Heart. *Science* 260(5109), pp. 807–809. doi: 10.1126/science.8387229.

Gyorke, S. and Terentyev, D. 2007. Modulation of ryanodine receptor by luminal calcium and accessory proteins in health and cardiac disease. *Cardiovascular Research* 77(2), pp. 245–255. doi: 10.1093/cvr/cvm038.

Haas, J. et al. 2015. Atlas of the clinical genetics of human dilated cardiomyopathy. *European Heart Journal* 36(18), pp. 1123–1135. doi: 10.1093/eurheartj/ehu301.

Haghighi, K., Gregory, K.N. and Kranias, E.G. 2004. Sarcoplasmic reticulum Ca-ATPase–phospholamban interactions and dilated cardiomyopathy. *Biochemical and Biophysical Research Communications* 322(4), pp. 1214–1222. doi: 10.1016/j.bbrc.2004.07.164.

Hakamata, Y., Nakai, J., Takeshima, H. and Imoto, K. 1992. Primary structure and distribution of a novel ryanodine receptor/calcium release channel from rabbit brain. *FEBS Letters* 312(2–3), pp. 229–235. doi: 10.1016/0014-5793(92)80941-9.

Halls, M.L. and Cooper, D.M.F. 2011. Regulation by Ca2+-Signaling Pathways of Adenylyl Cyclases. *Cold Spring Harbor Perspectives in Biology* 3(1), pp. a004143–a004143. doi: 10.1101/cshperspect.a004143.

Hamilton, S. 2017. *Functional heterogeneity of CPVTmutant human cardiac ryanodine receptors: evaluation of the influence of S2031 and S2808 phosphorylation sites*. Cardiff: Cardiff University.

Hamilton, S. et al. 2020. Increased RyR2 activity is exacerbated by calcium leak-induced mitochondrial ROS. *Basic Research in Cardiology* 115(4), p. 38. doi: 10.1007/s00395-020-0797-z.

Handhle, A., Ormonde, C.E., Thomas, N.L., Bralesford, C., Williams, A.J., Lai, F.A. and Zissimopoulos, S. 2016. Calsequestrin interacts directly with the cardiac ryanodine receptor luminal domain. *Journal of Cell Science* 129(21), pp. 3983–3988. doi: 10.1242/jcs.191643.

Hasenfuss, G. et al. 1994. Relation between myocardial function and expression of sarcoplasmic reticulum Ca(2+)-ATPase in failing and nonfailing human myocardium. *Circulation Research* 75(3), pp. 434–442. doi: 10.1161/01.RES.75.3.434.

Hasenfuss, G. and Pieske, B. 2002. Calcium Cycling in Congestive Heart Failure. *Journal of Molecular and Cellular Cardiology* 34(8), pp. 951–969. doi: 10.1006/jmcc.2002.2037.

Hauser, N.S., Solomon, B.D., Vilboux, T., Khromykh, A., Baveja, R. and Bodian, D.L. 2018. Experience with genomic sequencing in pediatric patients with congenital cardiac defects in a large community hospital. *Molecular Genetics & Genomic Medicine* 6(2), pp. 200–212. doi: 10.1002/mgg3.357.

Hawey, C. et al. 2023. Measuring Single-Cell Calcium Dynamics Using a Myofilament-Localized Optical Biosensor in hiPSC-CMs Derived from DCM Patients. *Cells* 12(21), p. 2526. doi: 10.3390/cells12212526.

Hayashi, M. et al. 2009. Incidence and Risk Factors of Arrhythmic Events in Catecholaminergic Polymorphic Ventricular Tachycardia. *Circulation* 119(18), pp. 2426–2434. doi: 10.1161/CIRCULATIONAHA.108.829267.

Hernández-Ochoa, E.O., Pratt, S.J.P., Lovering, R.M. and Schneider, M.F. 2016. Critical Role of Intracellular RyR1 Calcium Release Channels in Skeletal Muscle Function and Disease. *Frontiers in Physiology* 6. doi: 10.3389/fphys.2015.00420.

Hetz, C., Martinon, F., Rodriguez, D. and Glimcher, L.H. 2011. The Unfolded Protein Response: Integrating Stress Signals Through the Stress Sensor IRE1α. *Physiological Reviews* 91(4), pp. 1219–1243. doi: 10.1152/physrev.00001.2011.

Hilliard, F.A. et al. 2010. Flecainide inhibits arrhythmogenic Ca2+ waves by open state block of ryanodine receptor Ca2+ release channels and reduction of Ca2+ spark mass. *Journal of Molecular and Cellular Cardiology* 48(2), pp. 293–301. doi: 10.1016/j.yjmcc.2009.10.005.

Hiromoto, K., Shimizu, H., Furukawa, Y., Kanemori, T., Mine, T., Masuyama, T. and Ohyanagi, M. 2005. Discordant Repolarization Alternans-Induced Atrial Fibrillation is Suppressed by Verapamil. *Circulation Journal* 69(11), pp. 1368–1373. doi: 10.1253/circj.69.1368.

Hirose, S. et al. 2022. Loss-of-function mutations in cardiac ryanodine receptor channel cause various types of arrhythmias including long QT syndrome. *EP Europace* 24(3), pp. 497–510. doi: 10.1093/europace/euab250.

Hou, Y. et al. 2023a. Live-cell photoactivated localization microscopy correlates nanoscale ryanodine receptor configuration to calcium sparks in cardiomyocytes. *Nature Cardiovascular Research* 2(3), pp. 251–267. doi: 10.1038/s44161-022-00199-2.

Hou, Y. et al. 2023b. Live-cell photoactivated localization microscopy correlates nanoscale ryanodine receptor configuration to calcium sparks in cardiomyocytes. *Nature Cardiovascular Research* 2(3), pp. 251–267. doi: 10.1038/s44161-022-00199-2.

Hou, Y., Jayasinghe, I., Crossman, D.J., Baddeley, D. and Soeller, C. 2015. Nanoscale analysis of ryanodine receptor clusters in dyadic couplings of rat cardiac myocytes. *Journal of Molecular and Cellular Cardiology* 80, pp. 45–55. doi: 10.1016/j.yjmcc.2014.12.013.

Houser, S.R. 2014. Role of RyR2 Phosphorylation in Heart Failure and Arrhythmias. *Circulation Research* 114(8), pp. 1320–1327. doi: 10.1161/CIRCRESAHA.114.300569.

Hu, X.-F., Liang, X., Chen, K.-Y., Zhu, P.-H. and Hu, J. 2005. Depletion of FKBP does not affect the interaction between isolated ryanodine receptors. *Biochemical and Biophysical Research Communications* 336(1), pp. 128–133. doi: 10.1016/j.bbrc.2005.08.051.

Hu, Y., Iyer, K., Nayak, A., Kurebayashi, N., Murayama, T. and Samso, M. 2021. Purification of Recombinant Wild Type and Mutant Ryanodine Receptors Expressed in HEK293 Cells. *BIO-PROTOCOL* 11(15). doi: 10.21769/BioProtoc.4112.

Huke, S. and Bers, D.M. 2008. Ryanodine receptor phosphorylation at Serine 2030, 2808 and 2814 in rat cardiomyocytes. *Biochemical and Biophysical Research Communications* 376(1), pp. 80–85. doi: 10.1016/j.bbrc.2008.08.084.

Hwang, H.S. et al. 2011. Inhibition of Cardiac Ca $^{2+}$ Release Channels (RyR2) Determines Efficacy of Class I Antiarrhythmic Drugs in Catecholaminergic Polymorphic Ventricular

Tachycardia. *Circulation: Arrhythmia and Electrophysiology* 4(2), pp. 128–135. doi: 10.1161/CIRCEP.110.959916.

Ikemoto, N. 2002. Regulation of calcium release by interdomain interaction within ryanodine receptors. *Frontiers in Bioscience* 7(4), p. A803. doi: 10.2741/A803.

Ilari, A. et al. 2015. Structural basis of Sorcin-mediated calcium-dependent signal transduction. *Scientific Reports* 5(1), p. 16828. doi: 10.1038/srep16828.

Imai, K. and Mitaku, S. 2005. Mechanisms of secondary structure breakers in soluble proteins. *BIOPHYSICS* 1, pp. 55–65. doi: 10.2142/biophysics.1.55.

Ioannidis, N.M. et al. 2016. REVEL: An Ensemble Method for Predicting the Pathogenicity of Rare Missense Variants. *The American Journal of Human Genetics* 99(4), pp. 877–885. doi: 10.1016/j.ajhg.2016.08.016.

Janse, M. 2004. Electrophysiological changes in heart failure and their relationship to arrhythmogenesis. *Cardiovascular Research* 61(2), pp. 208–217. doi: 10.1016/j.cardiores.2003.11.018.

January, C.T. and Moscucci, A. 1992. Cellular Mechanisms of Early Afterdepolarizationsa. *Annals of the New York Academy of Sciences* 644(1), pp. 23–32. doi: 10.1111/j.1749-6632.1992.tb30999.x.

Jayasinghe, I. et al. 2018. True Molecular Scale Visualization of Variable Clustering Properties of Ryanodine Receptors. *Cell Reports* 22(2), pp. 557–567. doi: 10.1016/j.celrep.2017.12.045.

Jeyakumar, L.H. et al. 2001. FKBP Binding Characteristics of Cardiac Microsomes from Diverse Vertebrates. *Biochemical and Biophysical Research Communications* 281(4), pp. 979–986. doi: 10.1006/bbrc.2001.4444.

Jiang, D. et al. 2004. RyR2 mutations linked to ventricular tachycardia and sudden death reduce the threshold for store-overload-induced Ca^{2+} release (SOICR). *Proceedings of the National Academy of Sciences* 101(35), pp. 13062–13067. doi: 10.1073/pnas.0402388101.

Jiang, D. et al. 2005. Enhanced Store Overload–Induced Ca^{2+} Release and Channel Sensitivity to Luminal Ca^{2+} Activation Are Common Defects of RyR2 Mutations Linked to Ventricular

Tachycardia and Sudden Death. *Circulation Research* 97(11), pp. 1173–1181. doi: 10.1161/01.RES.0000192146.85173.4b.

Jiang, D., Chen, W., Wang, R., Zhang, L. and Chen, S.R.W. 2007. Loss of luminal Ca $^{2+}$ activation in the cardiac ryanodine receptor is associated with ventricular fibrillation and sudden death. *Proceedings of the National Academy of Sciences* 104(46), pp. 18309–18314. doi: 10.1073/pnas.0706573104.

Jiang, D., Xiao, B., Zhang, L. and Chen, S.R.W. 2002a. Enhanced Basal Activity of a Cardiac Ca $^{2+}$ Release Channel (Ryanodine Receptor) Mutant Associated With Ventricular Tachycardia and Sudden Death. *Circulation Research* 91(3), pp. 218–225. doi: 10.1161/01.RES.0000028455.36940.5E.

Jiang, M.T., Lokuta, A.J., Farrell, E.F., Wolff, M.R., Haworth, R.A. and Valdivia, H.H. 2002b. Abnormal Ca $^{2+}$ Release, but Normal Ryanodine Receptors, in Canine and Human Heart Failure. *Circulation Research* 91(11), pp. 1015–1022. doi: 10.1161/01.RES.0000043663.08689.05.

Jones, P.P., Jiang, D., Bolstad, J., Hunt, D.J., Zhang, L., Demaurex, N. and Chen, S.R.W. 2008. Endoplasmic reticulum Ca2+ measurements reveal that the cardiac ryanodine receptor mutations linked to cardiac arrhythmia and sudden death alter the threshold for store-overload-induced Ca2+ release. *Biochemical Journal* 412(1), pp. 171–178. doi: 10.1042/BJ20071287.

Jones, P.P., MacQuaide, N. and Louch, W.E. 2018. Dyadic Plasticity in Cardiomyocytes. *Frontiers in Physiology* 9. doi: 10.3389/fphys.2018.01773.

Joseph, T.T. et al. 2024. Propofol binds and inhibits skeletal muscle ryanodine receptor 1. *British Journal of Anaesthesia* 133(5), pp. 1093–1100. doi: 10.1016/j.bja.2024.06.048.

Jungmann, R., Avendaño, M.S., Woehrstein, J.B., Dai, M., Shih, W.M. and Yin, P. 2014. Multiplexed 3D cellular super-resolution imaging with DNA-PAINT and Exchange-PAINT. *Nature Methods* 11(3), pp. 313–318. doi: 10.1038/nmeth.2835.

Jungmann, R., Steinhauer, C., Scheible, M., Kuzyk, A., Tinnefeld, P. and Simmel, F.C. 2010. Single-Molecule Kinetics and Super-Resolution Microscopy by Fluorescence Imaging of

Transient Binding on DNA Origami. *Nano Letters* 10(11), pp. 4756–4761. doi: 10.1021/nl103427w.

Kajii, T. et al. 2020. Dantrolene prevents ventricular tachycardia by stabilizing the ryanodine receptor in pressure- overload induced failing hearts. *Biochemical and Biophysical Research Communications* 521(1), pp. 57–63. doi: 10.1016/j.bbrc.2019.10.071.

Kannankeril, P.J. et al. 2006. Mice with the R176Q cardiac ryanodine receptor mutation exhibit catecholamine-induced ventricular tachycardia and cardiomyopathy. *Proceedings of the National Academy of Sciences* 103(32), pp. 12179–12184. doi: 10.1073/pnas.0600268103.

Kapplinger, J.D. et al. 2018. Yield of the *RYR2* Genetic Test in Suspected Catecholaminergic Polymorphic Ventricular Tachycardia and Implications for Test Interpretation. *Circulation: Genomic and Precision Medicine* 11(2). doi: 10.1161/CIRCGEN.116.001424.

Karczewski, K.J. et al. 2020. The mutational constraint spectrum quantified from variation in 141,456 humans. *Nature* 581(7809), pp. 434–443. doi: 10.1038/s41586-020-2308-7.

Katra, R.P. and Laurita, K.R. 2005. Cellular Mechanism of Calcium-Mediated Triggered Activity in the Heart. *Circulation Research* 96(5), pp. 535–542. doi: 10.1161/01.RES.0000159387.00749.3c.

Kaya, L. et al. 2013. Direct association of the reticulon protein RTN1A with the ryanodine receptor 2 in neurons. *Biochimica et Biophysica Acta (BBA) - Molecular Cell Research* 1833(6), pp. 1421–1433. doi: 10.1016/j.bbamcr.2013.02.012.

Keefe, J.A., Moore, O.M., Ho, K.S. and Wehrens, X.H.T. 2023. Role of Ca2+ in healthy and pathologic cardiac function: from normal excitation–contraction coupling to mutations that cause inherited arrhythmia. *Archives of Toxicology* 97(1), pp. 73–92. doi: 10.1007/s00204-022-03385-0.

Kermode, H., Williams, A.J. and Sitsapesan, R. 1998. The Interactions of ATP, ADP, and Inorganic Phosphate with the Sheep Cardiac Ryanodine Receptor. *Biophysical Journal* 74(3), pp. 1296–1304. doi: 10.1016/S0006-3495(98)77843-9.

Kettlewell, S., Most, P., Currie, S., Koch, W.J. and Smith, G.L. 2005. S100A1 increases the gain of excitation–contraction coupling in isolated rabbit ventricular cardiomyocytes. *Journal of Molecular and Cellular Cardiology* 39(6), pp. 900–910. doi: 10.1016/j.yjmcc.2005.06.018.

Kimura, Y., Kurzydlowski, K., Tada, M. and MacLennan, D.H. 1996. Phospholamban Regulates the Ca2+-ATPase through Intramembrane Interactions. *Journal of Biological Chemistry* 271(36), pp. 21726–21731. doi: 10.1074/jbc.271.36.21726.

Kobayashi, S. et al. 2009. Dantrolene, a Therapeutic Agent for Malignant Hyperthermia, Markedly Improves the Function of Failing Cardiomyocytes by Stabilizing Interdomain Interactions Within the Ryanodine Receptor. *Journal of the American College of Cardiology* 53(21), pp. 1993–2005. doi: 10.1016/j.jacc.2009.01.065.

Kobayashi, S. et al. 2010. Dantrolene, a Therapeutic Agent for Malignant Hyperthermia, Inhibits Catecholaminergic Polymorphic Ventricular Tachycardia in a RyR2R2474S/+ Knock-In Mouse Model. *Circulation Journal* 74(12), pp. 2579–2584. doi: 10.1253/circj.CJ-10-0680.

Kobayashi, T. et al. 2022. Molecular basis for gating of cardiac ryanodine receptor explains the mechanisms for gain- and loss-of function mutations. *Nature Communications* 13(1), p. 2821. doi: 10.1038/s41467-022-30429-x.

Kolstad, T.R. et al. 2018. Ryanodine receptor dispersion disrupts Ca2+ release in failing cardiac myocytes. *eLife* 7. doi: 10.7554/eLife.39427.

Kong, H., Jones, P.P., Koop, A., Zhang, L., Duff, H.J. and Chen, S.R.W. 2008. Caffeine induces Ca2+ release by reducing the threshold for luminal Ca2+ activation of the ryanodine receptor. *Biochemical Journal* 414(3), pp. 441–452. doi: 10.1042/BJ20080489.

Kopljar, I., Lu, H.R., Van Ammel, K., Otava, M., Tekle, F., Teisman, A. and Gallacher, D.J. 2018. Development of a Human iPSC Cardiomyocyte-Based Scoring System for Cardiac Hazard Identification in Early Drug Safety De-risking. *Stem Cell Reports* 11(6), pp. 1365–1377. doi: 10.1016/j.stemcr.2018.11.007.

Kryshtal, D.O. et al. 2021. RYR2 Channel Inhibition Is the Principal Mechanism of Flecainide Action in CPVT. *Circulation Research* 128(3), pp. 321–331. doi: 10.1161/CIRCRESAHA.120.316819.

Kubalova, Z. et al. 2005. Abnormal intrastore calcium signaling in chronic heart failure. *Proceedings of the National Academy of Sciences* 102(39), pp. 14104–14109. doi: 10.1073/pnas.0504298102.

Kujala, K. et al. 2012. Cell Model of Catecholaminergic Polymorphic Ventricular Tachycardia Reveals Early and Delayed Afterdepolarizations. *PLoS ONE* 7(9), p. e44660. doi: 10.1371/journal.pone.0044660.

Lahat, H. et al. 2001. A Missense Mutation in a Highly Conserved Region of CASQ2 Is Associated with Autosomal Recessive Catecholamine-Induced Polymorphic Ventricular Tachycardia in Bedouin Families from Israel. *The American Journal of Human Genetics* 69(6), pp. 1378–1384. doi: 10.1086/324565.

Lai, A.F., Harold, E.P., Rousseau, E., Liu, Q.-Y. and Meissner, G. 1988. Purification and reconstitution of the calcium release channel from skeletal muscle. *Nature* 331(6154), pp. 315–319. doi: 10.1038/331315a0.

Laitinen, P.J., Swan, H. and Kontula, K. 2003. Molecular genetics of exercise-induced polymorphic ventricular tachycardia: identification of three novel cardiac ryanodine receptor mutations and two common calsequestrin 2 amino-acid polymorphisms. *European Journal of Human Genetics* 11(11), pp. 888–891. doi: 10.1038/sj.ejhg.5201061.

Lan, F. et al. 2013. Abnormal Calcium Handling Properties Underlie Familial Hypertrophic Cardiomyopathy Pathology in Patient-Specific Induced Pluripotent Stem Cells. *Cell Stem Cell* 12(1), pp. 101–113. doi: 10.1016/j.stem.2012.10.010.

Landrum, M.J. et al. 2016. ClinVar: public archive of interpretations of clinically relevant variants. *Nucleic Acids Research* 44(D1), pp. D862–D868. doi: 10.1093/nar/gkv1222.

Landstrom, A.P. et al. 2017a. Interpreting Incidentally Identified Variants in Genes Associated With Catecholaminergic Polymorphic Ventricular Tachycardia in a Large Cohort of Clinical Whole-Exome Genetic Test Referrals. *Circulation: Arrhythmia and Electrophysiology* 10(4). doi: 10.1161/CIRCEP.116.004742.

Landstrom, A.P., Dobrev, D. and Wehrens, X.H.T. 2017b. Calcium Signaling and Cardiac Arrhythmias. *Circulation Research* 120(12), pp. 1969–1993. doi: 10.1161/CIRCRESAHA.117.310083.

Lankipalli, R.S., Zhu, T., Guo, D. and Yan, G.-X. 2005. Mechanisms underlying arrhythmogenesis in long QT syndrome. *Journal of Electrocardiology* 38(4), pp. 69–73. doi: 10.1016/j.jelectrocard.2005.06.008.

Lanner, J.T., Georgiou, D.K., Joshi, A.D. and Hamilton, S.L. 2010. Ryanodine Receptors: Structure, Expression, Molecular Details, and Function in Calcium Release. *Cold Spring Harbor Perspectives in Biology* 2(11), pp. a003996–a003996. doi: 10.1101/cshperspect.a003996.

Laver, D. 2001. Proceedings of the Australian Physiological and Pharmacological Society Symposium: New Frontiers in Muscle Research. The power of single channel recording and analysis: its application to ryanodine receptors in lipid bilayers. *Clinical and Experimental Pharmacology and Physiology* 28(8), pp. 675–686. doi: 10.1046/j.1440-1681.2001.03503.x.

Laver, D. 2006. Regulation of Ryanodine Receptors from skeletal and cardiac muscle during rest and excitation. *Clinical and Experimental Pharmacology and Physiology* 33(11), pp. 1107–1113. doi: 10.1111/j.1440-1681.2006.04500.x.

Laver, D.R. 2007. Ca2+ Stores Regulate Ryanodine Receptor Ca2+ Release Channels via Luminal and Cytosolic Ca2+ Sites. *Biophysical Journal* 92(10), pp. 3541–3555. doi: 10.1529/biophysj.106.099028.

Laver, D.R. 2009. Luminal Ca2+ activation of cardiac ryanodine receptors by luminal and cytoplasmic domains. *European Biophysics Journal* 39(1), pp. 19–26. doi: 10.1007/s00249-009-0417-1.

Laver, D.R. 2018. Regulation of the RyR channel gating by Ca2+ and Mg2+. *Biophysical Reviews* 10(4), pp. 1087–1095. doi: 10.1007/s12551-018-0433-4.

Laver, D.R., Baynes, T.M. and Dulhunty, A.F. 1997. Magnesium Inhibition of Ryanodine-Receptor Calcium Channels: Evidence for Two Independent Mechanisms. *Journal of Membrane Biology* 156(3), pp. 213–229. doi: 10.1007/s002329900202.

Laver, D.R. and Honen, B.N. 2008. Luminal Mg2+, A Key Factor Controlling RYR2-mediated Ca2+ Release: Cytoplasmic and Luminal Regulation Modeled in a Tetrameric Channel. *The Journal of General Physiology* 132(4), pp. 429–446. doi: 10.1085/jgp.200810001.

Laver, D.R., Kong, C.H.T., Imtiaz, M.S. and Cannell, M.B. 2013. Termination of calcium-induced calcium release by induction decay: An emergent property of stochastic channel gating and molecular scale architecture. *Journal of Molecular and Cellular Cardiology* 54, pp. 98–100. doi: 10.1016/j.yjmcc.2012.10.009.

Laver, D.R. and Lamb, G.D. 1998. Inactivation of Ca2+ Release Channels (Ryanodine Receptors RyR1 and RyR2) with Rapid Steps in [Ca2+] and Voltage. *Biophysical Journal* 74(5), pp. 2352–2364. doi: 10.1016/S0006-3495(98)77944-5.

Laver, D.R., Roden, L.D., Ahern, G.P., Eager, K.R., Junankar, P.R. and Dulhunty, A.F. 1995. Cytoplasmic Ca2+ inhibits the ryanodine receptor from cardiac muscle. *The Journal of Membrane Biology* 147(1). doi: 10.1007/BF00235394.

Law, M.L., Cohen, H., Martin, A.A., Angulski, A.B.B. and Metzger, J.M. 2020. Dysregulation of Calcium Handling in Duchenne Muscular Dystrophy-Associated Dilated Cardiomyopathy: Mechanisms and Experimental Therapeutic Strategies. *Journal of Clinical Medicine* 9(2), p. 520. doi: 10.3390/jcm9020520.

Lee, Y.-S. and Keener, J.P. 2008. A calcium-induced calcium release mechanism mediated by calsequestrin. *Journal of Theoretical Biology* 253(4), pp. 668–679. doi: 10.1016/j.jtbi.2008.04.027.

Lehman, S.J., Tal-Grinspan, L., Lynn, M.L., Strom, J., Benitez, G.E., Anderson, M.E. and Tardiff, J.C. 2019. Chronic Calmodulin-Kinase II Activation Drives Disease Progression in Mutation-Specific Hypertrophic Cardiomyopathy. *Circulation* 139(12), pp. 1517–1529. doi: 10.1161/CIRCULATIONAHA.118.034549.

Lehnart, S.E. et al. 2004a. Sudden Death in Familial Polymorphic Ventricular Tachycardia Associated With Calcium Release Channel (Ryanodine Receptor) Leak. *Circulation* 109(25), pp. 3208–3214. doi: 10.1161/01.CIR.0000132472.98675.EC.

Lehnart, S.E. et al. 2006. Stabilization of cardiac ryanodine receptor prevents intracellular calcium leak and arrhythmias. *Proceedings of the National Academy of Sciences of the United States of America* 103(20), pp. 7906–10. doi: 10.1073/pnas.0602133103.

Lehnart, S.E. et al. 2008. Leaky Ca2+ release channel/ryanodine receptor 2 causes seizures and sudden cardiac death in mice. *Journal of Clinical Investigation*. doi: 10.1172/JCI35346.

Lehnart, S.E., Wehrens, X.H.T., Kushnir, A. and Marks, A.R. 2004b. Cardiac Ryanodine Receptor Function and Regulation in Heart Disease. *Annals of the New York Academy of Sciences* 1015(1), pp. 144–159. doi: 10.1196/annals.1302.012.

Leptihn, S. et al. 2013. Constructing droplet interface bilayers from the contact of aqueous droplets in oil. *Nature Protocols* 8(6), pp. 1048–1057. doi: 10.1038/nprot.2013.061.

Letsas, K.P. et al. 2020. A novel variant of RyR2 gene in a family misdiagnosed as congenital long QT syndrome: The importance of genetic testing. *Journal of Electrocardiology* 60, pp. 8–11. doi: 10.1016/j.jelectrocard.2020.03.001.

Li, P. and Chen, S.R.W. 2001. Molecular Basis of Ca2+ Activation of the Mouse Cardiac Ca2+ Release Channel (Ryanodine Receptor). *The Journal of General Physiology* 118(1), pp. 33–44. doi: 10.1085/jgp.118.1.33.

Li, Y. et al. 2021. Human RyR2 (Ryanodine Receptor 2) Loss-of-Function Mutations. *Circulation: Arrhythmia and Electrophysiology* 14(9). doi: 10.1161/CIRCEP.121.010013.

Lieve, K.V., Wilde, A.A. and Werf, C. van der. 2016. The Role of Flecainide in the Management of Catecholaminergic Polymorphic Ventricular Tachycardia. *Arrhythmia & Electrophysiology Review* 5(1), p. 45. doi: 10.15420/aer.2016.3.3.

Lima, B., Forrester, M.T., Hess, D.T. and Stamler, J.S. 2010. *S* -Nitrosylation in Cardiovascular Signaling. *Circulation Research* 106(4), pp. 633–646. doi: 10.1161/CIRCRESAHA.109.207381.

Lipp, P. and Niggli, E. 1996. Submicroscopic calcium signals as fundamental events of excitation--contraction coupling in guinea-pig cardiac myocytes. *The Journal of Physiology* 492(1), pp. 31–38. doi: 10.1113/jphysiol.1996.sp021286.

Lipshultz, S.E. et al. 2003. The Incidence of Pediatric Cardiomyopathy in Two Regions of the United States. *New England Journal of Medicine* 348(17), pp. 1647–1655. doi: 10.1056/NEJMoa021715.

Liu, B. et al. 2018. Gene Transfer of Engineered Calmodulin Alleviates Ventricular Arrhythmias in a Calsequestrin-Associated Mouse Model of Catecholaminergic Polymorphic Ventricular Tachycardia. *Journal of the American Heart Association* 7(10). doi: 10.1161/JAHA.117.008155.

Liu, C., Zhang, A., Yan, N. and Song, C. 2021. Atomistic Details of Charge/Space Competition in the Ca^{2+} Selectivity of Ryanodine Receptors. *The Journal of Physical Chemistry Letters* 12(17), pp. 4286–4291. doi: 10.1021/acs.jpclett.1c00681.

Liu, G. and Pessah, I.N. 1994. Molecular interaction between ryanodine receptor and glycoprotein triadin involves redox cycling of functionally important hyperreactive sulfhydryls. *The Journal of biological chemistry* 269(52), pp. 33028–34.

Liu, G.-S. et al. 2015. A novel human R25C-phospholamban mutation is associated with super-inhibition of calcium cycling and ventricular arrhythmia. *Cardiovascular Research* 107(1), pp. 164–174. Available at: https://academic.oup.com/cardiovascres/article-lookup/doi/10.1093/cvr/cvv127.

Liu, N., Rizzi, N., Boveri, L. and Priori, S.G. 2009. Ryanodine receptor and calsequestrin in arrhythmogenesis: What we have learnt from genetic diseases and transgenic mice. *Journal of Molecular and Cellular Cardiology* 46(2), pp. 149–159. doi: 10.1016/j.yjmcc.2008.10.012.

Liu, Y. et al. 2017. CPVT-associated cardiac ryanodine receptor mutation G357S with reduced penetrance impairs Ca2+ release termination and diminishes protein expression. *PLOS ONE* 12(9), p. e0184177. doi: 10.1371/journal.pone.0184177.

Liu, Y., Hiess, F., Tian, X., Wang, R. and Chen, S.R.W. 2013. The CPVT-Associated RyR2 Mutation G230C reduces the Threshold for Store Overload-Induced Ca Release (SOICR). *Biophysical Journal* 104(2), p. 442a. doi: 10.1016/j.bpj.2012.11.2454.

Loaiza, R. et al. 2013. Heterogeneity of Ryanodine Receptor Dysfunction in a Mouse Model of Catecholaminergic Polymorphic Ventricular Tachycardia. *Circulation Research* 112(2), pp. 298–308. doi: 10.1161/CIRCRESAHA.112.274803.

Lock, J.T., Parker, I. and Smith, I.F. 2015. A comparison of fluorescent Ca2+ indicators for imaging local Ca2+ signals in cultured cells. *Cell Calcium* 58(6), pp. 638–648. doi: 10.1016/j.ceca.2015.10.003.

Lopes, L.R. et al. 2015. Novel genotype–phenotype associations demonstrated by high-throughput sequencing in patients with hypertrophic cardiomyopathy. *Heart* 101(4), pp. 294–301. doi: 10.1136/heartjnl-2014-306387.

Luvisetto, S. et al. 2004. Modal Gating of Human CaV2.1 (P/Q-type) Calcium Channels. *The Journal of General Physiology* 124(5), pp. 445–461. doi: 10.1085/jgp.200409034.

Lv, T. et al. 2025. The Role of RyR2 Mutations in Congenital Heart Diseases: Insights Into Cardiac Electrophysiological Mechanisms. *Journal of Cardiovascular Electrophysiology* 36(3), pp. 683–692. doi: 10.1111/jce.16569.

MacDonnell, S.M., García-Rivas, G., Scherman, J.A., Kubo, H., Chen, X., Valdivia, H. and Houser, S.R. 2008. Adrenergic Regulation of Cardiac Contractility Does Not Involve Phosphorylation of the Cardiac Ryanodine Receptor at Serine 2808. *Circulation Research* 102(8). doi: 10.1161/CIRCRESAHA.108.174722.

Macquaide, N. et al. 2015. Ryanodine receptor cluster fragmentation and redistribution in persistent atrial fibrillation enhance calcium release. *Cardiovascular Research* 108(3), pp. 387–398. doi: 10.1093/cvr/cvv231.

Majid, N. and Khan, R.H. 2023. Protein aggregation: Consequences, mechanism, characterization and inhibitory strategies. *International Journal of Biological Macromolecules* 242, p. 125123. doi: 10.1016/j.ijbiomac.2023.125123.

Manders, E.M.M., Verbeek, F.J. and Aten, J.A. 1993. Measurement of co-localization of objects in dual-colour confocal images. *Journal of Microscopy* 169(3), pp. 375–382. doi: 10.1111/j.1365-2818.1993.tb03313.x.

Marban, E., Robinson, S.W. and Wier, W.G. 1986. Mechanisms of arrhythmogenic delayed and early afterdepolarizations in ferret ventricular muscle. *The Journal of clinical investigation* 78(5), pp. 1185–92. doi: 10.1172/JCI112701.

Marjamaa, A., Laitinen-Forsblom, P., Lahtinen, A.M., Viitasalo, M., Toivonen, L., Kontula, K. and Swan, H. 2009. Search for cardiac calcium cycling gene mutations in familial ventricular arrhythmias resembling catecholaminergic polymorphic ventricular tachycardia. *BMC Medical Genetics* 10(1), p. 12. doi: 10.1186/1471-2350-10-12.

Marks, A.R. 2023. Targeting ryanodine receptors to treat human diseases. *Journal of Clinical Investigation* 133(2). doi: 10.1172/JCI162891.

Maron, B.J., Maron, M.S. and Semsarian, C. 2012. Genetics of Hypertrophic Cardiomyopathy After 20 Years. *Journal of the American College of Cardiology* 60(8), pp. 705–715. doi: 10.1016/j.jacc.2012.02.068.

Marx, S.O., Gaburjakova, J., Gaburjakova, M., Henrikson, C., Ondrias, K. and Marks, A.R. 2001. Coupled Gating Between Cardiac Calcium Release Channels (Ryanodine Receptors). *Circulation Research* 88(11), pp. 1151–1158. doi: 10.1161/hh1101.091268.

Marx, S.O., Reiken, S., Hisamatsu, Y., Jayaraman, T., Burkhoff, D., Rosemblit, N. and Marks, A.R. 2000. PKA Phosphorylation Dissociates FKBP12.6 from the Calcium Release Channel (Ryanodine Receptor). *Cell* 101(4), pp. 365–376. doi: 10.1016/S0092-8674(00)80847-8.

Mathur, N. et al. 2009. Sudden Infant Death Syndrome in Mice With an Inherited Mutation in *RyR2*. *Circulation: Arrhythmia and Electrophysiology* 2(6), pp. 677–685. doi: 10.1161/CIRCEP.109.894683.

Maxwell, J.T., Domeier, T.L. and Blatter, L.A. 2012. Dantrolene prevents arrhythmogenic Ca^{2+} release in heart failure. *American Journal of Physiology-Heart and Circulatory Physiology* 302(4), pp. H953–H963. doi: 10.1152/ajpheart.00936.2011.

Mazzanti, A. et al. 2022. Outcomes of Patients With Catecholaminergic Polymorphic Ventricular Tachycardia Treated With β-Blockers. *JAMA Cardiology* 7(5), p. 504. doi: 10.1001/jamacardio.2022.0219.

McGarry, S.J. and Williams, A.J. 1994. Activation of the sheep cardiac sarcoplasmic reticulum Ca^{2+} -release channel by analogues of sulmazole. *British Journal of Pharmacology* 111(4), pp. 1212–1220. doi: 10.1111/j.1476-5381.1994.tb14874.x.

McKenna, W.J., Maron, B.J. and Thiene, G. 2017. Classification, Epidemiology, and Global Burden of Cardiomyopathies. *Circulation Research* 121(7), pp. 722–730. doi: 10.1161/CIRCRESAHA.117.309711.

Medeiros-Domingo, A. et al. 2009. The RYR2-Encoded Ryanodine Receptor/Calcium Release Channel in Patients Diagnosed Previously With Either Catecholaminergic Polymorphic Ventricular Tachycardia or Genotype Negative, Exercise-Induced Long QT Syndrome. *Journal of the American College of Cardiology* 54(22), pp. 2065–2074. doi: 10.1016/j.jacc.2009.08.022.

Meli, A.C. et al. 2011. A Novel Ryanodine Receptor Mutation Linked to Sudden Death Increases Sensitivity to Cytosolic Calcium. *Circulation Research* 109(3), pp. 281–290. doi: 10.1161/CIRCRESAHA.111.244970.

Melnikov, S. et al. 2016. Molecular insights into protein synthesis with proline residues. *EMBO reports* 17(12), pp. 1776–1784. doi: 10.15252/embr.201642943.

Melville, Z. et al. 2022. A drug and ATP binding site in type 1 ryanodine receptor. *Structure* 30(7), pp. 1025-1034.e4. doi: 10.1016/j.str.2022.04.010.

Meurs, K.M., Lacombe, V.A., Dryburgh, K., Fox, P.R., Reiser, P.R. and Kittleson, M.D. 2006a. Differential expression of the cardiac ryanodine receptor in normal and arrhythmogenic right ventricular cardiomyopathy canine hearts. *Human Genetics* 120(1), pp. 111–118. doi: 10.1007/s00439-006-0193-2.

Meurs, K.M., Lacombe, V.A., Dryburgh, K., Fox, P.R., Reiser, P.R. and Kittleson, M.D. 2006b. Differential expression of the cardiac ryanodine receptor in normal and arrhythmogenic right ventricular cardiomyopathy canine hearts. *Human Genetics* 120(1), pp. 111–118. doi: 10.1007/s00439-006-0193-2.

Meyers, M.B. et al. 2003. Sorcin Regulates Excitation-Contraction Coupling in the Heart. *Journal of Biological Chemistry* 278(31), pp. 28865–28871. doi: 10.1074/jbc.M302009200.

Meyers, M.B., Pickel, V.M., Sheu, S.-S., Sharma, V.K., Scotto, K.W. and Fishman, G.I. 1995. Association of Sorcin With the Cardiac Ryanodine Receptor. *Journal of Biological Chemistry* 270(44), pp. 26411–26418. doi: 10.1074/jbc.270.44.26411.

Michalak, M. 2024. Calreticulin: Endoplasmic reticulum Ca $^{2+}$ gatekeeper. *Journal of Cellular and Molecular Medicine* 28(5). doi: 10.1111/jcmm.17839.

Michalak, M., Corbett, E.F., Mesaeli, N., Nakamura, K. and Opas, M. 1999. Calreticulin: one protein, one gene, many functions. *The Biochemical journal* 344 Pt 2(Pt 2), pp. 281–92.

Milescu, L.S., Nicolai, C. and Bannen, J. 2000. QuB Software.

Miotto, M.C. et al. 2022. Structural analyses of human ryanodine receptor type 2 channels reveal the mechanisms for sudden cardiac death and treatment. *Science Advances* 8(29). doi: 10.1126/sciadv.abo1272.

Miotto, M.C. et al. 2024. Structural basis for ryanodine receptor type 2 leak in heart failure and arrhythmogenic disorders. *Nature Communications* 15(1), p. 8080. doi: 10.1038/s41467-024-51791-y.

Miura, M., Boyden, P.A. and Keurs, H.E.D.J. ter. 1999. Ca $^{2+}$ Waves During Triggered Propagated Contractions in Intact Trabeculae. *Circulation Research* 84(12), pp. 1459–1468. doi: 10.1161/01.RES.84.12.1459.

Most, P. et al. 2003. Transgenic Overexpression of the Ca2+-binding Protein S100A1 in the Heart Leads to Increased in Vivo Myocardial Contractile Performance. *Journal of Biological Chemistry* 278(36), pp. 33809–33817. doi: 10.1074/jbc.M301788200.

Mozneb, M., Moses, J., Arzt, M., Escopete, S. and Sharma, A. 2024. Recording and Interpretation of Active Calcium Transients in Induced Pluripotent Stem Cell-Derived Cardiomyocytes. *Current Protocols* 4(10). doi: 10.1002/cpz1.70030.

Muehlschlegel, S. and Sims, J.R. 2009. Dantrolene: Mechanisms of Neuroprotection and Possible Clinical Applications in the Neurointensive Care Unit. *Neurocritical Care* 10(1), pp. 103–115. doi: 10.1007/s12028-008-9133-4.

Mukherjee, S. 2014. *The Human Cardiac Ryanodine Receptor Gating Behaviour: A Study of Mechanisms*. Cardiff University, School of Medicine,.

Mukherjee, S., Thomas, N.L. and Williams, A.J. 2012. A mechanistic description of gating of the human cardiac ryanodine receptor in a regulated minimal environment. *Journal of General Physiology* 140(2), pp. 139–158. doi: 10.1085/jgp.201110706.

Muller, L., Jackson, S.N. and Woods, A.S. 2019. Histidine, the less interactive cousin of arginine. *European Journal of Mass Spectrometry* 25(2), pp. 212–218. doi: 10.1177/1469066718791793.

Munro, M.L. et al. 2016. Junctophilin-2 in the nanoscale organisation and functional signalling of ryanodine receptor clusters in cardiomyocytes. *Journal of Cell Science* 129(23), pp. 4388–4398. doi: 10.1242/jcs.196873.

Munro, M.L. et al. 2021. Human Atrial Fibrillation Is Not Associated With Remodeling of Ryanodine Receptor Clusters. *Frontiers in Cell and Developmental Biology* 9. doi: 10.3389/fcell.2021.633704.

Murayama, T. et al. 2016. Genotype-Phenotype Correlations of Malignant Hyperthermia and Central Core Disease Mutations in the Central Region of the RYR1 Channel. *Human Mutation* 37(11), pp. 1231–1241. doi: 10.1002/humu.23072.

Nakai, J., Imagawa, T., Hakamata, Y., Shigekawa, M., Takeshima, H. and Numa, S. 1990. Primary structure and functional expression from cDN A of the cardiac ryanodine receptor/calcium release channel. *FEBS Letters* 271(1–2), pp. 169–177. doi: 10.1016/0014-5793(90)80399-4.

Nakamura, Y. et al. 2019. Ryanodine receptor–bound calmodulin is essential to protect against catecholaminergic polymorphic ventricular tachycardia. *JCI Insight* 4(11). doi: 10.1172/jci.insight.126112.

Narayan, S.M., Franz, M.R., Clopton, P., Pruvot, E.J. and Krummen, D.E. 2011. Repolarization Alternans Reveals Vulnerability to Human Atrial Fibrillation. *Circulation* 123(25), pp. 2922–2930. doi: 10.1161/CIRCULATIONAHA.110.977827.

Nattel, S., Heijman, J., Voigt, N., Wehrens, X.H.T. and Dobrev, D. 2018. The Molecular Pathophysiology of Atrial Fibrillation. In: *Cardiac Electrophysiology: From Cell to Bedside*. Elsevier, pp. 396–408. doi: 10.1016/B978-0-323-44733-1.00042-0.

Ng, K. et al. 2020. An International Multicenter Evaluation of Inheritance Patterns, Arrhythmic Risks, and Underlying Mechanisms of *CASQ2* -Catecholaminergic Polymorphic Ventricular Tachycardia. *Circulation* 142(10), pp. 932–947. doi: 10.1161/CIRCULATIONAHA.120.045723.

Nikolaienko, R., Bovo, E., Kahn, D., Gracia, R., Jamrozik, T. and Zima, A. V. 2023. Cysteines 1078 and 2991 cross-linking plays a critical role in redox regulation of cardiac ryanodine receptor (RyR). *Nature Communications* 14(1), p. 4498. doi: 10.1038/s41467-023-40268-z.

Nishimura, S. et al. 2015. Abstract 13816: Dantrolene Enhances Binding of Calmodulin to RyR2 in CPVT Which Mutation Located at Central Domain but Does Not Enhance That in

CPVT With Mutation at CaM-like Domain. *Circulation* 132(suppl_3). doi: 10.1161/circ.132.suppl_3.13816.

Nishio, H., Iwata, M. and Suzuki, K. 2006. Postmortem Molecular Screening for Cardiac Ryanodine Receptor Type 2 Mutations in Sudden Unexplained Death R420W Mutated Case With Characteristics of Status Thymico-Lymphaticus. *Circulation Journal* 70(11), pp. 1402–1406. doi: 10.1253/circj.70.1402.

Nofi, C. et al. 2020. Chronic dantrolene treatment attenuates cardiac dysfunction and reduces atrial fibrillation inducibility in a rat myocardial infarction heart failure model. *Heart Rhythm O2* 1(2), pp. 126–135. doi: 10.1016/j.hroo.2020.03.004.

Nyegaard, M. et al. 2012. Mutations in Calmodulin Cause Ventricular Tachycardia and Sudden Cardiac Death. *The American Journal of Human Genetics* 91(4), pp. 703–712. doi: 10.1016/j.ajhg.2012.08.015.

Oda, T. et al. 2005. Defective Regulation of Interdomain Interactions Within the Ryanodine Receptor Plays a Key Role in the Pathogenesis of Heart Failure. *Circulation* 111(25), pp. 3400–3410. doi: 10.1161/CIRCULATIONAHA.104.507921.

Ohno, S. et al. 2014. Exon 3 deletion of RYR2 encoding cardiac ryanodine receptor is associated with left ventricular non-compaction. *Europace* 16(11), pp. 1646–1654. doi: 10.1093/europace/eut382.

Ohno, S. 2016. The genetic background of arrhythmogenic right ventricular cardiomyopathy. *Journal of Arrhythmia* 32(5), pp. 398–403. doi: 10.1016/j.joa.2016.01.006.

Okudaira, N., Kuwahara, M., Hirata, Y., Oku, Y. and Nishio, H. 2014. A knock-in mouse model of N-terminal R420W mutation of cardiac ryanodine receptor exhibits arrhythmogenesis with abnormal calcium dynamics in cardiomyocytes. *Biochemical and Biophysical Research Communications* 452(3), pp. 665–668. doi: 10.1016/j.bbrc.2014.08.132.

Olubando, D. et al. 2020. Classification and correlation of RYR2 missense variants in individuals with catecholaminergic polymorphic ventricular tachycardia reveals phenotypic relationships. *Journal of human genetics* 65(6), pp. 531–539. doi: 10.1038/s10038-020-0738-6.

Ondrias, K. and Mojzisová, A. 2001. Coupled gating between individual cardiac ryanodine calcium release channels. *Gen Physiol Biophys* 21(1), pp. 73–84.

Ono, M. et al. 2010. Dissociation of calmodulin from cardiac ryanodine receptor causes aberrant Ca2+ release in heart failure. *Cardiovascular Research* 87(4), pp. 609–617. doi: 10.1093/cvr/cvq108.

Oo, Y.W., Gomez-Hurtado, N., Walweel, K., van Helden, D.F., Imtiaz, M.S., Knollmann, B.C. and Laver, D.R. 2015. Essential Role of Calmodulin in RyR Inhibition by Dantrolene. *Molecular Pharmacology* 88(1), pp. 57–63. doi: 10.1124/mol.115.097691.

van Oort, R.J. et al. 2010. Ryanodine Receptor Phosphorylation by Calcium/Calmodulin-Dependent Protein Kinase II Promotes Life-Threatening Ventricular Arrhythmias in Mice With Heart Failure. *Circulation* 122(25), pp. 2669–2679. doi: 10.1161/CIRCULATIONAHA.110.982298.

van Oort, R.J. et al. 2011. Disrupted Junctional Membrane Complexes and Hyperactive Ryanodine Receptors After Acute Junctophilin Knockdown in Mice. *Circulation* 123(9), pp. 979–988. doi: 10.1161/CIRCULATIONAHA.110.006437.

Otsu, K., Willard, H.F., Khanna, V.K., Zorzato, F., Green, N.M. and MacLennan, D.H. 1990. Molecular cloning of cDNA encoding the Ca2+ release channel (ryanodine receptor) of rabbit cardiac muscle sarcoplasmic reticulum. *Journal of Biological Chemistry* 265(23), pp. 13472–13483. doi: 10.1016/S0021-9258(18)77371-7.

P. Landstrom, A. and J. Ackerman, M. 2012. Beyond the Cardiac Myofilament: Hypertrophic Cardiomyopathy- Associated Mutations in Genes that Encode Calcium-Handling Proteins. *Current Molecular Medicine* 12(5), pp. 507–518. doi: 10.2174/156652412800620020.

Park, H., Wu, S., Dunker, A.K. and Kang, C. 2003. Polymerization of Calsequestrin. *Journal of Biological Chemistry* 278(18), pp. 16176–16182. doi: 10.1074/jbc.M300120200.

Paul-Pletzer, K. et al. 2005. Probing a putative dantrolene-binding site on the cardiac ryanodine receptor. *Biochemical Journal* 387(3), pp. 905–909. doi: 10.1042/BJ20041336.

Pedrozo, Z. et al. 2010. Calpains and proteasomes mediate degradation of ryanodine receptors in a model of cardiac ischemic reperfusion. *Biochimica et Biophysica Acta (BBA) - Molecular Basis of Disease* 1802(3), pp. 356–362. doi: 10.1016/j.bbadis.2009.12.005.

Pedrozo, Z. et al. 2013. Cardiomyocyte ryanodine receptor degradation by chaperone-mediated autophagy. *Cardiovascular Research* 98(2), pp. 277–285. doi: 10.1093/cvr/cvt029.

Peng, W. et al. 2016. Structural basis for the gating mechanism of the type 2 ryanodine receptor RyR2. *Science* 354(6310). doi: 10.1126/science.aah5324.

Penttinen, K., Swan, H., Vanninen, S., Paavola, J., Lahtinen, A.M., Kontula, K. and Aalto-Setälä, K. 2015. Antiarrhythmic Effects of Dantrolene in Patients with Catecholaminergic Polymorphic Ventricular Tachycardia and Replication of the Responses Using iPSC Models. *PLOS ONE* 10(5), p. e0125366. doi: 10.1371/journal.pone.0125366.

Peterson, B.Z., DeMaria, C.D. and Yue, D.T. 1999. Calmodulin Is the Ca2+ Sensor for Ca2+-Dependent Inactivation of L-Type Calcium Channels. *Neuron* 22(3), pp. 549–558. doi: 10.1016/S0896-6273(00)80709-6.

Pioner, J.M. et al. 2020. Advances in Stem Cell Modeling of Dystrophin-Associated Disease: Implications for the Wider World of Dilated Cardiomyopathy. *Frontiers in Physiology* 11. doi: 10.3389/fphys.2020.00368.

Pogwizd, S. 2004. Cellular Basis of Triggered Arrhythmias in Heart Failure. *Trends in Cardiovascular Medicine* 14(2), pp. 61–66. doi: 10.1016/j.tcm.2003.12.002.

Pölönen, R.P., Penttinen, K., Swan, H. and Aalto-Setälä, K. 2018. Antiarrhythmic Effects of Carvedilol and Flecainide in Cardiomyocytes Derived from Catecholaminergic Polymorphic Ventricular Tachycardia Patients. *Stem Cells International* 2018, pp. 1–11. doi: 10.1155/2018/9109503.

Pölönen, R.P., Swan, H. and Aalto-Setälä, K. 2020. Mutation-specific differences in arrhythmias and drug responses in CPVT patients: simultaneous patch clamp and video imaging of iPSC derived cardiomyocytes. *Molecular Biology Reports* 47(2), pp. 1067–1077. doi: 10.1007/s11033-019-05201-y.

Poole-Wilson, P.A. et al. 2003. Comparison of carvedilol and metoprolol on clinical outcomes in patients with chronic heart failure in the Carvedilol Or Metoprolol European Trial (COMET): randomised controlled trial. *The Lancet* 362(9377), pp. 7–13. doi: 10.1016/S0140-6736(03)13800-7.

Porta, M. et al. 2011. Single Ryanodine Receptor Channel Basis of Caffeine's Action on Ca2+ Sparks. *Biophysical Journal* 100(4), pp. 931–938. doi: 10.1016/j.bpj.2011.01.017.

Porta, M., Diaz-Sylvester, P.L., Neumann, J.T., Escobar, A.L., Fleischer, S. and Copello, J.A. 2012. Coupled gating of skeletal muscle ryanodine receptors is modulated by Ca^{2+}, Mg^{2+}, and ATP. *American Journal of Physiology-Cell Physiology* 303(6), pp. C682–C697. doi: 10.1152/ajpcell.00150.2012.

Postma, A. V. 2005. Catecholaminergic polymorphic ventricular tachycardia: RYR2 mutations, bradycardia, and follow up of the patients. *Journal of Medical Genetics* 42(11), pp. 863–870. doi: 10.1136/jmg.2004.028993.

Potenza, D.M., Janicek, R., Fernandez-Tenorio, M., Camors, E., Ramos-Mondragón, R., Valdivia, H.H. and Niggli, E. 2019. Phosphorylation of the ryanodine receptor 2 at serine 2030 is required for a complete β-adrenergic response. *Journal of General Physiology* 151(2), pp. 131–145. doi: 10.1085/jgp.201812155.

Prajapati, C., Pölönen, R.-P. and Aalto-Setälä, K. 2018. Simultaneous recordings of action potentials and calcium transients from human induced pluripotent stem cell derived cardiomyocytes. *Biology Open*. doi: 10.1242/bio.035030.

Prestle, J. et al. 2001. Overexpression of FK506-Binding Protein FKBP12.6 in Cardiomyocytes Reduces Ryanodine Receptor–Mediated Ca^{2+} Leak From the Sarcoplasmic Reticulum and Increases Contractility. *Circulation Research* 88(2), pp. 188–194. doi: 10.1161/01.RES.88.2.188.

Priori, S.G. et al. 2002. Clinical and Molecular Characterization of Patients With Catecholaminergic Polymorphic Ventricular Tachycardia. *Circulation* 106(1), pp. 69–74. doi: 10.1161/01.CIR.0000020013.73106.D8.

Priori, S.G. and Corr, P.B. 1990. Mechanisms underlying early and delayed afterdepolarizations induced by catecholamines. *American Journal of Physiology-Heart and Circulatory Physiology* 258(6), pp. H1796–H1805. doi: 10.1152/ajpheart.1990.258.6.H1796.

Priori, S.G., Mazzanti, A., Santiago, D.J., Kukavica, D., Trancuccio, A. and Kovacic, J.C. 2021. Precision Medicine in Catecholaminergic Polymorphic Ventricular Tachycardia. *Journal of the American College of Cardiology* 77(20), pp. 2592–2612. doi: 10.1016/j.jacc.2020.12.073.

Priori, S.G. and Napolitano, C. 2005. Intracellular Calcium Handling Dysfunction and Arrhythmogenesis. *Circulation Research* 97(11), pp. 1077–1079. doi: 10.1161/01.RES.0000194556.41865.e2.

Pritchard, H.A.T., Griffin, C.S., Yamasaki, E., Thakore, P., Lane, C., Greenstein, A.S. and Earley, S. 2019. Nanoscale coupling of junctophilin-2 and ryanodine receptors regulates vascular smooth muscle cell contractility. *Proceedings of the National Academy of Sciences* 116(43), pp. 21874–21881. doi: 10.1073/pnas.1911304116.

Prosser, B.L. et al. 2008. S100A1 Binds to the Calmodulin-binding Site of Ryanodine Receptor and Modulates Skeletal Muscle Excitation-Contraction Coupling. *Journal of Biological Chemistry* 283(8), pp. 5046–5057. doi: 10.1074/jbc.M709231200.

Prosser, B.L., Ward, C.W. and Lederer, W.J. 2011. X-ROS Signaling: Rapid Mechano-Chemo Transduction in Heart. *Science* 333(6048), pp. 1440–1445. doi: 10.1126/science.1202768.

Pugh, T.J. et al. 2014. The landscape of genetic variation in dilated cardiomyopathy as surveyed by clinical DNA sequencing. *Genetics in Medicine* 16(8), pp. 601–608. doi: 10.1038/gim.2013.204.

Qin, F., Auerbach, A. and Sachs, F. 1997. Maximum likelihood estimation of aggregated Markov processes. *Proceedings of the Royal Society of London. Series B: Biological Sciences* 264(1380), pp. 375–383. doi: 10.1098/rspb.1997.0054.

Rajan, S. et al. 2007. Dilated Cardiomyopathy Mutant Tropomyosin Mice Develop Cardiac Dysfunction With Significantly Decreased Fractional Shortening and Myofilament Calcium Sensitivity. *Circulation Research* 101(2), pp. 205–214. doi: 10.1161/CIRCRESAHA.107.148379.

Rampazzo, A. et al. 1995. A new locus for arrhythmogenic right ventricular cardiomyopathy (ARVD2) maps to chromosome 1q42-q43. *Human Molecular Genetics* 4(11), pp. 2151–2154. doi: 10.1093/hmg/4.11.2151.

Rassaf, T., Totzeck, M., Hendgen-Cotta, U.B., Shiva, S., Heusch, G. and Kelm, M. 2014. Circulating Nitrite Contributes to Cardioprotection by Remote Ischemic Preconditioning. *Circulation Research* 114(10), pp. 1601–1610. doi: 10.1161/CIRCRESAHA.114.303822.

Reggiori, F. and Molinari, M. 2022. ER-phagy: mechanisms, regulation, and diseases connected to the lysosomal clearance of the endoplasmic reticulum. *Physiological Reviews* 102(3), pp. 1393–1448. doi: 10.1152/physrev.00038.2021.

Reiken, S. et al. 2003. Protein Kinase A Phosphorylation of the Cardiac Calcium Release Channel (Ryanodine Receptor) in Normal and Failing Hearts. *Journal of Biological Chemistry* 278(1), pp. 444–453. doi: 10.1074/jbc.M207028200.

Remme, W.J. 2010. Which Beta-Blocker is Most Effective in Heart Failure? *Cardiovascular Drugs and Therapy* 24(4), pp. 351–358. doi: 10.1007/s10557-010-6247-7.

Reynolds, J.O. et al. 2016. Junctophilin-2 gene therapy rescues heart failure by normalizing RyR2-mediated Ca2+ release. *International Journal of Cardiology* 225, pp. 371–380. doi: 10.1016/j.ijcard.2016.10.021.

Richardson, S.J., Thekkedam, C.G., Casarotto, M.G., Beard, N.A. and Dulhunty, A.F. 2023. FKBP12 binds to the cardiac ryanodine receptor with negative cooperativity: implications for heart muscle physiology in health and disease. *Philosophical transactions of the Royal Society of London. Series B, Biological sciences* 378(1879), p. 20220169. doi: 10.1098/rstb.2022.0169.

Ríos, E., Gillespie, D. and Franzini-Armstrong, C. 2019. The binding interactions that maintain excitation–contraction coupling junctions in skeletal muscle. *Journal of General Physiology* 151(4), pp. 593–605. doi: 10.1085/jgp.201812268.

Robinson, P., Griffiths, P.J., Watkins, H. and Redwood, C.S. 2007. Dilated and Hypertrophic Cardiomyopathy Mutations in Troponin and α-Tropomyosin Have Opposing Effects on the Calcium Affinity of Cardiac Thin Filaments. *Circulation Research* 101(12), pp. 1266–1273. doi: 10.1161/CIRCRESAHA.107.156380.

Rossi, D. and Sorrentino, V. 2004. The Ryanodine Receptors Gene Family: Expression and Functional Meaning . 14(5), pp. 323–343.

Roston, T.M. et al. 2017. A novel RYR2 loss-of-function mutation (I4855M) is associated with left ventricular non-compaction and atypical catecholaminergic polymorphic ventricular tachycardia. *Journal of Electrocardiology* 50(2), pp. 227–233. doi: 10.1016/j.jelectrocard.2016.09.006.

Rousseau, E., Smith, J.S. and Meissner, G. 1987. Ryanodine modifies conductance and gating behavior of single Ca2+ release channel. *American Journal of Physiology-Cell Physiology* 253(3), pp. C364–C368. doi: 10.1152/ajpcell.1987.253.3.C364.

Roux-Buisson, N. et al. 2012. Absence of triadin, a protein of the calcium release complex, is responsible for cardiac arrhythmia with sudden death in human. *Human Molecular Genetics* 21(12), pp. 2759–2767. doi: 10.1093/hmg/dds104.

Roux-Buisson, N. et al. 2014. Prevalence and significance of rare RYR2 variants in arrhythmogenic right ventricular cardiomyopathy/dysplasia: results of a systematic screening. *Heart rhythm* 11(11), pp. 1999–2009. doi: 10.1016/j.hrthm.2014.07.020.

Rowe, G.C. et al. 2017. Development of dilated cardiomyopathy and impaired calcium homeostasis with cardiac-specific deletion of ESRRβ. *American Journal of Physiology-Heart and Circulatory Physiology* 312(4), pp. H662–H671. doi: 10.1152/ajpheart.00446.2016.

Rubenstein, D.S., Zbilut, J.P., Webber, C.L. and Lipsius, S.L. 1993. Phase-dependent properties of the cardiac sarcoplasmic reticulum oscillator in cat right atrium: a mechanism contributing to dysrhythmias induced by Ca2+ overload. *Experimental physiology* 78(1), pp. 79–93. doi: 10.1113/expphysiol.1993.sp003672.

Saftenku, E., Williams, A.J. and Sitsapesan, R. 2001. Markovian Models of Low and High Activity Levels of Cardiac Ryanodine Receptors. *Biophysical Journal* 80(6), pp. 2727–2741. doi: 10.1016/S0006-3495(01)76241-8.

Samsó, M. 2017. A guide to the 3D structure of the ryanodine receptor type 1 by cryoEM. *Protein Science* 26(1), pp. 52–68. doi: 10.1002/pro.3052.

Samsó, M. and Wagenknecht, T. 2002. Apocalmodulin and Ca2+-Calmodulin Bind to Neighboring Locations on the Ryanodine Receptor. *Journal of Biological Chemistry* 277(2), pp. 1349–1353. doi: 10.1074/jbc.M109196200.

Santana, L.F., Cheng, E.P. and Lederer, W.J. 2010. How does the shape of the cardiac action potential control calcium signaling and contraction in the heart? *Journal of Molecular and Cellular Cardiology* 49(6), pp. 901–903. doi: 10.1016/j.yjmcc.2010.09.005.

Sato, D. and Bers, D.M. 2011. How Does Stochastic Ryanodine Receptor-Mediated Ca Leak Fail to Initiate a Ca Spark? *Biophysical Journal* 101(10), pp. 2370–2379. doi: 10.1016/j.bpj.2011.10.017.

Schaper, J., Kostin, S., Hein, S., Elsässer, A., Arnon, E. and Zimmermann, R. 2002. Structural remodelling in heart failure. *Experimental and clinical cardiology* 7(2–3), pp. 64–8.

Schindelin, J. et al. 2012. Fiji: an open-source platform for biological-image analysis. *Nature Methods* 9(7), pp. 676–682. doi: 10.1038/nmeth.2019.

Schmeckpeper, J., Kim, K., George, S.A., Blackwell, D.J., Brennan, J.A., Efimov, I.R. and Knollmann, B.C. 2023. RyR2 inhibition with dantrolene is antiarrhythmic, prevents further pathological remodeling, and improves cardiac function in chronic ischemic heart disease. *Journal of Molecular and Cellular Cardiology* 181, pp. 67–78. doi: 10.1016/j.yjmcc.2023.05.009.

Schnitzbauer, J., Strauss, M.T., Schlichthaerle, T., Schueder, F. and Jungmann, R. 2017. Super-resolution microscopy with DNA-PAINT. *Nature Protocols* 12(6), pp. 1198–1228. doi: 10.1038/nprot.2017.024.

Schröder, F. et al. 1998. Increased Availability and Open Probability of Single L-Type Calcium Channels From Failing Compared With Nonfailing Human Ventricle. *Circulation* 98(10), pp. 969–976. doi: 10.1161/01.CIR.98.10.969.

Schröder, M. and Kaufman, R.J. 2005. The Mammalian Unfolded Protein Response. *Annual Review of Biochemistry* 74(1), pp. 739–789. doi: 10.1146/annurev.biochem.73.011303.074134.

Schrödinger, L. and DeLano, W. 2020. PyMOL.

Schultheiss, H.-P. et al. 2019. Dilated cardiomyopathy. *Nature Reviews Disease Primers* 5(1), p. 32. doi: 10.1038/s41572-019-0084-1.

Schulz, R.A. and Yutzey, K.E. 2004. Calcineurin signaling and NFAT activation in cardiovascular and skeletal muscle development. *Developmental Biology* 266(1), pp. 1–16. doi: 10.1016/j.ydbio.2003.10.008.

Schwinger, R.H.G. 2021. Pathophysiology of heart failure. *Cardiovascular Diagnosis and Therapy* 11(1), pp. 263–276. doi: 10.21037/cdt-20-302.

Sedej, S. et al. 2010. Na+-dependent SR Ca2+ overload induces arrhythmogenic events in mouse cardiomyocytes with a human CPVT mutation. *Cardiovascular Research* 87(1), pp. 50–59. doi: 10.1093/cvr/cvq007.

Segura, A.M., Frazier, O.H. and Buja, L.M. 2014. Fibrosis and heart failure. *Heart Failure Reviews* 19(2), pp. 173–185. doi: 10.1007/s10741-012-9365-4.

Seidel, M., Lowri Thomas, N., Williams, A.J., Lai, F.A. and Zissimopoulos, S. 2015. Dantrolene rescues aberrant N-terminus intersubunit interactions in mutant pro-arrhythmic cardiac ryanodine receptors. *Cardiovascular Research* 105(1), pp. 118–128. doi: 10.1093/cvr/cvu240.

Seo, K. et al. 2023. Improved Cardiac Performance and Decreased Arrhythmia in Hypertrophic Cardiomyopathy With Non–β-Blocking R-Enantiomer Carvedilol. *Circulation* 148(21), pp. 1691–1704. doi: 10.1161/CIRCULATIONAHA.123.065017.

Shan, J. et al. 2010a. Phosphorylation of the ryanodine receptor mediates the cardiac fight or flight response in mice. *Journal of Clinical Investigation* 120(12), pp. 4388–4398. doi: 10.1172/JCI32726.

Shan, J. et al. 2010b. Role of chronic ryanodine receptor phosphorylation in heart failure and β-adrenergic receptor blockade in mice. *Journal of Clinical Investigation* 120(12), pp. 4375–4387. doi: 10.1172/JCI37649.

Shan, J., Xie, W., Betzenhauser, M., Reiken, S., Chen, B.-X., Wronska, A. and Marks, A.R. 2012. Calcium Leak Through Ryanodine Receptors Leads to Atrial Fibrillation in 3 Mouse

Models of Catecholaminergic Polymorphic Ventricular Tachycardia. *Circulation Research* 111(6), pp. 708–717. doi: 10.1161/CIRCRESAHA.112.273342.

Shannon, T.R., Ginsburg, K.S. and Bers, D.M. 2002. Quantitative Assessment of the SR Ca $^{2+}$ Leak-Load Relationship. *Circulation Research* 91(7), pp. 594–600. doi: 10.1161/01.RES.0000036914.12686.28.

Shapiro, S.S. and Wilk, M.B. 1965. An analysis of variance test for normality (complete samples). *Biometrika* 52(3–4), pp. 591–611. doi: 10.1093/biomet/52.3-4.591.

Sheard, T.M.D., Hurley, M.E., Smith, A.J., Colyer, J., White, E. and Jayasinghe, I. 2022. Three-dimensional visualization of the cardiac ryanodine receptor clusters and the molecular-scale fraying of dyads. *Philosophical Transactions of the Royal Society B: Biological Sciences* 377(1864). doi: 10.1098/rstb.2021.0316.

Shen, X. et al. 2019. 3D dSTORM imaging reveals novel detail of ryanodine receptor localization in rat cardiac myocytes. *The Journal of Physiology* 597(2), pp. 399–418. doi: 10.1113/JP277360.

Shimizu, W. et al. 1991. Early afterdepolarizations induced by isoproterenol in patients with congenital long QT syndrome. *Circulation* 84(5), pp. 1915–1923. doi: 10.1161/01.CIR.84.5.1915.

Shinnawi, R. et al. 2015. Monitoring Human-Induced Pluripotent Stem Cell-Derived Cardiomyocytes with Genetically Encoded Calcium and Voltage Fluorescent Reporters. *Stem Cell Reports* 5(4), pp. 582–596. doi: 10.1016/j.stemcr.2015.08.009.

Sibbles, E.T., Waddell, H.M.M., Mereacre, V., Jones, P.P. and Munro, M.L. 2022. The function and regulation of calsequestrin-2: implications in calcium-mediated arrhythmias. *Biophysical Reviews* 14(1), pp. 329–352. doi: 10.1007/s12551-021-00914-6.

Sikkel, M.B. et al. 2013. Flecainide reduces Ca2+ spark and wave frequency via inhibition of the sarcolemmal sodium current. *Cardiovascular Research* 98(2), pp. 286–296. doi: 10.1093/cvr/cvt012.

Sim, N.-L., Kumar, P., Hu, J., Henikoff, S., Schneider, G. and Ng, P.C. 2012. SIFT web server: predicting effects of amino acid substitutions on proteins. *Nucleic Acids Research* 40(W1), pp. W452–W457. doi: 10.1093/nar/gks539.

Sitsapesan, R., Montgomery, R.A.P. and Williams, A.J. 1995. New Insights Into the Gating Mechanisms of Cardiac Ryanodine Receptors Revealed by Rapid Changes in Ligand Concentration. *Circulation Research* 77(4), pp. 765–772. doi: 10.1161/01.RES.77.4.765.

Sitsapesan, R. and Williams, A.J. 1990. Mechanisms of caffeine activation of single calcium-release channels of sheep cardiac sarcoplasmic reticulum. *The Journal of Physiology* 423(1), pp. 425–439. doi: 10.1113/jphysiol.1990.sp018031.

Sitsapesan, R. and Williams, A.J. 1994. Regulation of the gating of the sheep cardiac sarcoplasmic reticulum ca2+-release channel by luminal Ca2+. *The Journal of Membrane Biology* 137(3). doi: 10.1007/BF00232590.

Sleiman, Y., Lacampagne, A. and Meli, A.C. 2022. Correction: “Ryanopathies” and RyR2 dysfunctions: can we further decipher them using in vitro human disease models? *Cell death & disease* 13(12), p. 1014. doi: 10.1038/s41419-022-05468-3.

Smania, M.A. 2025. Hypertrophic cardiomyopathy overview: Genetics, screening, and treatment. *Journal of the American Association of Nurse Practitioners* 37(3), pp. 142–144. doi: 10.1097/JXX.0000000000001109.

Smith, J.S., Coronado, R. and Meissner, G. 1986. Single channel measurements of the calcium release channel from skeletal muscle sarcoplasmic reticulum. Activation by Ca2+ and ATP and modulation by Mg2+. *The Journal of general physiology* 88(5), pp. 573–588. doi: 10.1085/jgp.88.5.573.

Sobie, E., Guatimosim, S., Gomezviquez, L., Song, L., Hartmann, H., Saleetjafri, M. and Lederer, W. 2006. The Ca2+ leak paradox and “rogue ryanodine receptors”: SR Ca2+ efflux theory and practice. *Progress in Biophysics and Molecular Biology* 90(1–3), pp. 172–185. doi: 10.1016/j.pbiomolbio.2005.06.010.

Sobie, E.A., Dilly, K.W., dos Santos Cruz, J., Lederer, W.J. and Saleet Jafri, M. 2002. Termination of Cardiac Ca2+ Sparks: An Investigative Mathematical Model of Calcium-

Induced Calcium Release. *Biophysical Journal* 83(1), pp. 59–78. doi: 10.1016/S0006-3495(02)75149-7.

Song, S., Tan, J., Miao, Y. and Zhang, Q. 2018. Crosstalk of ER stress-mediated autophagy and ER-phagy: Involvement of UPR and the core autophagy machinery. *Journal of Cellular Physiology* 233(5), pp. 3867–3874. doi: 10.1002/jcp.26137.

Sorrentino, V. and Volpe, P. 1993. Ryanodine receptors: how many, where and why? *Trends in Pharmacological Sciences* 14(3), pp. 98–103. doi: 10.1016/0165-6147(93)90072-R.

Souidi, M. et al. 2024. Ryanodine receptor dysfunction causes senescence and fibrosis in Duchenne dilated cardiomyopathy. *Journal of Cachexia, Sarcopenia and Muscle* 15(2), pp. 536–551. doi: 10.1002/jcsm.13411.

Stange, M., Xu, L., Balshaw, D., Yamaguchi, N. and Meissner, G. 2003. Characterization of Recombinant Skeletal Muscle (Ser-2843) and Cardiac Muscle (Ser-2809) Ryanodine Receptor Phosphorylation Mutants. *Journal of Biological Chemistry* 278(51), pp. 51693–51702. doi: 10.1074/jbc.M310406200.

Steinberg, C., Roston, T.M., van der Werf, C., Sanatani, S., Chen, S.R.W., Wilde, A.A.M. and Krahn, A.D. 2023. RYR2-ryanodinopathies: from calcium overload to calcium deficiency. *Europace* 25(6). doi: 10.1093/europace/euad156.

Stenson, P.D. et al. 2003. Human Gene Mutation Database (HGMD ®): 2003 update. *Human Mutation* 21(6), pp. 577–581. doi: 10.1002/humu.10212.

Stern, M.D. 1992. Theory of excitation-contraction coupling in cardiac muscle. *Biophysical Journal* 63(2), pp. 497–517. doi: 10.1016/S0006-3495(92)81615-6.

Stern, M.D., Song, L.-S., Cheng, H., Sham, J.S.K., Yang, H.T., Boheler, K.R. and Ríos, E. 1999. Local Control Models of Cardiac Excitation–Contraction Coupling. *The Journal of General Physiology* 113(3), pp. 469–489. doi: 10.1085/jgp.113.3.469.

Stewart, R. et al. 2008. Single-Channel Characterization of the Rabbit Recombinant RyR2 Reveals a Novel Inactivation Property of Physiological Concentrations of ATP. *Journal of Membrane Biology* 222(2), pp. 65–77. doi: 10.1007/s00232-008-9102-z.

Stoner, M.W., McTiernan, C.F., Scott, I. and Manning, J.R. 2020. Calreticulin expression in human cardiac myocytes induces ER stress-associated apoptosis. *Physiological Reports* 8(8). doi: 10.14814/phy2.14400.

Suetomi, T. et al. 2011. Mutation-Linked Defective Interdomain Interactions Within Ryanodine Receptor Cause Aberrant Ca $^{2+}$ Release Leading to Catecholaminergic Polymorphic Ventricular Tachycardia. *Circulation* 124(6), pp. 682–694. doi: 10.1161/CIRCULATIONAHA.111.023259.

Sun, B. et al. 2021. Cardiac ryanodine receptor calcium release deficiency syndrome. *Science Translational Medicine* 13(579). doi: 10.1126/scitranslmed.aba7287.

Sun, N. et al. 2012. Patient-Specific Induced Pluripotent Stem Cells as a Model for Familial Dilated Cardiomyopathy. *Science Translational Medicine* 4(130). doi: 10.1126/scitranslmed.3003552.

Takeshima, H. et al. 1989. Primary structure and expression from complementary DNA of skeletal muscle ryanodine receptor. *Nature* 339(6224), pp. 439–445. doi: 10.1038/339439a0.

Takeshima, H. 2000. JunctophilinsA Novel Family of Junctional Membrane Complex Proteins. *Molecular Cell* 6(1), pp. 11–22. doi: 10.1016/S1097-2765(00)00003-4.

Takeshima, H., Komazaki, S., Nishi, M., Iino, M. and Kangawa, K. 2000. Junctophilins. *Molecular Cell* 6(1), pp. 11–22. doi: 10.1016/S1097-2765(05)00005-5.

Tan, E., Chin, C.S.H., Lim, Z.F.S. and Ng, S.K. 2021. HEK293 Cell Line as a Platform to Produce Recombinant Proteins and Viral Vectors. *Frontiers in Bioengineering and Biotechnology* 9. doi: 10.3389/fbioe.2021.796991.

Tang, W. 2002. Calmodulin modulation of proteins involved in excitation-contraction coupling. *Frontiers in Bioscience* 7(1–3), p. d1583. doi: 10.2741/tang.

Tang, Y., Tian, X., Wang, R., Fill, M. and Chen, S.R.W. 2012. Abnormal Termination of Ca $^{2+}$ Release Is a Common Defect of RyR2 Mutations Associated With Cardiomyopathies. *Circulation Research* 110(7), pp. 968–977. doi: 10.1161/CIRCRESAHA.111.256560.

Tateishi, H. et al. 2008. Defective domain-domain interactions within the ryanodine receptor as a critical cause of diastolic Ca2+ leak in failing hearts. *Cardiovascular Research* 81(3), pp. 536–545. doi: 10.1093/cvr/cvn303.

Terentyev, D., Viatchenko-Karpinski, S., Gyorke, I., Terentyeva, R. and Gyorke, S. 2003. Protein Phosphatases Decrease Sarcoplasmic Reticulum Calcium Content by Stimulating Calcium Release in Cardiac Myocytes. *The Journal of Physiology* 552(1), pp. 109–118. doi: 10.1113/jphysiol.2003.046367.

Terentyev, D., Viatchenko-Karpinski, S., Valdivia, H.H., Escobar, A.L. and Györke, S. 2002. Luminal Ca $^{2+}$ Controls Termination and Refractory Behavior of Ca $^{2+}$ -Induced Ca $^{2+}$ Release in Cardiac Myocytes. *Circulation Research* 91(5), pp. 414–420. doi: 10.1161/01.RES.0000032490.04207.BD.

Tester, D.J., Dura, M., Carturan, E., Reiken, S., Wronska, A., Marks, A.R. and Ackerman, M.J. 2007. A mechanism for sudden infant death syndrome (SIDS): Stress-induced leak via ryanodine receptors. *Heart Rhythm* 4(6), pp. 733–739. doi: 10.1016/j.hrthm.2007.02.026.

Tester, D.J., Kopplin, L.J., Will, M.L. and Ackerman, M.J. 2005. Spectrum and prevalence of cardiac ryanodine receptor (RyR2) mutations in a cohort of unrelated patients referred explicitly for long QT syndrome genetic testing. *Heart Rhythm* 2(10), pp. 1099–1105. doi: 10.1016/j.hrthm.2005.07.012.

Tester, D.J., Medeiros-Domingo, A., Will, M.L., Haglund, C.M. and Ackerman, M.J. 2012. Cardiac channel molecular autopsy: insights from 173 consecutive cases of autopsy-negative sudden unexplained death referred for postmortem genetic testing. *Mayo Clinic proceedings* 87(6), pp. 524–39. doi: 10.1016/j.mayocp.2012.02.017.

Thomas, N.L., George, C.H. and Lai, F.A. 2004. Functional heterogeneity of ryanodine receptor mutations associated with sudden cardiac death. *Cardiovascular Research* 64(1), pp. 52–60. doi: 10.1016/j.cardiores.2004.06.009.

Thomas, N.L., Lai, F.A. and George, C.H. 2005. Differential Ca2+ sensitivity of RyR2 mutations reveals distinct mechanisms of channel dysfunction in sudden cardiac death. *Biochemical and Biophysical Research Communications* 331(1), pp. 231–238. doi: 10.1016/j.bbrc.2005.02.194.

Thomas, P. and Smart, T.G. 2005. HEK293 cell line: A vehicle for the expression of recombinant proteins. *Journal of Pharmacological and Toxicological Methods* 51(3), pp. 187–200. doi: 10.1016/j.vascn.2004.08.014.

Tian, X., Tang, Y., Liu, Y., Wang, R. and Chen, S.R.W. 2013. Calmodulin modulates the termination threshold for cardiac ryanodine receptor-mediated Ca2+ release. *Biochemical Journal* 455(3), pp. 367–375. doi: 10.1042/BJ20130805.

Timerman, A.P., Ogunbumni, E., Freund, E., Wiederrecht, G., Marks, A.R. and Fleischer, S. 1993. The calcium release channel of sarcoplasmic reticulum is modulated by FK-506-binding protein. Dissociation and reconstitution of FKBP-12 to the calcium release channel of skeletal muscle sarcoplasmic reticulum. *The Journal of biological chemistry* 268(31), pp. 22992–9.

Timerman, A.P., Onoue, H., Xin, H.-B., Barg, S., Copello, J., Wiederrecht, G. and Fleischer, S. 1996. Selective Binding of FKBP12.6 by the Cardiac Ryanodine Receptor. *Journal of Biological Chemistry* 271(34), pp. 20385–20391. doi: 10.1074/jbc.271.34.20385.

Tinker, A. et al. 1996. Electrophysiological effects of ryanodine derivatives on the sheep cardiac sarcoplasmic reticulum calcium-release channel. *Biophysical Journal* 70(5), pp. 2110–2119. doi: 10.1016/S0006-3495(96)79777-1.

Tinker, A. and Williams, A.J. 1992. Divalent cation conduction in the ryanodine receptor channel of sheep cardiac muscle sarcoplasmic reticulum. *The Journal of general physiology* 100(3), pp. 479–493. doi: 10.1085/jgp.100.3.479.

Tinker, A. and Williams, A.J. 1993. Using large organic cations to probe the nature of ryanodine modification in the sheep cardiac sarcoplasmic reticulum calcium release channel. *Biophysical Journal* 65(4), pp. 1678–1683. doi: 10.1016/S0006-3495(93)81201-3.

Tiso, N. 2001. Identification of mutations in the cardiac ryanodine receptor gene in families affected with arrhythmogenic right ventricular cardiomyopathy type 2 (ARVD2). *Human Molecular Genetics* 10(3), pp. 189–194. doi: 10.1093/hmg/10.3.189.

Tiso, N., Salamon, M., Bagattin, A., Danieli, G.A., Argenton, F. and Bortolussi, M. 2002. The binding of the RyR2 calcium channel to its gating protein FKBP12.6 is oppositely affected by

ARVD2 and VTSIP mutations. *Biochemical and Biophysical Research Communications* 299(4), pp. 594–598. doi: 10.1016/S0006-291X(02)02689-X.

Titus, E.W., Deiter, F.H., Shi, C., Wojciak, J., Scheinman, M., Jura, N. and Deo, R.C. 2020. The structure of a calsequestrin filament reveals mechanisms of familial arrhythmia. *Nature Structural & Molecular Biology* 27(12), pp. 1142–1151. doi: 10.1038/s41594-020-0510-9.

Tong, J., Du, G.G., Chen, S.R. and MacLennan, D.H. 1999a. HEK-293 cells possess a carbachol- and thapsigargin-sensitive intracellular Ca2+ store that is responsive to stop-flow medium changes and insensitive to caffeine and ryanodine. *The Biochemical journal* 343 Pt 1(Pt 1), pp. 39–44.

Tong, J., McCarthy, T. V. and MacLennan, D.H. 1999b. Measurement of Resting Cytosolic Ca2+ Concentrations and Ca2+ Store Size in HEK-293 Cells Transfected with Malignant Hyperthermia or Central Core Disease Mutant Ca2+ Release Channels. *Journal of Biological Chemistry* 274(2), pp. 693–702. doi: 10.1074/jbc.274.2.693.

Tordai, H., Torres, O., Csepi, M., Padányi, R., Lukács, G.L. and Hegedűs, T. 2024. Analysis of AlphaMissense data in different protein groups and structural context. *Scientific Data* 11(1), p. 495. doi: 10.1038/s41597-024-03327-8.

Toyofuku, T., Kurzydlowski, K., Tada, M. and MacLennan, D.H. 1994. Amino acids Glu2 to Ile18 in the cytoplasmic domain of phospholamban are essential for functional association with the Ca(2+)-ATPase of sarcoplasmic reticulum. *The Journal of biological chemistry* 269(4), pp. 3088–94.

Tripathy, A. and Meissner, G. 1996. Sarcoplasmic reticulum lumenal Ca2+ has access to cytosolic activation and inactivation sites of skeletal muscle Ca2+ release channel. *Biophysical Journal* 70(6), pp. 2600–2615. doi: 10.1016/S0006-3495(96)79831-4.

Uchinoumi, H. et al. 2010a. Catecholaminergic Polymorphic Ventricular Tachycardia Is Caused by Mutation-Linked Defective Conformational Regulation of the Ryanodine Receptor. *Circulation Research* 106(8), pp. 1413–1424. doi: 10.1161/CIRCRESAHA.109.209312.

Uchinoumi, H. et al. 2010b. Catecholaminergic Polymorphic Ventricular Tachycardia Is Caused by Mutation-Linked Defective Conformational Regulation of the Ryanodine

Receptor. *Circulation Research* 106(8), pp. 1413–1424. doi: 10.1161/CIRCRESAHA.109.209312.

Uchinoumi, H. et al. 2016. CaMKII-dependent phosphorylation of RyR2 promotes targetable pathological RyR2 conformational shift. *Journal of Molecular and Cellular Cardiology* 98, pp. 62–72. doi: 10.1016/j.yjmcc.2016.06.007.

Uchinoumi, H. et al. 2025. Structural instability of ryanodine receptor 2 causes endoplasmic reticulum (ER) dysfunction as well as sarcoplasmic reticulum (SR) dysfunction. *Journal of Cardiology*. doi: 10.1016/j.jjcc.2025.02.003.

Uehara, A. et al. 2017. Extensive Ca2+ leak through K4750Q cardiac ryanodine receptors caused by cytosolic and luminal Ca2+ hypersensitivity. *Journal of General Physiology* 149(2), pp. 199–218. doi: 10.1085/jgp.201611624.

Ullah, G., Daniel Mak, D.-O. and Pearson, J.E. 2012. A data-driven model of a modal gated ion channel: The inositol 1,4,5-trisphosphate receptor in insect Sf9 cells. *Journal of General Physiology* 140(2), pp. 159–173. doi: 10.1085/jgp.201110753.

Venetucci, L.A., Trafford, A.W., O'Neill, S.C. and Eisner, D.A. 2007a. The sarcoplasmic reticulum and arrhythmogenic calcium release. *Cardiovascular Research* 77(2), pp. 285–292. doi: 10.1093/cvr/cvm009.

Venetucci, L.A., Trafford, A.W., O'Neill, S.C. and Eisner, D.A. 2007b. The sarcoplasmic reticulum and arrhythmogenic calcium release. *Cardiovascular Research* 77(2), pp. 285–292. doi: 10.1093/cvr/cvm009.

Venturi, E., Galfré, E., O'Brien, F., Pitt, S.J., Bellamy, S., Sessions, R.B. and Sitsapesan, R. 2014. FKBP12.6 Activates RyR1: Investigating the Amino Acid Residues Critical for Channel Modulation. *Biophysical Journal* 106(4), pp. 824–833. doi: 10.1016/j.bpj.2013.12.041.

Veress, R., Terentyeva, R., Perger, F., Belevych, A.E., Terentyev, D.A. and Hamilton, S. 2024. ER stress contributes to cardiac arrhythmia in catecholaminergic polymorphic ventricular tachycardia. *Biophysical Journal* 123(3), p. 457a. doi: 10.1016/j.bpj.2023.11.2780.

Viero, C., Thomas, N.L., Euden, J., Mason, S.A., George, C.H. and Williams, A.J. 2012. Techniques and Methodologies to Study the Ryanodine Receptor at the Molecular, Subcellular and Cellular Level. pp. 183–215. doi: 10.1007/978-94-007-2888-2_8.

Völkers, M. et al. 2007. S100A1 decreases calcium spark frequency and alters their spatial characteristics in permeabilized adult ventricular cardiomyocytes. *Cell Calcium* 41(2), pp. 135–143. doi: 10.1016/j.ceca.2006.06.001.

Walker, M. 2003. Repolarization alternans: implications for the mechanism and prevention of sudden cardiac death. *Cardiovascular Research* 57(3), pp. 599–614. doi: 10.1016/S0008-6363(02)00737-X.

Walker, M.A. et al. 2014. Superresolution Modeling of Calcium Release in the Heart. *Biophysical Journal* 107(12), pp. 3018–3029. doi: 10.1016/j.bpj.2014.11.003.

Walsh, R. et al. 2017. Reassessment of Mendelian gene pathogenicity using 7,855 cardiomyopathy cases and 60,706 reference samples. *Genetics in Medicine* 19(2), pp. 192–203. doi: 10.1038/gim.2016.90.

Walweel, K. et al. 2017a. Ryanodine receptor modification and regulation by intracellular Ca2+ and Mg2+ in healthy and failing human hearts. *Journal of Molecular and Cellular Cardiology* 104, pp. 53–62. doi: 10.1016/j.yjmcc.2017.01.016.

Walweel, K., Beard, N., van Helden, D.F. and Laver, D.R. 2023a. Dantrolene inhibition of ryanodine channels (RyR2) in artificial lipid bilayers depends on FKBP12.6. *Journal of General Physiology* 155(8). doi: 10.1085/jgp.202213277.

Walweel, K., Beard, N., van Helden, D.F. and Laver, D.R. 2023b. Dantrolene inhibition of ryanodine channels (RyR2) in artificial lipid bilayers depends on FKBP12.6. *Journal of General Physiology* 155(8). doi: 10.1085/jgp.202213277.

Walweel, K., Oo, Y.W. and Laver, D.R. 2017b. The emerging role of calmodulin regulation of RyR2 in controlling heart rhythm, the progression of heart failure and the antiarrhythmic action of dantrolene. *Clinical and Experimental Pharmacology and Physiology* 44(1), pp. 135–142. doi: 10.1111/1440-1681.12669.

Wang, G., Zhao, N., Zhong, S., Wang, Y. and Li, J. 2019. Safety and efficacy of flecainide for patients with catecholaminergic polymorphic ventricular tachycardia. *Medicine* 98(34), p. e16961. doi: 10.1097/MD.0000000000016961.

Wang, W. et al. 2014. Reduced junctional Na^{+}/Ca^{2+} -exchanger activity contributes to sarcoplasmic reticulum Ca^{2+} leak in junctophilin-2-deficient mice. *American Journal of Physiology-Heart and Circulatory Physiology* 307(9), pp. H1317–H1326. doi: 10.1152/ajpheart.00413.2014.

Wang, Y. et al. 2025. Calcium handling remodeling in dilated cardiomyopathy: From molecular mechanisms to targeted therapies. *Channels* 19(1). doi: 10.1080/19336950.2025.2519545.

Watanabe, H. et al. 2009. Flecainide prevents catecholaminergic polymorphic ventricular tachycardia in mice and humans. *Nature Medicine* 15(4), pp. 380–383. doi: 10.1038/nm.1942.

Wehrens, X.H.T. et al. 2003. FKBP12.6 Deficiency and Defective Calcium Release Channel (Ryanodine Receptor) Function Linked to Exercise-Induced Sudden Cardiac Death. *Cell* 113(7), pp. 829–840. doi: 10.1016/S0092-8674(03)00434-3.

Wehrens, X.H.T. et al. 2004a. Protection from Cardiac Arrhythmia Through Ryanodine Receptor-Stabilizing Protein Calstabin2. *Science* 304(5668), pp. 292–296. doi: 10.1126/science.1094301.

Wehrens, X.H.T. 2007. Leaky ryanodine receptors cause delayed afterdepolarizations and ventricular arrhythmias. *European Heart Journal* 28(9), pp. 1054–1056. doi: 10.1093/eurheartj/ehm068.

Wehrens, X.H.T., Lehnart, S.E. and Marks, A.R. 2005. INTRACELLULAR CALCIUM RELEASE AND CARDIAC DISEASE. *Annual Review of Physiology* 67(1), pp. 69–98. doi: 10.1146/annurev.physiol.67.040403.114521.

Wehrens, X.H.T., Lehnart, S.E., Reiken, S., Vest, J.A., Wronska, A. and Marks, A.R. 2006. Ryanodine receptor/calcium release channel PKA phosphorylation: A critical mediator of heart failure progression. *Proceedings of the National Academy of Sciences* 103(3), pp. 511–518. doi: 10.1073/pnas.0510113103.

Wehrens, X.H.T., Lehnart, S.E., Reiken, S.R. and Marks, A.R. 2004b. Ca 2+ /Calmodulin-Dependent Protein Kinase II Phosphorylation Regulates the Cardiac Ryanodine Receptor. *Circulation Research* 94(6). doi: 10.1161/01.RES.0000125626.33738.E2.

Wei, J. et al. 2023. RyR2 Serine-2030 PKA Site Governs Ca2+ Release Termination and Ca 2+ Alternans. *Circulation Research* 132(2). doi: 10.1161/CIRCRESAHA.122.321177.

Weiss, J.N., Karma, A., Shiferaw, Y., Chen, P.-S., Garfinkel, A. and Qu, Z. 2006. From Pulsus to Pulseless. *Circulation Research* 98(10), pp. 1244–1253. doi: 10.1161/01.RES.0000224540.97431.f0.

Welch, W., Rheault, S., West, D.J. and Williams, A.J. 2004. A Model of the Putative Pore Region of the Cardiac Ryanodine Receptor Channel. *Biophysical Journal* 87(4), pp. 2335–2351. doi: 10.1529/biophysj.104.044180.

White, S.H. 1986. The Physical Nature of Planar Bilayer Membranes. In: *Ion Channel Reconstitution*. Boston, MA: Springer US, pp. 3–35. doi: 10.1007/978-1-4757-1361-9_1.

Williams, A.J., West, D.J. and Sitsapesan, R. 2001. Light at the end of the Ca2+-release channel tunnel: structures and mechanisms involved in ion translocation in ryanodine receptor channels. *Quarterly Reviews of Biophysics* 34(1), pp. 61–104. doi: 10.1017/S0033583501003675.

Winslow, R.L. and Greenstein, J.L. 2013. Extinguishing the Sparks. *Biophysical Journal* 104(10), pp. 2115–2117. doi: 10.1016/j.bpj.2013.04.010.

Woehlbier, U. and Hetz, C. 2011. Modulating stress responses by the UPRosome: A matter of life and death. *Trends in Biochemical Sciences* 36(6), pp. 329–337. doi: 10.1016/j.tibs.2011.03.001.

Woll, K.A., Haji-Ghassemi, O. and Van Petegem, F. 2021. Pathological conformations of disease mutant Ryanodine Receptors revealed by cryo-EM. *Nature Communications* 12(1), p. 807. doi: 10.1038/s41467-021-21141-3.

Wu, H.-D. et al. 2012. Ultrastructural remodelling of Ca2+ signalling apparatus in failing heart cells. *Cardiovascular Research* 95(4), pp. 430–438. doi: 10.1093/cvr/cvs195.

Xiao, B. et al. 2005. Characterization of a Novel PKA Phosphorylation Site, Serine-2030, Reveals No PKA Hyperphosphorylation of the Cardiac Ryanodine Receptor in Canine Heart Failure. *Circulation Research* 96(8), pp. 847–855. doi: 10.1161/01.RES.0000163276.26083.e8.

Xiao, B. et al. 2006. Ser-2030, but not Ser-2808, is the major phosphorylation site in cardiac ryanodine receptors responding to protein kinase A activation upon β-adrenergic stimulation in normal and failing hearts. *Biochemical Journal* 396(1), pp. 7–16. doi: 10.1042/BJ20060116.

Xiao, B. et al. 2007a. Functional Consequence of Protein Kinase A-dependent Phosphorylation of the Cardiac Ryanodine Receptor. *Journal of Biological Chemistry* 282(41), pp. 30256–30264. doi: 10.1074/jbc.M703510200.

Xiao, J. et al. 2007b. Removal of FKBP12.6 Does Not Alter the Conductance and Activation of the Cardiac Ryanodine Receptor or the Susceptibility to Stress-induced Ventricular Arrhythmias. *Journal of Biological Chemistry* 282(48), pp. 34828–34838. doi: 10.1074/jbc.M707423200.

Xiao, Z. et al. 2016. Enhanced Cytosolic Ca2+ Activation Underlies a Common Defect of Central Domain Cardiac Ryanodine Receptor Mutations Linked to Arrhythmias. *Journal of Biological Chemistry* 291(47), pp. 24528–24537. doi: 10.1074/jbc.M116.756528.

Xie, L.-H., Sato, D., Garfinkel, A., Qu, Z. and Weiss, J.N. 2008. Intracellular Ca Alternans: Coordinated Regulation by Sarcoplasmic Reticulum Release, Uptake, and Leak. *Biophysical Journal* 95(6), pp. 3100–3110. doi: 10.1529/biophysj.108.130955.

Xie, L.-H. and Weiss, J.N. 2009. Arrhythmogenic consequences of intracellular calcium waves. *American Journal of Physiology-Heart and Circulatory Physiology* 297(3), pp. H997–H1002. doi: 10.1152/ajpheart.00390.2009.

Xu, J., Liao, C., Yin, C.-C., Li, G., Zhu, Y. and Sun, F. 2024. In situ structural insights into the excitation-contraction coupling mechanism of skeletal muscle. *Science Advances* 10(12). doi: 10.1126/sciadv.adl1126.

Xu, L., Chirasani, V.R., Carter, J.S., Pasek, D.A., Dokholyan, N. V., Yamaguchi, N. and Meissner, G. 2018. Ca2+-mediated activation of the skeletal-muscle ryanodine receptor ion

channel. *Journal of Biological Chemistry* 293(50), pp. 19501–19509. doi: 10.1074/jbc.RA118.004453.

Xu, L., Eu, J.P., Meissner, G. and Stamler, J.S. 1998. Activation of the Cardiac Calcium Release Channel (Ryanodine Receptor) by Poly-S-Nitrosylation. *Science* 279(5348), pp. 234–237. doi: 10.1126/science.279.5348.234.

Xu, L., Mann, G. and Meissner, G. 1996. Regulation of Cardiac Ca2+ Release Channel (Ryanodine Receptor) by Ca 2+, H+ , Mg2+, and Adenine Nucleotides Under Normal and Simulated Ischemic Conditions. *Circulation Research* 79(6), pp. 1100–1109. doi: 10.1161/01.RES.79.6.1100.

Xu, L. and Meissner, G. 1998. Regulation of Cardiac Muscle Ca2+ Release Channel by Sarcoplasmic Reticulum Lumenal Ca2+. *Biophysical Journal* 75(5), pp. 2302–2312. doi: 10.1016/S0006-3495(98)77674-X.

Yakubovich, D., Pastushenko, V., Bitler, A., Dessauer, C.W. and Dascal, N. 2000. Slow modal gating of single G protein-activated K^+ channels expressed in *Xenopus* oocytes. *The Journal of Physiology* 524(3), pp. 737–755. doi: 10.1111/j.1469-7793.2000.00737.x.

Yamaguchi, N., Chakraborty, A., Huang, T.-Q., Xu, L., Gomez, A.C., Pasek, D.A. and Meissner, G. 2013. Cardiac hypertrophy associated with impaired regulation of cardiac ryanodine receptor by calmodulin and S100A1. *American Journal of Physiology-Heart and Circulatory Physiology* 305(1), pp. H86–H94. doi: 10.1152/ajpheart.00144.2013.

Yamaguchi, N., Xu, L., Pasek, D.A., Evans, K.E. and Meissner, G. 2003. Molecular Basis of Calmodulin Binding to Cardiac Muscle Ca2+ Release Channel (Ryanodine Receptor). *Journal of Biological Chemistry* 278(26), pp. 23480–23486. doi: 10.1074/jbc.M301125200.

Yan, Y., Liu, J., Wei, C., Li, K., Xie, W., Wang, Y. and Cheng, H. 2008. Bidirectional regulation of Ca2+ sparks by mitochondria-derived reactive oxygen species in cardiac myocytes. *Cardiovascular Research* 77(2), pp. 432–441. doi: 10.1093/cvr/cvm047.

Yang, Z., Ikemoto, N., Lamb, G. and Steele, D. 2006. The RyR2 central domain peptide DPc10 lowers the threshold for spontaneous Ca2+ release in permeabilized cardiomyocytes. *Cardiovascular Research* 70(3), pp. 475–485. doi: 10.1016/j.cardiores.2006.03.001.

Yano, M. et al. 2003. FKBP12.6-Mediated Stabilization of Calcium-Release Channel (Ryanodine Receptor) as a Novel Therapeutic Strategy Against Heart Failure. *Circulation* 107(3), pp. 477–484. doi: 10.1161/01.CIR.0000044917.74408.BE.

Yano, Y. et al. 2023. Stabilizing cardiac ryanodine receptor with dantrolene treatment prevents left ventricular remodeling in pressure-overloaded heart failure mice. *Biochemical and Biophysical Research Communications* 642, pp. 175–184. doi: 10.1016/j.bbrc.2022.12.063.

Yao, A. et al. 1998. Effects of Overexpression of the Na^{+}-Ca^{2+} Exchanger on $[Ca^{2+}]_i$ Transients in Murine Ventricular Myocytes. *Circulation Research* 82(6), pp. 657–665. doi: 10.1161/01.RES.82.6.657.

Yin, C.C. and Lai, F.A. 2000. Intrinsic lattice formation by the ryanodine receptor calcium-release channel. *Nature Cell Biology* 2(9), pp. 669–671. doi: 10.1038/35023625.

Yin, L. et al. 2021. Impaired Binding to Junctophilin-2 and Nanostructural Alteration in CPVT Mutation. *Circulation Research* 129(3). doi: 10.1161/CIRCRESAHA.121.319094.

Yonkunas, M.J., Fill, M. and Gillespie, D. 2012. Modeling Ca2+ Induced Ca2+ Release Between Neighboring Ryanodine Receptors. *Biophysical Journal* 102(3), p. 138a. doi: 10.1016/j.bpj.2011.11.762.

Yoon, G.S., Lee, H., Jung, Y., Yu, E., Moon, H.B., Song, K. and Lee, I. 2000. Nuclear matrix of calreticulin in hepatocellular carcinoma. *Cancer research* 60(4), pp. 1117–20.

Yuchi, Z., Lau, K. and Van Petegem, F. 2012. Disease Mutations in the Ryanodine Receptor Central Region: Crystal Structures of a Phosphorylation Hot Spot Domain. *Structure* 20(7), pp. 1201–1211. doi: 10.1016/j.str.2012.04.015.

Yuchi, Z., Yuen, S.M.W.K., Lau, K., Underhill, A.Q., Cornea, R.L., Fessenden, J.D. and Van Petegem, F. 2015. Crystal structures of ryanodine receptor SPRY1 and tandem-repeat domains reveal a critical FKBP12 binding determinant. *Nature Communications* 6(1), p. 7947. doi: 10.1038/ncomms8947.

Zahradníková, A. and Zahradník, I. 1995. Description of modal gating of the cardiac calcium release channel in planar lipid membranes. *Biophysical Journal* 69(5), pp. 1780–1788. doi: 10.1016/S0006-3495(95)80048-2.

Zahradníková, A. and Zahradník, I. 1999. Analysis of calcium-induced calcium release in cardiac sarcoplasmic reticulum vesicles using models derived from single-channel data. *Biochimica et Biophysica Acta (BBA) - Biomembranes* 1418(2), pp. 268–284. doi: 10.1016/S0005-2736(99)00036-X.

Zalk, R. et al. 2015. Structure of a mammalian ryanodine receptor. *Nature* 517(7532), pp. 44–49. doi: 10.1038/nature13950.

Zhang, H. et al. 2012. Hyperphosphorylation of the Cardiac Ryanodine Receptor at Serine 2808 Is Not Involved in Cardiac Dysfunction After Myocardial Infarction. *Circulation Research* 110(6), pp. 831–840. doi: 10.1161/CIRCRESAHA.111.255158.

Zhang, J., Jin, B., Li, L., Block, E.R. and Patel, J.M. 2005. Nitric oxide-induced persistent inhibition and nitrosylation of active site cysteine residues of mitochondrial cytochrome- *c* oxidase in lung endothelial cells. *American Journal of Physiology-Cell Physiology* 288(4), pp. C840–C849. doi: 10.1152/ajpcell.00325.2004.

Zhang, J.Z., Waddell, H.M.M., Wu, E., Dholakia, J., Okolo, C.A., McLay, J.C. and Jones, P.P. 2016. FKBPs facilitate the termination of spontaneous Ca2+ release in wild-type RyR2 but not CPVT mutant RyR2. *Biochemical Journal* 473(14), pp. 2049–2060. doi: 10.1042/BCJ20160389.

Zhang, T. and Brown, J.H. 2004. Role of Ca2+/calmodulin-dependent protein kinase II in cardiac hypertrophy and heart failure. *Cardiovascular Research* 63(3), pp. 476–486. doi: 10.1016/j.cardiores.2004.04.026.

Zhang, Y. et al. 2014. Oxidative Stress–Induced Calreticulin Expression and Translocation: New Insights into the Destruction of Melanocytes. *Journal of Investigative Dermatology* 134(1), pp. 183–191. doi: 10.1038/jid.2013.268.

Zhao, L. and Ackerman, S.L. 2006. Endoplasmic reticulum stress in health and disease. *Current Opinion in Cell Biology* 18(4), pp. 444–452. doi: 10.1016/j.ceb.2006.06.005.

Zhao, Y.-T. et al. 2015. Arrhythmogenesis in a catecholaminergic polymorphic ventricular tachycardia mutation that depresses ryanodine receptor function. *Proceedings of the National Academy of Sciences* 112(13). doi: 10.1073/pnas.1419795112.

Zhao, Z., Wen, H., Fefelova, N., Allen, C., Baba, A., Matsuda, T. and Xie, L.-H. 2012. Revisiting the ionic mechanisms of early afterdepolarizations in cardiomyocytes: predominant by Ca waves or Ca currents? *American Journal of Physiology-Heart and Circulatory Physiology* 302(8), pp. H1636–H1644. doi: 10.1152/ajpheart.00742.2011.

Zhong, X. et al. 2021. Identification of loss-of-function RyR2 mutations associated with idiopathic ventricular fibrillation and sudden death. *Bioscience Reports* 41(4). doi: 10.1042/BSR20210209.

Zhou, Q. et al. 2011. Carvedilol and its new analogs suppress arrhythmogenic store overload–induced Ca2+ release. *Nature Medicine* 17(8), pp. 1003–1009. doi: 10.1038/nm.2406.

Zima, A. and Blatter, L. 2006. Redox regulation of cardiac calcium channels and transporters. *Cardiovascular Research* 71(2), pp. 310–321. doi: 10.1016/j.cardiores.2006.02.019.

Zima, A. V. and Mazurek, S.R. 2016. Functional Impact of Ryanodine Receptor Oxidation on Intracellular Calcium Regulation in the Heart. pp. 39–62. doi: 10.1007/112_2016_2.

Zima, A. V., Picht, E., Bers, D.M. and Blatter, L.A. 2008. Termination of Cardiac Ca $^{2+}$ Sparks. *Circulation Research* 103(8). doi: 10.1161/CIRCRESAHA.107.183236.

Zissimopoulos, S. et al. 2013. Amino-terminus oligomerization regulates cardiac ryanodine receptor function. *Journal of Cell Science*. doi: 10.1242/jcs.133538.

Zissimopoulos, S. and Lai, F.A. 2005. Interaction of FKBP12.6 with the Cardiac Ryanodine Receptor C-terminal Domain. *Journal of Biological Chemistry* 280(7), pp. 5475–5485. doi: 10.1074/jbc.M412954200.

Zissimopoulos, S., Seifan, S., Maxwell, C., Williams, A.J. and Lai, F.A. 2012. Disparate Ryanodine Receptor Association with the FK506-binding Proteins in Mammalian Heart. *Journal of Cell Science*. doi: 10.1242/jcs.098012.

Zissimopoulos, S., Thomas, N.L., Jamaluddin, W.W. and Lai, F.A. 2009. FKBP12.6 binding of ryanodine receptors carrying mutations associated with arrhythmogenic cardiac disease. *Biochemical Journal* 419(2), pp. 273–278. doi: 10.1042/BJ20082324.

Zorzato, F. et al. 1990. Molecular cloning of cDNA encoding human and rabbit forms of the Ca2+ release channel (ryanodine receptor) of skeletal muscle sarcoplasmic reticulum. *The Journal of biological chemistry* 265(4), pp. 2244–56.